ABSTRACT

System, energy, and flavor dependence of jets through di-hadron correlations in heavy ion collisions

Christine Nattrass
Yale University
December 2009

QCD predicts a phase transition in nuclear matter at high energy densities. This matter, called a Quark Gluon Plasma (QGP), should have very different properties from normal nuclear matter due to its high temperature and density. The Relativistic Heavy Ion Collider (RHIC) was built to study the QGP. Jets can act as a calibrated probe to examine the QGP, however, reconstruction of jets in a heavy ion environment is difficult. Therefore jets have been studied in heavy ion collisions by investigating the spatial correlations between two intermediate to high-p_T hadrons in an event.

Previous studies have shown that the near-side di-hadron correlation peak can be decomposed into two components, a jet-like correlation and the *Ridge*. The jet-like correlation is narrow in both azimuth and pseudorapidity, while the *Ridge* is narrow in azimuth but independent of pseudorapidity within STAR's acceptance. STAR's data from Cu+Cu and Au+Au collisions at $\sqrt{s_{NN}} = 62$ GeV and $\sqrt{s_{NN}} = 200$ GeV allow comparative studies of these components in different systems and at different energies.

Data on correlations with both identified trigger particles and identified associated particles are presented, including the first studies of identified particle correlations in Cu+Cu and the energy dependence of these correlations. The yields are studied as a function of collision centrality, transverse momentum of the trigger particle, transverse momentum of the associated particle, and trigger and associated particle type. The data in this thesis indicate that the jet-like correlation component in heavy ion collisions is dominantly produced by vacuum fragmentation of hard scattered partons.

The *Ridge* component is not present in p+p or d+Au collisions. The *Ridge* yield is consistent between systems for the same N_{part} and has properties similar to the bulk. Theoretical mechanisms for the production of the *Ridge* include parton recombination, collisional energy loss in the medium (momentum kicks), and gluon brehmsstrahlung. Comparisons between the expectations of these models and the data are discussed. The data in this thesis provide key measurements to distinguish production mechanisms.

System, energy, and flavor dependence of jets through di-hadron correlations in heavy ion collisions

A Dissertation
Presented to the Faculty of the Graduate School
of
Yale University
in Candidacy for the Degree of
Doctor of Philosophy

By
Christine Nattrass

Dissertation Director: Professor John Harris

December 2009

Acknowledgements

Twenty six years ago when I was in day care, I sat on the floor scribbling on a pad of paper, ripping a sheet of paper off, wadding it up, and throwing it in the trash can. The staff at the day care came over and asked me what I was doing and I said that I was writing my dissertation. This thesis has been twenty six years in the making and many people have helped me along the way.

Many thanks to my parents for their support, encouragement, patience, and tolerance. They had to put up with science experiments all over the house - although my mother's good canning jars were off limits - and had the creativity to come up with rules such as, "You can only keep it as a pet if you can identify it," and, "No eating while standing on your head." My mother set a wonderful example for me; many of the lessons I learned watching her establish herself in psychology as I grew up are more relevant today in physics than they should be. I got my curiosity and sense of humor from my father, who taught me how to solder, taught me how to make an electromagnet, and helped me write my first computer program. Thanks to my older brother Scott, who never let me take the easy route, and taught me things that he learned in school - including what our mother termed "bus words." He has been my role model, my teacher, my coach, and the best college roommate I ever had. Thanks to my husband Ondřej, whose support has been invaluable and whose faith in my abilities has never waivered. It is a very special man who brings his wife chocolate and extra memory for her computer while she is writing up.

Many people provided company, support, and mentorship throughout my graduate studies - including, in no particular order: Sevil Salur, my Turkish sister, for unwaivering support, friendship, pan cleaning services, rides, and fun sound effects.

Sevil, I can't thank you enough for all of your support. Anthony Timmins, mi duck, for support, physics discussions, last minute plots, friendship, and always being willing to lend an ear. Àstrid Morreale, my friend and co-conspirator - when we work together, no one can stop us. Anders Knospe for support, friendship, rides, doing dishes, reaching high shelves, and serving as an excellent guide through New York city. I even forgive you for Harry Potter. Jana Bielčíková, for friendship, mentorship, teaching me how to really program well, and occasional Czech lessons. Latchezar Benetov and Peter Orth, my second semester quantum field theory study partners, for friendship and comiseration. Oana Catu, my office mate and partner in crime, for friendship, help making loud noises, rides, entertainment, and occasional venison. Just no more police motorcycles, ok? Giorgio Torrieri, for friendship and many, many, many useful physics conversations. Sarah LaPointe, for friendship, plants, chickens, and pigs. Jaro Bielčík, for friendship and always saying something funny. Betty Abelev - thanks especially for showing me the tricks to Ξ and Ω reconstruction. Thanks to Monika Sharma and Sadhana Dash for sari lessons. Thanks to Rashmi Raniwala for Indian food and Indian cooking lessons and friendship. Thanks to Elena Bruna (who gave me 🐿!), Stephen Baumgart, Richard Witt, Jörn Putschke, Boris Hippolyte, Mark Heinz, Thomas Ullrich, Xieyue Fan, Jon Gans, Mike Miller, Nikolai Smirnoff, Sofia Magkiriadou, Jonathan Bouchet, Spiros Margetis, Gene Van Buren, Jérôme Lauret, Terry Tarnowsky, Cristina Suárez, Martin Codrington, Michael Daugherity, Jan Kapitán, Petr Chaloupka, Lee Barnby, Leon Galliard, Marek Bombara, Essam Elhalhuli, George Moschelli, Jason Ulery, Lanny Ray, Jun Takahashi, Fuqiang Wang, Rene Bellwied, Christina Markert, Marco van Leeuwen, Tim Hallman, Jamie Dunlop, Bedanga Mohanty, Carla Vale, Sean Gavin, Sergei Voloshin, and Cheuk-yin Wong. Thanks to the STAR collaboration, the strangeness working group, the high-p_T working group, the jet correlations working group, and the Yale heavy ion group. Thanks to the RHIC community and the Yale Physics Department - I have been amazed by the support I've received, especially from unexpected sources.

Thanks also to my Roomba and my Scooba, my floor cleaning robots, wedding gifts from my parents-in-law, and to my dishwasher and my bread machine. Collectively these comprised the army of robots at my command, capable of doing anything short of writing my thesis. Lindt, Orion, and Figaro deserve special note for having made my Thesis Chocolate, and thanks to my in-laws for two metric tons of Thesis Chocolate. Thanks to Saccharomyces cerevisae for the sustainence and entertainment.

Some of my teachers were instrumental in undoing the damage wreaked by others and these teachers deserve a special thanks. My high school trigonometry teacher, Mrs. Connie Dotson, reminded me that not only did math not have to be painful but it actually could be fun, and her nonchalant confidence in my abilities stood in stark contrast to my math teachers the preceeding three years. My undergraduate calculus teacher, Dr. Gerald Taylor, reinforced these messages and didn't even mind when I limped into class late for the half of a semester when I was on crutches. I met for the first time with Dr. Richard Eykholt as college sophomore biochemistry major taking first year physics - the first physics class I'd taken. I told him I wanted to add a physics major, spend a semester abroad, and still graduate in a total of five years. Dr. Eykholt, who would become my academic advisor, not only did not laugh me out of his office but instead helped me draft a plan to do it. I followed that plan and it eventually led me here, thanks in no small part to his advice and support.

Many thanks to Bonnie Flemming and Meg Urry, both of whom have been invaluable mentors and role models. Thanks to Liz Atlas for all of your help. Thanks to my committee, Richard Easther, Dan McKinsey, Keith Baker, Helen Caines, and John Harris, for their time and useful comments.

Words cannot convey my graditude towards John Harris, my advisor, and Helen Caines, my mentor. I really wouldn't have made it without you. Helen, I hope some day that I can be as good of a physicist and as good of a person as you are. And I believe I still owe you a car wash? John, thanks for all of your support and for giving me so many opportunities to become a better physicist and prove myself. (And sorry about the exploding root beer!)

Contents

List of Figures

List of Tables

Chapter 1

Introduction

1.1 A new phase of matter

The most successful theory for explaining the behavior of nuclear matter so far is Quantum ChromoDynamics (QCD), and fundamental attributes of QCD indicate that there is a new phase of nuclear matter at high energy densities. Figure 1.1 shows the QCD coupling constant α_s as a function of the momentum transfer, Q. Unlike Quantum ElectroDynamics (QED), the coupling constant in QCD is large at low momentum transfer and perturbative calculations do not converge. A direct consequence of the energy dependence of the coupling constant is asymptotic freedom, which a Nobel prize was awarded for in 2004. Unlike the macroscopic forces we are familiar with, the strong force is weaker at very short distances (large Q^2) than at large distances (small Q^2). As a consequence, if bound quarks are separated, it eventually becomes energetically favorable to create a new quark-antiquark pair rather than to continue moving the quarks farther apart. Hence free quarks are not observed in nature. The QCD analog to electric charge in QED is color charge, which carries the strong force. Only color neutral states, the color singlets, can exist as stable nuclear matter at normal densities.

However, when quarks are close together, the attraction between individual quarks is weak. T. D. Lee proposed in 1974 that quarks and gluons could therefore be created in a state where they would behave as if they were free within the bounds of the

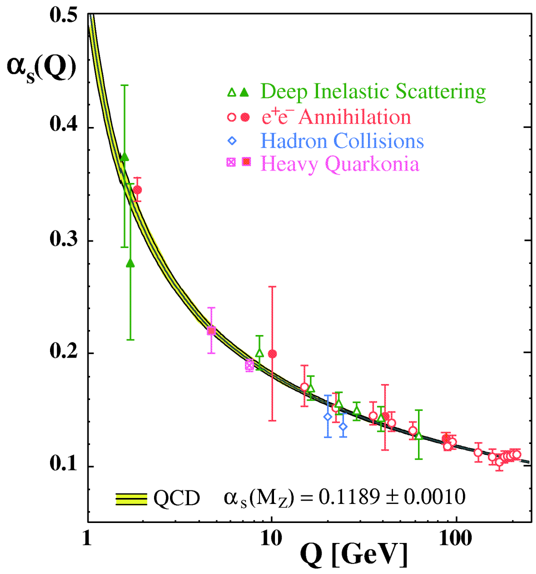

Figure 1.1: The QCD coupling constant as a function of energy [1].

volume [2], and that this phase of matter would be similar to what existed at early stages of the universe. In 1974 the Bear Mountain Workshop was held in New York to discuss how one could create and study this state and measure its properties [2]. In the late 70's this new phase of matter was named the Quark Gluon Plasma (QGP) [2]. These early theoretical ideas which justified the study of a Quark Gluon Plasma were further developed in the early 1980's.

It was proposed that a QGP could be created in high energy collisions of nuclei [2–4]. The first dedicated program to create a QGP through heavy ion collisions was at the Super Proton Synchrotron (SPS) at the European Organisation for Nuclear Research (CERN). The SPS is a fixed target heavy ion collider which took data from 1984 to 2003. The program to search for a QGP used primarily $Pb + Pb$ collisions at a center of mass energy per nucleon ($\sqrt{s_{NN}}$) ranging from 9 to 17.3 GeV. The Alternating Gradient Synchrotron (AGS) was a fixed target collider at Brookhaven National Laborarory which began operation in 1986 and could collide ions ranging in mass from protons to ^{32}S at energies up to 28 GeV/u. In 1991 it was modified to allow ions up to ^{197}Au for use in the Relativistic Heavy Ion Collider (RHIC) [5]. The proposal for RHIC was developed in 1983 when plans for the Isabelle, a proton-proton

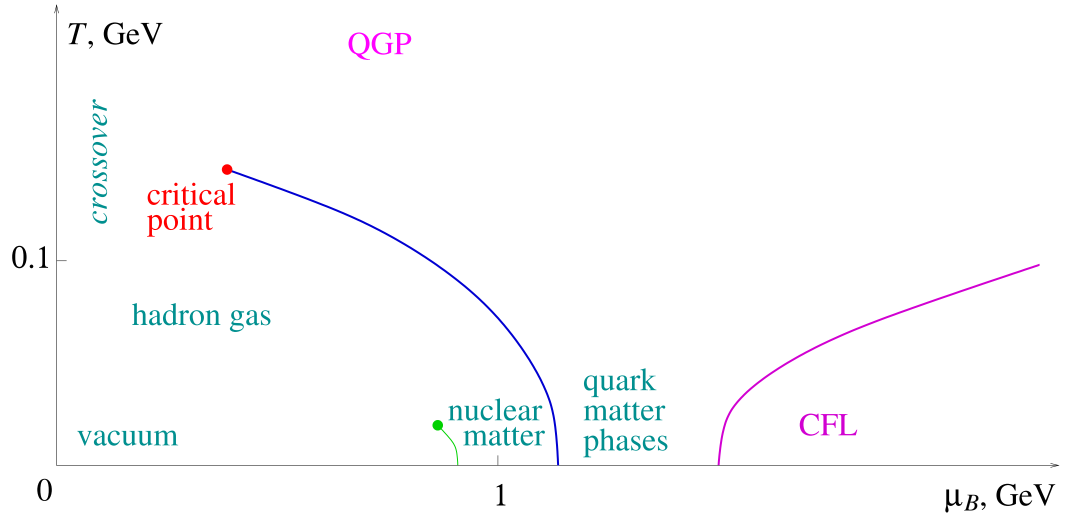

Figure 1.2: Schematic phase diagram of nuclear matter from [6] showing the current consensus about the key features.

accelerator, were abandoned, clearing the way for the tunnel to be used for RHIC. RHIC is capable of colliding many ion species, ranging from $p+p$ to $Au+Au$. It can collide $Au+Au$ with $\sqrt{s_{NN}}$ ranging from 5 GeV to 200 GeV.

1.2 The phase diagram of nuclear matter

From the beginning, the field of heavy ion physics was driven by a desire for a better understanding of nuclear matter and its phase diagram. The flexibility of RHIC means that a large part of the phase diagram of nuclear matter can be studied there. Our understanding of what the phase diagram looks like has improved significantly since the 1980's, however, few quantitative features of the phase diagram are universally agreed upon in the field.

Figure 1.2 shows a simple phase diagram of nuclear matter as a function of temperature and baryo-chemical potential (μ_B) showing the key features. The detailed structure of the phase diagram and the exact locations of transitions are still debated. We understand the region occupied by cold nuclear matter, such as nuclei, better than any other part of the phase diagram, however, it is worth noting that we still have an incomplete understanding of even the proton. The proton's spin cannot be explained by the spin of its valence quarks alone, and the contributions of gluons and the orbital momentum are still being measured [7]. We know that cool nuclear matter at moderate densities exists at a μ_B of about 1 GeV, meaning that it takes a little more than 1 GeV to add a baryon to the system [6].

At moderate densities and low temperatures, there are ordered phases of cold quark matter, similar to the various phases of ice [6]. At somewhat higher densities nuclear matter is expected to be color-flavor locked, meaning that the quarks are expected to form Cooper pairs, coupling is expected to be weak, and strong correlations between flavor and color are expected. This matter is expected to behave as a color superconductor [8]. Nuclear matter at these densities is not directly experimentally accessible, however, the matter in the center of neutron stars may occupy this region of the phase diagram.

We know that if we heat nuclear matter at densities comparable to those found in nuclei to moderate temperatures, it forms a hadron gas, comprising low mass baryons and mesons made of mostly u and d quarks. At higher temperatures we expect a quark-gluon plasma, characterized by both chiral symmetry restoration and free quarks and gluons. At baryo-chemical potentials at and below those of normal nuclear matter we therefore expect a phase transition from a hadron gas to a quark-gluon plasma.

The question of the order of the phase transition has been the subject of much debate. Predictions have been made by lattice QCD. An approximation is made that space can be discretized, making calculations in the non-perturbative regime of QCD possible. Lattice simulations indicate that for $\mu_B = 0$, the transition is a crossover rather than a phase transition [9]. This means that the hadron gas and the QGP coexist. A similar crossover transition exists for water. At high temperature and pressure, the density of water decreases and the density of water vapor increases, making the two phases indistinguishable. Similarly, the density of the hadron gas is high and the density of the QGP is low in the crossover region, making the phases indistinguishable.

Lattice calculations for $\mu_B = 0$ converge, however, at $\mu_B \neq 0$ lattice calculations

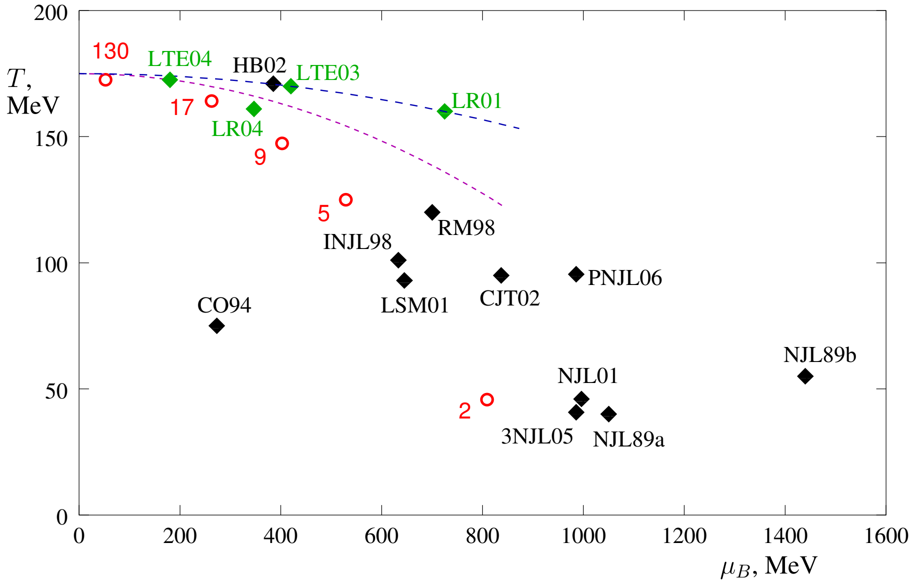

Figure 1.3: Model predictions for the location of the critical point from [6]. Black points are predictions from extrapolations from lattice calculations at $\mu_B = 0$, green points are lattice predictions, and red circles are the chemical freezeout points for heavy ion collisions at the $\sqrt{s_{NN}}$ indicated by the point. Dashed lines correspond to extrapolations of the transition point at $\mu_B = 0$ using different estimations of the slope $\dfrac{dT}{d\mu_B^2}$ at $\mu_B = 0$.

do not reliably converge so it is more difficult to make definitive statements [6]. For larger μ_B, evidence points towards a first order phase transition [10]. This would mean there must be a critical point. This would be a tricritical point where confined nuclear matter and the QGP meet if chiral symmetry has been restored and the u and d quarks can be considered massless [11].

The location of the tricritical point has been calculated by making assumptions about how to extrapolate to finite μ_B from $\mu_B = 0$, and these calculations are based on models rather than being solidly rooted in QCD [6]. Figure 1.3 shows model predictions for the location of the tricritical point, demonstrating that there is still no consensus. There is therefore no consensus on the location of the line corresponding to the first order phase transition, although more recent calculations are in better agreement than earlier calculations. The matter produced at RHIC is generally believed

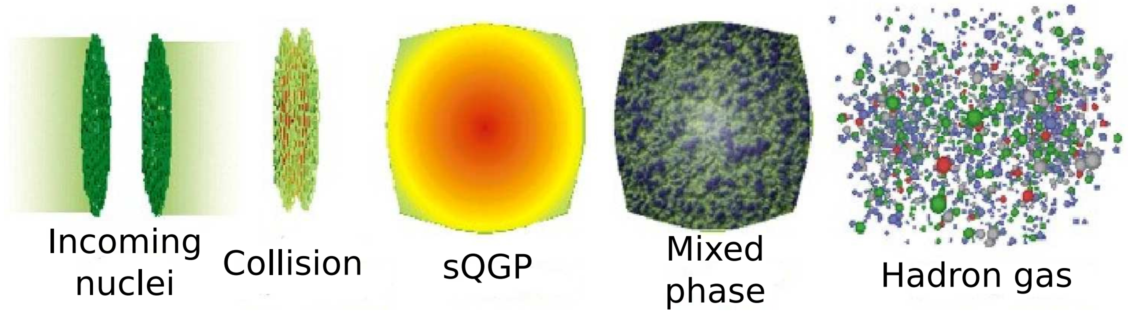

Figure 1.4: Cartoon of the stages of a heavy ion collision [12].

to be in the crossover region and has been termed a strongly coupled quark-gluon plasma (sQGP).

1.3 Phases of the collision

Figure 1.4 is a cartoon showing the different stages of a heavy ion collision. This figure is not drawn to scale. Incoming nuclei are relativistically contracted due to their high momenta. When the collision occurs, the quarks and gluons in each nucleus interact. The centers of mass of collisions between quarks and gluons are not generally the same as the center of mass of the collision. The highest densities and hottest temperatures are shortly after the collision. A QGP is formed, likely at a temperature higher than the first order phase transition line but at lower μ_B than the critical point. The medium enters a mixed phase of a hadron gas and a QGP as it expands and cools. Hadronization of quarks and gluons occurs at this time. As the medium cools further it enters a pure hadron gas phase.

This process is depicted on a space-time diagram in Figure 1.5. The incoming nuclei move very close to the speed of light; collisions with a center of mass energy per nucleon $\sqrt{s_{NN}}$ of 200 GeV correspond to a Lorentz factor of about 200, and collisions at a $\sqrt{s_{NN}}$ of 62 GeV correspond to a Lorentz factor of about 62. The left-hand side depicts what occurs for a collision where no QGP is formed. In this case, immediately after the collision there is a period of non-equilibrium when quarks and gluons which participated in the collision form into hadrons, followed by a hadronic

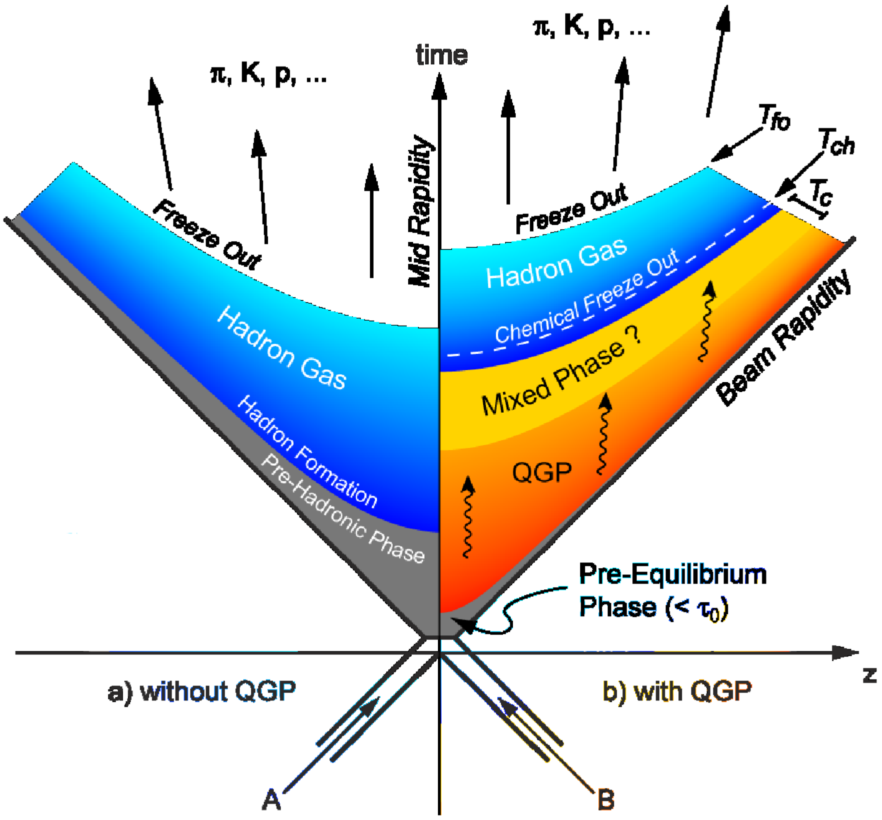

Figure 1.5: Spacetime diagram of a heavy ion collision [13]. The left depicts events for a collision where no QGP is formed and the right depicts a collision where a QGP is formed.

gas phase. The right-hand side depicts what occurs for a collision where a QGP is formed. Again there is a period before equilibrium, followed by a QGP phase, a mixed phase in the case of a crossover region, and a hadronic gas phase. The temperature where the transition from a QGP occurs is called the critical temperature, T_c. In the case of a crossover transition, the hadronic gas phase may be so dense that there is little distinction between the hadronic gas and the QGP. The lifetime of the QGP phase depends on the highest temperature reached in the collision and on the rate of expansion of the medium.

In the hadronic gas phase, inelastic collisions continue until the chemical freeze out, T_{ch}, is reached. At this point the relative distributions of different hadrons are fixed. The hadrons are not necessarily in complete chemical equilibrium at this point. Elastic collisions continue until the thermal freeze out, T_{fo}. At this point the momenta of the hadrons are fixed.

1.4 Theoretical frameworks to describe heavy ion ccollisions

Many different theoretical frameworks have been used to describe heavy ion collisions. This is not a comprehensive review and emphasis is deliberately on theories and models which have been connected to the results presented in this thesis. Only broad descriptions of a QGP are discussed here; theories directly related to the results will be discussed in Chapter 7.

There are two different classes of theoretical frameworks, those which attempt to describe the QGP describing the interactions between quarks and gluons from first principles and those which make assumptions about the QGP and are a more phenomenological description of the data. Theories which attempt to describe the interactions of quarks and gluons from first principles, such as energy loss models and the Color Glass Condensate, are more solidly founded in QCD, however, assumptions about the initial state and hadronization are made to relate these theories to data. Statistical models and hydrodynamical models are dependent on assumptions about the medium created. These classes of models both depend on the medium reaching equilibrium, at least locally.

1.4.1 Jet quenching models

The ratio of hadron spectra in $A+A$ collisions to that in $p+p$ collisions is a measure of the degree to which hadron spectra and yields are modified in heavy ion collisions. This ratio is divided by the number of binary collisions in an $A+A$ collision to give

$$R_{AA} = \frac{d^2N_{AA}/dp_T d\eta}{T_{AA} d^2\sigma^{pp}/dp_T d\eta}. \tag{1.1}$$

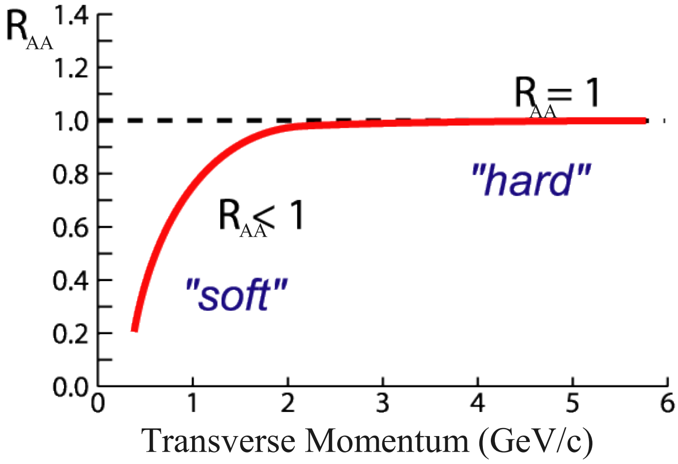

Figure 1.6: Schematic diagram showing R_{AA} for an $A + A$ collision that can be described as a superposition of nucleon-nucleon collisions [14].

The overlap integral, $T_{AA} = \frac{<N_{bin}>}{\sigma_{inel}^{NN}}$ where $< N_{bin} >$ is the average number of binary collisions and σ_{inel}^{NN} is the inelastic nucleon-nucleon cross section, accounts for the collision geometry.

R_{AA} is 1 at high p_T if the $A+A$ collision only comprises multiple nucleon-nucleon collisions since high-p_T processes should scale with the number of nucleon-nucleon collisions. At low p_T R_{AA} would be less than 1 because soft processes are expected to scale with the number of nuclei which participate in the collision. R_{AA} is depicted schematically in Figure 1.6.

It was predicted that a QGP would be dense and therefore that production of high-p_T hadrons would be suppressed because energy would be lost by fast moving partons traversing the medium [16]. When there is a hard scattering of two partons in a QGP, the dense medium should slow or stop the parton, a process called jet quenching. The partons that escape the medium are assumed to be biased towards the surface of the medium. A theoretical calculation of the distribution of the origins hadrons produced relative to an 8 GeV/c hadron in a dense medium are shown in Figure 1.7, demonstrating that the measured high-p_T hadrons are expected to be biased towards those produced near the surface. This would lead to $R_{AA} < 1$ because there would be fewer high-p_T partons in an $A + A$ collision than in a $p + p$ collision.

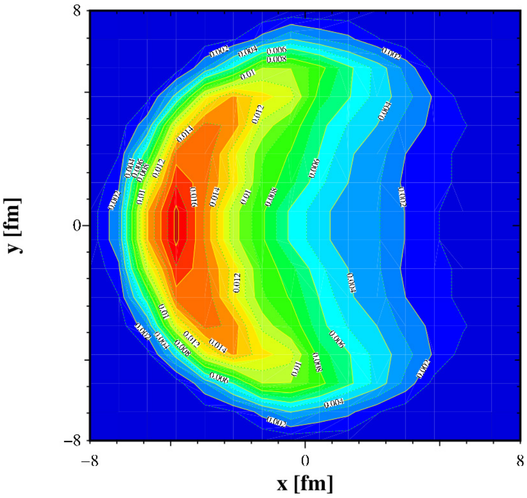

Figure 1.7: Distribution of the origin of hadrons in a dense medium [15]. An 8 GeV/c parton was heading in the -x direction.

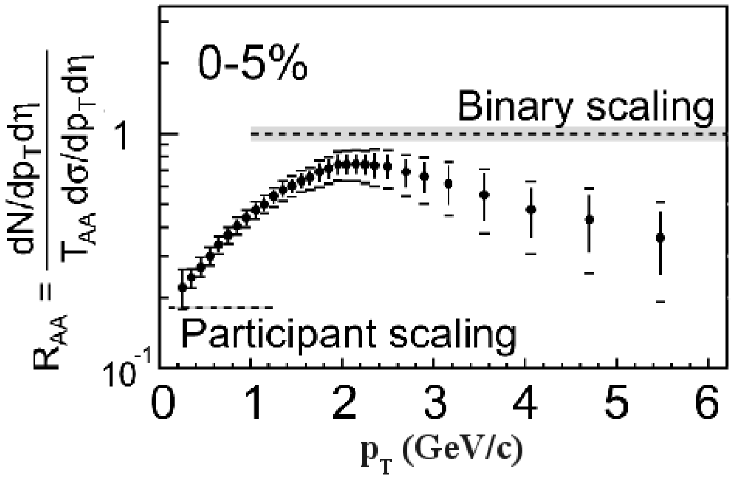

Figure 1.8: R_{AA} for unidentified hadrons in $Au + Au$ collisions at $\sqrt{s_{NN}} = 130$ GeV [17].

Data from R_{AA} in heavy ion collisions are shown are Figure 1.8. The data show roughly a factor of five suppression of hadron spectra at high-p_T in central $Au + Au$ collisions relative to $p + p$, rather than the suppression by roughly a factor of two predicted before RHIC data were available [16]. The enhancement around $p_T \approx 2$ is from the Cronin effect, first observed in $d + Au$ collisions by J. Cronin in 1975 [18] and has also been observed in $d + Au$ collisions at RHIC [19]. It is believed to result from multiple scattering of initial state partons.

Other models are capable of producing higher suppression but they require larger partonic energy loss. Energy loss in these models is often parameterized by the average transverse momentum lost by the parton squared per unit length, $\hat{q}$. Attempts have been made to determine the size of $\hat{q}$ from experimental data [20]. However, the theoretical uncertainties are still large and estimates for $\hat{q}$ range from 0.5 - 20 GeV^2/fm [21–23]. While most models can describe the suppression of light hadrons (π, K, p) and even hadrons containing strange quarks (Λ, $\bar{\Lambda}$, K^0_S) with a sufficiently high $\hat{q}$, most have trouble describing the R_{AA} of light (u,d,s) and heavy (c,b) quarks simultaneously [24].

1.4.2 The Glasma and the Color Glass Condensate

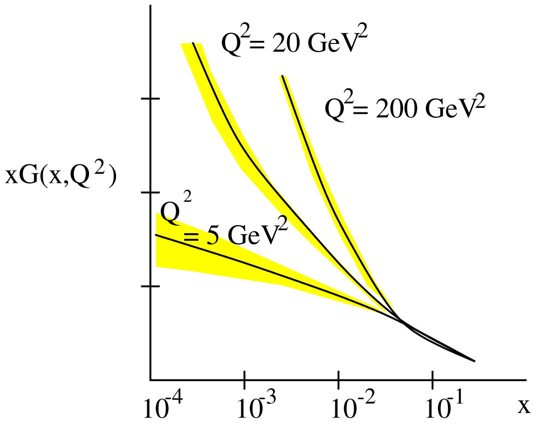

Figure 1.9: Distribution of gluons as a function of x = E_{gluon}/E_{hadron} as measured by the HERA experiment [25, 26].

The Glasma and the Color Glass Condensate (CGC) are closely linked. The Glasma is a description of nuclei moving at relativistic speeds. Figure 1.9 shows the distribution of gluons as a function of x = E_{gluon}/E_{hadron} as measured at HERA for different values of Q^2, the momentum transfered in a collision. At low energies, states of nuclei with few gluons are dominant, while at high energies, the states with multiple gluons are dominant. This motivated the picture of a fast-moving nucleus as a wall of gluons, as depicted in Figure 1.10. The Glasma is the state comprising a dense, coherent condensate of gluons expected to exist in a fast nucleus [25]. The high density of gluons means that they can be described as a classical gluon field. The Glasma picture can describe many measurements from $e + A$ collisions.

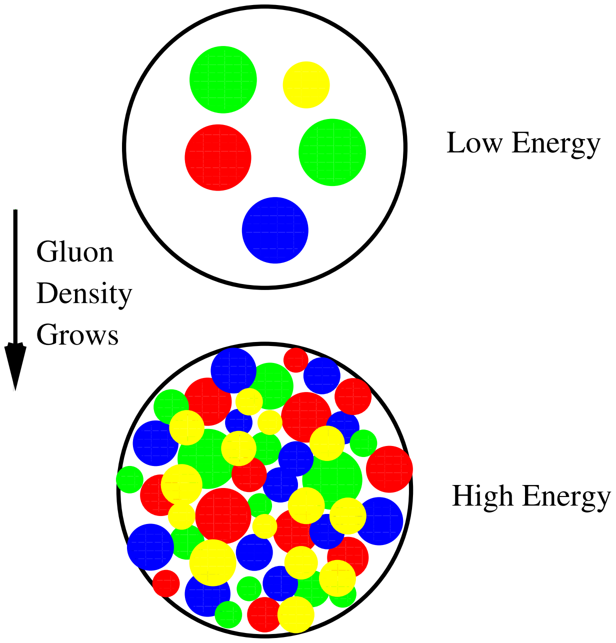

Figure 1.10: A schematic diagram of the Glasma in a nucleus [25]. The gluons are coherent and dense for a fast moving nucleon.

The Color Glass Condensate (CGC) describes an $A + A$ collision as two sheets of Glasma colliding to form a fluid [25]. "Color" comes the fact that quarks and gluons have color charge and "Glass" from the fact that the natural time scale of evolution of the gluons is much longer than the time scale of the evolution of the state, similar to glass. "Condensate" comes from the high density of gluons in the initial state. Because the gluons in the incoming nuclei are coherent and can be described as classical gluon fields, the interactions of the nuclei are similar to the interactions between classical electromagnetic fields. The initial color magnetic fields are transverse to the direction of motion of the nuclei. As the two nuclei approach, color charges on one nucleus generate image charges on the other nucleius, and in a short period of time the direction of the fields changes from transverse to parallel to the direction of the movement nuclei. The medium produced from the interaction of quarks and gluons in these fields is the CGC [25].

1.4.3 Statistical models

Hadronization of quarks and gluons is not calculable from QCD first principles. Statistical models are one of the models describing the hadronization of quarks and gluons. The first statistical models for hadronization were proposed before the development of QCD and interest was renewed when it was proposed that an equilibrated hadron gas might be a signature for a QGP [27]. These models calculated particle ratios in a hadron gas at chemical equilibrium and deal with the conserved quantities: baryon number (B), strangeness (S), and charge (C). Calculations for elementary collisions such as $e^{+} + e^{-}$, $p + p$, and $p + \bar{p}$ must use a canonical ensemble to describe hadron production. In heavy ion collisions the volume of the system is large enough that it can be described by a grand canonical ensemble and the conserved quantities have corresponding chemical potentials [28]. The log of the partition function in the grand canonical ensemble is given by

$$ln(Z) = \sum_{species i} \frac{g_i V}{(2\pi)^3} \int ln(1 \pm e^{-\beta(E_i - \mu_i)})^{\pm 1} d^3p \tag{1.2}$$

where g_i is the degeneracy of the state, V is the volume of the system, $\beta = \frac{1}{kT}$, k is the Boltzman constant, T is the temperature, $E_i = \sqrt{p^2 + m_i^2}$ is the particle energy, m_i is the particle mass, p is the particle momentum, and μ_i is the particle's chemical potential. The μ_i are given by

$$\mu_i = B_i \mu_B + S_i \mu_S + Q_i \mu_Q \tag{1.3}$$

where μ_B is the baryon chemical potential, μ_S is the strangeness chemical potential, and μ_Q is the chemical potential corresponding to charge. The number of particles of each species is given by

$$N_i = T \frac{\partial lnZ}{\partial \mu_i} = \frac{g_i V}{2\pi^2} \sum_{k=1}^{\infty} \frac{m_i^2 T}{k} K_2(\frac{k m_i}{T}) e^{\beta k \mu_i} \tag{1.4}$$

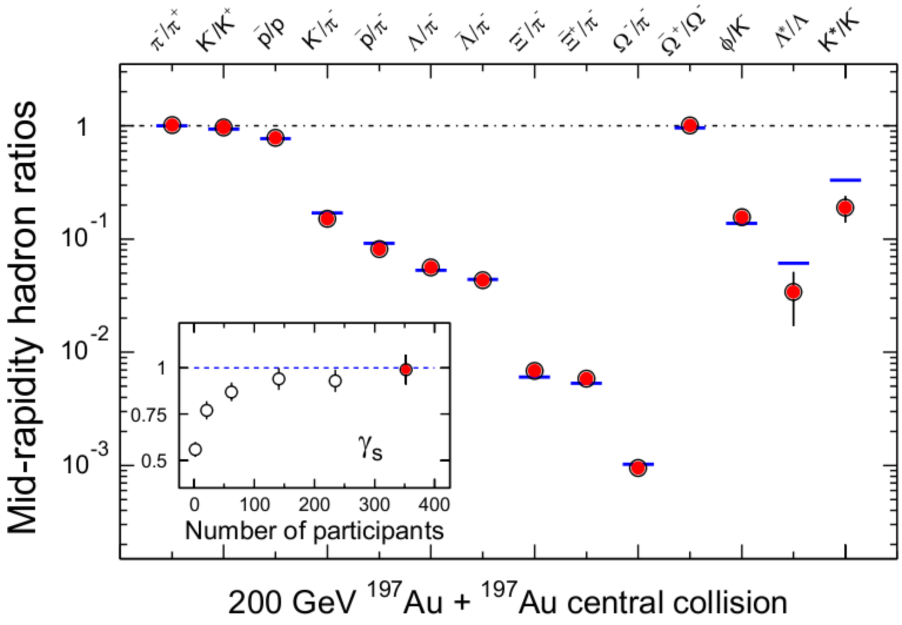

Figure 1.11: Thermal fit to RHIC data on yields of hadrons [29]. γ_s is a factor indicating the degree of equilibration of strange quarks. $\gamma_s = 1$ indicates complete equilibration.

where K_2 is the modified Bessel function.

Since the volume of the medium produced in a heavy ion collision cannot be measured directly, statistical models cannot be used to calculate the absolute yields, however, they can be used to calculate the relative yields of particles. Statistical models do not describe strangeness well so an ad hoc parameter γ_s was introduced to account for the suppression of hadrons with strange valence quarks relative to their equilibrium value. $\gamma_s = 1$ if strangeness is in equilibrium. Measured particle ratios are fit to determine μ_B, μ_S, μ_Q, γ_s and T. Further details of these calculations can be found in [27] and the references therein.

Figure 1.11 shows a fit of a statistical model described in [30] to particle ratios in $Au + Au$ collisions at $\sqrt{s_{NN}} = 200$ GeV, demonstrating that statistical models describe the data well. The inset shows γ_s as a function of the number of participants in the collisions, with collision centrality increasing with the number of participants. $\gamma_s \approx 1$ for central collisions.

If the medium does reach equilibrium, statistical models must describe the data, however, this is not a sufficient condition to prove that the medium has reached equilibrium. Statistical models also describe $e^+ + e^-$, $p + p$, and $p + \bar{p}$ collisions reasonably well with γ_s in the range of 0.4-0.8 [27]. The interpretation of this fact has been much debated. It is possible that the hadrons are produced in equilibrium, but it means that statistical models alone cannot be interpreted as proof of an equilibrated medium.

Regardless of the collision system, the temperature attained from thermal fits is remarkably constant at around 160 MeV, with the fits of STAR data in Figure 1.11 giving T = 163 ± 4 MeV [29]. This should not be interpreted as the temperature of the QGP, but rather as the chemical freeze out temperature T_{ch}. Statistical models cannot describe the full spectra of hadrons produced in a heavy ion collision but rather are limited to describing the overall yield of particles.

1.4.4 Hydrodynamics

Hydrodynamical models describe the medium as a relativistic fluid. Several of these models describe a fluid with a viscosity of zero [31–34]. These models are not restricted to describing a QGP but rather can describe any relativistic fluid.

Hydrodynamical observables are related to two major features in heavy ion collisions. First, the region where the incoming nuclei overlap is asymmetric and this spatial anisotropy in the initial state results in a momentum anisotropy in the final state. This phenomenon is called anisotropic flow. Second, the large pressure gradients lead the medium to expand and particles to move away from the collision point. This phenomenon is called radial flow.

Figure 1.12 shows the geometric relationship between the reaction plane and the incoming nuclei. The overlap region between the two incoming nuclei is almond shaped, and the reaction plane is the plane formed by the beam axis and the centers of both nuclei. For a large impact parameter, the distance between the centers of the the two nuclei, the overlap region is more oblong while for a smaller impact parameter the overlap region is closer to circular.

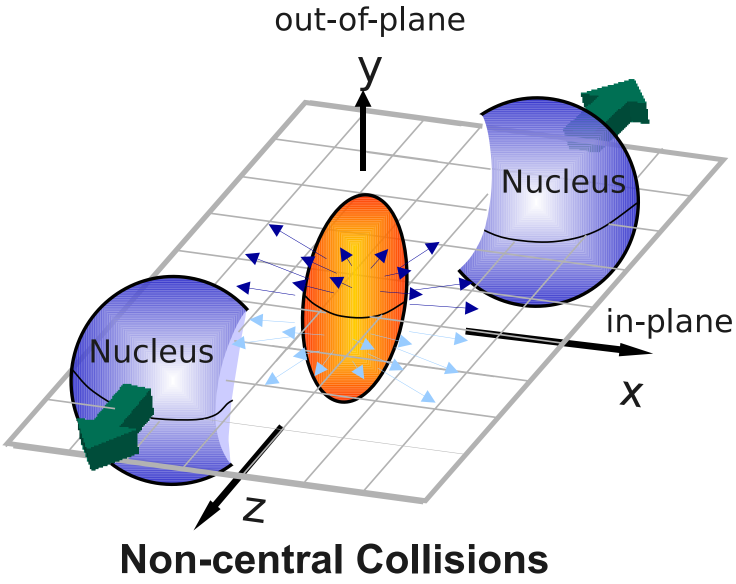

Figure 1.12: Diagram showing the location of the reaction plane relative to the incoming nuclei [13].

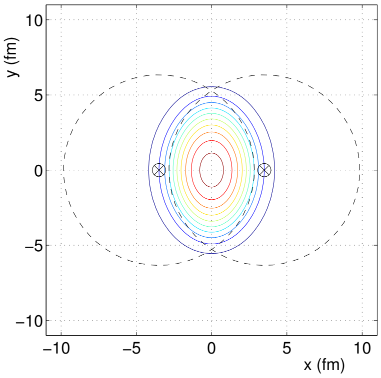

Figure 1.13: Contours of constant density in a hydrodynamical model [35]. The projections of the incoming nuclei are shown as dashed lines. The impact parameter is 7 fm.

It is assumed that the azimuthal momentum anisotropy originates from the collective movement of a fluid formed at early stages of the collision. This is the most universally accepted mechanism for the production of an azimuthal anisotropy, however, other mechanisms have been proposed [36–39]. In a hydrodynamical model, the initial anisotropy in the distribution of particles leads to a pressure gradient. Figure 1.13 shows theoretical calculations for the contours of constant density. The pressure gradient is perpendicular to these lines, meaning that it is azimuthally anisotropic. As the system evolves, the spatial azimuthal anisotropy in the distribution of particles will disappear. The anisotropy in the momentum distribution of particles due to the pressure gradient will remain.

The initial azimuthal anisotropy is often described in terms of the Fourier expansion of the distribution of particles in momentum:

$$E\frac{d^3N}{d^3p_T} = \frac{1}{2\pi}\frac{d^2N}{p_T dp_T dy}(1 + \sum_{n=1}^{\infty} 2v_n cos(n(\phi - \psi_{RP}))). \tag{1.5}$$

v_1 is called directed flow and describes the preference for particles to move in the direction along the beam axis. v_2 is called elliptic flow and describes the tendency for particles to have a preferred direction of motion in the x-y plane as a result of the spatial anisotropy in the initial condition [40]. Experimentally, the v_n are small and decreasing with increasing n in heavy ion collisions. v_2 has been studied most extensively.

Figure 1.14 shows the magnitude of v_2 in $A + A$ collisions as a function of the energy per nucleon in the collision. At very low energies, the nucleons simply scatter off each other (bounce-off), leading to a positive v_2. At intermediate collision energies, particles created in the collision cannot move in the direction of the short axis of the overlap region because they would collide with the constituent nucleons of the colliding nuclei, bouncing them back in towards the overlap region. The only direction where particles could escape is in the direction of the long axis of the overlap region since there is no matter there to stop particles from escaping, leading to a negative v_2 (squeeze-out).

At higher collision energies, the incoming nuclei are Lorentz contracted so that the nucleus is effectively flat and all nucleons interact at nearly the same time. Any nucleons which did not participate in the interaction have already moved past the interaction region and can no longer collide with the particles created in the collision. v_2 becomes positive again.

Figure 1.15 shows measurements of v_2 at various collision energies compared to

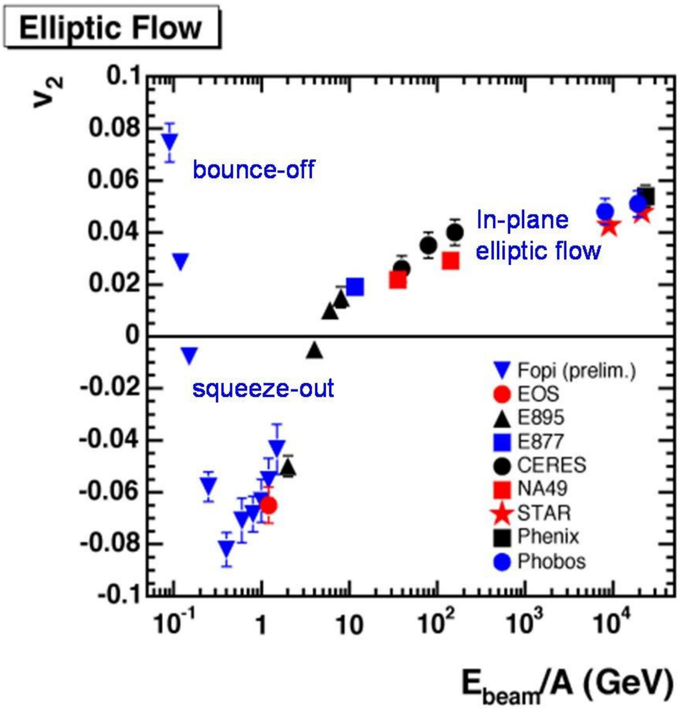

Figure 1.14: v_2 versus collision energy per nucleon [40].

hydrodynamical predictions for the upper limit of v_2. The x-axis is the number of particles produced per unit rapidity[1] divided by the transverse area of overlap of the nuclei, S. The y-axis is v_2 divided by the eccentricity, ϵ, of the overlap area. S and ϵ are determined using a Glauber Monte Carlo model for nuclear collisions [41]. This normalization leads to the cancellation of trivial geometric effects. The predictions are from ideal hydrodynamics, meaning that the viscosity is assumed to be zero. A non-zero viscosity would only decrease the observed v_2 so these are upper limits for v_2, shown as green lines in Figure 1.15. If these limits are correct, then the medium created in central collisions at RHIC is very close to hydrodynamical limits and therefore the viscosity must be very low.

Other interesting results from v_2 measurements at RHIC include the dependence of v_2 on the particle type. In a hydrodynamical model, at a fixed p_T particles with

---

[1] Defined in Appendix A

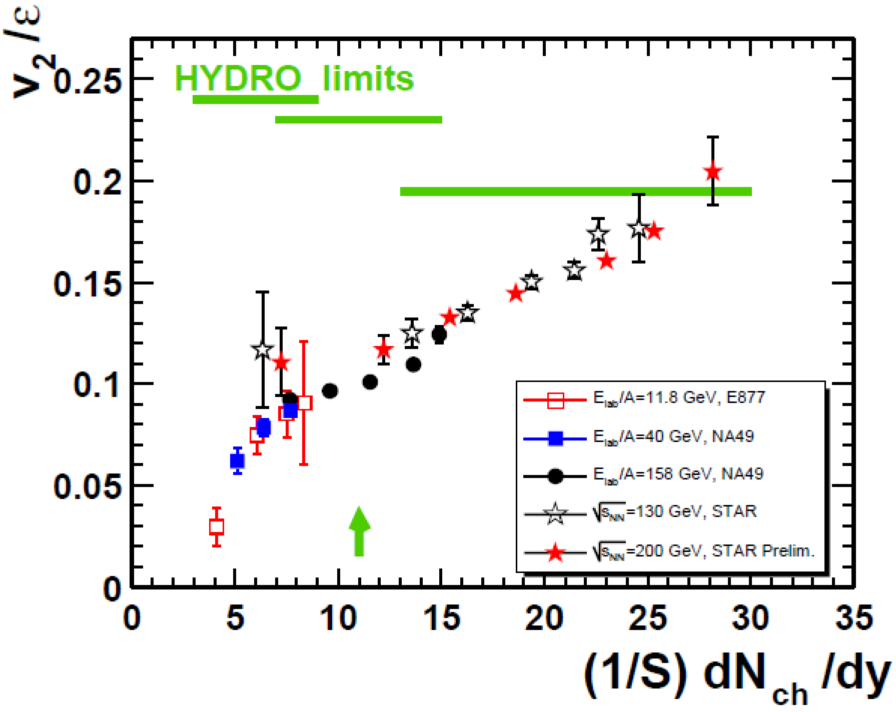

Figure 1.15: v_2 measurements compared to hydroynamical limits in different models [40]. The x-axis is a measure of the number of particles produced per unit of rapidity at mid-rapidity divided by the transverse overlap area in the collision. The y-axis is v_2 divided by the eccentricity of the overlap area. The green arrow indicates the predicted position of a color percolation phase transition. The green lines indicate the ideal hydrodynamics predictions for AGS, SPS, and RHIC energies.

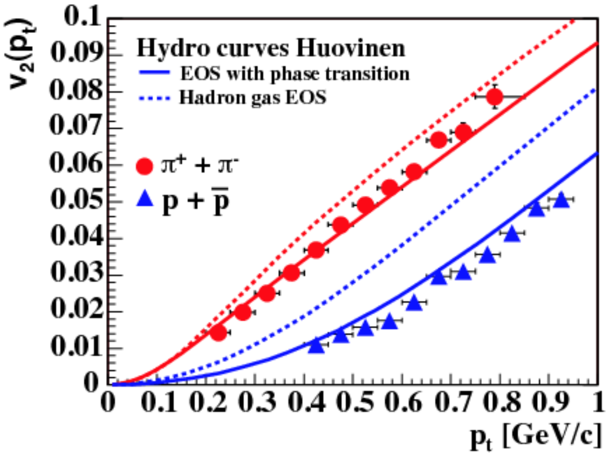

Figure 1.16: Particle species dependence of v_2 at low-p_T [40].

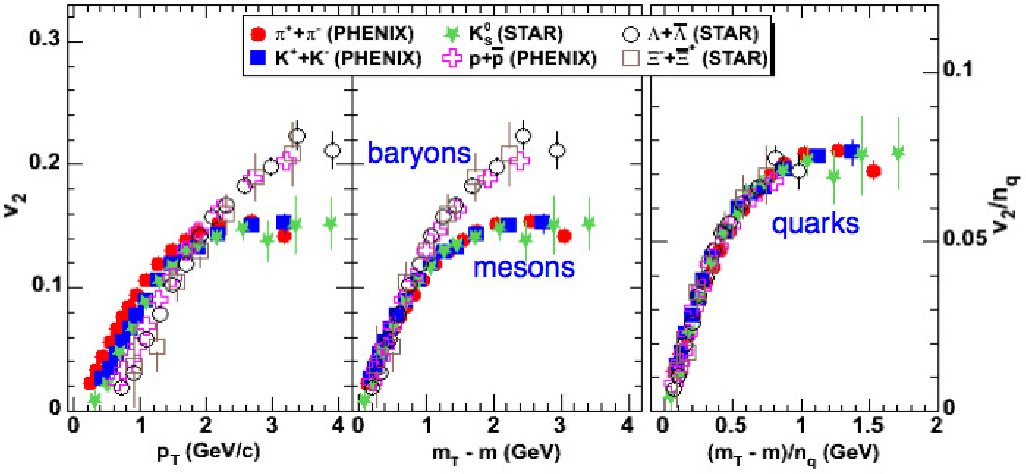

Figure 1.17: Particle species dependence of v_2 versus p_T (left), v_2 versus m_T-m (middle) and v_2/n_q versus $(m_T$-m$)/n_q$ (right). [40, 42].

lower mass should have a higher v_2 [40]. At low-p_T this is the dominant effect, as seen in Figure 1.16. The dominant trend in the dependence of v_2 on particle type at high-p_T, shown in Figure 1.17(a), is instead a splitting between baryons and mesons.

Figure 1.17(b) shows that all baryons follow a single trend and all mesons follow a separate trend if v_2 is plotted as a function of the transverse mass[2], m_T, instead of p_T. This scaling of v_2 with transverse mass is expected at low p_T from the basic equations of hydrodynamics [42], supporting the description of the medium produced at RHIC as a fluid.

If the QGP is a fluid of quarks and gluons, then the appropriate degrees of freedom to describe the medium are quarks rather than hadrons. There are some indications of this in the scaling of v_2, since there is a clear separation between baryons and mesons and baryons have a larger v_2 than mesons. Figure 1.17(c) shows that the baryons and mesons follow the same trend for v_2 divided by the number of constituent quarks, n_q, as a function of $(m_T$-m$)/n_q$ implying that the fluid which flows in order to create v_2 comprises quarks rather than hadrons.

It is worth noting that this scaling is found for one method of measuring v_2, the

---

[2] Defined in Appendix A

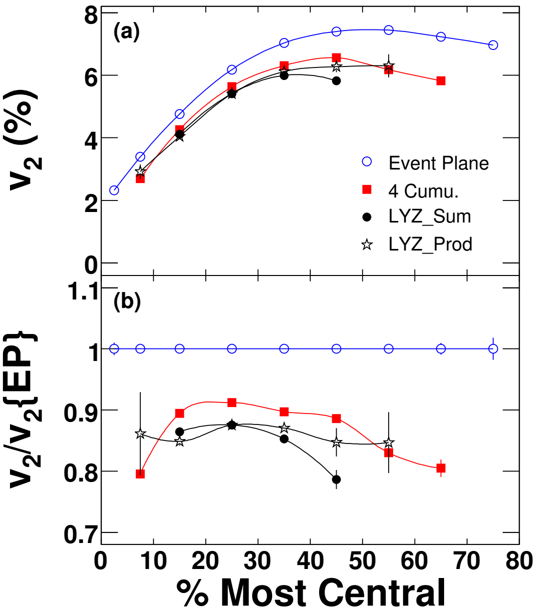

Figure 1.18: (a) v_2 as a function of centrality for various methods of measuring v_2 and (b) the ratio of v_2 as determined from the event plane method to v_2 determined from other methods [43]. Data are from $Au + Au$ collisions at $\sqrt{s_{NN}} = 200$ GeV.

event plane method, and that the v_2 in Figure 1.17 is integrated over all centralities. Figure 1.18 shows comparisons of v_2 as determined by the event plane method to other methods. The event plane method uses the azimuthal anisotropy in particles observed at midrapidity to determine the direction of the event plane [3], and v_2 as measured by this method is systematically higher than v_2 measured by other methods. The 4 particle cumulant (4 Cumu.) method looks at azimuthal correlations between four particles and the Lee-Yang Zero (LYZ) method is an all-particle correlation designed to subtract nonflow effects to all orders [40]. The event plane method should be more susceptible to non-flow correlations, such as jets and resonances, and the ratio of v_2 determined by the event plane method to other methods shows a centrality dependence. The scaling of v_2 with the number of quarks as a function of p_T, rather than m_T, scaled by the number of quarks has been demonstrated at different centralities [43, 44].

---

[3] The experimentally determined location of the reaction plane is called the event plane.

Since hydrodynamics assumes thermalization, the success of ideal hydrodynamics at describing many aspects of RHIC data implies that the medium is thermalized when v_2 is formed. Figure 1.17 demonstrates that hadrons containing strange quarks follow the same trends for v_2, implying that strangeness is also thermalized. Furthermore, not only is strangeness thermalized, but measurements of electrons from decays of hadrons including charm quarks indicate that the v_2 of charm quarks is probably comparable to that of light quarks [24].

Radial flow is also predicted by hydrodynamics. The medium is expanding because of pressure gradients, as depicted in Figure 1.13. This means that on average particles are moving away from the center of the interaction region. Both radial flow and anisotropic flow alter the spectra of particles, since both affect the momentum of particles. Radial flow is expected to have a mass dependence, similar to anisotropic flow. Fits of data to a hydrodynamical model inspired parameterization of spectra called a Blast Wave Model give values for radial flow consistent with those expected from hydrodynamics. These models yield anisotropic flow comparable to independent measurements [40].

1.4.5 Recombination

R_{CP} is similar to R_{AA} except that the spectrum in central $A+A$ collisions is compared to that in peripheral collisions:

$$R_{CP} = \frac{N_{bin}^{peripheral} d^2 N_{AA}^{central}/dp_T d\eta}{N_{bin}^{central} d^2 N_{AA}^{peripheral}/dp_T d\eta}. \tag{1.6}$$

Figure 1.19 shows R_{CP} for identified hadrons as a function of p_T and as a function of p_T/n_q. The R_{AA} for baryons and mesons clearly follow different trends. If R_{CP} is plotted as a function of p_T/n_q instead of p_T, the trends for baryons and mesons are the same. The scaling of v_2 and R_{CP} with the quark content of hadrons motivated Coalescence and Recombination models to explain these phenomena at intermediate p_T (2-6 GeV/c). These models posit that, rather than hadrons being produced by vacuum fragmentation, hadrons in a heavy ion collision can be formed by quarks combining with other quarks from the medium.

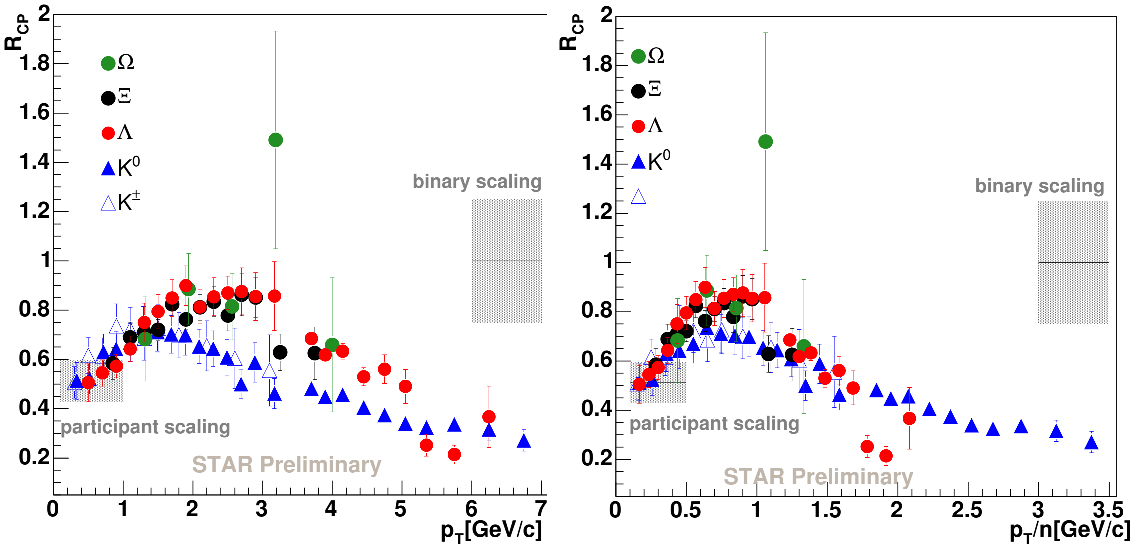

Figure 1.19: Identified particle R_{CP} (left) as a function of p_T and (right) as a function of p_T scaled by the number of quarks in $Au + Au$ collisions at $\sqrt{s_{NN}} = 200$ GeV. [45]

These models also explain the large baryon/meson ratio found in heavy ion collisions [46]. For example, in order to form a 3 GeV/c baryon, it would take three 1 GeV/c quarks, whereas to form a 3 GeV/c meson, it would take two 1.5 GeV/c quarks. Most parton spectra fall of steeply with increasing p_T, so there are many more 1 GeV/c quarks than 1.5 GeV/c quarks. This is illustrated in Figure 1.20. This leads to a larger baryon/meson ratio at intermediate p_T than in vacuum fragmentation. These models have successfully described many features of RHIC data qualitatively, although the models could be refined quantitatively [46].

Recombination models do not conflict with hydrodynamical models of the QGP, since they only propose that hadronization may occur by a different mechanism in heavy ion collisions. Indeed, models which combine hydrodynamics with recombination are able to describe the data at RHIC well [46]. Recombination does not require complete thermalization of the medium [46].

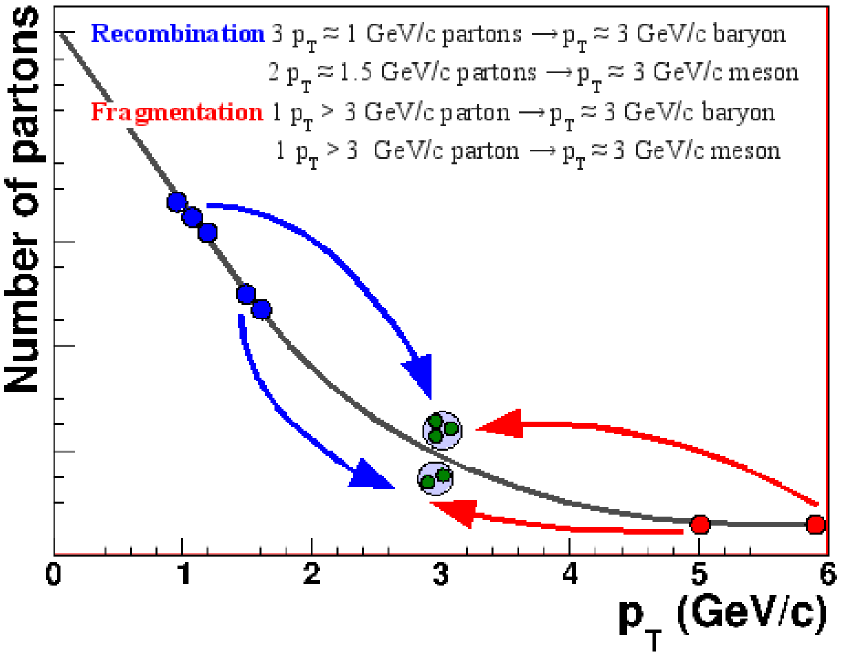

Figure 1.20: Cartoon demonstrating recombination.

1.5 Conclusions and overview

QCD predicts the presence of a new phase of matter for sufficiently hot and dense nuclear matter. RHIC was built to study this phase of matter so that we can better understand the phase diagram of nuclear matter. Our current understanding indicates that collisions at RHIC most likely produce a medium in a cross-over region between a hadronic gas and QGP. The most energetic of these collisions are believed to be above the crossover region.

The medium expands and cools rapidly, however, and experimental observations are influenced by phases other than the QGP. Initial state effects may also influence the results. The presence of a QGP may influence the hadronization of partons. Additionally, as the medium cools it is expected to go through a hadronic gas phase and during this time hadrons can have additional interactions.

Our understanding of the QGP and the phase diagram of matter has improved significantly since the beginning of the RHIC program. Many methods that have been used to describe a QGP qualitatively describe the features of the data, however, we do not yet have a complete quantitative description of the data. Some methods attempt to make predictions by calculating results directly from QCD. Provided that the approximations are valid, these theories should describe the partonic phases well, however, they are dependent on models of hadronization and interactions in a hadronic gas phase. Our knowledge of hadronization is heavily dependent upon experimental data because hadronization is a non-perturbative process. If the medium goes through a hadronic gas phase for any significant amount of time and hadrons reinteract, this would also change the properties of measured hadrons. Either of these effects or invalid assumptions made in calculations could be responsible for deviations between QCD-based theories and experimental data.

Many phenomenological models have been successfully used to describe the experimental data. Hydrodynamics in particular has been useful to describe not only azimuthal anisotropies but also hadron spectra. The success of hydro at describing many features of the data implies that the medium produced is a fluid made up of partons instead of hadrons. Hydrodynamics, however, is heavily dependent on thermalization of the medium and there is no conclusive proof that the medium has reached thermal equilibrium. Statistical models are consistent with the data but the agreement with these models is not sufficient to prove that the medium has reached thermal equilibrium. Recombination models have successfully described many aspects of the data and also point towards a picture of a medium characterized by partonic rather than hadronic degrees of freedom. Recombination models, which posit a modified hadronization mechanism in heavy ion collisions, are not dependent on complete thermalization and are consistent with hydrodynamical models.

These models and theories are not all mutually exclusive and may be valid in different regimes. The best way to test these models is compare them to as many measurements as possible. The studies presented in this thesis will focus on studies of jets formed by partons which have traversed the medium, taking advantage of the wealth of data available at RHIC. Jet-like di-hadron correlations are studied as a function of the collision system ($Cu + Cu$ versus $Au + Au$), the collision energy ($\sqrt{s_{NN}} = 62$ GeV versus $\sqrt{s_{NN}} = 200$ GeV), and particle type and strangeness content (unidentified hadrons, Λ, K^0_S, and Ξ).

Chapter 2 will introduce high-p_T triggered di-hadron correlations and discuss other relevant studies, performed either previously or concurrently. Here the two prominent features in di-hadron correlations, the jet-like correlation and the *Ridge*, will be introduced. These features are from particles close in azimuth to the trigger particle, called the near-side of the correlation. The properties learned from studies of the near-side in $Au + Au$ collisions at $\sqrt{s_{NN}} = 200$ GeV will be discussed. This will be followed by an overview of the experiment in Chapter 3. The analysis methods will be presented in Chapter 4 and Chapter 5, first discussing how particles used in the analysis are selected and then discussing the method for measuring di-hadron correlations. The results for the system, energy, and particle type dependence will be discussed in Chapter 6 and their interpretation in light of other data and of models will be discussed in Chapter 7. Chapter 8 will conclude and discuss the outlook for future studies of jets in heavy ion collisions. Di-hadron correlations after background subtraction

Chapter 2

Jets as a probe of a Quark-Gluon Plasma

Due to confinement, particles which carry a color charge, such as quarks and gluons, cannot be directly observed. Instead, they fragment into hadrons, which are color-neutral, and these hadrons are detected. In hard scattering processes the majority of the hadrons are produced roughly colinear to the fragmenting partons, resulting in a narrow cone of hadrons called a jet. At RHIC energies most jets are produced in 2→2 scattering of hard partons from the incoming nuclei. Since the incoming partons have momenta nearly parallel with the nuclei, momentum conservation causes the scattered partons to be separated by roughly 180° in azimuth. Events with jets at RHIC energies are dominantly back-to-back di-jets. Figure 2.1 shows an example of a di-jet event in STAR. The beam goes through the center and the lines show the different sectors of the Time Projection Chamber.

The jet cross section can be calculated in perturbative QCD as the average of quark, anti-quark, and gluon processes. For two partons scattering the jet cross section is given by

$$\sigma_{i,j\to k} = \sum_{i,j} \int dx_1 dx_2 dt f_i^1(x_1, Q^2) f_j^2(x_2, Q^2) \frac{d\sigma_{i,j\to k}}{dt} \tag{2.1}$$

where x_1 and x_2 are the fraction of the nucleon's momentum carried by the parton, Q^2 is the momentum transfer in the scattering, f_i^1 and f_j^2 are the parton distribution

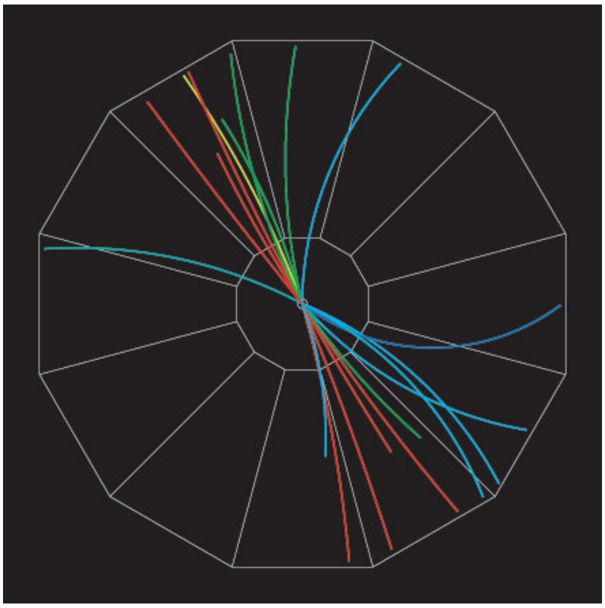

Figure 2.1: Sample jet observed in STAR in a real $p+p$ collision at $\sqrt{s_{NN}} = 200$ GeV

functions in the nucleons, and $\sigma_{i,j\rightarrow k}$ is the cross section for the reaction $ij \rightarrow k$ [47]. Parton distribution functions are the probability densities for finding a parton as a function of Q^2 and x.

After the hard scattering, the scattered partons hadronize. The process of hadronization is non-perturbative. It is described by fragmentation functions, which represent the probability for a parton to fragment into a particular hadron. Fragmentation functions have not been determined from first principles, however, it is possible to parameterize them as functions of the parton energy and the fraction of energy carried by the parton and then determine the fragmentation functions from data. Vacuum fragmentation functions have been well constrained by data from elementary collisions.

In heavy ion collisions, jets are formed from parton scattering which likely occurs early in the collision. The partons then travel through the medium and therefore serve as a probe of the medium. This scenario is depicted in Figure 2.2. Since jets have been studied extensively in $p+p$ collisions, modifications of jets in $A+A$ collisions relative to $p+p$ can be attributed to interactions with the medium. These modifications may

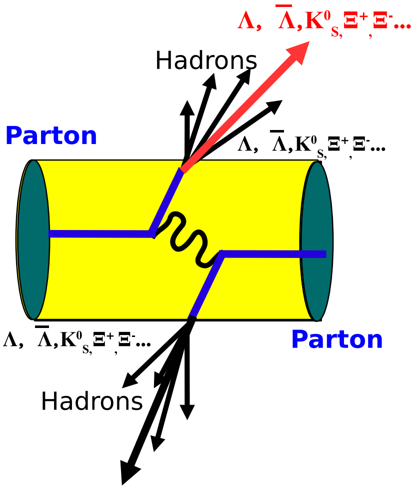

Figure 2.2: Schematic diagram of a di-jet in a heavy ion collision. The red arrow denotes the leading hadron, the one with the highest p_T, and the black arrows denote other hadrons produced during hadronization.

come in the form of parton energy loss before fragmentation or modification of the fragmentation functions for partons that fragment in the medium.

There have been many different approaches to studying jets at RHIC. In this chapter the various methods and key results from RHIC are reviewed. Some of these studies occurred concurrently with the analyses presented in this thesis, and discussion of these results is necessary to form a complete picture of what can be learned from the data on jets at RHIC.

2.1 Studies of jets through high-p_T triggered di-hadron correlations

In di-hadron correlations, a high momentum particle is selected and the distribution of particles relative to that particle is determined. The former particle is called the trigger particle and the latter are called the associated particles. The primary criterion used to determine trigger and associated particles is their momenta and the method neglects contributions from any sources of correlations between high-p_T particles other than jets and anisotropic flow. Anisotropic flow is a background and its subtraction is discussed further in Chapter 5. The momenta of the trigger and associated particles are restricted to high-p_T to increase the probability that the particles come from a jet and therefore decrease the combinatorial background. It has been argued that contributions from other sources are non-negligible. In particular it has been proposed that a significant fraction of trigger particles may not come from jets [48]. The STAR collaboration presented correlations normalized per trigger particle and with this normalization, results from different systems ($p + p$, $d + Au$, $Cu + Cu$, and $Au + Au$) would be identical if there were no modification of the jet [49–55]. The PHENIX collaboration typically used a different normalization where the amplitude of the correlation is interpreted as the probability for an associated particle to be correlated with the jet [56–62].

2.1.1 Early studies of jets at RHIC

Figure 2.3 shows di-hadron correlations from STAR [53]. The peak near $\Delta\phi = 0$ comes from hadrons which fragmented from the same parton as the trigger hadron and is called the near-side jet. The peak near $\Delta\phi \approx \pi$ comes from a momentum conserving jet opposite the near-side jet and is called the away-side jet. Figure 2.3(a) compares correlations from $p + p$, minimum bias $d + Au$, and the 0-20% highest multiplicity $d + Au$ collisions and demonstrates that while the background is higher in $d + Au$, there are no dramatic differences between $p + p$ and $d + Au$. This implies that initial state effects do not significantly modify the shape of jets, which would be evident in the $d + Au$ data. Even though there is no jet quenching in $d + Au$, the away-side is broadened in pseudorapidity. This effect is present in simple models of $p+p$ collisions and is due to (1) the difference between the center of mass frame of the scattered partons and the lab frame and (2) the difference between the jet axis and the direction of the momentum of the leading parton. Figure 2.3(b) compares $p + p$, $d + Au$, and central $Au + Au$ after background subtraction. Whereas there is a clear near-side peak in all systems, the away-side peak is not evident in central $Au + Au$

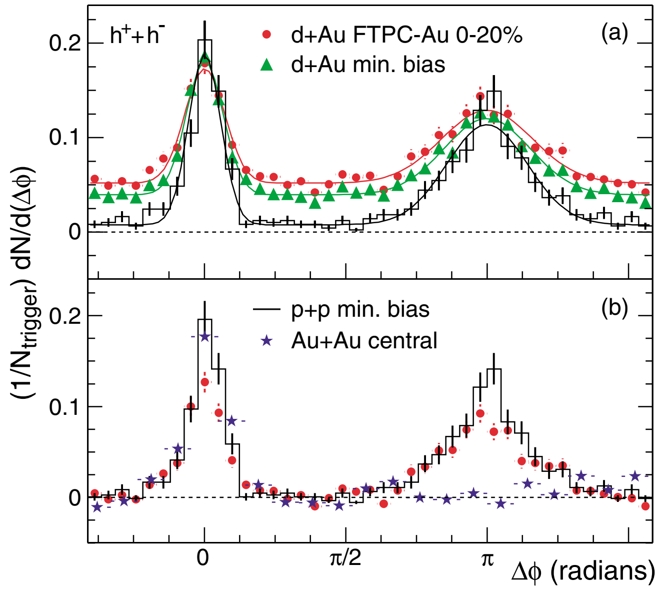

Figure 2.3: Di-hadron correlations from $p+p$, $d+Au$, and $Au+Au$ collisions at $\sqrt{s_{NN}} = 200$ GeV [53]. (a) Correlations for $p+p$, minimum bias $d+Au$, and central $d+Au$ collisions with no background subtraction. (b) Correlations for $p+p$, $d+Au$, and 0-10% central $Au+Au$ collisions after background subtraction. Data are for 2 GeV/c $< p_T^{associated} <$ 4 GeV/c and 4 GeV/c $< p_T^{trigger} <$ 6 GeV/c.

data. The disappearance of the away-side jet is called jet quenching. High-p_T partons are biased towards the surface, as shown in Figure 1.7. The surface bias is expected to be greater for di-hadron correlations because two high-p_T partons are required [15]. This is significant for the interpretation of di-hadron correlations, as it implies that the near-side jet is more likely to come from the surface.

Theoretical studies of correlations usually treat the near-side and the away-side separately. It is generally assumed that the near-side comes from surface-biased partons, while the away-side comes from partons which have traveled through the medium.

2.1.2 The Away-side

Figure 2.3 shows the di-hadron correlation for relatively high-p_T associated particles, however, the momentum contained in the jet must be conserved so there should be

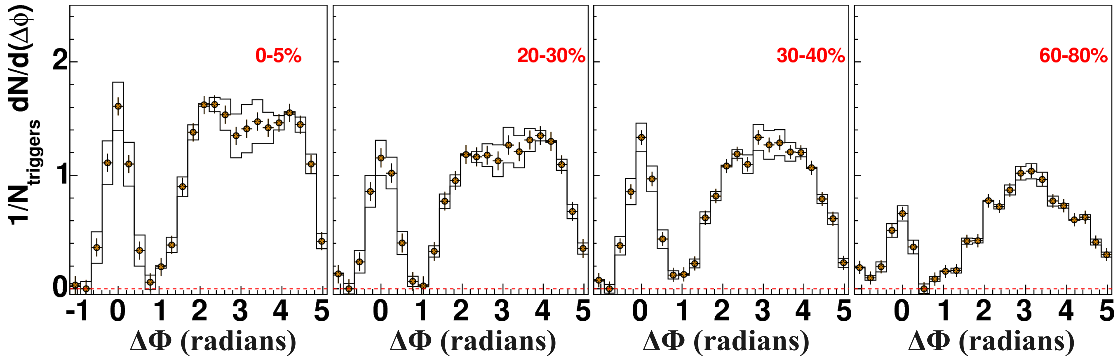

Figure 2.4: Di-hadron correlations after background subtraction for 0.15 GeV/c < $p_T^{associated}$ < 4 GeV/c and 4 GeV/c < $p_T^{trigger}$ < 6 GeV/c from $Au + Au$ collisions at $\sqrt{s_{NN}} = 200$ GeV [63].

some evidence that the away-side jet was produced even if it is quenched. Figure 2.4 shows di-hadron correlations for lower momentum associated particles. The away-side reappears at lower p_T, but it is broader than in $p+p$ or $d+Au$ collisions (not shown, [63]). Many mechanisms were proposed for the production of this structure, including global momentum conservation [64], away-side jets deflected 180° away from the near-side jet [65]; Čerenkov radiation of gluons [66]; and the formation of a Mach cone as the away-side jet moves through the medium [67, 68]. In these models particles on the away-side will have different correlations with each other, so evidence for these mechanisms was investigated by looking at three-particle correlations [69–73]. 3-particle correlations are very sensitive to assumptions about the shape of the background and are statistically limited, therefore, the data are not conclusive as of yet. However, a simple jet deflection model is ruled out because it cannot explain all of the structures in the data.

Figure 2.5 shows that for higher $p_T^{associated}$ and $p_T^{trigger}$ the away-side reappears. At sufficiently high p_T the shape is not dramatically modified relative to the away-side in $p+p$ and $d+Au$ collisions, however, the magnitude of the correlation is significantly lower [50]. This phenomenon is called punch-through. It is believed that the selection of high momenta hadrons biases the measurement towards jets produced by partons which have not lost much energy. This may be because the partons originated from collisions near the surface of the medium or that the initial hard scattering gave the

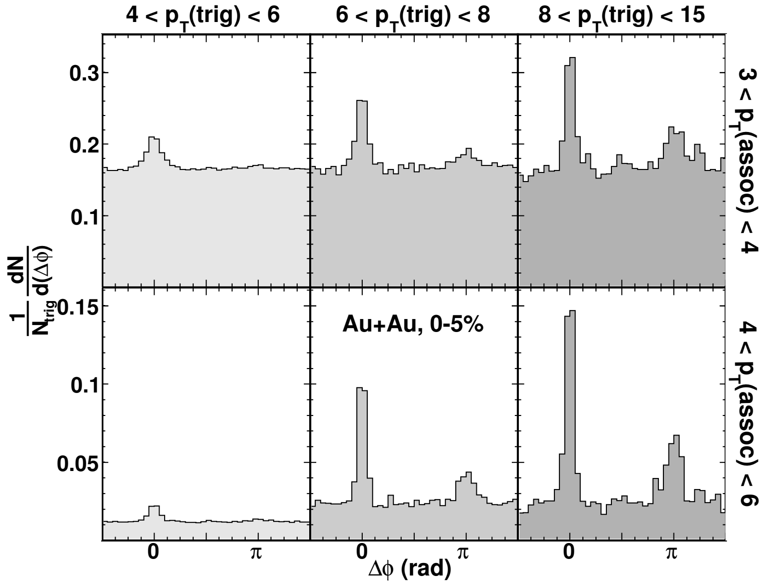

Figure 2.5: Di-hadron correlation before background subtraction with various kinematic cuts from $Au + Au$ collisions at $\sqrt{s_{NN}} = 200$ GeV [50].

partons enough energy that they could “punch through” the medium.

2.1.3 The near-side

The away-side was expected to have modifications due to interaction with the medium, however, the near-side is also modified relative to $p + p$ and $d + Au$ collisions. Figure 2.6 shows di-hadron correlations as a function of $\Delta\phi$ and $\Delta\eta$ in $d + Au$ and $Au + Au$ collisions.

The near-side peak in $d + Au$ is narrow in both azimuth and pseudorapidity, as expected for vacuum fragmentation. The peak that is present in $d + Au$ is called the jet-like correlation and is also evident in $Au + Au$. However there is a new component that is narrow in azimuth but broad in pseudorapidity; it is independent of pseudorapidity within the acceptance of the STAR TPC. This long range pseudorapidity correlation is called the *Ridge*. The *Ridge* has also been observed by PHENIX [75] and PHOBOS [76]. The measurement in [76] demonstrated that the *Ridge* extends to $\Delta\eta = 4$ for 2.5 GeV/c $< p_T^{trigger}$ and 0.35 GeV/c $< p_T^{associated}$.

Experimentally, a reasonably complete picture of the *Ridge* in $Au + Au$ collisions

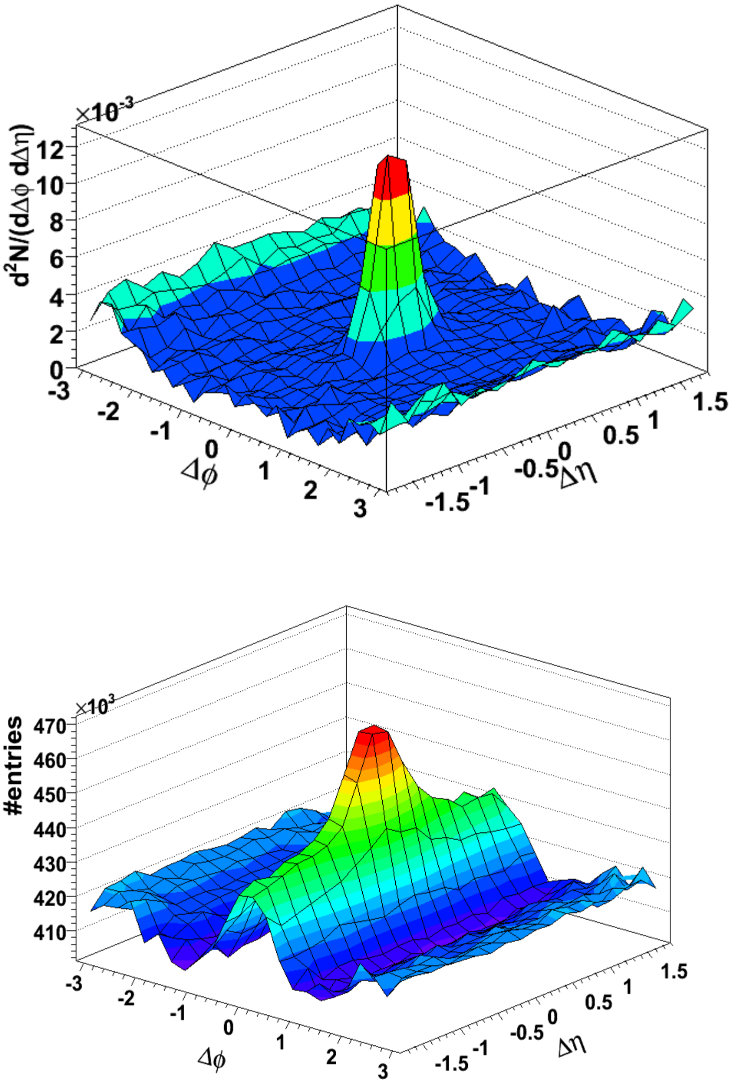

Figure 2.6: Di-hadron correlations in $d+Au$ (upper panel) and 0-12% central $Au+Au$ (lower panel) collisions at $\sqrt{s_{NN}} = 200$ GeV for 4.0 GeV/c $< p_T^{trigger} <$ 6.0 GeV/c and $2.0 < p_T^{associated} < p_T^{trigger}$. $\Delta\phi$ is in radians. In $d+Au$ there is one peak on the near-side that is narrow in $\Delta\phi$ and $\Delta\eta$ called the jet-like correlation. This peak is evident in the $Au+Au$ but there is an additional correlation that is narrow in $\Delta\phi$ but broad in $\Delta\eta$ called the *Ridge* [74].

at $\sqrt{s_{NN}} = 200$ GeV can be drawn since the multiplicity in $Au+Au$ collisions is high and STAR collected a data set with high statistics for $Au+Au$ collisions at $\sqrt{s_{NN}}$

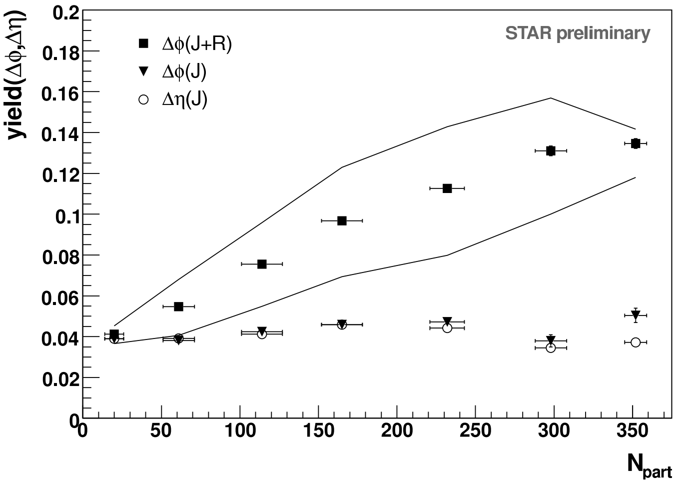

Figure 2.7: The number of particles in the *Ridge* and the jet-like correlation (J+R) and in the jet-like correlation alone (J) as a function of N_{part} for 4.0 < $p_T^{trigger}$ < 6.0 GeV/c and 2.0 < $p_T^{associated}$ < 4.0 GeV/c within -1.75 < $\Delta\eta$ < 1.75 for 0-12% central $Au + Au$ collisions at $\sqrt{s_{NN}}$ = 200 GeV [74]. The solid lines show the systematic error.

= 200 GeV in 2004. Figure 2.7 shows the number of particles in both the *Ridge* and the jet-like correlation combined and in the jet-like correlation alone as a function of N_{part}. The number of particles in the jet-like correlation is determined using two methods: (1) by subtracting the contribution from the *Ridge* and (2) determining the yield in azimuth and determining the number of particles in the peak above the plateau in pseudorapidity. These methods are discussed futher in Chapter 5. The jet-like correlation alone is almost independent of N_{part}, while the *Ridge* grows with N_{part}. The *Ridge* is not present in $d + Au$ [77].

The jet-like yield normalized per trigger should remain constant as a function of N_{part} if jet production in $A + A$ collisions is identical to jet production in $p + p$ collisions. If the yield per trigger changes as a function of N_{part} this may indicate that jet production is modified by the medium. Figure 2.7 indicates that the jet-like correlation may result from processes that occur in $p + p$ collisions while the *Ridge* results from processes that either do not occur in $p + p$ collisions or those which are more prominent in $A + A$ collisions.

Figure 2.8 shows the number of particles in the *Ridge* as a function of $p_T^{trigger}$.

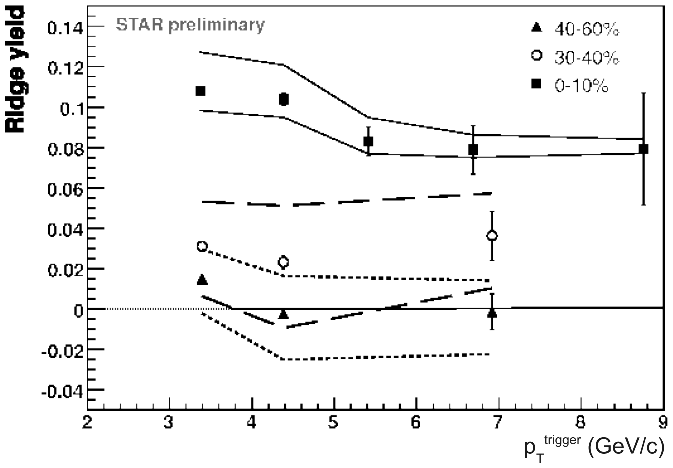

Figure 2.8: Number of particles in the *Ridge* as a function of $p_T^{trigger}$ for 2.0 $< p_T^{associated} <$ 4.0 GeV/c in $Au + Au$ collisions at $\sqrt{s_{NN}}$ = 200 GeV [74]. The solid lines correspond to the systematic errors for the number of particles in the 0-10% most central collisions, the dashed lines for 30-40%, and the dotted lines for 40-60%.

The yield of the *Ridge* is roughly independent of $p_T^{trigger}$ and is present even for very high $p_T^{trigger}$. The number of particles in the jet-like correlation, by comparison, grows with the trigger momentum (not shown, [77]), which would be expected for vacuum fragmentation since a higher momentum trigger is more likely to come from a higher momentum jet and therefore the total number of particles produced within the $p_T^{associated}$ range should be larger.

Figure 2.9 shows the spectra of particles in the *Ridge* as compared to particles in the jet-like correlation and the spectrum of all unidentified hadrons. The spectrum of particles in the jet-like correlation gets harder the higher the momentum of the trigger particle. Jets in $p+p$ would lead to the same effect, since higher momentum hadrons are likely to come from higher energy jets. The *Ridge* has a spectrum comparable to inclusive unidentified hadrons. This suggests that the particles in the *Ridge* may originate from the medium.

Traditional studies of fragmentation functions cannot be done precisely without full jet reconstruction because the total parton energy is not known, however, an approximation of the fragmentation function can be made using $p_T^{trigger}$ in place of

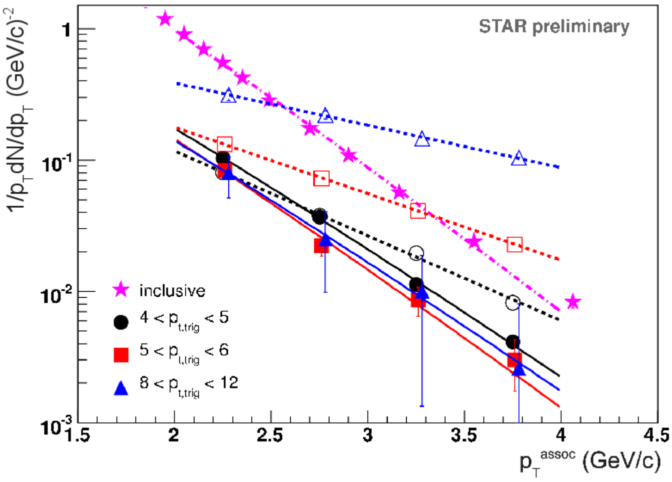

Figure 2.9: Spectra of particles in the *Ridge* (closed symbols) and the jet-like correlation (open symbols) in 0-12% $Au + Au$ collisions at $\sqrt{s_{NN}} = 200$ GeV [74].

the jet energy [78]. This is shown in Figure 2.10 for various trigger momenta. When the *Ridge* and the jet-like correlation are combined, there is a clear dependence on $p_T^{trigger}$, however, when the *Ridge* is subtracted, there is no dependence on $p_T^{trigger}$ for the jet-like correlation alone. Again, this supports a picture where the production of the jet-like correlation is similar to processes that occur in $p + p$ collisions while the *Ridge* occurs by a novel mechanism.

The composition of the *Ridge* and the jet-like correlation can also be determined by identifying the associated particles. Figure 2.11 shows the baryon/meson ratios for strange and non-strange particles in the *Ridge* and jet-like correlation as compared to the inclusive ratios in $Au + Au$ and $p + p$ as a function of p_T. The particle ratios in the jet-like correlation are comparable to those in $p + p$, consistent with a jet-like correlation produced dominantly by fragmentation. The particle ratios in the *Ridge* are consistent with the inclusive particle ratios in $Au + Au$ collisions. Systematic errors are large, but these data hint at the same trends shown in Figure 2.9 - that the jet-like correlation is dominantly produced by fragmentation and that the *Ridge* comprises particles from the bulk.

No trigger particle type dependence is seen in $Au + Au$ collisions for either the *Ridge* or the jet-like correlation [77]. There is no apparent difference between baryon

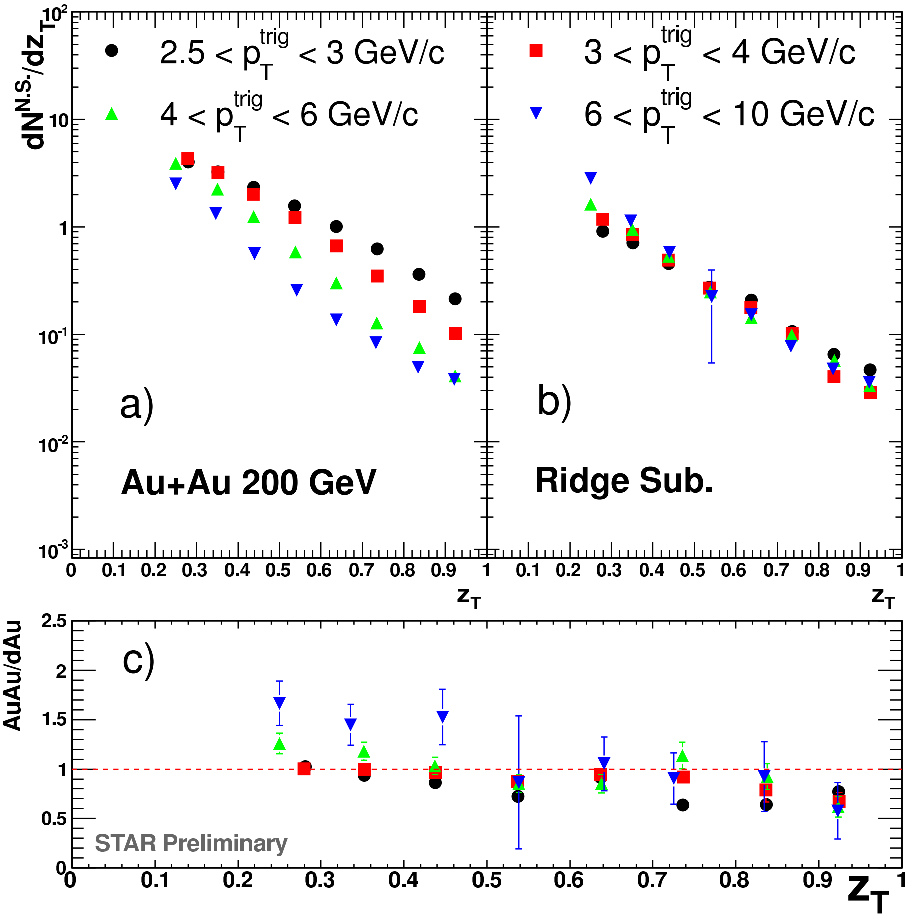

Figure 2.10: Di-hadron fragmentation function $z_T = \frac{p_T}{p_T^{trigger}}$ with and without *Ridge* subtraction in 0-12% central $Au + Au$ collisions at $\sqrt{s_{NN}} = 200$ GeV [74] (a) shows the di-hadron fragmentation for the jet-like correlation and the *Ridge* combined. (b) shows the di-hadron fragmentation function for the jet-like correlation alone after subtracting the *Ridge*. (c) shows the ratio of the di-hadron fragmentation function for the jet-like correlation alone to the di-hadron fragmentation function measured in $d + Au$.

and meson triggers, even though there are dramatic differences between baryons and mesons in nuclear modification factors (shown in Figure 1.19) and azimuthal anisotropies (shown in Figure 1.17). A trigger particle dependence might be expected if there were a dramatic difference between quark and gluon jets, as the rates of production of Λ and $\bar{\Lambda}$ are comparable in gluon jets but many more Λ than $\bar{\Lambda}$ are

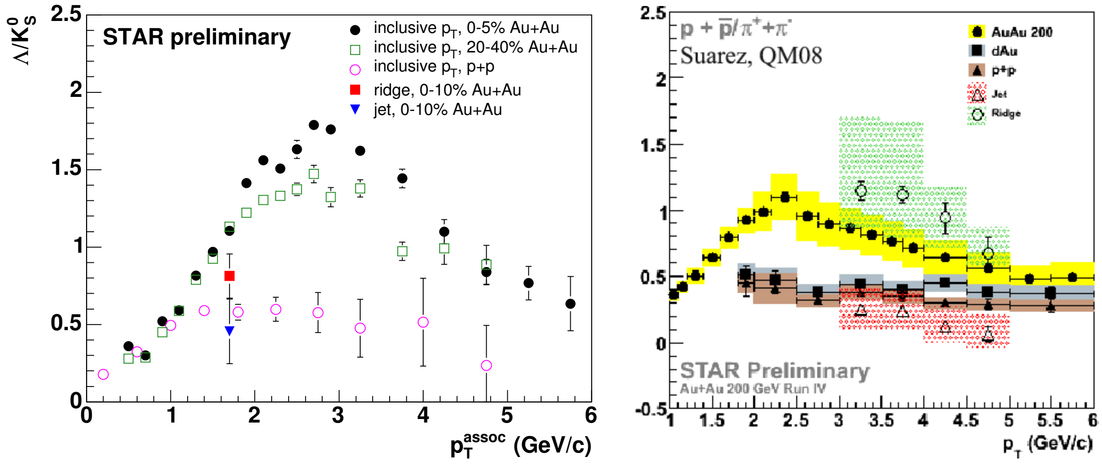

Figure 2.11: Comparisons of the Λ/K^0_S ratio (left) [79] and of the p/π ratio (right) [80] in the *Ridge* and the jet-like correlation to the inclusive ratios. Systematic errors are added in quadrature to the statistical errors for the Λ/K^0_S ratio and shown as bands for the p/π ratio.

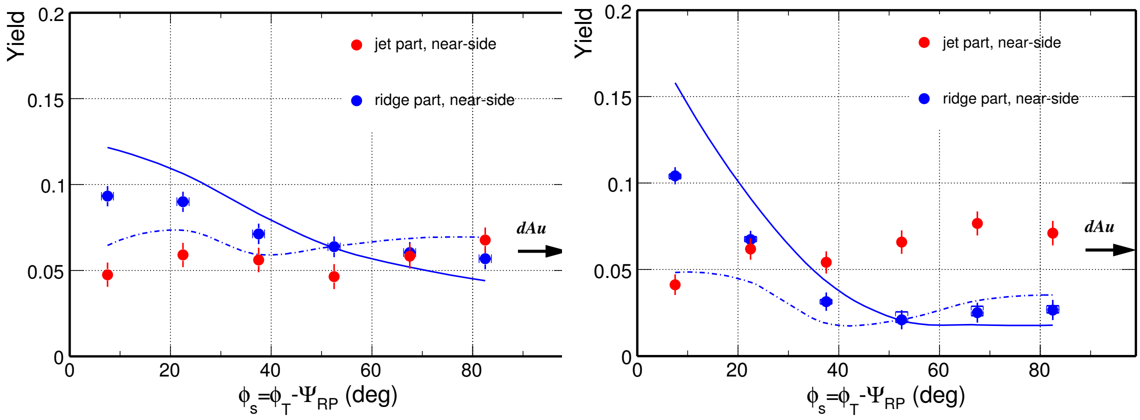

Figure 2.12: Reaction plane dependence of number of particles in the jet-like correlation and the *Ridge* for 0-5% central (left) and 20-60% central (right) $Au + Au$ collisions at $\sqrt{s_{NN}} = 200$ GeV [82]. The lines correspond to the systematic errors on the number of particles in the *Ridge*. The arrow corresponds to the reaction plane averaged jet-like yield in $d + Au$. The lines correspond to the systematic errors.

predicted to be produced by quark jets. No difference between Λ and $\bar{\Lambda}$ trigger particles is observed (not shown). This independence of the yield on the trigger particle type extends even to the Ω^- [81].

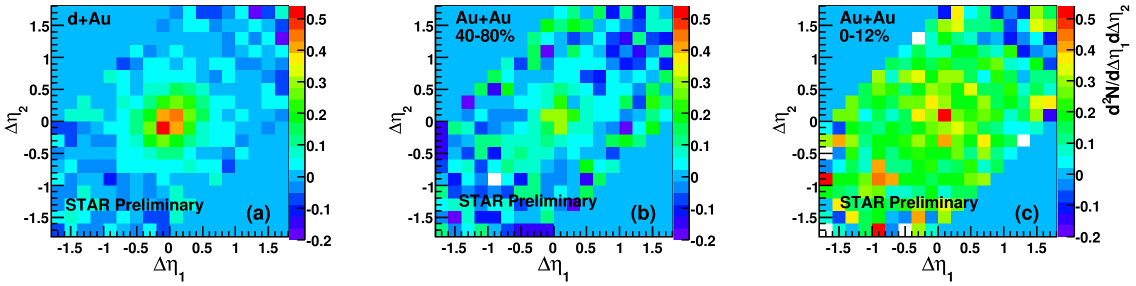

Figure 2.13: 3-particle correlations for $3.0 < p_T^{trigger} < 10.0$ GeV/c and $1.0 < p_T^{associated} < 3.0$ GeV/c for both associated particles on the near-side in $d + Au$, peripheral $Au + Au$, and central $Au + Au$ collisions at $\sqrt{s_{NN}} = 200$ GeV [83].

Figure 2.12 shows the reaction plane dependence of the *Ridge* and the jet-like correlations in two different centrality bins. The jet-like correlation shows little dependence on the direction relative to the reaction plane, as would be expected if the jet-like correlation originates from vacuum fragmentation. The *Ridge* is largest in plane, where the mean path length traveled by the parton would be shortest. If the *Ridge* is produced by parton energy loss, these results would indicate that jets produced out of plane are either produced on the surface or completely quenched.

Additionally, measurements were done to determine if particles in the *Ridge* are correlated with each other. 3-particle correlations on the near-side are shown in Figure 2.13. A trigger particle with $3.0 < p_T^{trigger} < 10.0$ GeV/c is selected and defines the origin. Only events with at least two associated particles in the range $1.0 < p_T^{associated} < 3.0$ GeV/c are selected and Figure 2.13 shows the location of the first associated particle relative to the trigger versus the location of the second associated particle relative to the trigger. A narrow peak around the trigger particle is observed in the $d + Au$, peripheral $Au + Au$, and central $Au + Au$ data and comes from the same process that produces the jet-like correlation in di-hadron correlations. In the $Au + Au$, this peak sits on top of a plateau; this is the *Ridge*. If the two associated particles came from the same source - for instance, from gluon radiation - they would be expected to be correlated in space. Instead, within the the acceptance of the detector and the statistical errors, particles in the *Ridge* do not appear to be correlated. However, an understanding of the effects of the kinematic cuts is required

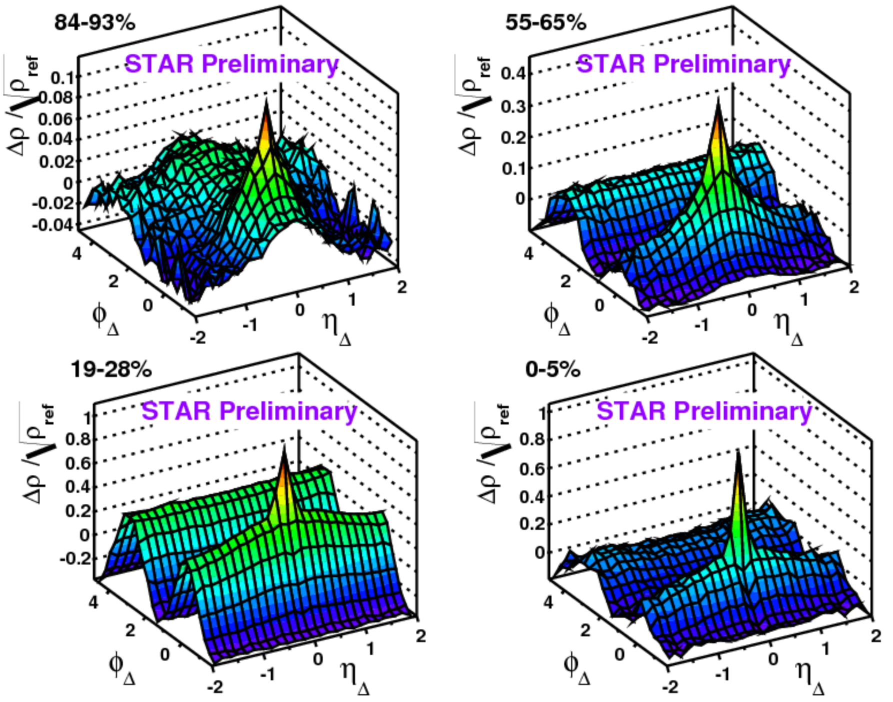

Figure 2.14: Di-hadron correlations without p_T cuts for different centralities in $Au+Au$ collisions at $\sqrt{s_{NN}} = 200$ GeV [84]. The z-axis is the probability for two particles to be correlated. ϕ_Δ is in radians.

to interpret the results properly. The lower cut of 1.0 GeV/c on $p_T^{associated}$ is necessary to reduce the combinatorial background, which may make the results more difficult to interpret. If, for instance, the *Ridge* were caused by gluon radiation, requiring two particles above 1.0 GeV/c could select only those events where two gluons were radiated and these gluons would not necessarily be correlated in space. It is therefore important to understand the effect of these kinematic cuts on the measured signal in various models for the production of the *Ridge*.

2.2 Untriggered di-hadron correlations

Di-hadron correlations have also been done with no cuts on the momenta of either the trigger or the associated particles. The motivation behind restricting the p_T of hadrons studied to high-p_T is to enhance the fraction of pairs coming from jets and reduce the background. Samples of correlations without p_T cuts are shown in Figure 2.14. When studies are done without cuts, all correlations between particles are evident, including those due to anisotropic flow, resonance decays, Hanbury-Brown-Twiss (HBT) correlations, Dalitz decays, conversion electrons, and jets. Anisotropic flow leads to a $\cos(2\Delta\phi)$ independent of $\Delta\eta$. There is almost no contribution from anisotropic flow in the most peripheral collisions and the contribution is largest in the 19-28% central events. Dalitz decays, conversion electrons, and HBT correlations all lead to the sharp peak at $\Delta\phi$ =0, $\Delta\eta$ =0. The contributions from resonances is greatest near $\Delta\phi$ =0, $\Delta\eta$ =0 and create structures that are dependent on the decay kinematics. Resonance contributions were determined to be negligible for unidentified hadrons. The contribution from jets contributes 2 peaks, one on the near-side and one on the away-side. Both of these peaks are evident in the most peripheral bin. The whole correlation is fit to determine the relative contributions from these sources. The near-side jet is the dominant feature near $\Delta\phi$ =0, $\Delta\eta$ =0 in peripheral collisions. This feature evolves from peripheral to central collisions into a peak which is much broader in pseudorapidity. This feature may or may not be the same as the *Ridge* observed for high-p_T triggered correlations.

2.3 Jet reconstruction

Full jet reconstruction allows determination of the parton energy and therefore would allow more careful measurements of partonic energy loss. It also overcomes the uncertainty of whether or not a hadron comes from a jet, one of the most significant limitations of di-hadron correlations. Full jet reconstruction was long thought to be impossible in heavy ion collisions at RHIC energies because the background is large and collisions were not expected to produce jets at a high enough energy to stand out above the background. However, there have been improvements in the background subtraction method [87, 88] and the STAR collaboration has recently successfully reconstructed jets in heavy ion collisions [85,89–91]. Figure 2.15 shows the jet spectrum in central $Au + Au$ collisions at $\sqrt{s_{NN}} = 200$ GeV compared to the jet spectrum in $p + p$ collisions scaled by the number of binary collisions. If all of the energy of the

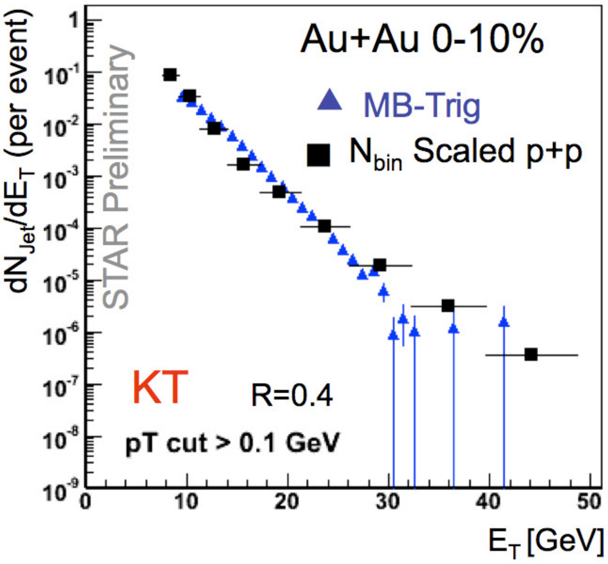

Figure 2.15: Reconstructed jet spectrum in central $Au+Au$ collisions at $\sqrt{s_{NN}} = 200$ GeV as compared to the jet spectrum in $p+p$ scaled by N_{bin} [85, 86]. Only statistical errors are shown for $Au+Au$ data. The systematic errors on the overall scale of the $p+p$ spectrum are 50%.

jet is measured, the spectra in $Au+Au$ and in $p+p$ collisions scaled by N_{bin} should be the same, as it appears to be. This does not mean that the parton did not lose energy, only that this energy must appear somewhere because of energy conservation. The systematic error on the $p+p$ spectrum is 50% [86] and the systematic errors on the $Au+Au$ spectrum are not yet determined. The jets' shape in azimuth and pseudorapidity could still be modified and the fragmentation functions are not necessarily vacuum fragmentation functions.

Jet reconstruction and correlation studies are complementary. If the shape is changed too dramatically, jet reconstruction algorithms may not recognize the modified jets. Additionally, some studies of rare particles in jets are best suited to correlation studies due to statistics.

2.4 Summary

Studies of di-hadron correlations and nuclear modification factors at RHIC have demonstrated that jets are considerably modified by the medium. This could be through partonic energy loss before fragmentation or through modification of the fragmentation functions in the medium. These modifications have typically been classified as being on the near-side or the away-side. A note of caution is warranted since the near-side and the away-side are defined only by their relation to the trigger particle and the only indication that the trigger particle might come from a jet is its momentum.

For an intermediate p_T trigger (roughly $3.0 < p_T^{trigger} < 6.0$ GeV/c), particles on the away-side are observed at lower momentum than in $p+p$ and $d+Au$ collisions. The away-side is not observed at $p_T^{associated} \approx 2$ GeV/c (Figure 2.3), but at lower momenta the away-side is broadened and develops a double-peaked structure (Figure 2.4). When the momenta of the trigger and associated particles are increased, the away-side reappears (Figure 2.5); this is interpreted as a greater bias towards unmodified jet fragmentation, perhaps through greater surface bias. The *Ridge* is the dominant feature on the near-side for intermediate p_T triggers (Figure 2.6). It persists out to $p_T^{trigger} \approx 8$ GeV/c, however, a greater percentage of the particles correlated with the trigger particle are in the jet-like correlation (Figure 2.8). As $p_T^{associated}$ is increased, a greater percentage of the particles correlated with the trigger particle are in the jet-like correlation (Figure 2.9); at lower $p_T^{associated}$, measurements are overwhelmed by systematic errors and precise data are unavailable. The features observed in correlation studies are momentum dependent, presumably reflecting differences in the relative importance of various mechanisms which produce correlations as a function of p_T.

The jet-like correlation shows the N_{part}, $p_T^{associated}$, and $p_T^{trigger}$ dependence that would be expected from vacuum fragmentation, although a more quantitative understanding of the jet-like correlation is needed. The *Ridge* is a new feature that appears to be made of particles from the bulk due to its similar composition (Figure 2.11).

The spectra of particles in the *Ridge* are comparable to the inclusive spectra of particles, and the ratios of particles in the *Ridge* are similar to those in the bulk. The *Ridge* is clearly correlated in space with a high-p_T particle, but that does not prove that the production of the two are related. The full breadth of the data and an understanding of various models for the production of the *Ridge* are necessary to determine what this feature is, where it comes from, and what it can tell us about the QGP and relativistic heavy ion collisions. The studies presented in this thesis will add to our understanding of the jet-like correlation and the *Ridge* by investigating their dependence on collision energy and system size and their particle type dependence.

Chapter 3

Experiment

3.1 The Relativistic Heavy Ion Collider

The Relativistic Heavy Ion Collider (RHIC) is located in Upton, NY on Long Island and is approximately 1.2 km in diameter. An aerial view of RHIC is shown in Figure 3.1. RHIC spans nearly two orders of magnitude in collision energy per nucleon. RHIC was designed to collide nuclei with an atomic mass, A, ranging from A = 1 to A $\approx$ 200. It is also capable of asymmetric collisions, those between ions with different masses, such as $d + Au$. Asymmetric collisions are useful for distinguishing the effects of cold nuclear matter (modification of the initial state in a nucleus) versus hot nuclear matter (such as a QGP). To date RHIC has taken data from the collision energies and systems shown in Table 3.1. RHIC is also the only collider in the world capable of colliding both longitudinally and transversely polarized protons. Polarized proton collisions are used to study the origin of the spin of the proton. RHIC has now collided polarized protons at 500 GeV. Design specifications for RHIC are listed in Table 3.2. These specifications have now been exceeded. $Au + Au$ collisions can reach energies as low as 2.5 GeV/u. $p + p$ collisions with up to 109 bunches in each ring and at luminosities of up to 9 x 10^{31} cm^{-2} s^{-1} were obtained in the 2009 run.

The ion beams are created by stripping the electrons off of the nuclei and accelerating the nuclei to their full energy in several stages. For gold ions, negatively charged

Collision system	$\sqrt{s_{NN}}$ (GeV)
$p+p$	200, 500
$d+Au$	200
$Cu+Cu$	62, 200
$Au+Au$	9, 20, 62, 130, 200

Table 3.1: Collision systems and energies produced at RHIC so far.

ions from a pulsed sputter ion source are stripped of some of their electrons by shooting them through a foil on the positive terminal of the Tandem Van de Graaff. In the second stage the ions, now positively charged, are accelerated towards the negative

Figure 3.1: Aerial view of the Relativistic Heavy Ion Collider [92].

	$Au+Au$	$p+p$
Beam energy	9-100 GeV/u	30-250 GeV/u
Number of bunches/ring	60	60
Luminosity	12 x 10^{26}cm^{-2} s^{-1}	2 x 10^{31} cm^{-2} s^{-1}
Luminosity lifetime	10 hr	> 10 hr

Table 3.2: RHIC design specifications [92, 93].

terminal of the Van de Graaff. After exiting the Van de Graaff the nuclei have an energy per nucleon of 1 MeV/u. More electrons are stripped as the ions exit the Van de Graaff. The ions are passed through bending magnets to select only +32 charge states. The Booster Synchrotron accelerates these ions to 95 MeV/u, and more electrons are stripped as the ions leave the Booster synchrotron leaving the ions in a +77 charge state. The Alternating Gradient Synchrotron (AGS) accelerates these ions to 10.8 GeV/u. As the ions leave the AGS, the remaining electrons are stripped and ions are brought to their injection energy and charge of +79. They are injected into RHIC through the transfer AGS-to-RHIC Beam Transfer Line four bunches at a time. Protons are injected from a linear proton accelerator, the LINAC, into the AGS and then into RHIC. Full details are given in [93].

RHIC is two concentric storage rings for beams moving in opposite directions and has six interaction points where the beams can be collided. There were experiments in four of these interaction points. Phobos and BRAHMS (Broad RAnge Hadron Magnetic Spectrometers) both took their last data in the spring of 2006. PHENIX (Pioneering High Energy Nuclear Interactions eXperiment) and STAR (Solenoidal Tracker At RHIC) are both still taking data. The data in this thesis are from the STAR detector taken in 2004 and 2005.

3.2 The STAR detector

The Solenoidal Tracker At RHIC (STAR) detector comprises multiple subsystems. Figure 3.2 shows a cut-away view of STAR and Figure 3.3 shows a profile view in the

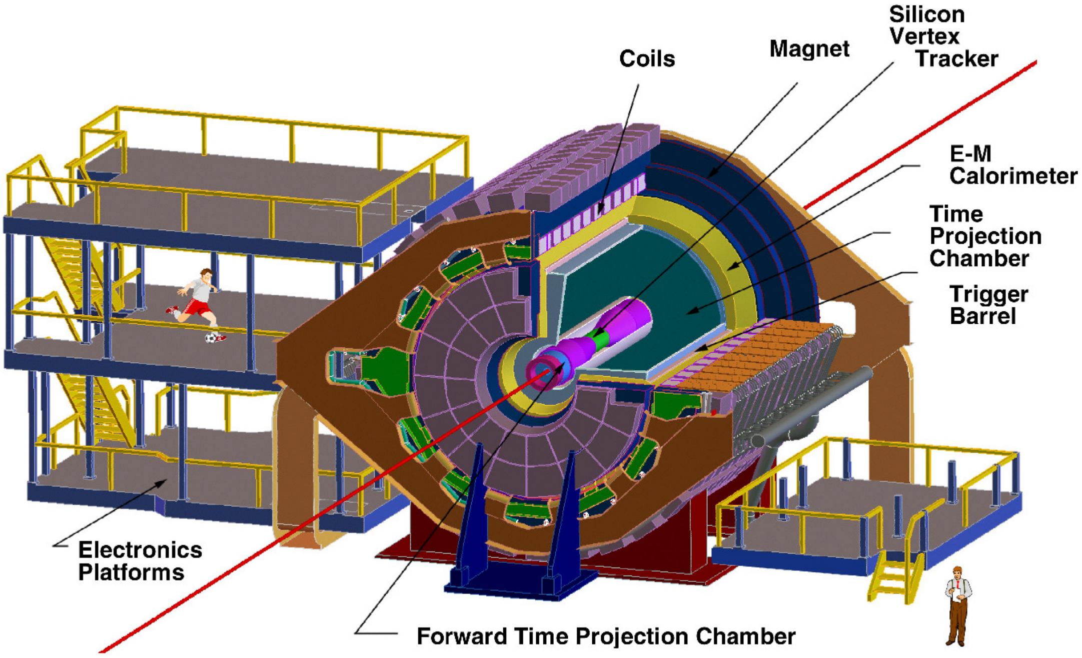

Figure 3.2: The STAR detector with a section cut away to show the inner detectors [94].

detector configuration for the 2001 run. STAR was designed to be most sensitive to charged hadrons. Most subsystems sit inside of the STAR magnet, a large solenoidal magnet with a roughly uniform magnetic field up to 0.5 T parallel to the beam pipe. The primary tracking detector is the Time Projection Chamber (TPC), discussed in greater detail in Section 3.2.1. The TPC has full azimuthal acceptance and a maximum acceptance in pseudorapidity of $|\eta| \leq 1.8$. The TPC extends from a radius of 50 cm to 200 cm from the beam axis and is 4.2 m in length along the beam axis. The TPC is only sensitive to charged particles, although the decay vertices from neutral hadrons can be reconstructed from tracks of charged decay products left in the TPC.

In addition to the TPC, there are Forward Time Projection Chambers (FTPC) with coverage in pseudorapidity of $2.5 < |\eta| < 4$ and complete azimuthal coverage. The maximum number of hits possible in the FTPC is 10. Due to this small number of hits, the momentum resolution of these tracks is worse than in the TPC. The FTPC

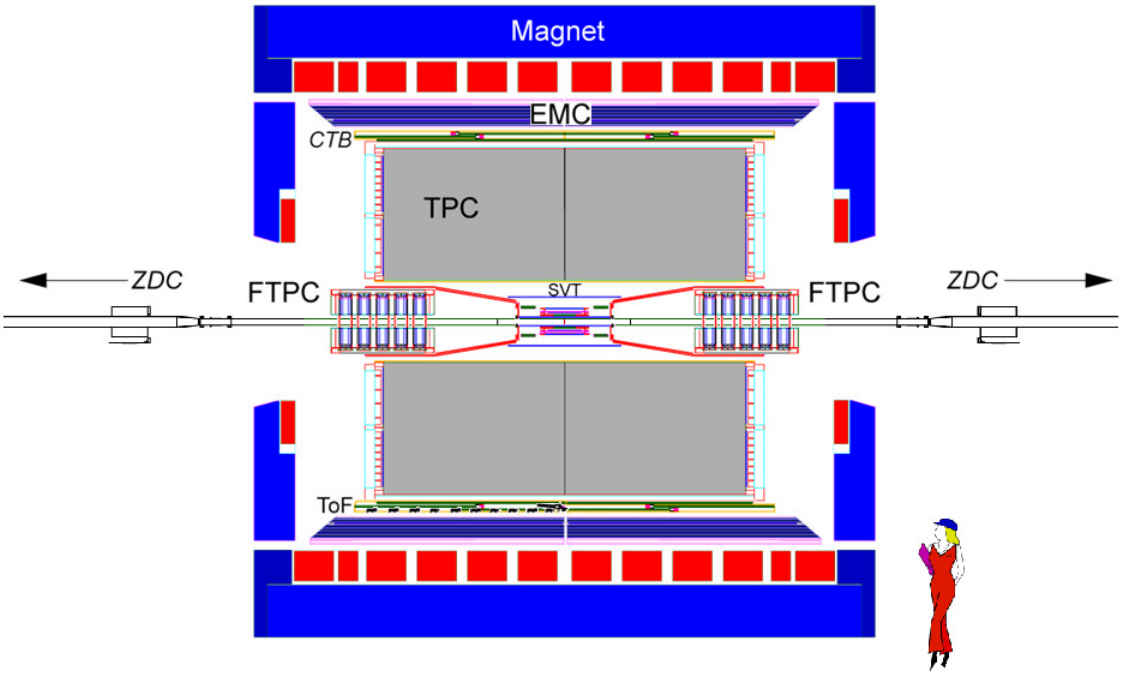

Figure 3.3: A profile view of the STAR detector [94]. This was the detector configuration for the $Cu+Cu$ run in 2005.

can also be used to determine the reaction plane.

There are two silicon detectors, the Silicon Vertex Tracker (SVT) and the Silicon Strip Detector (SSD) inside the inner field cage of the TPC. These detectors have hit resolutions of approximately 100 μm and 200 μm, respectively. The three layers of the SVT range from radii of 7, 11, and 15 cm from the beam pipe. The single silicon layer SSD is located at 23 cm radially from the beam pipe. These silicon detectors have the capacity to provide more accurate tracking closer to the beam pipe, but these detectors were only used in the 2005 run and later.

There are two electromagnetic calorimeters that can be used for measurements of electrons, photons, and triggering. The Barrel Electromagnetic Calorimeter (BEMC) has full acceptance in azimuth and an acceptance of $|\eta| < 1$. The Endcap Electromagnetic Calorimeters (EEMC) have full azimuthal acceptance and an acceptance of $1 < \eta < 2$. All electromagnetic calorimeters have shower maximum detectors to distinguish signals left by hadrons from those left by photons and electrons.

The Central Trigger Barrel (CTB) and the Zero Degree Calorimeters (ZDC) are primarily used for triggering on central events. The CTB is an array of scintillator slats that surround the TPC and trigger on the flux of charged particles at midrapidity. The ZDCs sit 18 m away from the interaction region at an angle of <2 mrad from the interaction region along the beam pipe. The ZDCs measure the energy deposited by neutral particles in the forward direction, primarily the spectator neutrons. In $d + Au$ collisions, a signal is required in the ZDC from the neutron in the deuteron to ensure that a collision occurred. The ZDCs can also be used to determine the reaction plane. Each experiment at RHIC has identical ZDCs to allow experiments to cross-calibrate centrality definitions.

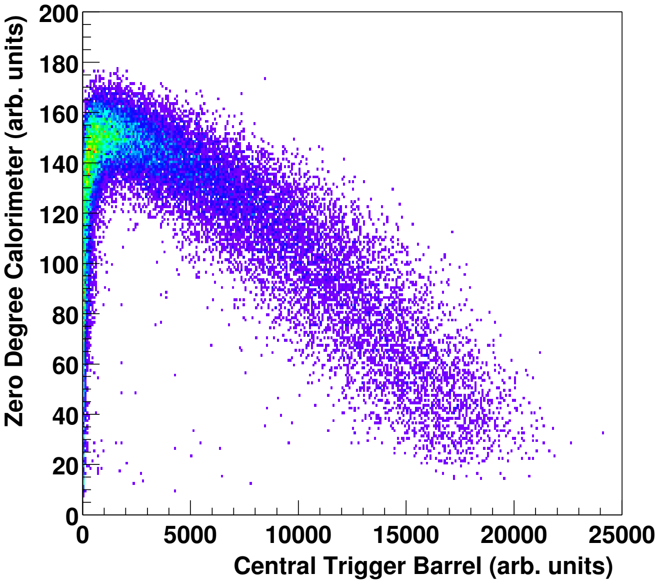

Figure 3.4: The signals recorded in the Zero Degree Calorimeter versus the signals recorded in the Central Trigger Barrel in $Au+Au$ collisions at $\sqrt{s_{NN}} = 130$ GeV [94].

Figure 3.4 shows the signal in the ZDCs versus the signal in the central trigger barrel. Peripheral events deposit energy in the ZDCs because fragments from the nucleus are only slightly deflected from the beam pipe. The energy deposit in the

ZDC does not constrain the centrality because a small signal in the ZDCs may be recorded in both peripheral and central collisions. Peripheral collisions may only leave a few neutrons traveling along the beam axis to be measured by the ZDCs; in the most central collisions, all of the neutrons participate in the collision, leaving no neutrons for detection by the ZDCs. However, the larger the signal in the central trigger barrel the more central the collision. The CTB and ZDC combined allow STAR to trigger on a variety of collision centralities.

3.2.1 The Time Projection Chamber

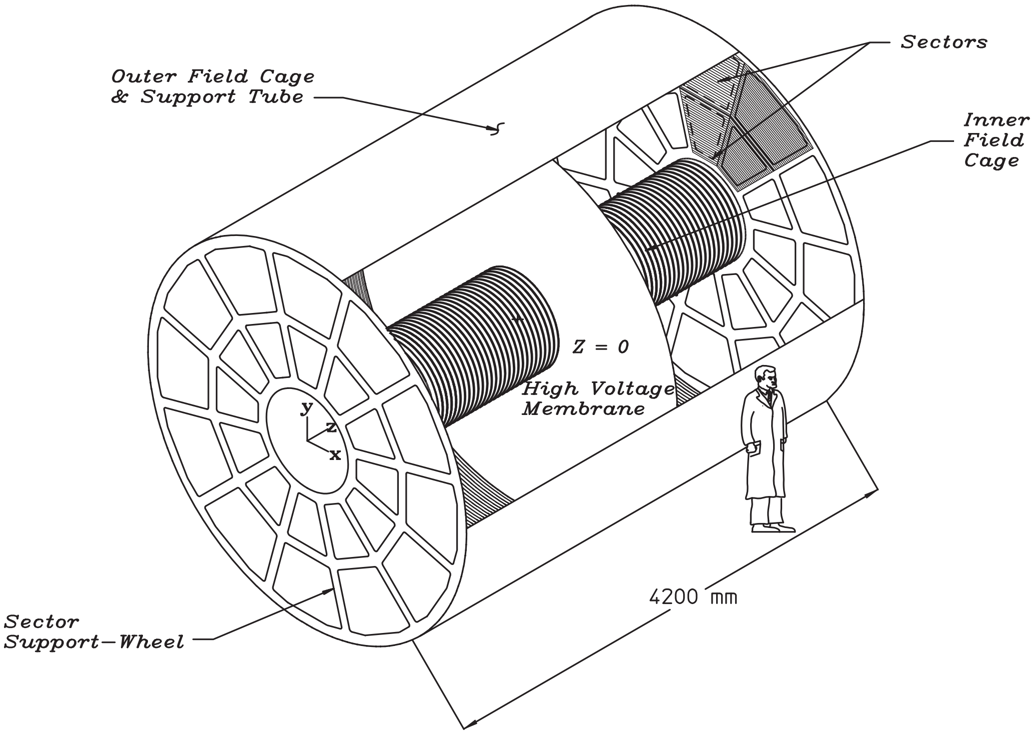

Figure 3.5: Diagram of the field cage of the TPC [95].

In a Time Projection Chamber (TPC), charged particles travel through a volume of gas, leaving a trail of ionization behind them which reveals the path followed by the particle. The STAR TPC is cylindrical around the beam pipe and sits inside the STAR magnet with a magnetic field of up to 0.5 T parallel to the beam pipe. The TPC central membrane and field cage create an electric field of 135 V/cm that is parallel to the beam pipe. The TPC is 4.2 m long with an outer diameter of 4 m and an inner diameter of 1 m. The magnetic field bends charged particles as they move through the TPC, allowing determination of momentum.

When a charged particle travels through the TPC, it knocks off electrons from the molecules in the gas. These ionization electrons are accelerated through the TPC by the electric field until they reach a constant speed which is a characteristic of the gas and the electric field. They move roughly two orders of magnitude faster than the ionized gas and therefore will be collected first. For sufficiently low event rates, the ions can be neglected; for higher rates of events, ions can create significant local distortions in the electric field that alter the trajectory of nearby ionization electrons and can impair momentum resolution unless these field distortions are corrected for. The position in the plane perpendicular to the beam (the x-y plane) is determined by the location where the ionization electrons are collected on the readout pads. The position in the direction along the beam axis (the z-axis) is determined by the time that it takes the ionization electrons to reach the endcap, hence the name Time Projection Chamber.

A significant advantage of the TPC is its low material budget (2.43% X_0) which reduces the probability of photon conversion as they pass through the TPC and reduces the probability for hadrons to scatter in the TPC. The drift volume of the TPC is filled with P10 gas (10% methane and 90% argon) held at 2 mbar above atmospheric pressure. The slight overpressure reduces impurities in the gas since any leaks will cause P10 to leak out instead of causing air to leak in. Water and oxygen dramatically change the drift velocity of electrons and can capture electrons, reducing the efficiency of the response of the TPC to charged particles. Operating the TPC near the maximum electron drift speed reduces the effect of symmetry magazine slight fluctuations in the electric field. P10 gas has its maximum electron drift speed (5.45 cm/s) at a relatively low electric field, reducing the overall electric field needed.

The drift volume sits in a uniform field of $\approx$ 135 V/cm created by the field cage of the TPC shown in Figure 3.5. The central membrane of the field cage is at roughly the center of the interaction region and is held at a voltage of 28 kV. The end caps are grounded, and the field is made more uniform by 182 equipotential rings on each of the inner and outer field cages, connected by 2 Ω resistors. This results in variations in the electric field of no more than about 2% in the entire TPC volume [95,96]. The field accelerates the ionization electrons towards the endcaps.

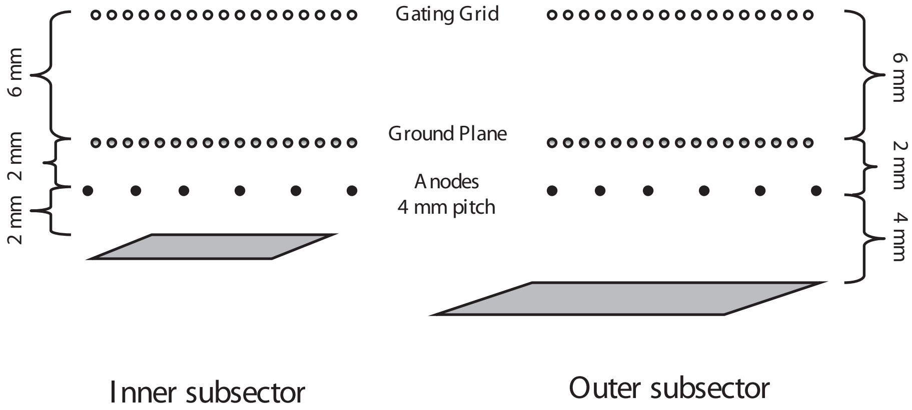

Figure 3.6: Arrangement of a readout chamber of the TPC [97].

The endcaps comprise Multiwire Proportional Chambers (MWPC) with readout pads, as shown in Figure 3.6. The readout chambers have three wire planes, a gating grid, a ground plane, and anode wires. When the gating grid is closed, voltages on neighboring wires alternate between ±75V, creating an electric field that allows neither positive nor negative charges to pass. To open the grid all wires are held at 110V. Field lines for a gating grid in open and closed configurations are shown in Figure 3.7.

The gating grid is normally closed to minimize the buildup of ions in the readout chamber. The gating grid opens when a trigger is received. Since electrons knocked out of gas molecules in the drift region of the TPC move much faster than the ions and travel in the opposite direction, only electrons will enter the readout chamber while the gating grid is open. Electrons passing through the gating grid will accelerate towards the anodes, initiating an avalanche. In the STAR TPC, the number of electrons in the avalanche is roughly proportional to the initial charge. Electrons from this avalanche

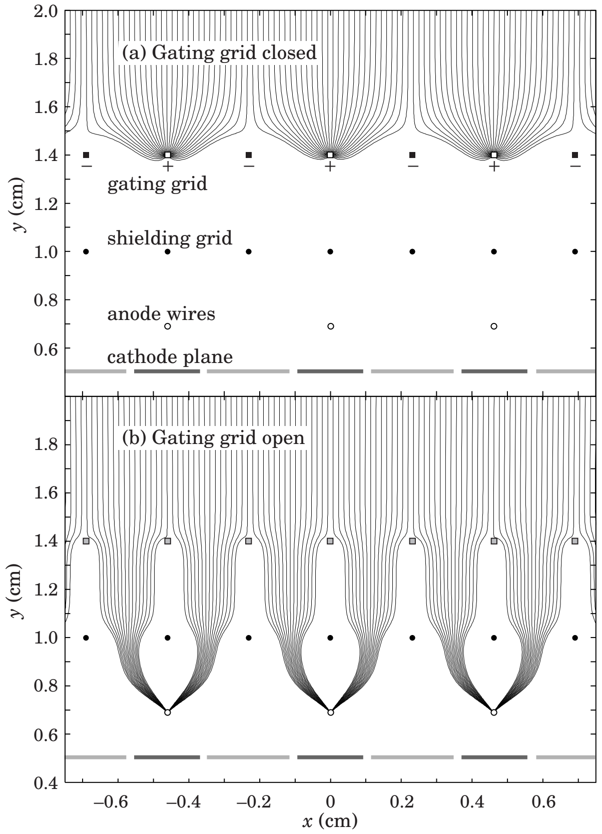

Figure 3.7: Field lines for a gating grid in the (a) closed and (b) open configurations [98].

are collected on the wires, but a cloud of positively charged ions remains. An image charge will form on the readout plane and it is the image charge that is recorded.

The width of the cloud of charge in the STAR TPC is diffused by 185 μm/$\sqrt{cm}$ and 320 μm/$\sqrt{cm}$ traveled through TPC in the transverse and longitudinal directions, respectively. The width of the image charge collected on the readout pad is also dependent on the dip angle and crossing angle of the track. The dip angle is the angle between the particle's momentum and the drift direction. The crossing angle is that between the particle's momentum and the direction normal to the pad row. The size of the image charge is smallest for short drift distances, small crossing angles, and small dip angles. The average width of the image charge is 350 μm in the transverse direction and 700 μm in the longitudinal direction, smaller than the typical TPC pad.

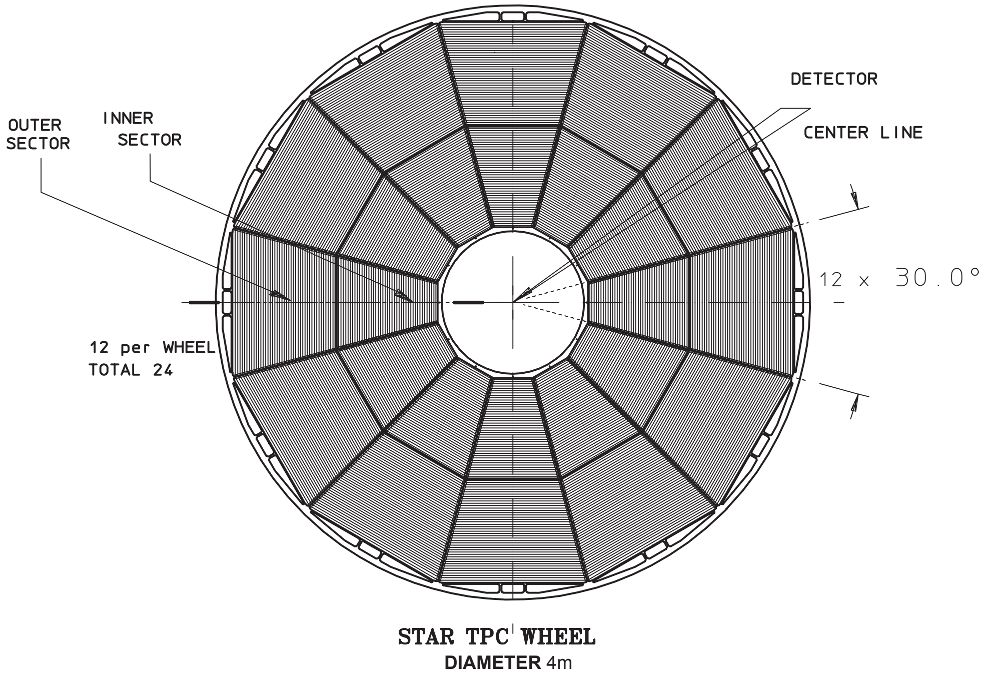

Figure 3.8: Arrangement of the readout modules of the TPC [99].

The readout modules are split into 12 sectors on each end, as shown in Figure 3.8. The beampipe goes through the center. The small gaps between the readout pads lead to a slightly lower geometric acceptance roughly every 30°. Each sector of the readout plane is divided into outer and inner sectors. In the inner sector the density of tracks is greater, so the pads are smaller (2.85 mm x 11.5 mm). In the outer sector the pads are larger (6.2 mm x 19.5 mm) to increase the charge collected by each pad. The greater the charge collected the greater the resolution in the energy loss per unit length, dE/dx, measured in the TPC.

dE/dx can be used to identify particles. The energy loss per unit length of particles traveling through matter at rest is described by the Bethe-Bloch equation:

$$-\frac{dE}{dx} = \frac{4\pi}{m_e c^2} \cdot \frac{nz^2}{\beta^2} \cdot (\frac{e^2}{4\pi\epsilon_0})^2 \cdot [ln(\frac{2m_e c^2\beta^2}{I \cdot (1-\beta^2)}) - \beta^2]. \tag{3.1}$$

m_e is the mass of the election, z is the charge of the particle in units of the charge of the electron, e, c is the speed of light, ϵ is the permittivity of free space, β is the particle's speed in units of the speed of light, n is the electron density of the target,

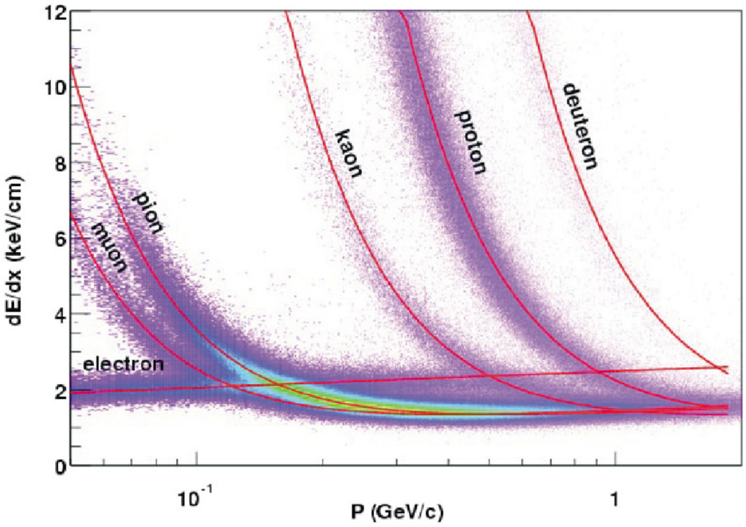

Figure 3.9: The energy loss per unit length in the STAR TPC in $Au + Au$ collisions at $\sqrt{s_{NN}} = 130$ GeV [95].

and I is the mean excitation potential of the target. Energy loss due to interactions with electrons in atoms is ≈ 4000 times greater than energy loss with nuclei. As Equation 3.1 shows, this energy loss is dependent on the velocity, allowing separation of particles when their momentum is known. The distribution of the measured dE/dx versus the reconstructed track momentum is plotted in Figure 3.9. Clear bands are seen for π, K, p, μ, e, and deuterons.

The readout from the TPC gives a series of points along the trajectory of charged particles, called hits. This collection of hits comes from all charged particles from an event and individual tracks must be reconstructed from these hits. This is done using a Kalman filter, an optimal recursive data processing algorithm used for solving for the location of a particle from the measurements of its position at discrete times [100]. The Kalman filter takes the TPC hits and their errors as input and returns the tracks left by particles in an event.

Figure 3.10 shows a typical central $Au + Au$ collision at $\sqrt{s_{NN}} = 130$ GeV in the TPC. Such an event in $Au + Au$ leaves over 1000 charged particles in the TPC. The

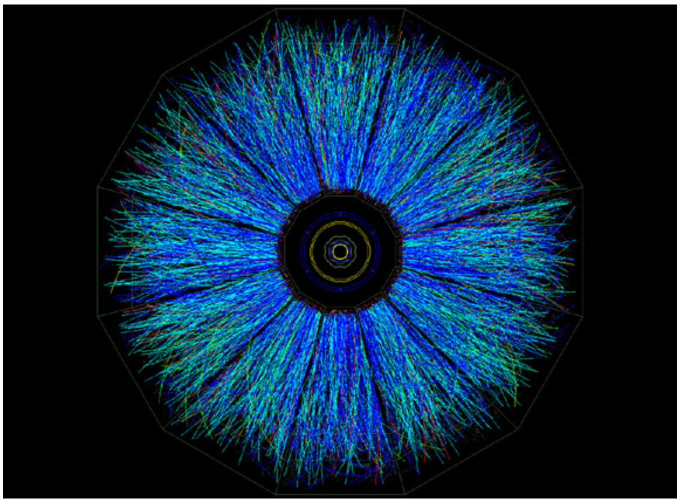

Figure 3.10: An $Au + Au$ event at $\sqrt{s_{NN}} = 130$ GeV in the STAR TPC [94].

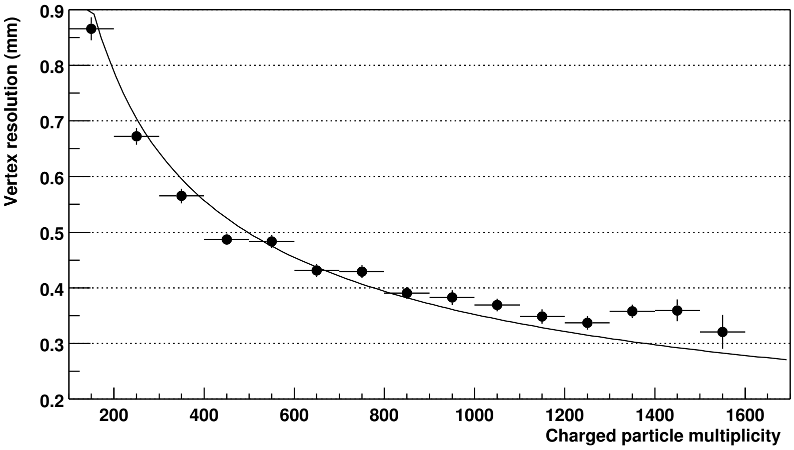

Figure 3.11: Vertex resolution in the TPC in $Au + Au$ collisions at $\sqrt{s_{NN}} = 130$ GeV [95].

more tracks in an event the better the location of the primary vertex can be determined. The resolution increases with the number of tracks, as shown in Figure 3.11. Central events in $Cu+Cu$ leave $\approx$ 200 tracks in the TPC, so the error on the location of the vertex is around 0.4 mm in a central $Au+Au$ collisions but more than 0.7 mm in central $Cu + Cu$ collisions.

The momentum resolution of tracks fit through the primary vertex as a function

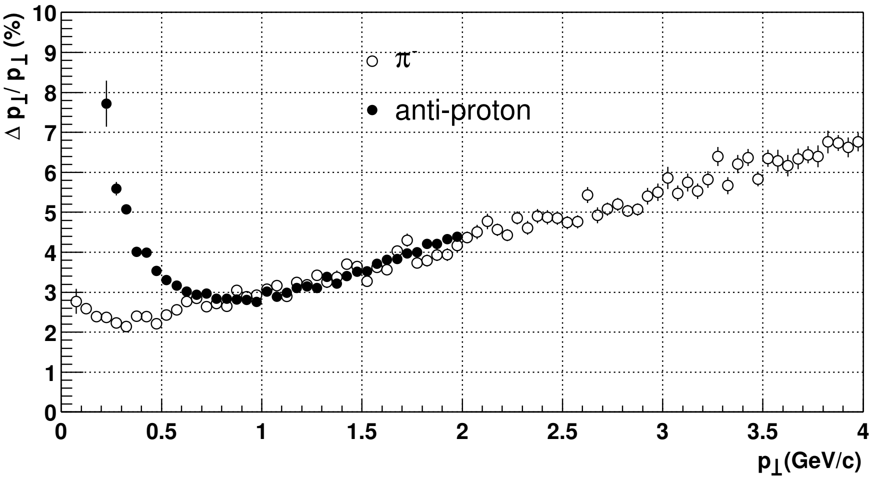

Figure 3.12: Transverse momentum resolution of the TPC in $Au + Au$ collisions at $\sqrt{s_{NN}} = 130$ GeV [95].

of p_T in the TPC is shown in Figure 3.12. Above 1 GeV/c, it becomes more difficult to distinguish the curvature of the track. This means that at high p_T the relative error in the momentum increases with p_T. At low momenta, the resolution is affected by the energy loss in the TPC because the dE/dx is a greater percentage of the particle's energy. Particles which lose a significant proportion of their energy in the TPC will not travel all the way through the TPC and these tracks will be shorter, also decreasing the momentum resolution. Energy loss in the TPC is dependent on the mass of the particle so there are differences in the resolution at low momenta, as seen in Figure 3.12.

Chapter 4

Particle selection and identification

The Λ and $\bar{\Lambda}$ baryons and K_S^0 meson are neutral particles which decay into charged hadrons with a decay length, $c\tau$, of a few centimeters. While neutral particles cannot be detected in the TPC, the charged hadron daughters can be observed and these daughters form a neutral vertex, or V^0. The Λ, $\bar{\Lambda}$, and K_S^0 hadrons can be identified by reconstructing their secondary decay vertices. Particles which decay into a Λ or $\bar{\Lambda}$, such as the Ξ and the Ω, can also be reconstructed by first reconstructing the tertiary decay vertex of the Λ or $\bar{\Lambda}$ decay and then reconstructing the secondary decay vertex of the Ξ or Ω. This method has been applied successfully by STAR to study the Λ, Ξ, and Ω baryons and their respective antiparticles and the K_S^0 meson [101–113]. Data on these particles and the decay channels used to identify them are given in Table 4.1.

The advantage of particle identification by reconstruction of decay vertices is that this method is effective at high-p_T. Identification of π, K, and p by dE/dx is difficult above 1 GeV/c in STAR because the bands overlap. Studies of particles identified in STAR by vertex reconstruction are limited at high-p_T by statistics rather than the applicability of the method. A disadvantage of particle identification by vertex reconstruction is the efficiency. Identification of a V^0 through its decay vertex has an efficiency of about 10% - 50% and identification of Ξ and Ω baryons through reconstruction of their decay vertices have an efficiency on the order of a few percent. By comparison, the efficiency for reconstructing a charged hadron ranges from about 70% in central $Au + Au$ collisions to about 90% in $p + p$ collisions.

Table 4.1: Data on particles which can be reconstructed from their decay vertices [114].

particle	mass (MeV/c^2)	quark content	decay channel	decay length $c\tau$ (cm)	branching ratio
Λ	1115.683 ± 0.006	uds	$\Lambda \rightarrow p\pi^-$	7.893 ± 0.060	64.1 ± 0.5%
$\bar{\Lambda}$	1115.683 ± 0.006	$\bar{u}\bar{d}\bar{s}$	$\bar{\Lambda} \rightarrow \bar{p}\pi^+$	7.893 ± 0.060	64.1 ± 0.5%
K^0_S	497.648 ± 0.022	$\frac{d\bar{s}-s\bar{d}}{\sqrt{2}}$	$K^0_S \rightarrow \pi^+\pi^-$	2.6859 ± 0.0015	69.20 ± 0.05%
Ξ^-	1321.31 ± 0.31	dss	$\Xi^- \rightarrow \Lambda\pi^-$	4.917 ± 0.045	99.887 ± 0.035%
Ξ^+	1321.31 ± 0.31	$\bar{d}\bar{s}\bar{s}$	$\Xi^+ \rightarrow \bar{\Lambda}\pi^+$	4.917 ± 0.045	99.887 ± 0.035%
Ω^-	1672.45 ± 0.29	sss	$\Omega^- \rightarrow \Lambda K^-$	2.463 ± 0.033	67.8 ± 0.7%
Ω^+	1672.45 ± 0.29	$\bar{s}\bar{s}\bar{s}$	$\bar{\Omega}^+ \rightarrow \bar{\Lambda}K^+$	2.463 ± 0.033	67.8 ± 0.7%

Di-hadron correlations presented in this thesis use unidentified hadrons (h), V^0s (Λ, $\bar{\Lambda}$, K^0_S), or multistrange baryons (Ξ^-, Ξ^+, Ω^-, Ω^+). Di-hadron correlations of V^0s, Ξ, and Ω are only presented for $Cu+Cu$ at $\sqrt{s_{NN}} = 200$ GeV. The data from $Cu+Cu$ and $Au+Au$ collisions at $\sqrt{s_{NN}} = 62$ GeV were investigated but the statistics did not allow for meaningful studies, and previous studies were done in $Au+Au$ at $\sqrt{s_{NN}} = 200$ GeV [77,79,115–123]. Therefore, identification of these particles is only discussed for $Cu+Cu$ collisions at $\sqrt{s_{NN}} = 200$ GeV.

All particles are restricted to $|\eta| < 1.0$ since the acceptance of the STAR TPC is limited in η and tracks at higher η typically have fewer hits in the TPC and worse momentum resolution due to the angle they make with the read out pads in the TPC. All tracks used in these studies, including those of daughter particles, are required to have at least 15 hits in the TPC associated with the track.

4.1 Selection of charged tracks

Particles with $p_T > 1$ GeV/c are dominantly pions and protons, with the proton contribution as much as 50% in central $Au+Au$ collisions at $\sqrt{s_{NN}} = 200$ GeV [80]. This means that unidentified hadrons are mostly a mixture of protons and pions. Figure 4.1 shows the distribution of the distance of closest approach (DCA) of charged

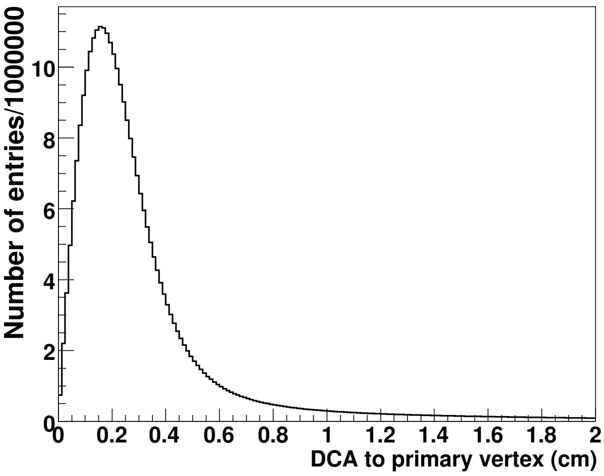

Figure 4.1: Distance of closest approach to the primary vertex for unidentified hadrons with $p_T > 1.0$ GeV/c within $|\eta| < 1.0$ in $Cu + Cu$ collisions at $\sqrt{s_{NN}} = 200$ GeV.

tracks with $p_T > 1.0$ GeV/c to the primary vertex of an event. Tracks are restricted to a DCA < 1.0 cm, limiting contributions from decay particles.

The number of hits in the TPC associated with a track is also restricted to ensure the quality of the track. Tracks with few hits are often randomly associated hits rather than those left by a charged particle and if they represent a real particle, their momentum resolution is poor. Also, tracks from a single particle may be split and reconstructed as two tracks; requiring a minimum number of hits on a track prevents double counting of these split tracks. Figure 4.2 shows the distribution of the number of hits associated with unidentified hadron tracks with $p_T > 1.0$ GeV/c. The maximum number of hits possible in the TPC depends on the trajectory of the track but is usually 45 for a particle within $|\eta| < 1.0$. Only tracks with at least 15 tracks were accepted.

Unidentified hadron efficiency

To determine the efficiency for reconstructing tracks, the response to the particle as it traverses the STAR detector is simulated. For unidentified hadrons, the response of the detector is simulated for pions. There are significant contributions from protons in the data, however, the efficiency for the reconstruction of pions and protons is similar

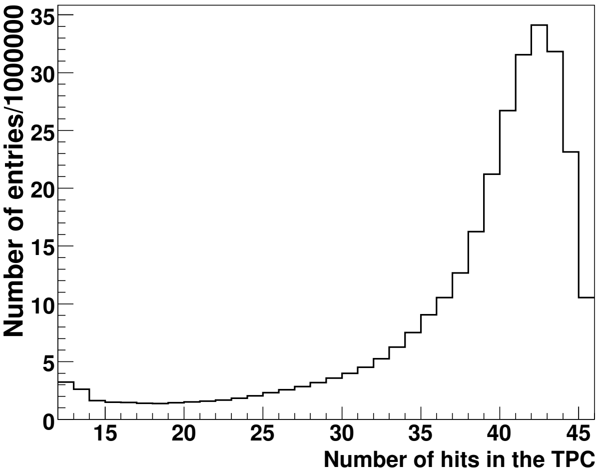

Figure 4.2: The number of TPC hits associated with unidentified hadrons with $p_T >$ 1.0 GeV/c within $|\eta| < 1.0$ in $Cu + Cu$ collisions at $\sqrt{s_{NN}} = 200$ GeV.

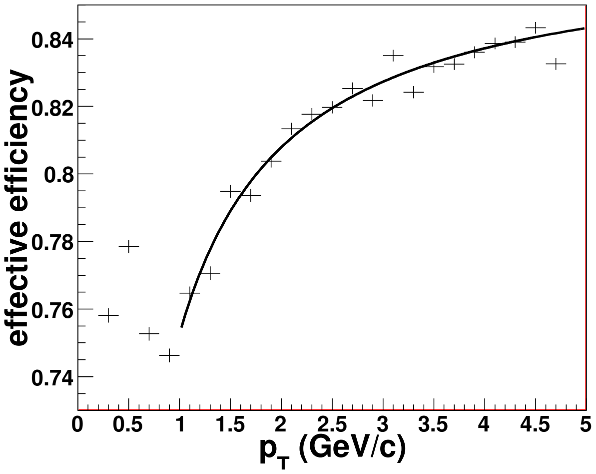

Figure 4.3: The effective efficiency, including acceptance effects, for reconstructing unidentified hadrons in 0-10% central $Cu + Cu$ collisions at $\sqrt{s_{NN}} = 200$ GeV. The curve is a fit to the data.

for particles with $p_T > 1$ GeV/c. The charge which would be recorded by the detector is simulated, and the simulated charge is embedded into a real event. The software used by STAR to reconstruct hits and tracks in real data is used to reconstruct tracks in the data-simulation hybrid. The reconstructed track must have at least 10 of the simulated hits for the simulated track to be considered reconstructed. The ratio of the

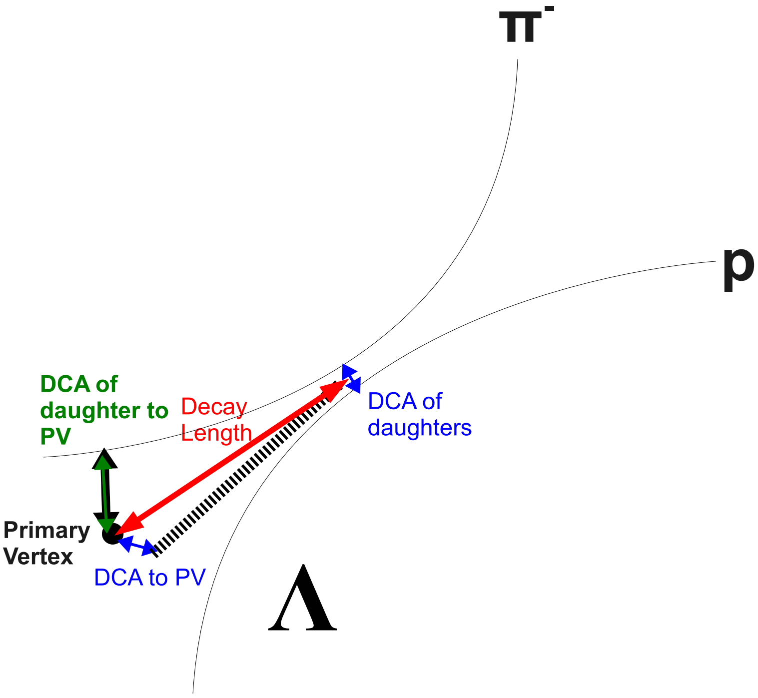

Figure 4.4: Schematic diagram of a Λ decay showing the different parameters of a V^0 candidate's reconstructed decay vertex. Primary vertex is abbreviated PV.

number of reconstructed tracks to the number of simulated tracks gives the effective efficiency, including acceptance effects. The effective reconstruction efficiency was determined for tracks meeting the quality requirements applied in the analysis and was determined as a function of p_T and centrality for each data set. This was fit to a curve $a\ exp((\frac{b}{p_T})^c)$. An example of the effective efficiency for the reconstruction of unidentified hadrons in 0-10% central $Cu + Cu$ collisions at $\sqrt{s_{NN}} = 200$ GeV is shown in Figure 4.3. The parameters for the fits to the efficiency as a function of p_T for each centrality bin in each data set are in Appendix C.1.

4.2 V^0 reconstruction

A schematic diagram of the geometry of a Λ decay is shown in Figure 4.4. The K_S^0 decay is similar except for the identity of the daughters. This shows the different parameters describing the reconstructed decay vertex. Restrictions of these parameters can be varied to alter the purity and the efficiency of reconstructed V^0 candidates.

To get a sample of V^0 candidates, all pairs of global tracks - those which are not forced to go through the primary vertex - are combined. The invariant mass of the track pair is calculated assuming that they are the decay daughters of a V^0. The mass of a V^0 candidate is given by

$$\begin{aligned} m_\Lambda &= \sqrt{(m_\pi + m_p)^2 - (\overrightarrow{p_{\pi^-}} + \overrightarrow{p_p})^2} \\ m_{\bar{\Lambda}} &= \sqrt{(m_\pi + m_p)^2 - (\overrightarrow{p_{\pi^+}} + \overrightarrow{p_{\bar{p}}})^2} \\ m_{K_S^0} &= \sqrt{(m_\pi + m_\pi)^2 - (\overrightarrow{p_{\pi^+}} + \overrightarrow{p_{\pi^-}})^2} \end{aligned} \tag{4.1}$$

with the momentum given by

$$\begin{aligned} \overrightarrow{p_\Lambda} &= \overrightarrow{p_{\pi^-}} + \overrightarrow{p_p} \\ \overrightarrow{p_{\bar{\Lambda}}} &= \overrightarrow{p_{\pi^+}} + \overrightarrow{p_{\bar{p}}} \\ \overrightarrow{p_{K_S^0}} &= \overrightarrow{p_{\pi^-}} + \overrightarrow{p_{\pi^+}}. \end{aligned} \tag{4.2}$$

The combinatorial background in a heavy ion collision is considerably higher than in $e^+ + e^-$ or $p + p$ collisions, and is large for high particle multiplicities. This means that the background is greater in central collisions than in peripheral collisions. The background is dominated by primary tracks, or those which originate from the primary vertex (PV). Some default cuts on track quality, daughter particle identification, and geometry of the reconstructed vertex are applied to keep file sizes reasonable before finer tuning of cuts. The list of default cuts is given in Table 4.2.

Figure 4.5 shows the DCA of the daughter tracks to each other and to the primary vertex versus the invariant mass of the V^0 candidate. Plots with the parameter on the y-axis and the mass of the candidate on the x-axis easily show the difference between the signal and the background. The signal sits near the mass of the particles and has

Table 4.2: Default geometric cuts for V^0 candidates.

	$p_T^{V^0} < 3.5$ GeV/c	$p_T^{V^0} > 3.5$ GeV/c
DCA of V^0 to PV $<$	0.8 cm	0.8 cm
DCA of daughters $<$	0.8 cm	0.8 cm
DCA of daughters to PV $>$	0.7 cm	0 cm
Decay length $>$	2 cm	2 cm
N_{hits} on daughter track $>$	15	15
$\mid n_{\sigma,dE/dx} \mid \geq$	3	3

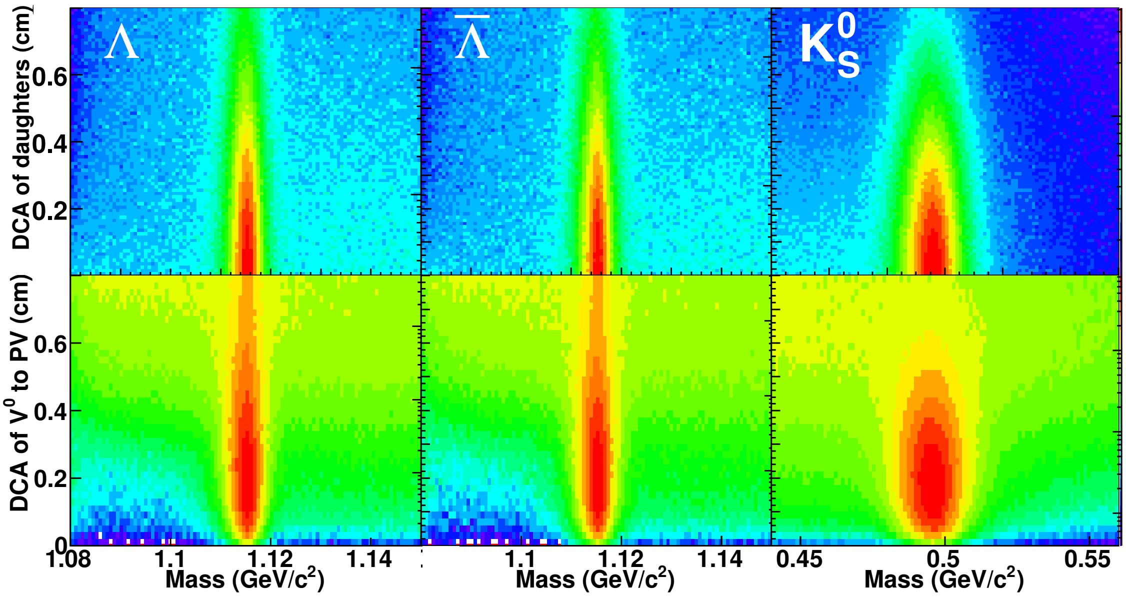

Figure 4.5: DCA of V^0 to primary vertex and of V^0 daughters to each other for V^0 candidates between 1.0 GeV/c $< p_T <$ 1.5 GeV/c versus the reconstructed mass of the candidate. These were produced with the default cuts in Table 4.2 with $Cu+Cu$ collisions at $\sqrt{s_{NN}} = 200$ GeV. The vertical scale is logarithmic.

a lower DCA on average than the background. These plots show similar patterns for both the DCA of the daughters and the DCA of the V^0 to the primary vertex because these paramters are dominated by the resolution of the detector. Restrictions on the DCA of the V^0 daughters to each other and to the primary vertex eliminate background efficiently, and future detector upgrades at STAR will allow better resolution

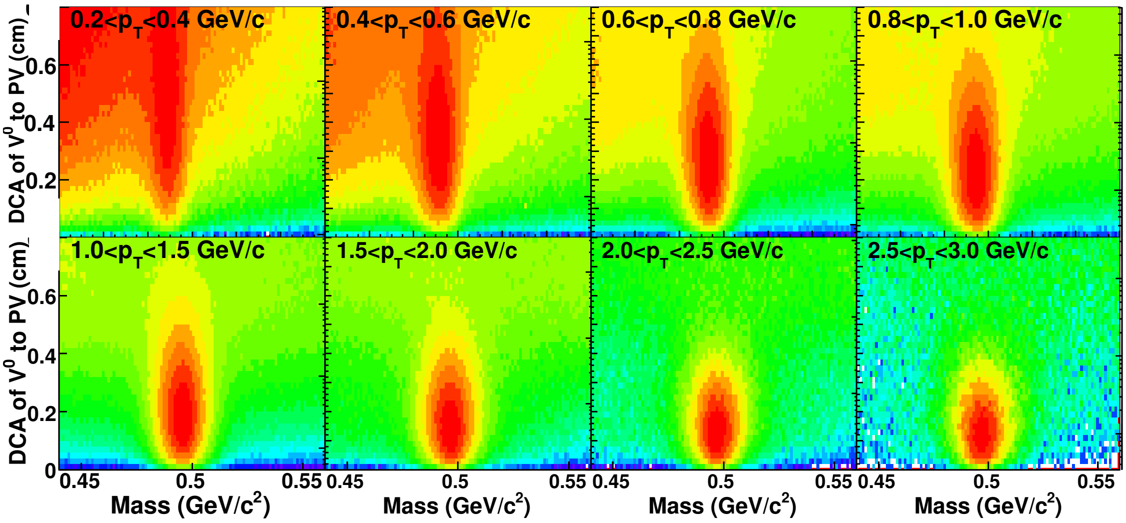

Figure 4.6: DCA of V^0 to primary vertex versus the reconstructed mass of the candidate for different momenta. These were produced with the default cuts in Table 4.2 in $Cu + Cu$ events at $\sqrt{s_{NN}} = 200$ GeV. The vertical scale is logarithmic.

of these parameters.

Figure 4.6 shows the reconstructed DCA in different bins in p_T. A single hit in the STAR TPC has a resolution on the order of a few hundred μm. The resolution of the trajectory of each track depends on its momentum and on the number of hits in the TPC. Lower momentum daughter tracks are not only more likely to have fewer hits in the TPC, but have greater energy loss, reducing both their momentum resolution and the resolution of the trajectory of the track. This means the resolution of the DCA of the daughter tracks will be worse at low p_T. The fact that the resolution gets better with higher momentum demonstrates that this method is better, not worse, at higher p_T.

Figure 4.7 shows the distribution of the decay daughters' DCA to the primary vertex and of the decay length versus the invariant mass of Λ candidates. Similar trends are observed for K^0_S candidates. Since most of the background comes from tracks originating at the primary vertex, most of the background has a small reconstructed decay length and the daughter tracks are close to the primary vertex. The signal has an exponential distribution of decay lengths, meaning that much of the

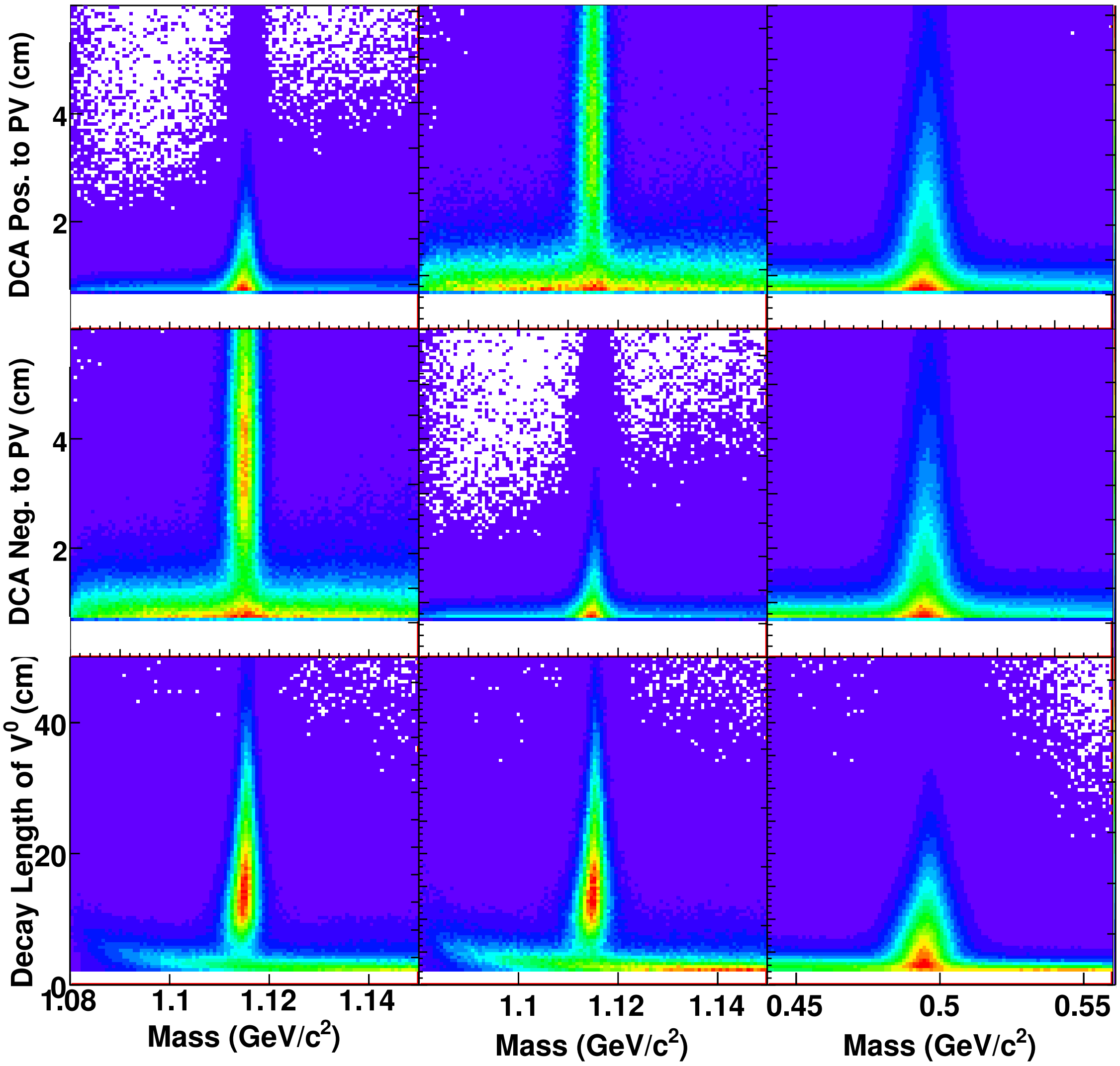

Figure 4.7: DCA of positive and negative Λ daughters to the primary vertex and the decay length of Λ candidates versus the reconstructed mass of the candidate. These were produced with the default cuts in Table 4.2 with $Cu + Cu$ collisions at $\sqrt{s_{NN}}$ = 200 GeV.

signal also has a small decay length. Requiring a minimum decay lenth improves the signal to background ratio, but also significantly reduces the signal. Likewise, requiring that the decay daughters do not come close to the primary vertex also reduces the background, but significantly reduces the signal.

The dE/dx of daughter tracks can also be used to reduce the background. The

Table 4.3: V^0 center fit parameters from fit of data in Figure 4.10 to $Ae^{-(b/p_T)^c}$.

particle	a	b	c
Λ	1116.25 ± 0.02	$3.9 \cdot 10^{-4} \pm 0.4 \cdot 10^{-4}$	0.86 ± 0.01
$\bar{\Lambda}$	1116.03 ± 0.02	$2.4 \cdot 10^{-3} \pm 0.3 \cdot 10^{-3}$	1.16 ± 0.03
K_S^0	501.5 ± 0.2	$1.7 \cdot 10^{-4} \pm 0.3 \cdot 10^{-4}$	0.50 ± 0.02

number of standard deviations away from the center of the band is calculated and a 3σ cut was applied by default. Figure 4.8 shows the distributions of the number of σ away from the center of the dE/dx band versus the mass for the daughters for Λ candidates. The dE/dx bands from different particles begin to merge above 1 GeV/c in the STAR TPC, but at higher momenta the bands begin to separate so some resolution is possible. This is evident in Figure 4.8 because the distribution of p daughters is not centered around $n_{\sigma,dE/dx} = 0$. It is more effective for the p and $\bar{p}$ daughters of the Λ and $\bar{\Lambda}$ since there are more primary pions than protons produced [124].

The widths of the mass peaks as a function of p_T are shown in Figure 4.9 and the centers of the mass peaks as a function of p_T are shown in Figure 4.10. These parameters are determined from a fit of a Breit-Wigner distribution

$$f(M_{reco}) = N\frac{(\frac{\Gamma}{2})^2}{(M_{reco} - M_{center})^2 + (\frac{\Gamma}{2})^2} \tag{4.3}$$

plus a linear background to the mass peak, where Γ is the width of the distribution, M_{center} is the center of the distribution, M_{reco} is the reconstructed mass, and N is the total number of particles. The mass resolution is dominated by detector effects from the single track momentum resolution and the shape of the reconstructed mass peak is altered by the geometric cuts. A Breit-Wigner is used because this function fits the mass peak best; the fits were only used for determining the purity of the sample. Since the purpose of these studies was only identification of V^0s for di-hadron correlations, the p_T dependence of the centers and widths of the mass peaks was not investigated in detail.

Starting with the geometric cuts given in Table 4.2, the restrictions on the DCA

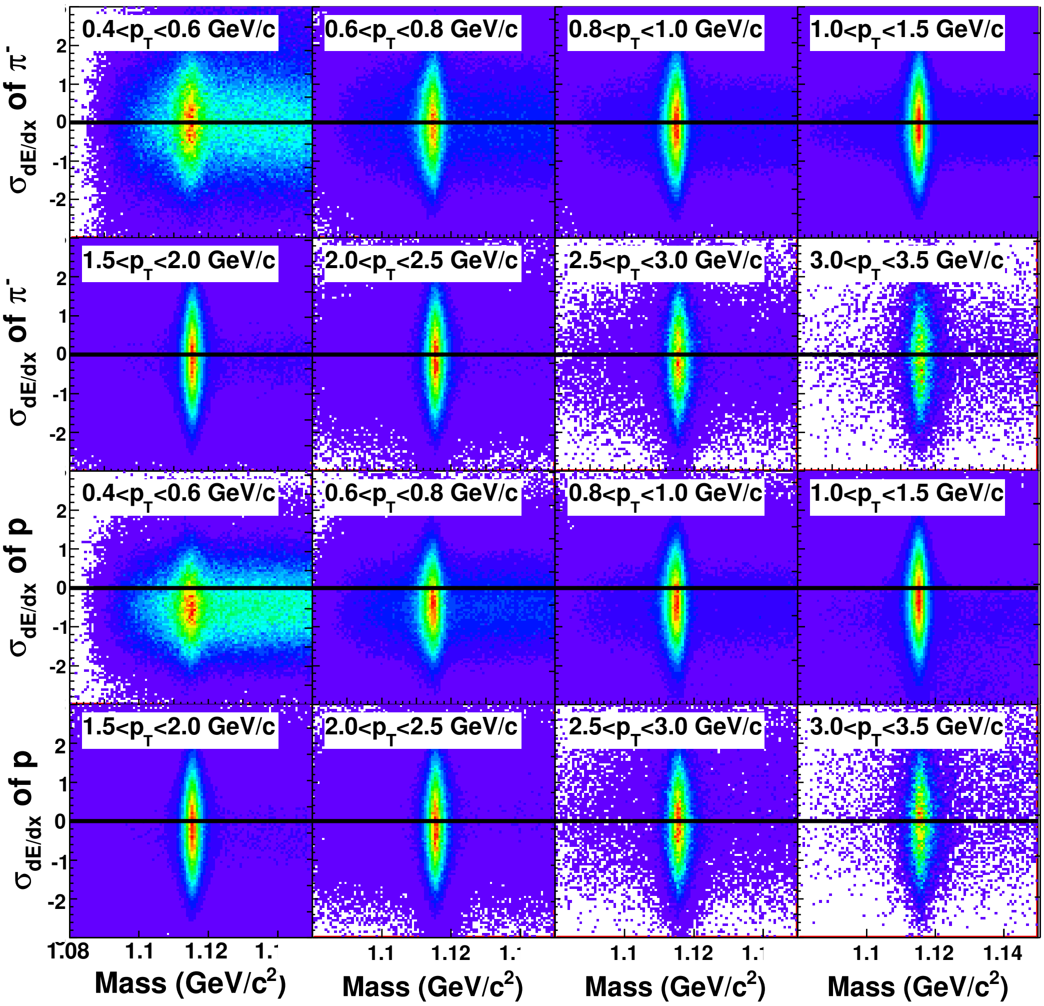

Figure 4.8: The $n_{\sigma,dE/dx}$ for Λ decay daughters at different momenta versus the invariant mass. These were produced with the default cuts in Table 4.2 with $Cu+Cu$ collisions at $\sqrt{s_{NN}} = 200$ GeV.

of the V^0 to the primary vertex, the DCA of the daughters to each other, the DCA of the daughters to the primary vertex, the decay length, the number of TPC hits on each daughter, the $n_{\sigma,dE/dx}$ and the distance from the center of the mass peak for each daughter were tuned until a purity of about 95% was reached in each centrality bin and at each momentum. The final cuts are given in Appendix B. These tight restrictions on the purity were used to reduce the impact of impurities on di-hadron correlations. The purity as a function of p_T, shown in Figure 4.11, was determined by

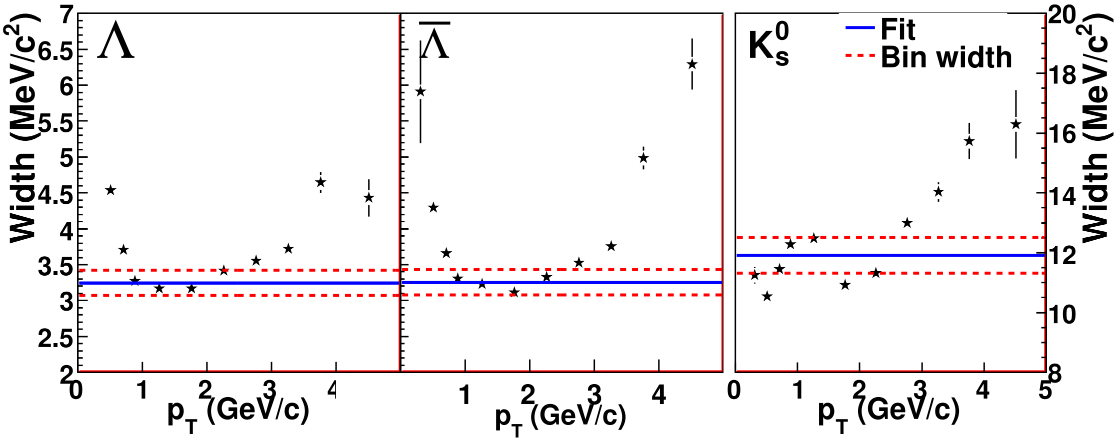

Figure 4.9: V^0 mass widths as a function of p_T. The solid black line indicates the PDG value and the red dashed lines indicate the PDG value ± the bin width.

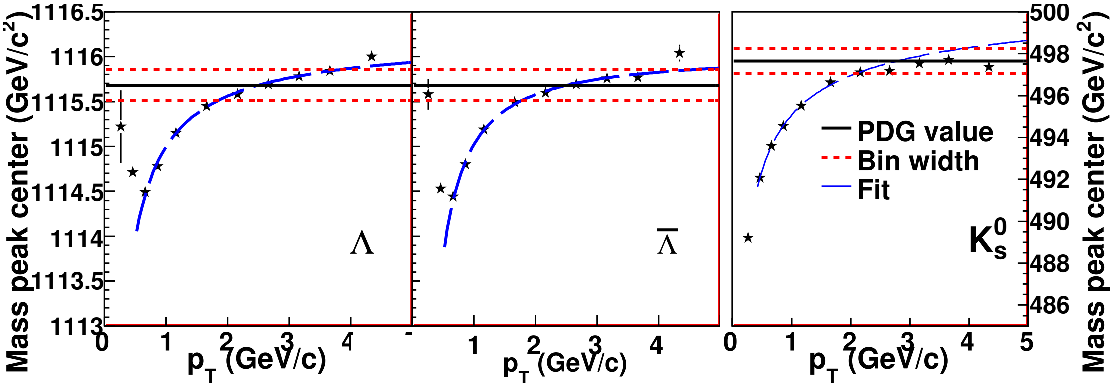

Figure 4.10: V^0 mass peak centers as a function of p_T. These were fit to $Ae^{-(b/p_T)^c}$, shown as a black dashed line. These parameters are given in Table 4.3. The solid black line indicates the PDG value and the red dashed lines indicate the PDG value ± the bin width.

fitting the mass peak with a Breit-Wigner distribution. The center was determined from a fit to the center as a function of p_T to $Ae^{-(b/p_T)^c}$. The parameters of these fits are given in Table 4.3.

V^0 efficiency

The effective V^0 reconstruction efficiencies were determined by embedding simulated tracks in a STAR event, as for unidentified hadrons. The efficiency of reconstructing

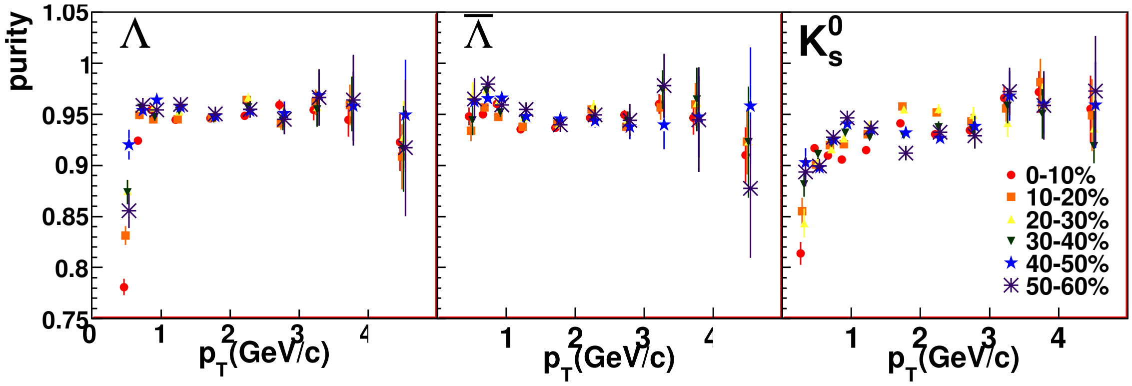

Figure 4.11: V^0 purity as a function of p_T after tuning the geometric cuts.

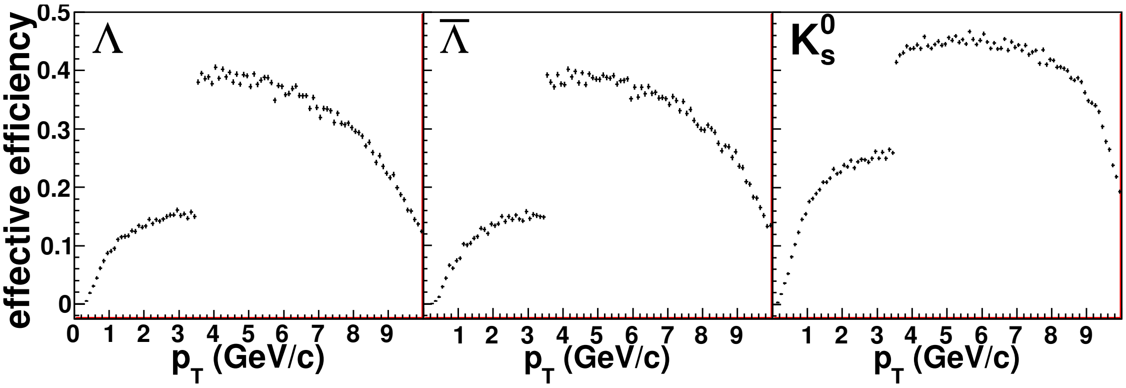

Figure 4.12: Sample effective V^0 reconstruction efficiency for the default cuts listed in Table 4.2.

a V^0 in the STAR detector is limited by the single track efficiency (≤ 0.90) and the branching ratio (69.2% for K_S^0 and 64.1% for Λ and $\bar{\Lambda}$.) These effects combined put an upper limit on the efficiency of about 55% before applying any geometric cuts. As for charged hadrons, the cuts were applied to the embedded, reconstructed data, compared to the number of simulated tracks, and the ratio fit to give an efficiency. A sample effective efficiency, including acceptance effects and the branching ratio, for the default cuts listed in Table 4.2 is shown in Figure 4.12. The large jump in the efficiency at $p_T = 3.5$ GeV/c is from the change in the cuts at $p_T = 3.5$ GeV/c. The fit parameters in each p_T and centrality bin are given in Appendix C.

Table 4.4: Default geometric cuts for Ξ and Ω candidates.

	$p_T < 3.5$ GeV/c	$p_T < 3.5$ GeV/c
DCA of V^0 daughters	< 0.8 cm	< 0.8 cm
DCA of V^0 daughters to PV	> 0.4 cm	> 0.0 cm
DCA of Ξ to PV	< 0.8 cm	< 0.8 cm
DCA of Ξ daughters	< 0.8 cm	< 0.8 cm
Ξ Decay length	> 2 cm	> 2 cm
N_{hits} on daughter track	> 15	> 15
$n_{\sigma,dE/dx}$	$-3 < n_{\sigma,dE/dx} < 3$	$-3 < n_{\sigma,dE/dx} < 3$

4.3 Ξ and Ω reconstruction

The identification of a Ξ or Ω through their decay vertices is a straightforward extension of V^0 identification. Instead of π or p daughters, one of the daughter tracks is a Λ. There are more parameters describing the geometry of the reconstructed decay, those describing the Λ decay vertex and those describing the Ξ or Ω decay vertex. The efficiency is also significantly lower than for the reconstruction of a V^0 because three tracks must be reconstructed rather than two and the branching ratios of both the Λ and the Ξ or Ω are relevant.

As with V^0 reconstruction, default cuts were applied and these cuts were tightened to reach the desired purity. Most of the cuts applied are exactly analogous to those applied for V^0 recontruction and only cuts unique to Ξ and Ω recontruction will be reviewed here. Table 4.4 lists the default cuts used for Ξ and Ω reconstruction.

4.3.1 Ξ reconstruction

As for V^0 reconstruction, the background for the Ξ is dominated by random combinations of primary tracks. This means that on average the distance of closest approach to the primary vertex of the Ξ will be lower on average than to the background and the DCA to the primary vertex of the Λ will be higher on average than the background. The DCA of the Λ daughter to the primary vertex and the DCA of the Ξ candidate are strongly correlated for real Ξ.

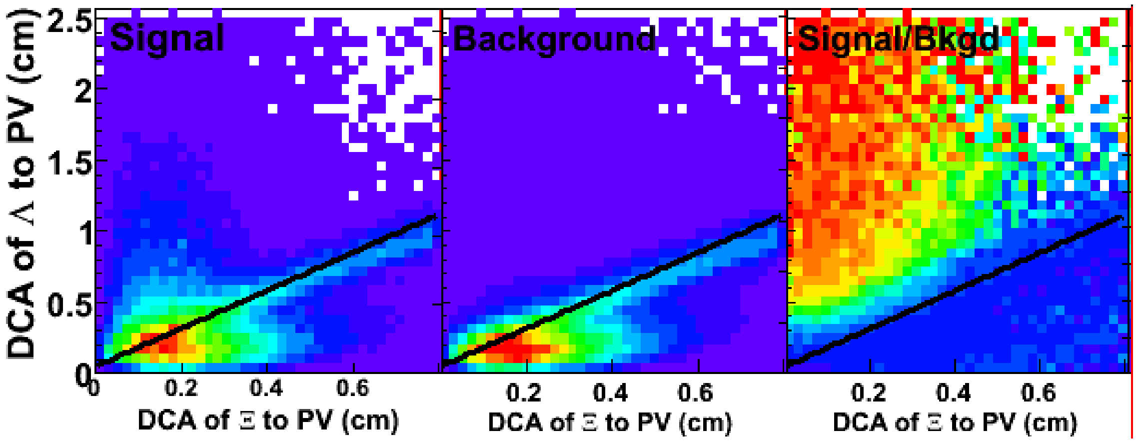

Figure 4.13: The DCA of the Λ daughter to the primary vertex versus the DCA of the Ξ candidate to the primary vertex in the signal region (1315< m_ξ <1325), the background region (1270< m_Ξ <1312 and 1133< m_Ξ <1350 MeV/c) and the ratio of the two for all Ξ candidates with $p_T > 1$ GeV/c in the $Cu + Cu$ data at $\sqrt{s_{NN}}$ = 200 GeV. The line shows where the cut is applied to reduce the background in Figure 4.14.

Figure 4.13 shows the DCA of the Λ daughter to the primary vertex versus the DCA of the Ξ candidate in the signal region (1315< m_Ξ <1325), the background region (1270< m_Ξ <1312 and 1133< m_Ξ <1350 MeV/c) and the ratio of the two for all Ξ candidates with $p_T > 1$ GeV/c in $Cu+Cu$ collisions at $\sqrt{s_{NN}} = 200$ GeV. The strong correlation between the DCA of the Ξ candidate to the primary vertex and of the DCA of the V^0 daughter to the primary vertex was demonstrated in [125] to be an efficient way to reduce the background in the Ξ mass peak. The line drawn in Figure 4.13 shows an example of a correlated cut

$$\mathrm{DCA\,of\,V^0\,to\,PV} > A * \sqrt{\mathrm{DCA\,of\,\Xi\,to\,PV}} + B \tag{4.4}$$

which can be used to eliminate background. A tighter cut is applied by either increasing either A or B.

Figure 4.14 shows the mass peak for Ξ candidates in $Cu+Cu$ at $\sqrt{s_{NN}} = 200$ GeV above $p_T > 1.0$ GeV/c before applying the cut in Equation 4.4, after applying the cut in Equation 4.4, and the difference between the two. This cut clearly eliminates mostly background. This was one of the most efficient cuts for reducing the background.

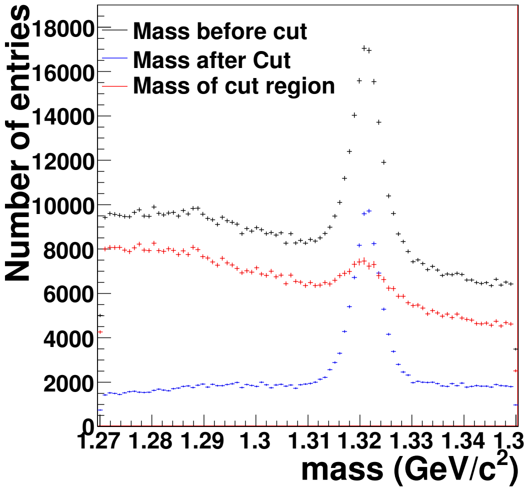

Figure 4.14: Ξ mass peak before (black) and after (blue) applying the correlated cut. The difference is shown in red. The cut applied, DCA of the V^0 to the primary vertex $>$ 1.33 times the DCA of the Ξ candidate to the primary vertex, is shown in Figure 4.13.

Table 4.5: Ξ center fit parameters from fits to the data in Figure 4.15

particle	a	b	c
Ξ^-	1323.1 ± 0.3	$8.0 \cdot 10^{-5} \pm 9.0 \cdot 10^{-5}$	0.643 ± 0.088
Ξ^+	1323.1 ± 0.1	$3.8 \cdot 10^{-5} \pm 0.5 \cdot 10^{-5}$	0.595 ± 0.009

The width and centers of the mass peaks as a function of p_T as determined from fits of the mass peaks to Breit-Wigner distributions are given in Figure 4.15. The center was then fit as a function of p_T to $Ae^{-(b/p_T)^c}$. The parameters from these fits are given in Table 4.5. The purity was calculated as the number of particles in the mass peak as determined from the fit divided by the total in the mass peak. The geometric cuts were tuned until the purity was around 90%. The final geometric cuts are given in Appendix B and the purity is shown in Figure 4.16. Ξ baryons are only used as trigger particles so no reconstruction efficiency is necessary.

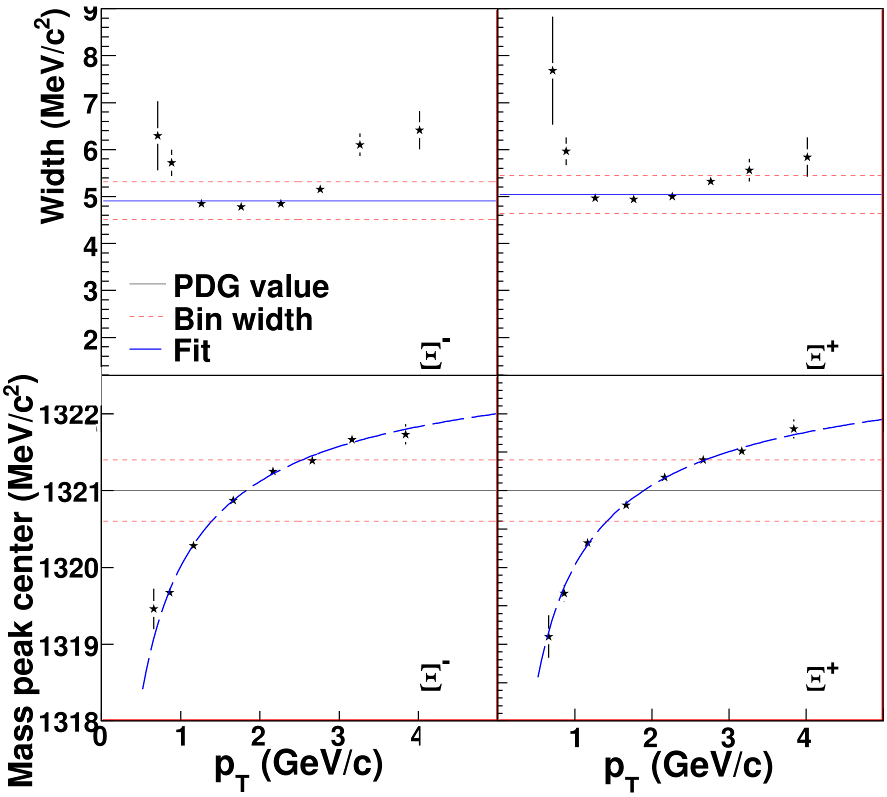

Figure 4.15: Centers of Ξ mass peaks as determined from fits of the mass peaks to a Breit-Wigner distribution

4.3.2 Ω reconstruction

The Ω is more difficult to reconstruct than a V^0 or the Ξ because there are fewer Ω baryons produced. The default cuts are the same as those in Table 4.4. The geometry of an Ω decay is the same as the geometry of a Ξ decay so similar cuts are applied. The cut described in Equation 4.4, also works to efficiently reconstruct Ω decay vertices. An Ω baryon has two decay daughters, a Λ and a K^-, so an analogous cut can also be applied:

$$\text{DCA of } \pi \text{ to PV} > C * \sqrt{\text{DCA of } \Omega \text{ to PV}} + D. \tag{4.5}$$

While this cut was not found to be useful for Ξ reconstruction, it was very useful for Ω reconstruction.

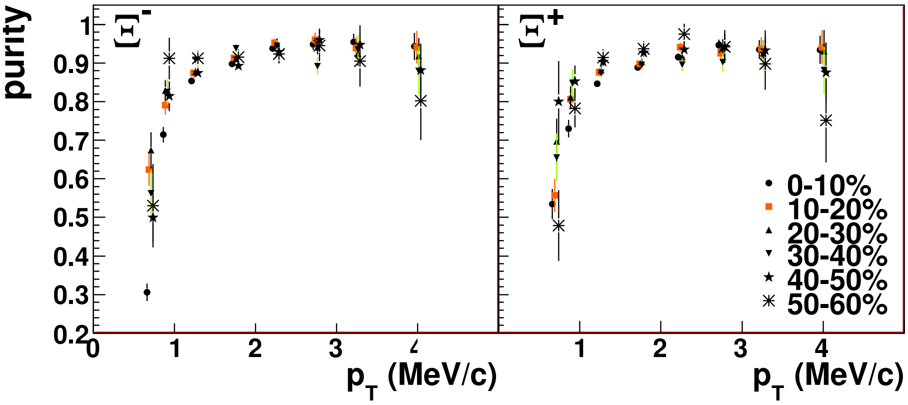

Figure 4.16: Ξ center

Three different cut sets, listed in Table 4.6, were used with varying purities. Because the number of Ω baryons reconstructed is small, there is a trade off between purity and the number of Ω baryons which could be used as trigger particles for correlation analyses. The mass peaks are shown in Figure 4.17. Since there are fewer Ω baryons, the PDG value was used. The center of the mass peak was within error of the PDG value. The widths of the mass peaks were determined from a fit of a Breit-Wigner function to the mass peak integrated over $p_T > 1$ GeV/c. The widths used for determining the purity were 5.6 MeV/c^2 for the Ω^- and 5.9 MeV/c^2 for the Ω^+.

Table 4.6: Cut sets for Ω candidates. A and B are the parameters in Equation 4.4 and C and D are the parameters in Equation 4.5.

Parameter	Cut set 1	Cut set 2	Cut set 3
DCA of Ω to primary vertex $<$	0.6 cm (0.55 cm)	0.35 cm	0.6 cm
DCA of bachelor π to primary vertex $>$	0.0 cm	0.0 cm	0.5 cm
DCA of V^0 daughters to each other $<$	0.5 cm (0.65 cm)	0.35 cm	0.5 cm
DCA of Ω daughters to each other $<$	0.5 cm (0.7 cm)	0.35 cm	0.5 cm
Number of widths, Γ, from the PDG mass	1.5	1	1.5
$\lvert n^{\pi}_{\sigma,dE/dx}\rvert <$	3	3	3
$\lvert n^{p}_{\sigma,dE/dx}\rvert <$	2	2	2
$\lvert n^{K}_{\sigma,dE/dx}\rvert <$	3	3	3
$(m_{\Lambda}$-1.1156$)\leq$	0.007	0.007	0.007
A	0.7 (0.7)	0.7	0.5
B	0.1 (0.13)	0.1	0.1
C	1.1 (1.1)	1.1	1.1
D	0.1 (0.12)	0.1	0.1
Purity	61%	73%	53%

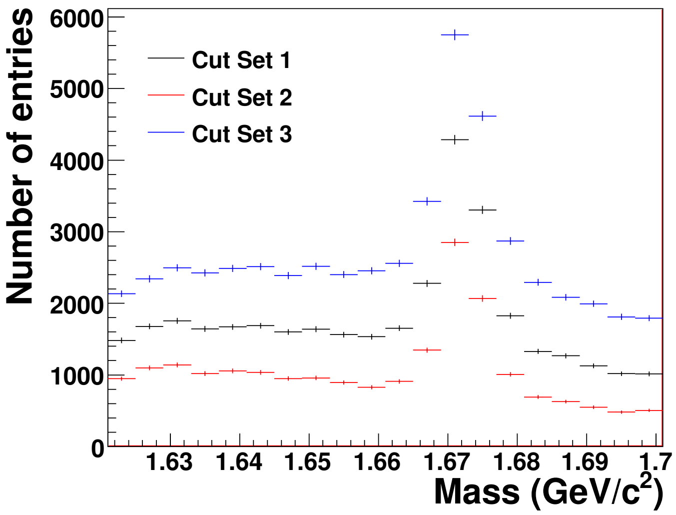

Figure 4.17: Ω mass peaks for each cut set described in Table 4.6.

Chapter 5

Correlation Method

5.1 Event selection

Data in this thesis are from $Au + Au$ collisions at $\sqrt{s_{NN}} = 62$ GeV from RHIC's fourth run (2004) and $Cu + Cu$ collisions at $\sqrt{s_{NN}} = 62$ GeV and $\sqrt{s_{NN}} = 200$ GeV from RHIC's fifth run (2005.) These data are compared to previous studies done in $Au + Au$ collisions at $\sqrt{s_{NN}} = 200$ GeV from RHIC's fourth year run. In order to be usable for analyses, events must have a clearly defined vertex. For all systems and energies, the vertex is limited to within 30 cm of the center of the TPC along the beam axis. The further an event is from the center of the TPC the lower the geometric acceptance; a 30 cm cut allows reasonably uniform geometric acceptance.

The impact parameter of events cannot be directly measured, so instead the centrality of the collision is given as a percentage of events in a sample. These percentages are determined by dividing the event sample into percentages of centrality as determined by the reference multiplicity[1]. This is compared to the distribution of impact parameters expected in a Glauber Monte Carlo model [41] so that the 0-10% central events roughly corresponds to the highest 10% of impact parameters. The Glauber model assumes a realistic distribution of nucleons in nuclei, such as a Woods-Saxon density profile, and samples collisions with a uniform impact parameter, b, ranging

---

[1] The reference multiplicity is defined as the uncorrected number of tracks in the TPC within $|\eta| < 0.5$.

between 0 and a cut-off b_{max}. Based on the assumption that nucleons travel in a straight line as the nuclei interact and that nucleons interact with the same cross section as protons, the number of nuclei which participate in the collision at least once (N_{part}) and the total number of nucleon-nucleon collisions (N_{bin}) is calculated. N_{part} is bounded by the sum of the nucleons in the colliding nuclei and N_{bin} is bounded by the product of the number of nucleons in the two nuclei. Soft particle production is expected to scale with N_{part} and hard particle production, such as that from jets, is expected to scale with N_{bin}. Details of Glauber Monte Carlo models and how they are used in heavy ion collisions can be found in [41]. The Glauber model is compared to the data to determine the centrality of an event from its reference multiplicity. The centrality bins used in this analysis and their corresponding reference multiplicities, N_{bin}, and N_{part} are given in Appendix D.

Events from $Au + Au$ collisions have a more clearly defined vertex because there are more tracks produced in an $Au+Au$ collision which can be used to reconstruct the vertex position. The 80% most central events were usable in $Au+Au$ collisions. Fewer tracks are produced in $Cu+Cu$ collisions and the luminosity was significantly higher in 2005 than in 2006. The higher luminosity meant that particles from a previous event could still be traversing the TPC when a new event triggered the detector to begin reading out data, a problem called pile-up. For higher multiplicities, it is still possible to determine the primary vertex, but the lower the multiplicity the harder it is to determine where the vertex from the event which triggered the detector is. For this reason only the 60% most central data from these events was usable. For more peripheral events, the vertex which triggered the event could not be found in more than 2% of events, in large part because vertices from pile-up events usually had a greater multipicity. Full details of the separation of the vertices from the triggered event and from pile-up events can be found in [126].

5.2 Correlation technique

In a given event, a high-p_T track, called the trigger particle, is selected and the distribution of all lower momentum particles, called associated particles, relative to that track in $\Delta\eta$ and $\Delta\phi$ is determined. Tracks are selected as described in Chapter 4, with no additional restrictions on the high momentum track other than the p_T. Multiple tracks in a single event may be counted as trigger particles. The data are symmetric about $\Delta\phi = 0$ and $\Delta\eta = 0$ because the sign of $\Delta\phi$ and $\Delta\eta$ are determined by an arbitrary choice of coordinates. Since many of these measurements are limited by statistics, the data are reflected about $\Delta\phi = 0$ and $\Delta\eta = 0$ to minimize statistical fluctuations. The single track efficiency, described in Chapter 4, is dependent on particle type, collision system and energy, p_T, and centrality and the correction for associated particles is applied on a track-by-track basis. The final distribution is normalized by the number of trigger particles, so no correction for the efficiency of reconstructing the trigger particle is necessary. Two corrections for the acceptance of track pairs in $\Delta\phi$ and $\Delta\eta$, described below, are applied. This is done for the full sample of events to give the average distribution of associated particles relative to a high-p_T trigger particle $\frac{1}{N_{trigger}}\frac{d^2N}{d\Delta\phi d\Delta\eta}$.

Two key features of the STAR TPC affect the geometric acceptance of track pairs. Tracks in the TPC can only be resolved well for -1 $< \eta <$ 1 because the lower geometric acceptance leads to tracks with fewer hits in the TPC, so only tracks within -1 $< \eta <$ 1 are used for this analysis. Track pairs with $\Delta\eta \approx 0$ are nearly always accepted, however, track pairs with $|\Delta\eta\ | \approx 2$ are only accepted if the tracks are near opposite edges of the detector. Therefore acceptance is roughly 100% near $\Delta\eta \approx 0$ but roughly 0% near $|\Delta\eta\ | \approx 2$. This leads to an acceptance in $\Delta\eta$ with a triangular shape.

In addition, as discussed in Chapter 3, there are gaps between each of the 12 TPC sectors. This leads to holes in the acceptance in azimuth. Most tracks will have hits in multiple sectors, however, the loss of hits leads to a decrease in the reconstruction efficiency for tracks at the angles of the sector boundaries. A sample distribution of tracks reconstructed in the TPC is shown in Figure 5.1 showing the lower efficiency at the TPC sector boundaries.

To correct for these effects, the distributions of tracks for both the associated and the trigger particles are recorded. A random trigger (ϕ,η) is chosen from this

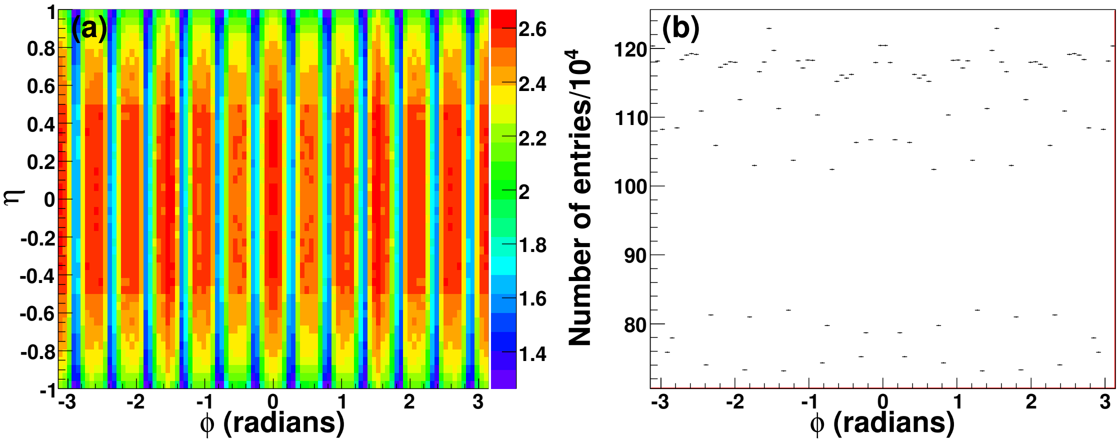

Figure 5.1: Distribution of tracks in (a) ϕ and η and (b) ϕ in $Cu + Cu$ events at $\sqrt{s_{NN}}$ = 200 GeV for 1.5 GeV/c < p_T <6.0 GeV/c. Note the suppressed zero.

distribution of trigger particles and a random associated (ϕ,η) is chosen from the distribution of associated particles. In this way a simulated distribution of uncorrelated track pairs that includes detector acceptance effects is attained. This distribution is normalized to 1 at the peak at $\Delta\eta \approx 0$ to give an efficiency for finding a pair of tracks as a function of ($\Delta\phi$,$\Delta\eta$). A sample of the efficiency due to detector effects is shown in Figure 5.2 and the effects of the geometric acceptance are evident.

5.2.1 Track merging correction

If two tracks have small separations in pseudorapidity and azimuth, they are more difficult to resolve because hits from each particle may not be resolved by the TPC. Therefore, if the particles have nearly identical momenta, their tracks are not distinguished. This effect is called track merging and causes an artificial dip in the raw correlations centered at ($\Delta\phi$,$\Delta\eta$) = (0,0). Another similar effect is evident in the TPC from the crossing of high-p_T tracks. While the hits are not lost in this case, one track will lose hits near the crossing point and this particle's track gets split into two shorter tracks. Shorter tracks are less likely to meet the track quality cuts in Chapter 4 because they have fewer hits. This effect causes artificial dips near ($\Delta\phi$,$\Delta\eta$) = (0,0) but slightly displaced in $\Delta\phi$. The location of these dips in $\Delta\phi$ is dependent on

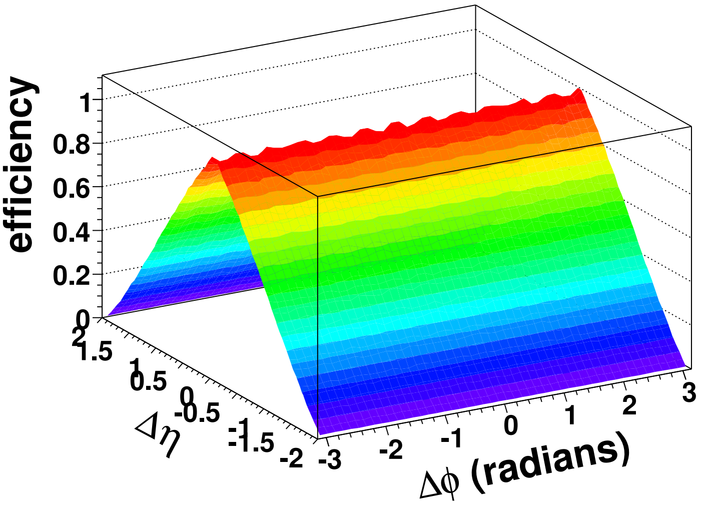

Figure 5.2: Sample efficiency due to detector effects for $Cu + Cu$ events at $\sqrt{s_{NN}} =$ 200 GeV with 1.5 GeV/c $< p_T^{associated} < p_T^{trigger}$ and 3.0 $< p_T^{trigger} <$ 6.0 GeV/c

the relative helicities of the trigger and associated particles. The helicity is given by

$$h = -\frac{qB}{|qB|} \tag{5.1}$$

where q is the charge of the particle and B is the magnetic field [116].

A method for correcting high-p_T triggered di-hadron correlations was developed in [116, 120], building on a method for correcting for track merging in studies of Hanbury-Brown-Twiss correlations [127].

Correction for unidentified hadrons

Figure 5.3 shows a sample of raw di-hadron correlations between unidentified hadrons for all four helicity combinations in $Au + Au$ events at $\sqrt{s_{NN}} = 62$ GeV. When the helicities of the trigger and associated particles are the same, the percentage of overlapping hits is greater. Track pairs are lost whether the pair is part of the combinatorial background or part of the signal so the magnitude of the dip is greater when the background is greater. $Au + Au$ collisions were chosen to demonstrate the

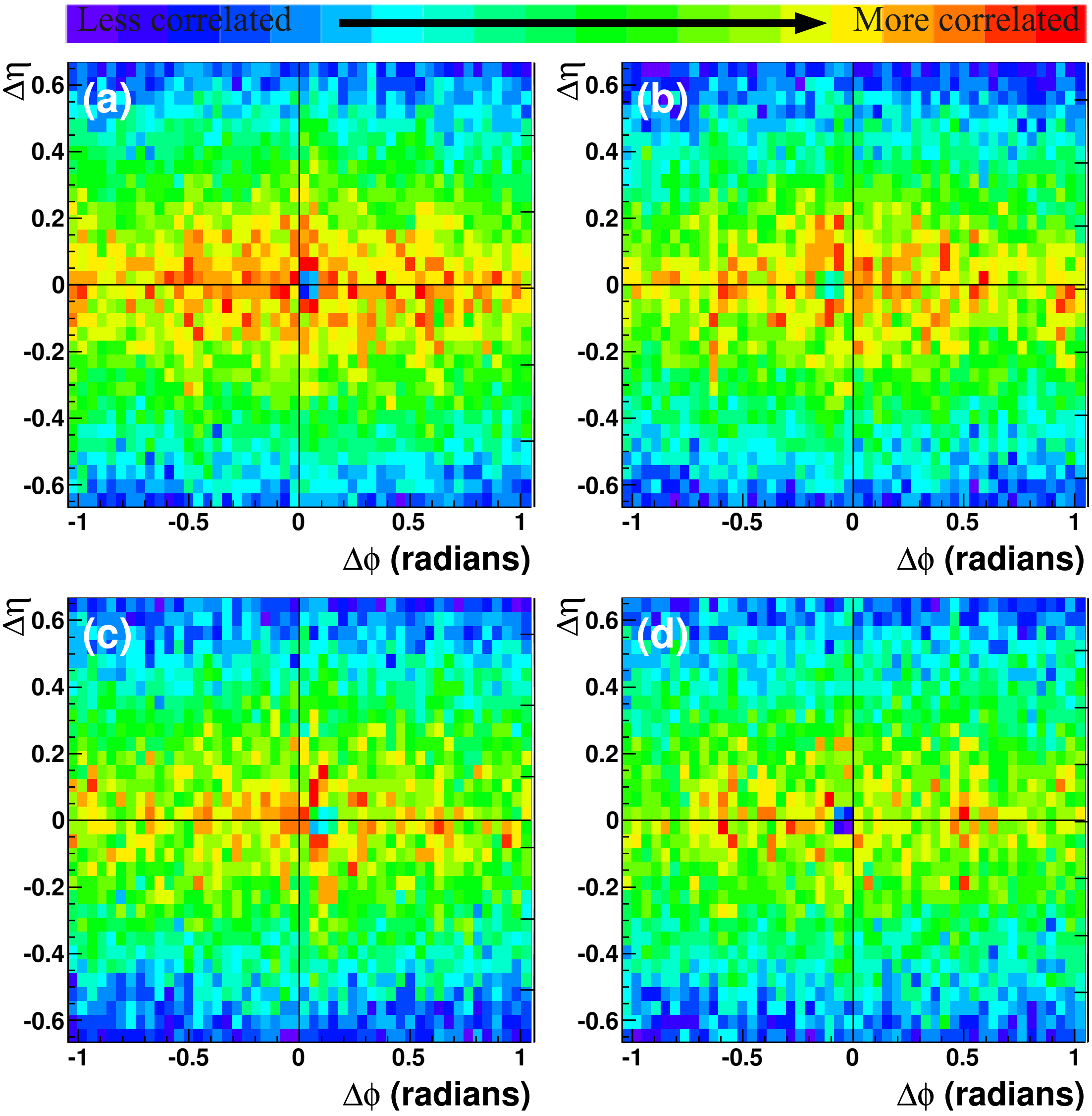

Figure 5.3: Raw correlations for (a) trigger particle helicity 1 and associated particle helicity 1 (b) trigger particle helicity 1 and associated particle helicity -1 (c) trigger particle helicity -1 and associated particle helicity 1 (d) trigger particle helicity -1 and associated particle helicity -1 in 0-40% central $Au+Au$ collisions at $\sqrt{s_{NN}} = 62$ GeV for $1.5 < p_T^{associated} < p_T^{trigger}$ GeV/c and $3.0 < p_T^{trigger} < 6.0$ GeV/c.

effect because the background is largest for these collisions, making the effect easy to see.

The number of hits shared by two tracks is calculated based on the trajectory of the track and if more than 10% of hits are shared between two tracks, the tracks are considered merged and the track pair is discarded. To get an acceptance correction for this effect, the trigger particle is mixed with associated particles from another event. This procedure is called event mixing. The trigger and associated particles from separate events will have no real correlations so any structures in the resulting ($\Delta\phi$,$\Delta\eta$) distribution will result only from detector acceptance effects, including track merging. In the mixed events, the origin of the associated track must be shifted to the new vertex so that the percentage of merged hits can be calculated accurately. In addition, mixed events are required to have vertices within 2 cm of each other along the beam axis in order to ensure similar geometric acceptance in both events. The reference multiplicities of both events are required to be within 10. The calculation of the number of hits which may be shared by the tracks does not describe the performance of the TPC perfectly and some track pairs which were calculated to share more than 10% of their hits are reconstructed. These pairs are discarded even if they were reconstructed so that the percentage of merged track pairs is the same in the data and the mixed events. The mixed events are then used to determine an acceptance correction as a function of $\Delta\phi$ and $\Delta\eta$ for track pairs. Most of the dip is corrected away when the data are divided by the efficiency from mixed events [116, 120]. While the method discused in Section 5.2 corrects for the geometric acceptance of the detector, this method corrects for both the geometric acceptance and for track merging. This method is much more CPU-intensive and therefore was only applied for small ($\Delta\phi$,$\Delta\eta$).

Figure 5.4(a) shows the data and Figure 5.4(b) shows the mixed events for a sample correlation. The dip has a different shape when the helicities of the tracks are the same and when they are opposite. To do the correction the data and mixed events are rotated so that the dip is in the same location. The same helicity data are divided by the acceptance correction from the same helicity events and the opposite helicity data are divided by the acceptance correction from the opposite helicity mixed events. These data are then added after the acceptance correction. A small residual dip remains because mixed events to do not recreate the dip perfectly. The remaining dip is corrected for using the symmetry of the correlations. Since the data are symmetric about $\Delta\phi = 0$, the data on the same side as the dip are discarded and replaced by the data on the side without the dip. Then the data are reflected about $\Delta\eta = 0$ and added to the unreflected data to minimize statistical fluctuations.

This method is only applied to $|\Delta\phi\ | <1.05$ and $|\Delta\eta\ | <0.67$ because it is CPU-intensive and track merging only affects small $\Delta\phi$ and small $\Delta\eta$. For large $\Delta\phi$ and $\Delta\eta$, the method described in Section 5.2 is applied. Figure 5.4(c) shows the data after the track merging correction and Figure 5.4(d) shows the data using the method described in Section 5.2 - without the track merging correction - for all helicity combinations for 0-40% central $Au + Au$ collisions at $\sqrt{s_{NN}} = 62$ GeV.

Correction for identified particles

Correlations with an identified V^0 also have a significant loss of tracks at small $\Delta\phi$ and $\Delta\eta$ due to track merging. For correlations with particles identified through decay vertex reconstruction, the associated particle may be merged with any of the daughter particles. The method developed by [116, 120] for unidentified (h-h) correlations was extended to identified particle correlations and is similar to that for h-h correlations. The only correlations studied here are those where either the trigger or the associated particle is an unidentified hadron. A track pair is thrown out if the unidentified hadron shares more than 10% of its hits total with any of the decay particles. As for h-h correlations, this is done for both data and mixed events and the efficiency as a function of $\Delta\phi$ and $\Delta\eta$ is used to correct the data for both detector acceptance and track merging.

The residual dip is corrected by reflection, so the location of the dip must be established for different trigger particles. Figure 5.5 shows the raw correlations for V^0 triggered correlations for associated hadrons with different helicities. Since the V^0 is neutral, its helicity is zero. Data from $Au + Au$ collisions at $\sqrt{s_{NN}} = 200$ GeV are used because the multiplicities are higher, making the dip larger, and more statistics were available, making the location of the dip more evident. The event selection and particle identification are as described in [77, 79, 117–119]. The dip is larger for Λ and $\bar{\Lambda}$ trigger particles than for K^0_S trigger particles. The location and size of the dip

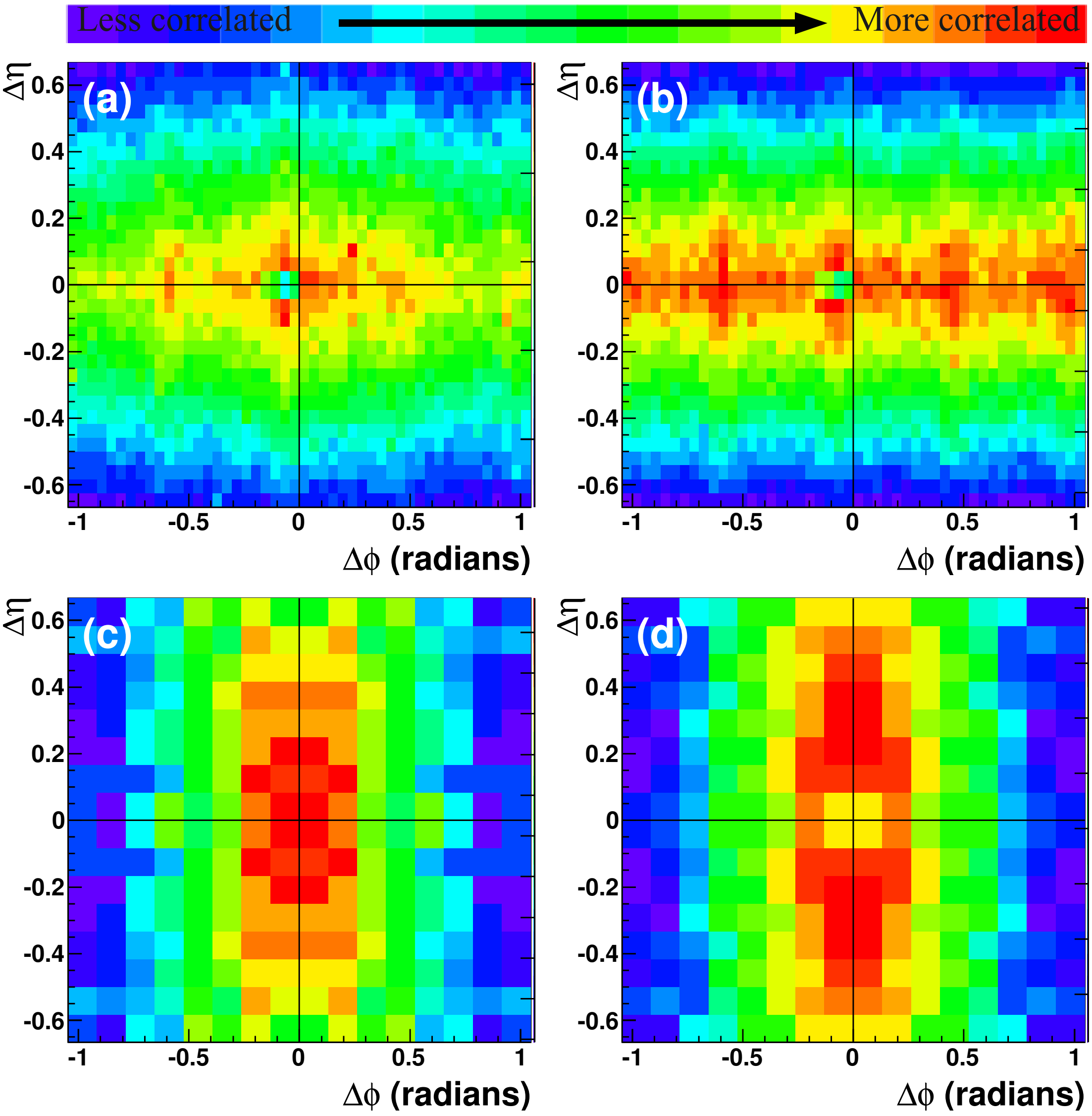

Figure 5.4: The region around the dip for (a) data (b) mixed events (c) data after track merging correction (d) data using the method described in Section 5.2 (no track merging correction) in 0-40% central $Au + Au$ collisions at $\sqrt{s_{NN}} = 62$ GeV for 1.5 $< p_T^{associated} < p_T^{trigger}$ GeV/c and 3.0 $< p_T^{trigger} <$ 6.0 GeV/c.

is dependent on the momenta of the decay daughters and the decay kinematics are different for the Λ and $\bar{\Lambda}$ than for the K_S^0.

Figure 5.6 shows the location of the dip for Ξ^- and Ξ^+ trigger particles with

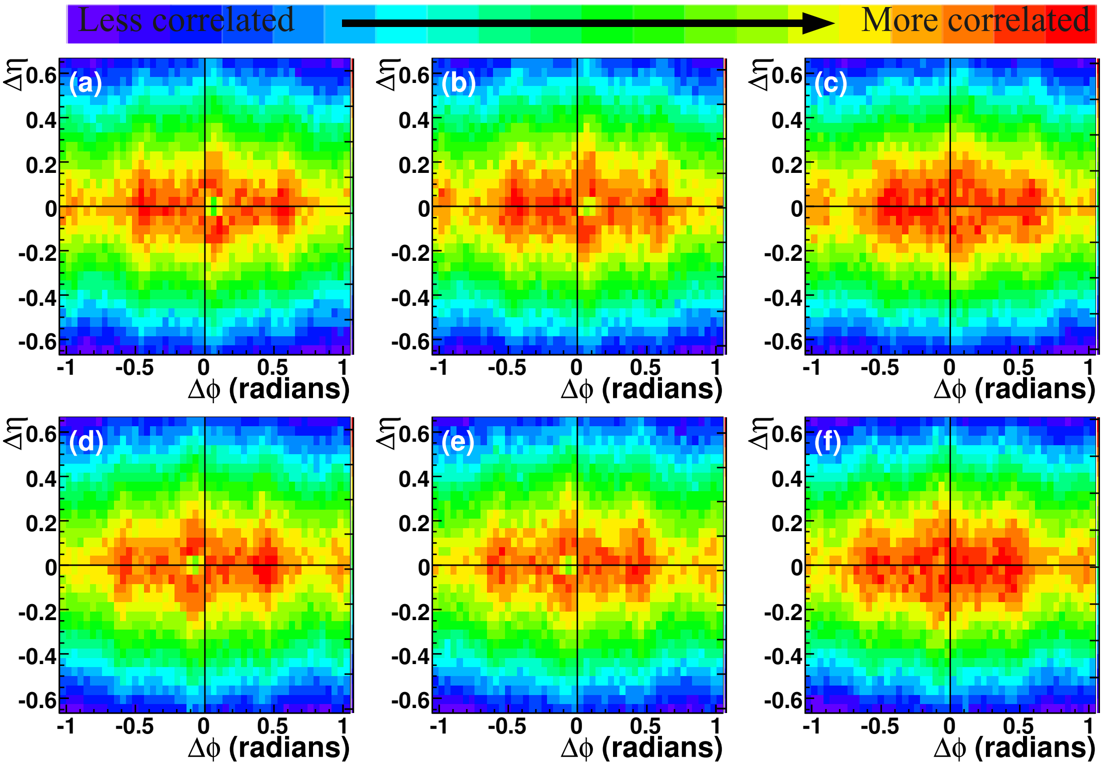

Figure 5.5: The location of the track merging dip in V^0 triggered correlations for a (a) Λ trigger with an associated particle with helicity 1 (b) $\bar{\Lambda}$ trigger with an associated particle with helicity 1 (c) K_S^0 trigger with an associated particle with helicity 1 (d) Λ trigger with an associated particle with helicity -1 (e) $\bar{\Lambda}$ trigger with an associated particle with helicity -1 (f) K_S^0 trigger with an associated particle with helicity -1 in 0-80% central $Au + Au$ collisions at $\sqrt{s_{NN}} = 200$ GeV.

different combinations of helicities. As for V^0 trigger particles, data from $Au + Au$ collisions at $\sqrt{s_{NN}} = 200$ GeV are used. The magnitude of the dip is greater for a multistrange trigger particle than for a V^0 because of the greater number of decay particles involved.

Figure 5.7 shows the location of the dip for V^0 associated particles. All helicities of associated particles have been added together since the dip is independent of the trigger particle helicity. The dip is clearly visible for Λ and $\bar{\Lambda}$ associated particles, however, the dip is considerably less pronounced for K_S^0 associated particles.

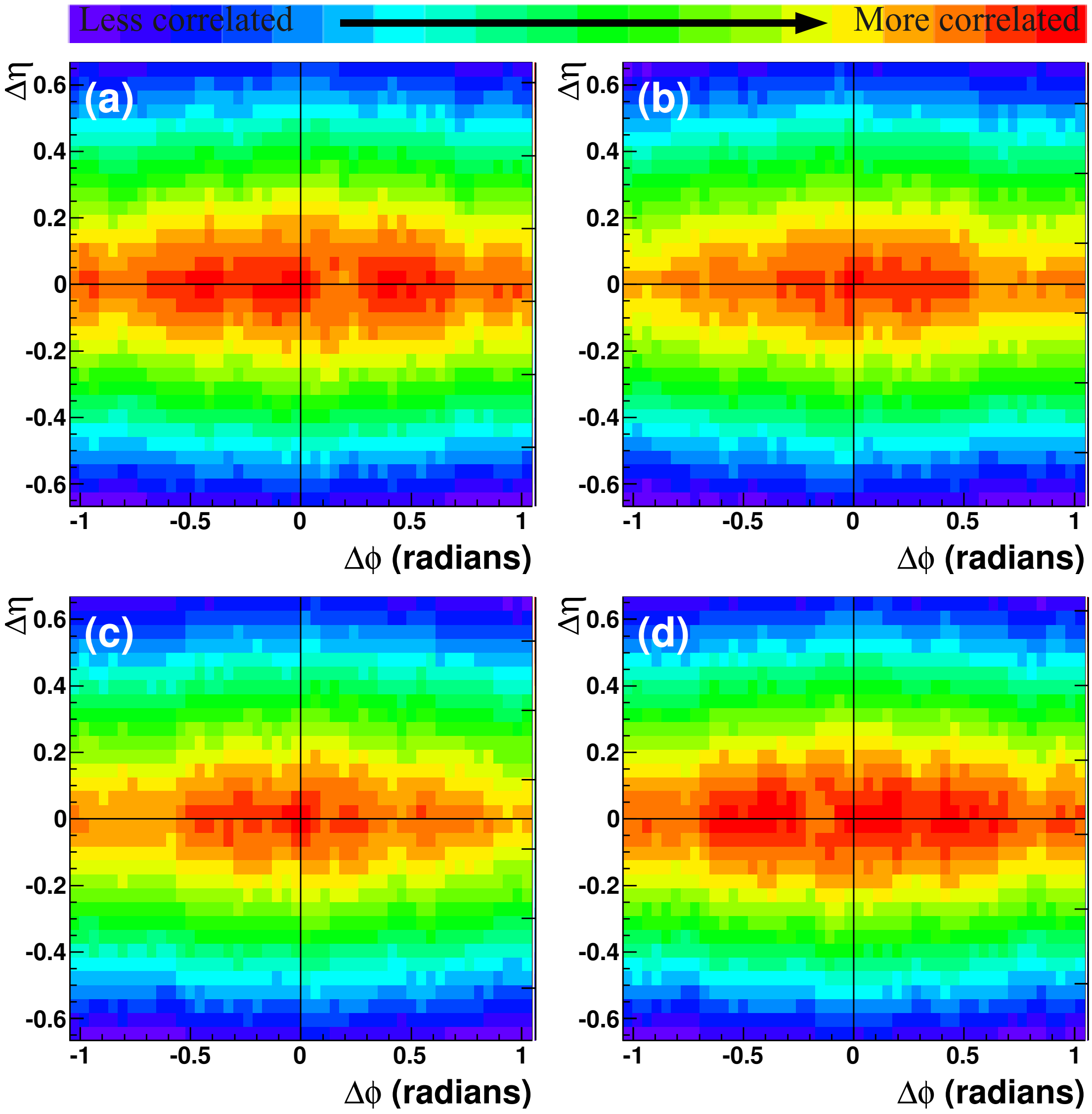

Figure 5.6: Raw Ξ-h correlations for (a) trigger particle helicity 1 and associated particle helicity 1 (b) trigger particle helicity 1 and associated particle helicity -1 (c) trigger particle helicity -1 and associated particle helicity 1 (d) trigger particle helicity -1 and associated particle helicity -1 in 0-80% central $Au + Au$ collisions at $\sqrt{s_{NN}} =$ 200 GeV for $1.5 < p_T^{associated} < p_T^{trigger}$ GeV/c and $3.0 < p_T^{trigger} < 6.0$ GeV/c.

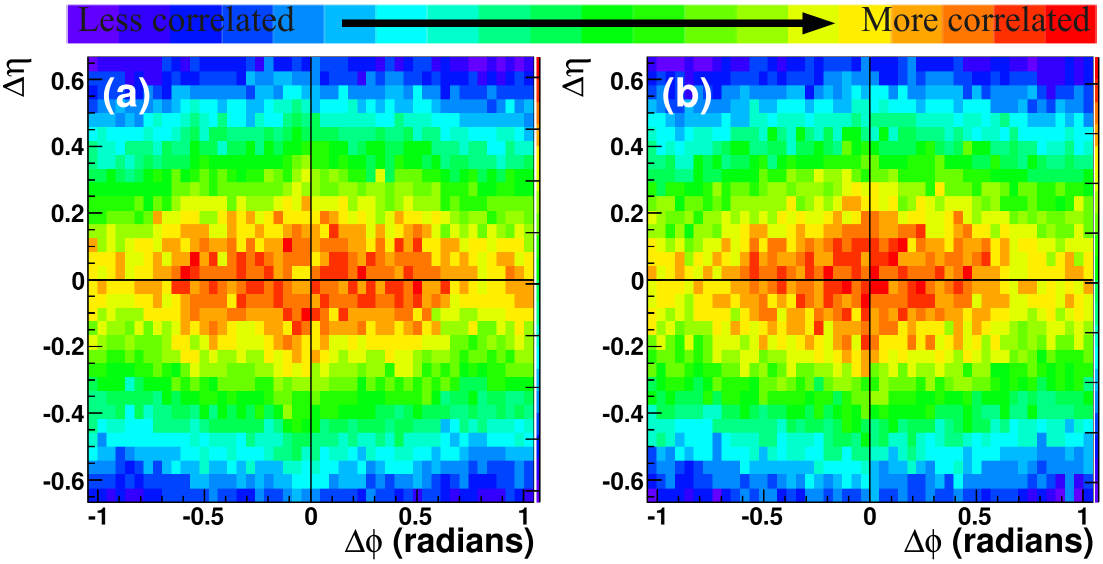

Figure 5.7: The location of the track merging dip in correlations with V^0 associated particles for a (a) Λ and $\bar{\Lambda}$ associated particles (b) (c) K_S^0 associated particles in 0-80% central $Au + Au$ collisions at $\sqrt{s_{NN}} = 200$ GeV.

5.3 Separation of the jet-like correlation and the *Ridge*

Figure 5.8 shows a sample correlation after detector acceptance and track merging corrections. To study the near-side of di-hadron correlations, the two components are separated and the yield, number of particles in each within limits on $p_T^{associated}$ and $p_T^{trigger}$, is studied. As discussed in Chapter 2, the *Ridge* was previously observed to be roughly independent of $\Delta\eta$ within the acceptance of the STAR TPC while the jet-like correlation is confined to $|\Delta\eta\,| < 0.75$.

5.3.1 Extraction of the jet-like yield

The raw correlation consists of a combinatorial background modulated by elliptic flow, v_2, and the signal, which consists of the jet-like correlation and the *Ridge* on the near-side. There are two methods used to extract the jet-like yield from the raw correlation. The first method uses different projections in $\Delta\phi$, the fact that the

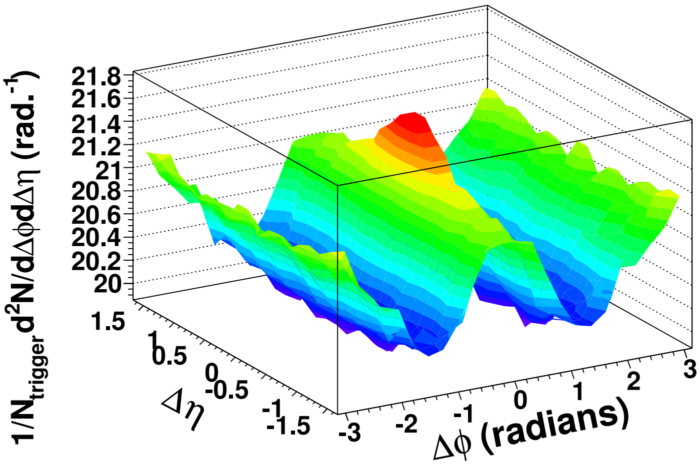

Figure 5.8: Sample correlation after acceptance corrections for $3.0 < p_T^{trigger} < 6.0$ GeV/c and 1.5 GeV/c $< p_T^{associated} < p_T^{trigger}$ from 0-40% most central $Au+Au$ collisions at $\sqrt{s_{NN}} = 62$ GeV.

jet-like correlation is not present at large $\Delta\eta$, and the fact that the combinatorial background and the *Ridge* are both roughly independent of $\Delta\eta$ to isolate the jet-like correlation as a function of $\Delta\phi$. The second method involves taking a projection in $\Delta\eta$ for $-1 < \Delta\phi < 1$ and subtracting a constant background to determine the jet-like correlation as a function of $\Delta\eta$. Elliptic flow, v_2, does not lead to a systematic error on the jet-like yield using either of these methods because v_2 is roughly independent of $\Delta\eta$ within the STAR acceptance [128,129]. Previous studies in $Au+Au$ collisions at $\sqrt{s_{NN}} = 200$ GeV have found these methods to be consistent at high-p_T [130], with some indications that there may be greater deviations at lower p_T [131]. Both methods are described in greater detail below.

$\Delta\phi$ method

To determine the jet-like yield, Y_{Jet}, the projection of the distribution of particles $\frac{d^2N}{d\Delta\phi d\Delta\eta}$ is taken in two different ranges in pseudorapidity:

$$\frac{dY_{ridge}}{d\Delta\phi} = \frac{1}{N_{trigger}}\int_{-1.75}^{-0.75}\frac{d^2N}{d\Delta\phi d\Delta\eta}d\Delta\eta + \frac{1}{N_{trigger}}\int_{0.75}^{1.75}\frac{d^2N}{d\Delta\phi d\Delta\eta}d\Delta\eta \quad (5.2)$$

$$\frac{dY_{jet+ridge}}{d\Delta\phi} = \frac{1}{N_{trigger}}\int_{-0.75}^{0.75}\frac{d^2N}{d\Delta\phi d\Delta\eta}d\Delta\eta \quad (5.3)$$

where the former contains only the *Ridge* and the latter contains both the jet-like correlation and the *Ridge*. The jet-like yield, Y_{Jet}, is determined using bin counting in the region $-1 < \Delta\phi < 1$:

$$Y_{jet}^{\Delta\phi} = \int_{-1}^{1}(\frac{dY_{jet+ridge}}{d\Delta\phi} - \frac{0.75}{1}\frac{dY_{ridge}}{d\Delta\phi})d\Delta\phi. \quad (5.4)$$

The factor in front of the second term is the ratio of the $\Delta\eta$ width in the region containing the jet-like correlation and the *Ridge* to the width of the region containing only the *Ridge*. In practice because the data have been reflected about $\Delta\phi = 0$ and $\Delta\eta = 0$, the projections in $\Delta\phi$ and $\Delta\eta$ and the bin counting are done over half of the range and then scaled up to ensure that the errors are correct.

$\Delta\eta$ method

In this method the projection of the distribution of particles $\frac{d^2N}{d\Delta\phi d\Delta\eta}$ on the near-side is taken:

$$\frac{1}{N_{trigger}}\frac{dN}{d\Delta\eta} = \frac{1}{N_{trigger}}\int_{-1}^{1}\frac{d^2N}{d\Delta\phi d\Delta\eta}d\Delta\phi. \quad (5.5)$$

This contains both a background due to combinatorics and the *Ridge*, both of which are independent of $\Delta\eta$. The background is determined first by fitting a Gaussian signal plus a constant background, A, to Equation 5.6 and then using the background from that for background subtraction. If statistics permitted, the background could be determined from $|\Delta\eta\ | > 0.75$, however, many of the correlations presented here have limited statistics and using a fit of the whole region to determine the background prevents statistical fluctuations from skewing the background subtraction. The jet-like yield is:

$$Y_{jet}^{\Delta\eta} = \frac{1}{N_{trigger}} \int_{-1}^{1} (\frac{d^2N}{d\Delta\phi d\Delta\eta} - A) d\Delta\phi. \tag{5.6}$$

The yield is determined by bin counting in the range $|\Delta\eta\ | < 1$. To get the proper errors, the projection and the bin counting are also done over half of the range and scaled because the data have been reflected. The statistical error on A from the fit is used to determine the error on the final yield by adding it in quadrature to the statistical error from bin counting. The magnitudes of these two errors are comparable.

Figure 5.9 shows the jet-like correlation from both the $\Delta\phi$ and the $\Delta\eta$ method after background subtraction for all systems and energies using $3.0 < p_T^{trigger} < 6.0$ GeV/c and 1.5 GeV/c $< p_T^{associated} < p_T^{trigger}$, the limits used for most studies presented here. For all collision systems and energies the jet-like correlation is within $|\Delta\eta\ | < 0.75$.

5.3.2 Extraction of the *Ridge* yield

There is a large combinatorial background which is dependent on $\Delta\phi$. The raw signal has a background due to particles correlated indirectly with each other in azimuth due to their correlation with the reaction plane. This random background is estimated by

$$\frac{dY_{bkgd}}{d\phi} = B(1 + 2\langle v_2^{trigger}\rangle\langle v_2^{associated}\rangle \cos(2\Delta\phi)) \tag{5.7}$$

where v_2 is the second order harmonic in a Fourier expansion of the momentum anisotropy relative to the reaction plane [132]. The derivation of this parameterization of the background is dependent on the assumption that di-jet production is not correlated with the reaction plane so that the correlation between particles in the jet and random particles in event are not correlated in azimuth through a mutual correlation with the reaction plane. Systematic errors come from the errors on B, $\langle v_2^{trigger}\rangle$ and $\langle v_2^{associated}\rangle$. v_2 is determined from independent measurements. It is

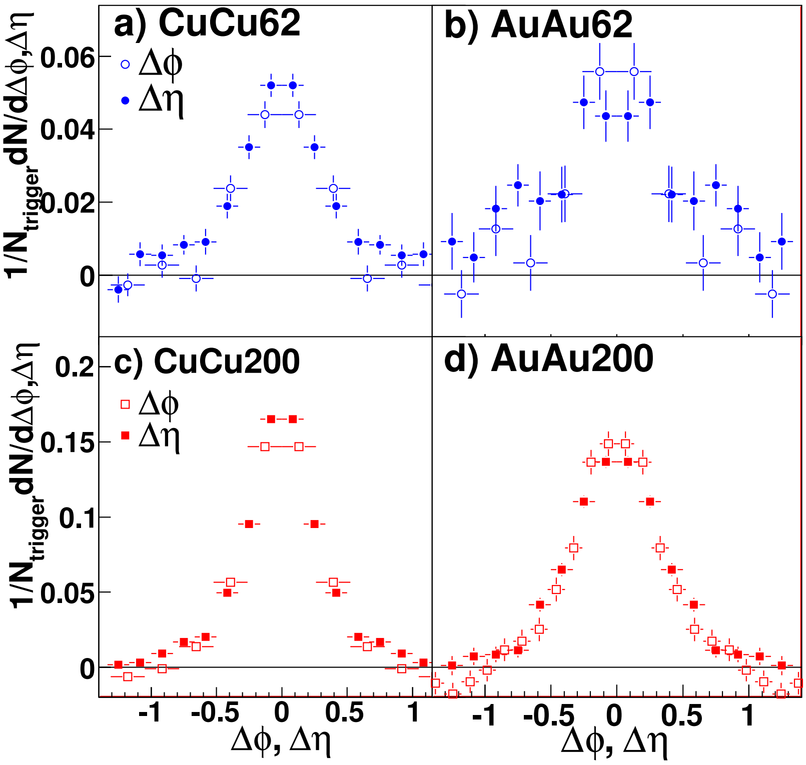

Figure 5.9: Sample jet-like correlations for $3.0 < p_T^{trigger} < 6.0$ GeV/c and 1.5 GeV/c $< p_T^{associated} < p_T^{trigger}$ from both the $\Delta\phi$ and the $\Delta\eta$ method for (a) 0-60% central $Cu+Cu$ collisions at $\sqrt{s_{NN}}$ = 62 GeV (b) 0-80% central $Au+Au$ collisions at $\sqrt{s_{NN}}$ = 62 GeV (c) 0-60% central $Cu+Cu$ collisions at $\sqrt{s_{NN}}$ = 200 GeV and (d) 0-80% central $Au+Au$ collisions at $\sqrt{s_{NN}}$ = 200 GeV. $\Delta\phi$ is in radians.

assumed that v_2 is the same for events with a trigger particle as for minimum bias events and that v_2 is independent of $\Delta\eta$. For each data set $v_2(p_T)$ was fit in centrality bins to determine $\langle v_2^{trigger}\rangle$ and $\langle v_2^{associated}\rangle$.

Measurements of v_2

The best method for the determination of v_2 depends on the collision system. Since v_2 is a momentum anisotropy in azimuth, the tracks produced in an event can be used to reconstruct the reaction plane. v_2 in Equation 5.7 is the azimuthal momentum anisotropy due to the collective flow of particles, however, there are other sources of azimuthal momentum anisotropy. For particles above 1 GeV/c, jets are the largest known non-flow source of momentum anisotropy. Various methods for measuring v_2 have different non-flow contributions. The systematic error is determined by comparing these different methods. Generally, the higher the multiplicity of an event and the greater the eccentricity of the overlap region, the easier it is to reconstruct the event plane. Therefore that the event plane is more difficult to reconstruct in $Cu + Cu$ collisions.

For $Cu + Cu$ collisions, the upper limit for v_2 was taken from a measurement of v_2 using tracks from the FTPCs for reconstruction of the event plane. v_2 measured in $Cu + Cu$ using the event plane from the FTPCs is shown as a function of p_T and centrality in Figure 5.10 for collisions at $\sqrt{s_{NN}} = 62$ GeV and in Figure 5.11 for collisions at $\sqrt{s_{NN}} = 200$ GeV [133]. These data were fit to a parameterization which was used for the subtraction of v_2 using Equation 5.7. The fit parameters are given in Table 5.1. Statistical errors on the fits are neglected in the determination of the error due to v_2 since the systematic errors on v_2 are several times larger than the statistical errors. The event plane reconstructed from tracks measured in both of the FTPCs is expected to be less biased by jets since tracks in the FTPCs are separated by more than two units of pseudorapidity. Particles produced in di-jets in $p + p$ collisions do not exhibit long range correlations in pseudorapidity. However, the observation of the *Ridge* in $A + A$ collisions indicates that some azimuthal anisotropy may be present in $A + A$ collisions which is not due to the collective flow of particles in a fluid, therefore this gives an upper limit on v_2. The lower bound on the v_2 is either 0 for the 0-10% centrality bin or

$$\sqrt{v^2_{2,centrality} - v^2_{2,0-10\%}\frac{M_{centrality}}{M_{0-10\%}}} \tag{5.8}$$

where M is the mean reference multiplicity, for the other bins. The lower limit is based on the assumption that the measured v_2 in central collisions is entirely due to non-flow and this non-flow scales with multiplicity [134, 135].

v_2 and the systematic errors on v_2 in $Au + Au$ collisions at $\sqrt{s_{NN}} = 62$ GeV were taken from [103]. The dominant systematic errors were determined by comparing the reaction plane method to the four-particle cumulant method. The four-particle cumulant method determines v_2 by looking at correlations between four particles, which

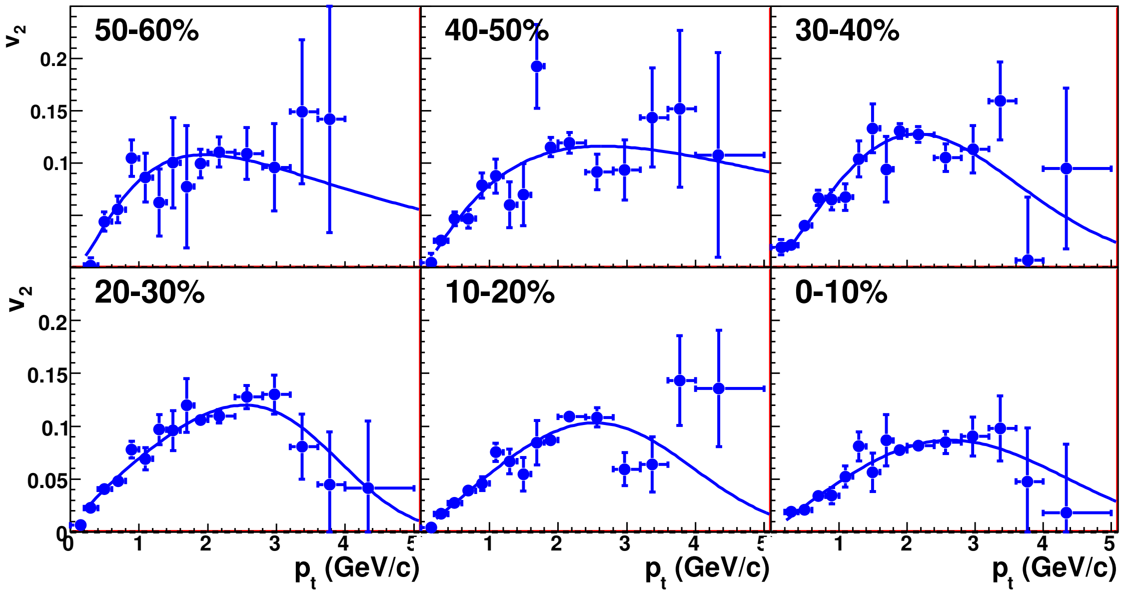

Figure 5.10: v_2 measured using the event plane from the FTPCs in $Cu+Cu$ collisions at $\sqrt{s_{NN}}$ = 62 GeV. Fit parameters are given in Table 5.1

Table 5.1: Fit parameters from fits of v_2 measured using the event plane reconstructed using the FTPC in $Cu + Cu$ shown in Figure 5.10 and Figure 5.11 to v_2 (p_T)=$ap_T^b e^{-(p_T/c)^d}$ $exp(\frac{b}{p_T}^c)$

	62 GeV				200 GeV			
centrality	a	b	c	d	a	b	c	d
0-10%	0.049	0.97	3.85	2.67	0.364	1.64	0.35	0.53
10-20%	0.056	1.01	3.64	3.14	0.184	1.40	1.31	0.76
20-30%	0.070	0.79	3.80	4.00	0.246	1.49	1.07	0.75
30-40%	0.094	1.22	2.73	1.94	4.403	2.29	0.04	0.41
40-50%	0.373	1.66	0.48	0.60	0.102	0.74	4.50	2.33
50-60%	17.572	3.00	0.02	0.42	0.217	1.50	1.41	0.99

significantly reduces its sensitivity to non-flow. v_2 and the magnitude of the negative systematic error on v_2 in $Au+Au$ collisions at $\sqrt{s_{NN}} = 62$ GeV as a function of p_T and centrality from [103] are shown in Figure 5.12. These were fit to a parameterization of v_2 and the fit parameters are given in Table 5.2. Statistical errors on the fits are also neglected for $Au + Au$ collisions at $\sqrt{s_{NN}} = 62$ GeV since the systematic errors

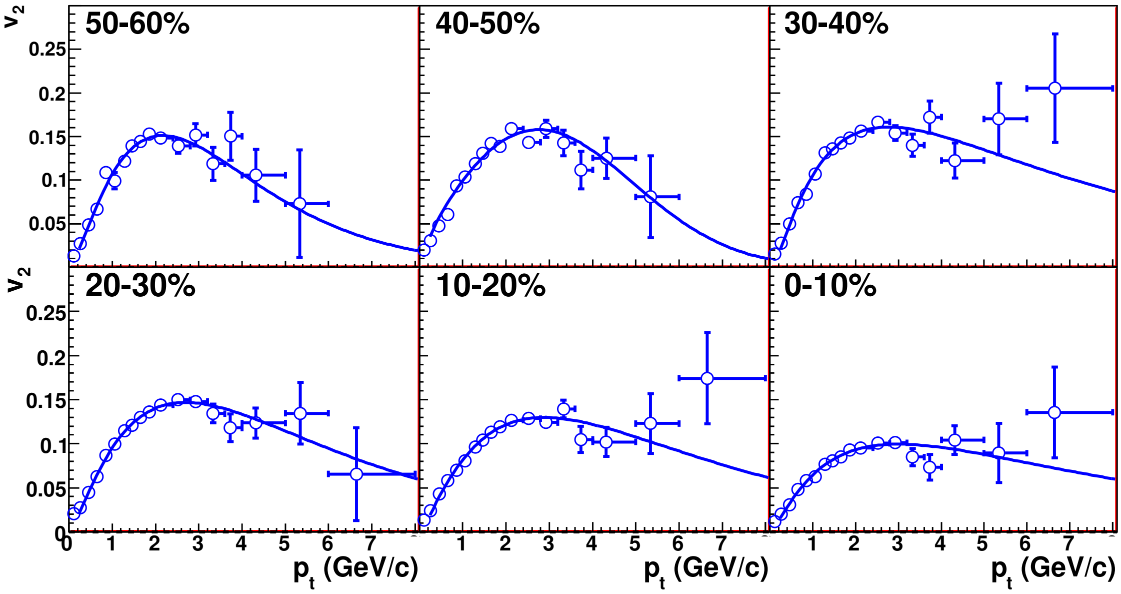

Figure 5.11: v_2 measured using the event plane from the FTPCs in $Cu+Cu$ collisions at $\sqrt{s_{NN}} = 200$ GeV. Fit parameters are given in Table 5.1

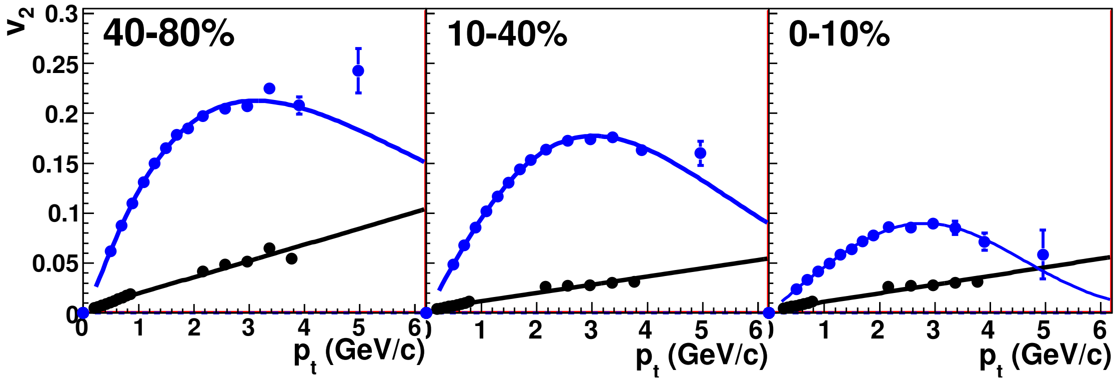

Figure 5.12: v_2 (blue) and the negative systematic error on v_2 (black) in $Au + Au$ collisions at $\sqrt{s_{NN}} = 62$ GeV. Fit parameters are given in Table 5.2.

on v_2 are several times larger than the statistical errors. The positive systematic error in $Au + Au$ collisions at $\sqrt{s_{NN}} = 62$ GeV is a constant, 0.003, for all centralities and p_T.

v_2 for Λ, Ξ^-, and Ω^- baryons and K_S^0 mesons has been observed to follow quark scaling in $Au+Au$ collisions at both $\sqrt{s_{NN}} = 62$ GeV and $\sqrt{s_{NN}} = 200$ GeV [103] and

Table 5.2: Fit parameters from fits of v_2 from [103] to v_2 (p_T)=$ap_T^b e^{-(p_T/c)^d}$ $exp(\frac{b}{p_T}^c)$ and of the negative systematic error on v_2 to $mp_T + b$

	v_2				systematic error	
centrality	a	b	c	d	m	b
0-10%	0.205	1.30	2.08	0.90	0.0163	0.0035
10-40%	0.105	1.04	4.03	1.67	0.0082	0.0038
40-80%	0.047	0.96	4.11	2.72	0.0087	0.0026

in $Cu + Cu$ collisions at $\sqrt{s_{NN}} = 200$ GeV [136]. The systematic errors on identified particle v_2 in $Cu+Cu$ collisions are more difficult due to low statistics. Quark scaling is assumed and the systematic error is estimated from unidentified hadron v_2. For a hadron comprising n_q quarks:

$$v_2^{n_q} = \frac{n_q}{n_\pi} v_2 (\frac{n_\pi}{n_q} p_T) \tag{5.9}$$

where $n_\pi = 2$. It is assumed that unidentified hadron v_2 is dominated by π v_2.

B is determined using the Zero Yield At Minimum (ZYAM) method [51,129]. This method fixes B by assuming that there is no signal at the minimum of the correlation in azimuth. For measurements with low statistics the statistical error on the minimum data point is a significant contribution to the error on the *Ridge* yield. This error is added in quadrature to the statistical error.

To determine the yield of the *Ridge*, Y_{Ridge}, the di-hadron correlation $\frac{d^2N}{d\Delta\phi d\Delta\eta}$ is projected over the entire $\Delta\eta$ region. To minimize the effects of statistical fluctuations in the determination of the background, $\frac{dY_{bkgd}}{d\phi}$, Y_{Jet} is subtracted after the projection in $\Delta\eta$:

$$Y_{Ridge} = 1/N_{trigger} \int_{-1.75}^{1.75} \int_{-1}^{1} (\frac{d^2N}{d\Delta\phi d\Delta\eta} - \frac{dY_{bkgd}}{d\phi}) d\Delta\phi d\Delta\eta - Y_{Jet}^{\Delta\eta}. \tag{5.10}$$

The integration over $\Delta\phi$ is done by bin counting. $Y_{Jet}^{\Delta\eta}$ is used for the subtraction of Y_{Jet} because it is less sensitive to the assumption that the jet-like correlation is contained within $|\Delta\eta\ | < 0.75$. Sample correlations in azimuth after the projection

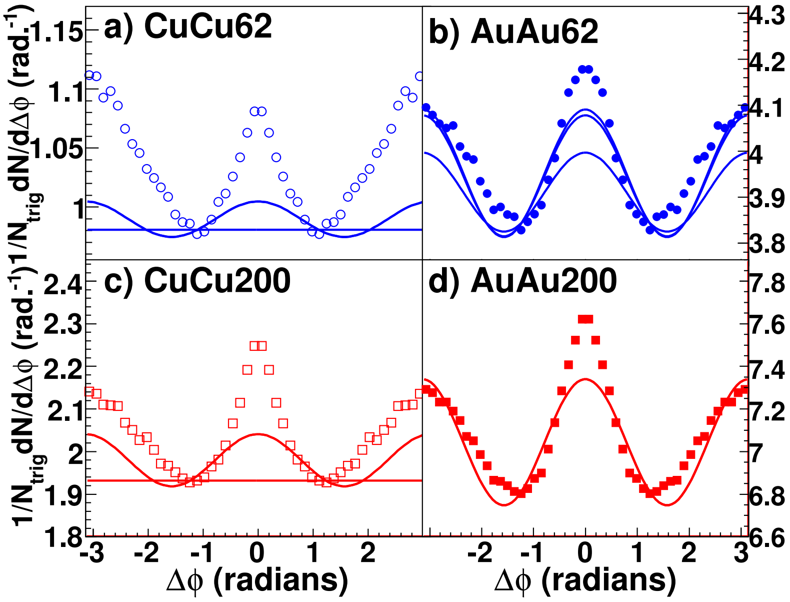

Figure 5.13: Sample correlations in $\Delta\phi$ integrated over $|\Delta\eta| < 1.75$ for 3.0 $< p_T^{trigger}$ $<$ 6.0 GeV/c and 1.5 GeV/c $< p_T^{associated} < p_T^{trigger}$ from (a) 0-60% central $Cu+Cu$ collisions at $\sqrt{s_{NN}} = 62$ GeV (b) 0-80% central $Au+Au$ collisions at $\sqrt{s_{NN}} = 62$ GeV (c) 0-60% central $Cu+Cu$ collisions at $\sqrt{s_{NN}} = 200$ GeV and (d) 0-80% central $Au+Au$ collisions at $\sqrt{s_{NN}} = 200$ GeV showing the background level and shape for high and low bounds on v_2 from each data set.

over $\Delta\eta$ are shown in Figure 5.13 for all data sets. These correlations show the background level and shape for the high and low bounds on v_2.

Chapter 6

Results

6.1 The jet-like correlation

If the jet-like correlation is produced by fragmentation, no dependence on collision system or system size would be expected. The particle ratios of the jet-like correlation should be consistent with what was observed in $p+p$ collisions since $p+p$ collisions are expected to be dominated by jet production at high-p_T. The jet-like yield should increase with $p_T^{trigger}$ because higher p_T trigger particles come on average from higher energy jets and the spectra of particles in the jet-like correlation should be harder than that observed in the inclusive. Studies of the jet-like yield as a function of collision system and energy were done for unidentified hadrons for $Cu + Cu$ and $Au + Au$ collisions at $\sqrt{s_{NN}} = 62$ GeV and $\sqrt{s_{NN}} = 200$ GeV to determine whether the data are consistent with the jet-like correlation being produced by fragmentation.

6.1.1 Energy and system dependence

The dependence of jet-like yield, Y_{Jet}, on $p_T^{trigger}$ is shown in Figure 6.1 for $Cu + Cu$ and $Au + Au$ collisions at $\sqrt{s_{NN}} = 62$ GeV and $d + Au$, $Cu + Cu$, and $Au + Au$ collisions at $\sqrt{s_{NN}} = 200$ GeV. No *Ridge* is observed in $d + Au$ collisions so it was not necessary to subtract the *Ridge*. The jet-like yields are the same as a function of $p_T^{trigger}$ within errors for all systems at a given collision energy.

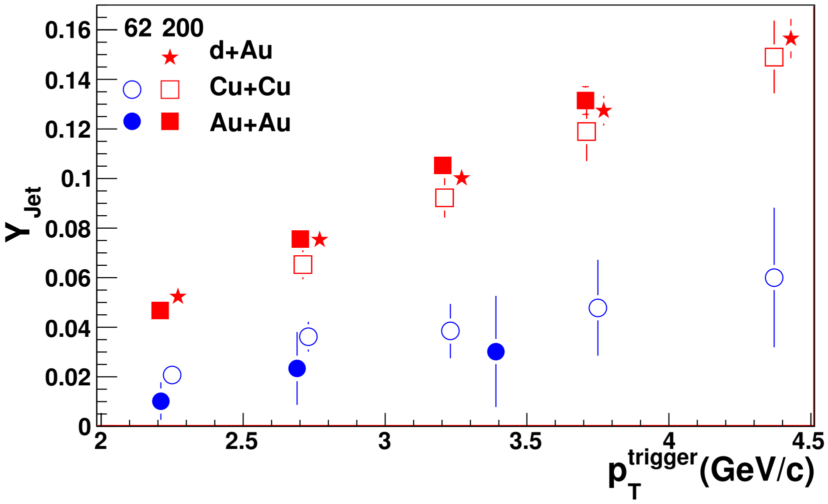

Figure 6.1: $p_T^{trigger}$ dependence of Y_{Jet} for unidentified hadrons for 1.5 GeV/c < $p_T^{associated} < p_T^{trigger}$ for 0-60% central $Cu+Cu$ and 0-80% central $Au+Au$ collisions at $\sqrt{s_{NN}}$ = 62 GeV and minimum bias $d+Au$, 0-60% central $Cu+Cu$ and 0-12% central $Au+Au$ collisions at $\sqrt{s_{NN}}$ = 200 GeV. Data from $d+Au$ and $Au+Au$ collisions at $\sqrt{s_{NN}}$ = 200 GeV are from [77, 79, 117–119, 137].

Table 6.1: Inverse slope parameter k (MeV/c) of $p_T^{associated}$ for unidentified hadrons for fits of data in Figure 6.2 to A$e^{-p_T/k}$. Statistical errors only.

	$\sqrt{s_{NN}}$ = 62 GeV h-h	$\sqrt{s_{NN}}$ = 200 GeV h-h
$Au+Au$	291 ± 28	478 ± 8
$Cu+Cu$	359 ± 41	424 ± 20
$d+Au$		469 ± 8

The $p_T^{associated}$ dependence of the jet-like yield is shown in Figure 6.2 for $Cu+Cu$ and $Au+Au$ collisions at $\sqrt{s_{NN}}$ = 62 GeV and $d+Au$, $Cu+Cu$, and $Au+Au$ collisions at $\sqrt{s_{NN}}$ = 200 GeV. The $\Delta\phi$ method is used for Y_{Jet} for $Au+Au$ collisions at $\sqrt{s_{NN}}$ = 62 GeV because these studies are statistically limited and the jet-like correlation is considerably broader in $\Delta\eta$ in these collisions. This makes the determination of the background difficult in the $\Delta\eta$ method. As for the $p_T^{trigger}$ dependence, the data are within errors for all collision systems at a given energy.

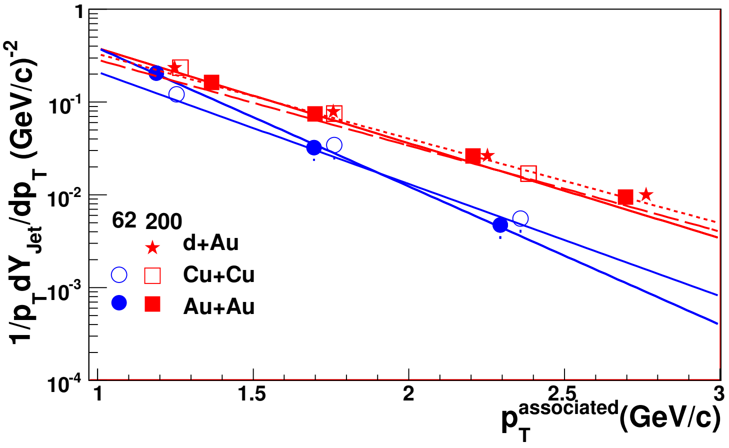

Figure 6.2: $p_T^{associated}$ dependence of Y_{Jet} for 1.5 GeV/c $< p_T^{associated} < p_T^{trigger}$ for $3.0 < p_T^{trigger} < 6.0$ GeV/c for 0-60% central $Cu+Cu$ and 0-80% central $Au+Au$ collisions at $\sqrt{s_{NN}} = 62$ GeV and minimum bias $d+Au$, 0-60% central $Cu+Cu$ and 0-12% central $Au+Au$ collisions at $\sqrt{s_{NN}} = 200$ GeV. Data from $d+Au$ and $Au+Au$ collisions at $\sqrt{s_{NN}} = 200$ GeV are from [77, 79, 117–119, 137].

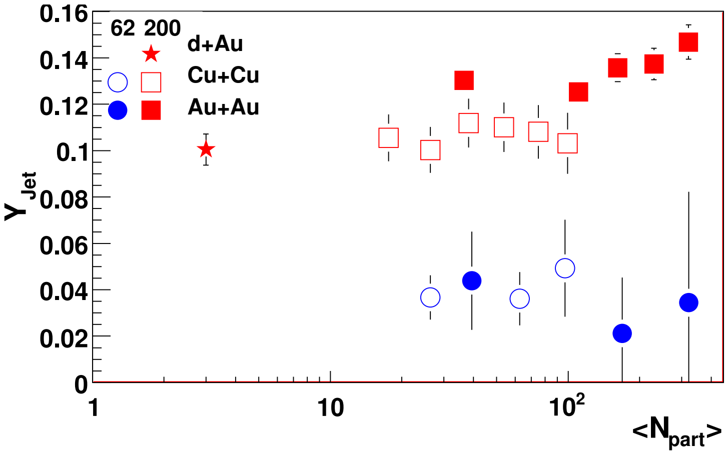

Figure 6.3: N_{part} dependence of Y_{Jet} for unidentified hadrons for $3.0 < p_T^{trigger} < 6.0$ GeV/c and 1.5 GeV/c $< p_T^{associated} < p_T^{trigger}$ for unidentified hadrons for $Cu+Cu$ and $Au+Au$ collisions at $\sqrt{s_{NN}} = 62$ GeV and $d+Au$, $Cu+Cu$ and $Au+Au$ collisions at $\sqrt{s_{NN}} = 200$ GeV. Data from $d+Au$ and $Au+Au$ collisions at $\sqrt{s_{NN}} = 200$ GeV are from [77, 79, 117–119, 137].

Figure 6.3 shows the N_{part} dependence of Y_{Jet} for $Cu+Cu$ and $Au+Au$ collisions at $\sqrt{s_{NN}}$ = 62 GeV and for $d+Au$, $Cu+Cu$, and $Au+Au$ collisions at $\sqrt{s_{NN}}$ = 200 GeV. There is a slight increase of Y_{Jet} with N_{part} in $Au+Au$ collisions at $\sqrt{s_{NN}}$ = 200 GeV. The jet-like yields in $Au+Au$ collisions at $\sqrt{s_{NN}}$ = 200 GeV are slighly higher than those in $Cu+Cu$ collisions at $\sqrt{s_{NN}}$ = 200 GeV and Y_{Jet} is about 50% larger in central $Au+Au$ collisions at $\sqrt{s_{NN}}$ = 200 GeV than in $d+Au$ collisions at $\sqrt{s_{NN}}$ = 200 GeV.

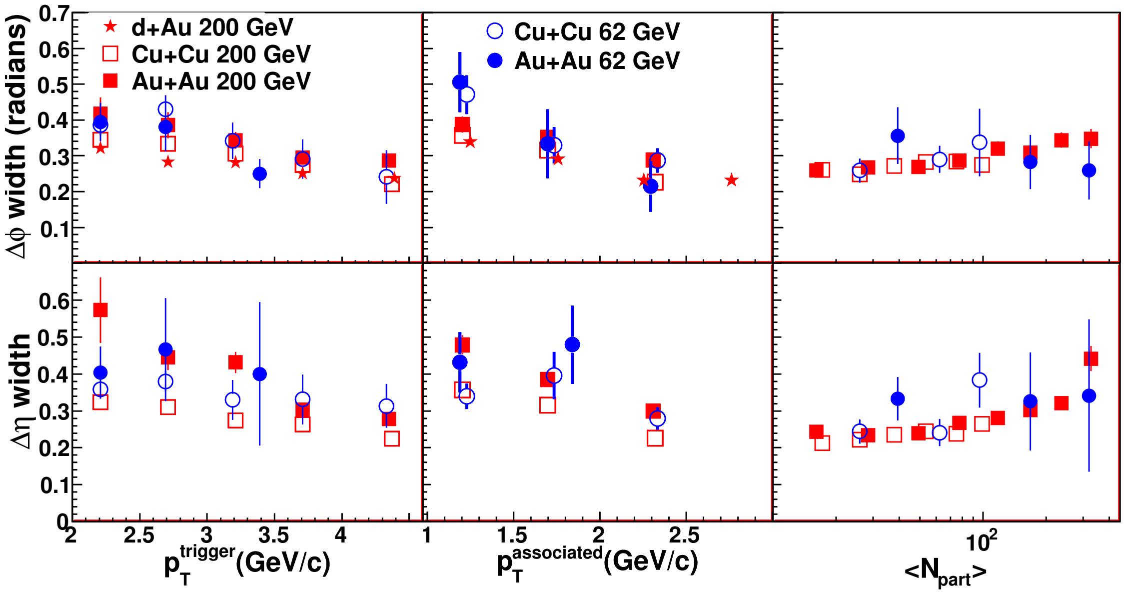

Figure 6.4: Collision energy and system size dependence of Gaussian widths in $\Delta\phi$ and $\Delta\eta$ as a function of $p_T^{trigger}$, $p_T^{associated}$, and N_{part} for unidentified hadrons for $Cu+Cu$ and $Au+Au$ collisions at $\sqrt{s_{NN}}$ = 62 GeV and $d+Au$, $Cu+Cu$ and $Au+Au$ collisions at $\sqrt{s_{NN}}$ = 200 GeV. Kinematic cuts and centralities are the same as used in Figure 6.1, Figure 6.2, and Figure 6.3 except that the $Au+Au$ data at $\sqrt{s_{NN}}$ = 200 GeV are from 0-80% central collisions for the dependence of Y_{Jet} on $p_T^{trigger}$ and $p_T^{associated}$.

Figure 6.4 shows the Gaussian widths in $\Delta\eta$ and $\Delta\phi$ as a function of $p_T^{trigger}$, $p_T^{associated}$, and N_{part} for $Cu+Cu$ and $Au+Au$ collisions at $\sqrt{s_{NN}}$ = 62 GeV and $d+Au$, $Cu+Cu$, and $Au+Au$ collisions at $\sqrt{s_{NN}}$ = 200 GeV. The widths in $\Delta\phi$ and $\Delta\eta$ are slightly greater in $Au+Au$ collisions at $\sqrt{s_{NN}}$ = 200 GeV. Data from $Au+Au$ collisions at $\sqrt{s_{NN}}$ = 62 GeV are consistent with the same trends observed at $\sqrt{s_{NN}} = 200$ GeV, however, they are also within error of the data from peripheral $Cu + Cu$ collisions at $\sqrt{s_{NN}} = 200$ GeV.

6.1.2 Flavor and system dependence

Differences between baryons and mesons have been observed in R_{AA} and in v_2 and models such as Recombination hypothesizes novel methods for production of baryons and mesons in $A + A$ collisions to explain the observed differences. If particles in jets are produced by vacuum fragmentation, baryon/meson ratios would be expected to be comparable to $p+p$. Jets with leading baryons may have different properties than jets with leading mesons. Particles produced by mechanisms such as Recombination would have baryon/meson ratios comparable to the bulk. No statistically significant differences were observed between Λ and $\bar{\Lambda}$ triggers or Ξ^- and Ξ^+ so these trigger particles were added together to increase the statistical significance of the results for comparisons to K_S^0 trigger particles. The $\Delta\phi$ was used because these measurements were statistically limited and the jet-like correlation is broader for identified particles than for unidentified particles.

Identified trigger particles

Figure 6.5 shows the $p_T^{trigger}$ dependence of Y_{Jet} for identified trigger particles in $d+Au$, $Cu + Cu$, and $Au + Au$ collisions at $\sqrt{s_{NN}} = 200$ GeV for unidentified hadron, Λ, K_S^0, and Ξ trigger particles. The $Au + Au$ data have not been corrected for the track merging effects discussed in Chapter 5, so the slightly lower yield for identified particles in $Au + Au$ collisions at $\sqrt{s_{NN}} = 200$ GeV may be due to track merging. There is no system dependence within errors. The most central K_S^0 trigger in $Cu+Cu$ collisions at $\sqrt{s_{NN}} = 200$ GeV is about three sigma above the other data; this data point may be an outlier or may be an indication of a slight particle type dependence. There is no other observed dependence on the trigger particle type.

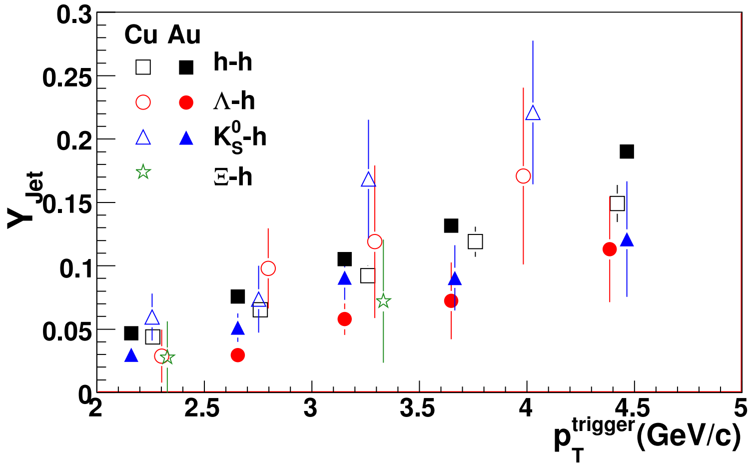

Figure 6.5: $p_T^{trigger}$ dependence of Y_{Jet} for 1.5 GeV/c $< p_T^{associated} < p_T^{trigger}$ in 0-60% central $Cu+Cu$ and 0-12% central $Au+Au$ collisions at $\sqrt{s_{NN}}$ = 200 GeV for unidentified hadrons, Λ, K^0_S, and Ξ trigger particles. Data from $Au+Au$ collisions at $\sqrt{s_{NN}}$ = 200 GeV are from [77]. The identified trigger particle data have been horizontally offset for visibility. The $Au+Au$ data have not been corrected for the track merging effects discussed in Chapter 5.

The $p_T^{associated}$ dependence of Y_{Jet} for unidentified hadrons, Λ, K^0_S, and Ξ trigger particles is shown in Figure 6.6. Due to limited statistics, it was only possible to extract Y_{Jet} for two bins in $p_T^{associated}$ for Λ and K^0_S trigger particles and one bin bor Ξ trigger particles. The jet-like yields from identified trigger particles are within errors of the jet-like yields for unidentified hadron trigger particles. The data in $Au+Au$ collisions at $\sqrt{s_{NN}} = 200$ GeV also showed no dependence on trigger particle type [77].

The N_{part} dependence of Y_{Jet} is shown in Figure 6.7 for Λ, K^0_S, and Ξ trigger particles. The $Au+Au$ data have not been corrected for track merging effects, and this may explain the difference between identified trigger particles and unidentified trigger particles.

No statistically significant differences between different trigger particles are observed for the jet-like correlations, including non-strange, singly strange, and doubly strange hadrons. Studies in $Au+Au$ collisions at $\sqrt{s_{NN}}$ = 200 GeV indicated that there is no trigger particle dependence for even the trebly strange Ω [81, 138].

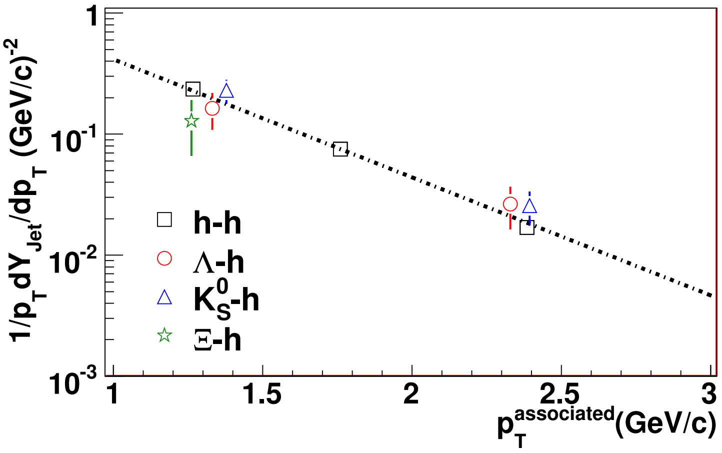

Figure 6.6: $p_T^{associated}$ dependence of Y_{Jet} for $3.0 < p_T^{trigger} < 6.0$ GeV/c in 0-60% central $Cu + Cu$ collisions at $\sqrt{s_{NN}} = 200$ GeV for unidentified hadrons, Λ, K_S^0, and Ξ trigger particles. The line is from a fit of the h-h data to $Ae^{-p_T/k}$. The inverse slope parameter is given in Table 6.1. The identified trigger particle data have been horizontally offset for visibility.

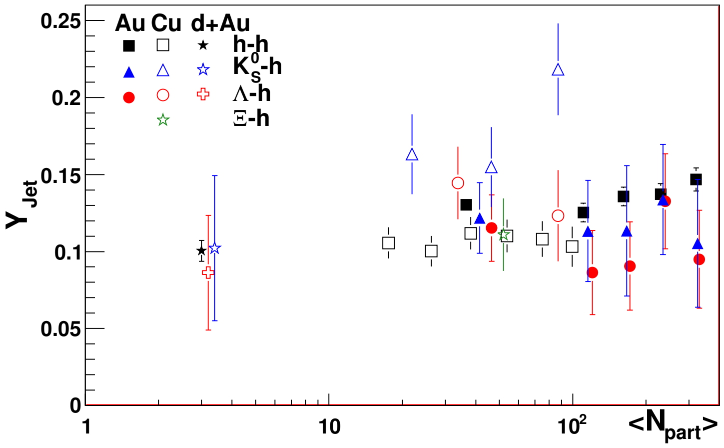

Figure 6.7: N_{part} dependence of Y_{Jet} for $3.0 < p_T^{trigger} < 6.0$ GeV/c and 1.5 GeV/c $< p_T^{associated} < p_T^{trigger}$ for identified trigger particles in $d + Au$, $Cu + Cu$, and $Au + Au$ collisions at $\sqrt{s_{NN}} = 200$ GeV for Λ, K_S^0, and Ξ trigger particles. Data from $d + Au$ and $Au + Au$ collisions at $\sqrt{s_{NN}} = 200$ GeV are from [77, 79, 117–119]. The $Au + Au$ data have not been corrected for the track merging effects discussed in Chapter 5.

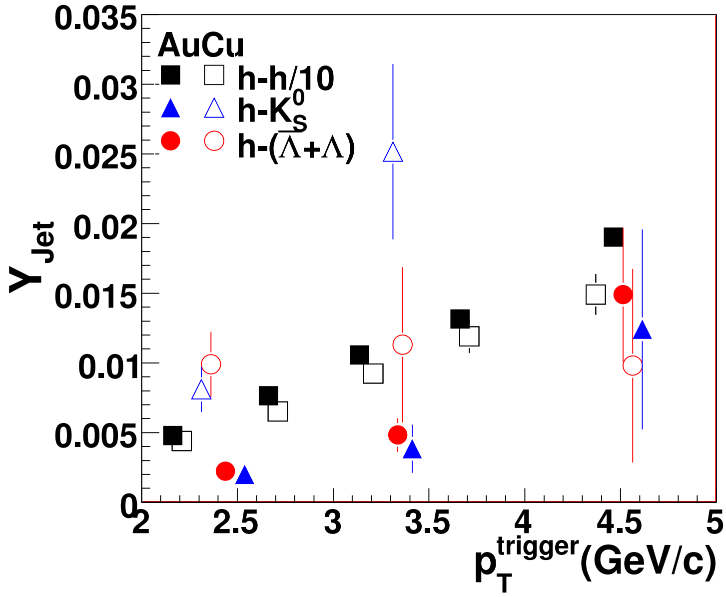

Figure 6.8: $p_T^{trigger}$ dependence of Y_{Jet} for 1.5 GeV/c $< p_T^{associated} < p_T^{trigger}$ of Y_{Jet} in 0-60% central $Cu + Cu$ and 0-12% central $Au + Au$ collisions at $\sqrt{s_{NN}} = 200$ GeV for identified associated particles. The unidentified hadron associated particles are scaled to fit on the same plot. Data from $Au + Au$ collisions at $\sqrt{s_{NN}} = 200$ GeV are from [77]. The $Au + Au$ data have not been corrected for the track merging effects discussed in Chapter 5.

Table 6.2: Inverse slope parameter k (MeV/c) of $p_T^{associated}$ for fits of data from the jet-like correlation in Figure 6.9 to $Ae^{-p_T/k}$. Statistical errors only.

	h-h	h-K_S^0	h-$\Lambda + \bar{\Lambda}$
k (MeV/c)	445 ± 20	505 ± 87	510 ± 55

Identified associated particles

Figure 6.8 shows the $p_T^{trigger}$ dependence of Y_{Jet} for identified associated particles. Similar trends are observed for unidentified associated particles and strange associated particles.

Figure 6.9 shows the dependence of Y_{Jet} on $p_T^{associated}$ for identified associated particles. The ratio $\frac{\Lambda+\bar{\Lambda}}{2K_S^0}$ is roughly 0.5 for the full $p_T^{associated}$ range shown.

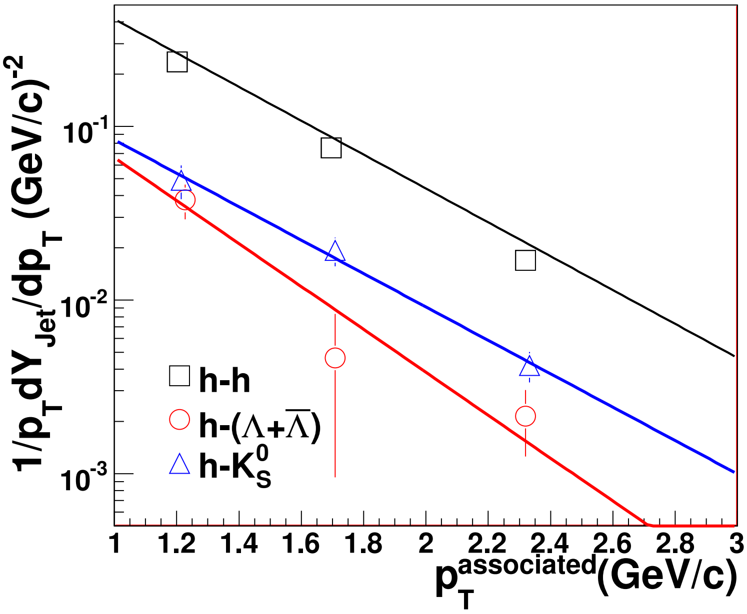

Figure 6.9: $p_T^{associated}$ dependence of Y_{Jet} for $3.0 < p_T^{trigger} < 6.0$ GeV/c for $\sqrt{s_{NN}}$ = 62 GeV and $\sqrt{s_{NN}}$ = 200 GeV. Data from $d + Au$ and $Au + Au$ collisions at $\sqrt{s_{NN}}$ = 200 GeV are from [77, 79, 117–119, 137]. Parameters from fits of the data are listed in Table 6.2.

6.2 The *Ridge*

The *Ridge* is an unexpected phenomenon first observed in $Au+Au$ collisions. In order to understand its origins and to provide a robust test of models for the production of the *Ridge*, the *Ridge* is studied as a function of as many variables as possible. The collision energy, collision system, system size, and trigger particle type dependence of the *Ridge* are presented here.

6.2.1 Energy and system dependence

Figure 6.10 shows the dependence of the *Ridge* yield, Y_{Ridge}, on N_{part} for $Cu + Cu$ and $Au + Au$ collisions at $\sqrt{s_{NN}}$ = 62 GeV and $\sqrt{s_{NN}}$ = 200 GeV. No difference is observed between $Cu+Cu$ and $Au+Au$ collisions at either energy. Y_{Ridge} is larger at $\sqrt{s_{NN}}$ = 200 GeV than $\sqrt{s_{NN}}$ = 62 GeV, as was observed for Y_{Jet}. Figure 6.11 shows that the ratios Y_{Ridge}/Y_{Jet} are the same for collisions at both $\sqrt{s_{NN}}$ = 62 GeV and

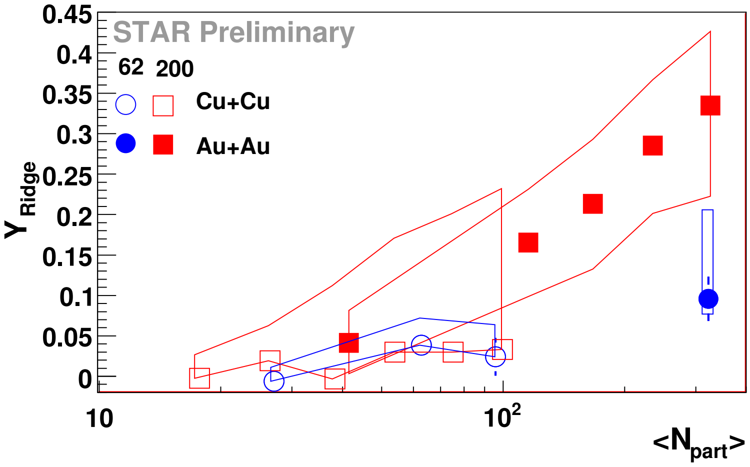

Figure 6.10: N_{part} dependence of Y_{Ridge} for unidentified hadrons for $3.0 < p_T^{trigger} <$ 6.0 GeV/c and 1.5 GeV/c $< p_T^{associated} < p_T^{trigger}$ for $Cu+Cu$ and $Au+Au$ collisions at $\sqrt{s_{NN}} = 62$ GeV and $Cu+Cu$ and $Au+Au$ collisions at $\sqrt{s_{NN}} = 200$ GeV. Data from $Au+Au$ collisions at $\sqrt{s_{NN}} = 200$ GeV are from [77, 79, 117–119, 137]. Lines indicate systematic errors due to v_2.

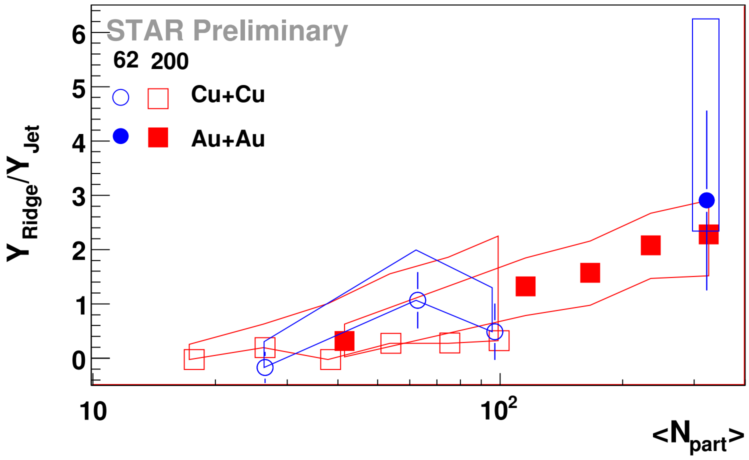

Figure 6.11: N_{part} dependence of Y_{Ridge}/Y_{Jet} for unidentified hadrons for $3.0 < p_T^{trigger}$ < 6.0 GeV/c and 1.5 GeV/c $< p_T^{associated} < p_T^{trigger}$ for $Cu+Cu$ and $Au+Au$ collisions at $\sqrt{s_{NN}} = 62$ GeV and $Cu+Cu$ and $Au+Au$ collisions at $\sqrt{s_{NN}} = 200$ GeV. Data from $d+Au$ and $Au+Au$ collisions at $\sqrt{s_{NN}} = 200$ GeV are from [77,79,117–119].

$\sqrt{s_{NN}} = 200$ GeV; both the jet-like correlation and the *Ridge* are about 40% smaller in collisions at $\sqrt{s_{NN}} = 62$ GeV than in collisions at $\sqrt{s_{NN}} = 200$ GeV.

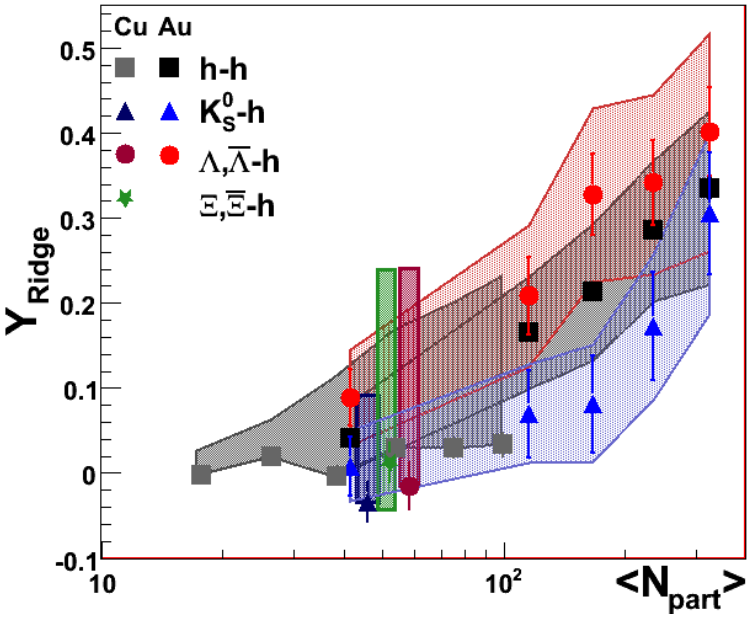

Figure 6.12: N_{part} dependence of Y_{Ridge} for $3.0 < p_T^{trigger} < 6.0$ GeV/c and 1.5 GeV/c $< p_T^{associated} < p_T^{trigger}$ for identified trigger particles in $Cu+Cu$ and $Au+Au$ collisions at $\sqrt{s_{NN}} = 200$ GeV. Data from $Au + Au$ collisions at $\sqrt{s_{NN}} = 200$ GeV are from [77, 79, 117–119]. Systematic errors are shown as bands in the same color as the data points.

6.2.2 Flavor dependence

Figure 6.12 shows the dependence of Y_{Ridge} on N_{part} for identified Λ, K^0_S, and Ξ trigger particles for $Cu + Cu$ and $Au + Au$ collisions at $\sqrt{s_{NN}} = 200$ GeV. The data for identified trigger particles in $Cu + Cu$ collisions at $\sqrt{s_{NN}} = 200$ GeV are consistent, within large errors, of Y_{Ridge} in $Au + Au$ at the same N_{part}.

6.3 Ω triggered correlations

Ω triggered correlations were statistically limited even in $Au + Au$ [81, 123]. To minimize the effects of statistical fluctuations, the detector acceptance corrections were determined using Ξ distributions in azimuth and pseudorapidity. Since statistical fluctuations were much larger than track losses due to track merging, track merging corrections were not applied. To investigate the feasibility of studies of Ω triggered

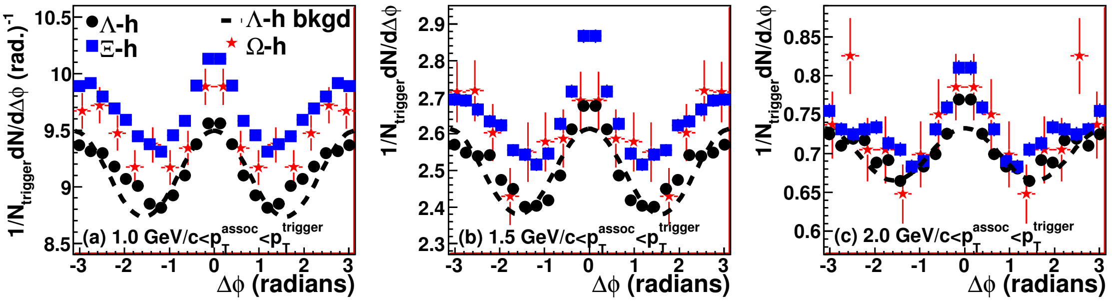

Figure 6.13: Ω triggered correlations for different $p_T^{associated}$ cuts for $3.0 < p_T^{trigger} < 6.0$ GeV/c in 0-60% central $Cu + Cu$ collisions at $\sqrt{s_{NN}} = 200$ GeV for cut set 1 described in Chapter 4. Data are compared to Λ and Ξ triggered correlations for the same kinematic cuts. The background shown as a dashed line is the background from the nominal value of v_2 from Λ triggered correlations.

correlations in $Cu + Cu$ at $\sqrt{s_{NN}} = 200$ GeV, kinematic cuts were varied to find the cuts which maximize the signal to background ratio. Lowering the lower limit on $p_T^{associated}$ or $p_T^{trigger}$ increases the statistics, however, it also increases the combinatorial background. Ω^- and Ω^+ were added in order to increase statistics.

Figure 6.13 shows Ω triggered correlations in $Cu + Cu$ collisions at $\sqrt{s_{NN}} = 200$ GeV for different $p_T^{associated}$ cuts for cut set 1 described in Chapter 4. No background subtraction is done. The background from Λ triggered correlations is shown. The v_2 modulated combinatorial background is significant, however, it has roughly the same shape for the Λ, Ξ, and Ω. The slight differences in the level of the background for Ξ and Ω triggers are due to the higher average multiplicities in these events. For all cases the Ω triggered correlations are within error of both the correlations observed for other trigger particles and of the v_2 modulated background.

Figure 6.14 shows Ω triggered correlations in $Cu + Cu$ collisions at $\sqrt{s_{NN}} = 200$ GeV for different $p_T^{trigger}$ cuts. As for different $p_T^{associated}$ cuts, the Ω triggered correlations are within error of both the correlations observed for other trigger particles and of the v_2 modulated background.

Figure 6.15 compares the Ω correlations using cut set 1 to those using cut sets 2 and 3. Cut set 2 provides the purest Ω sample, which might make the signal stronger if contamination from the background in the Ω mass peak weakens the signal.

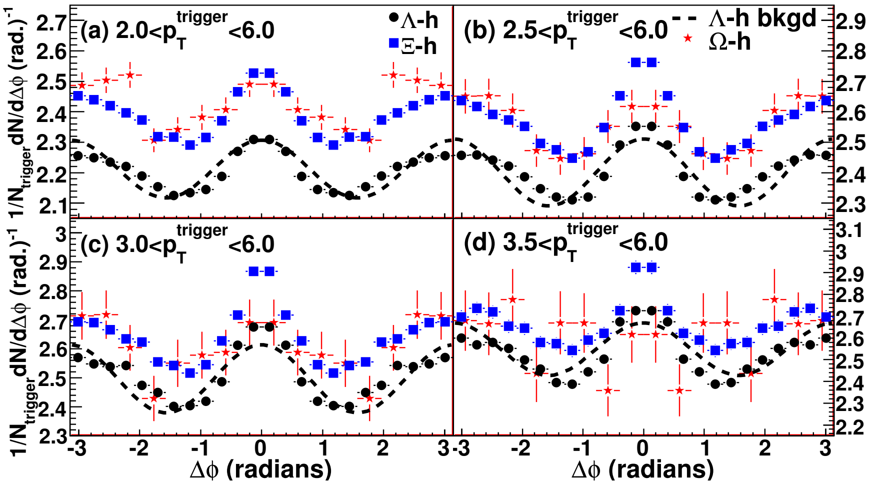

Figure 6.14: Ω triggered correlations for different $p_T^{trigger}$ cuts for $1.5 < p_T^{associated} < p_T^{trigger}$ GeV/c in 0-60% central $Cu+Cu$ collisions at $\sqrt{s_{NN}} = 200$ GeV for the three different cut sets described in Chapter 4. Data are compared to Λ and Ξ triggered correlations for the same kinematic cuts.

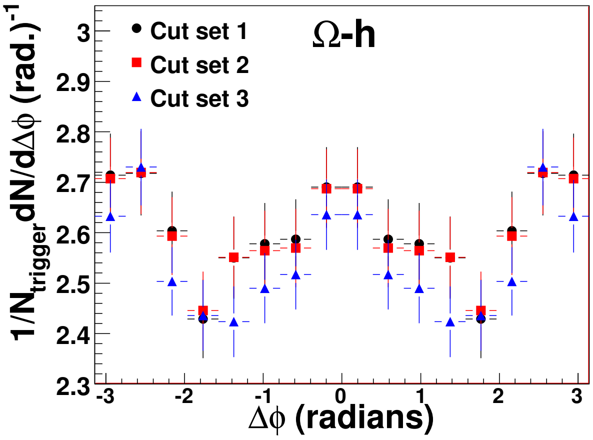

Figure 6.15: Ω triggered correlations for $1.5 < p_T^{associated} < p_T^{trigger}$ GeV/c and $3.0 < p_T^{trigger} < 6.0$ GeV/c in 0-60% central $Cu+Cu$ collisions at $\sqrt{s_{NN}} = 200$ GeV for the three different cut sets described in Chapter 4. Data are compared to Λ and Ξ triggered correlations for the same kinematic cuts.

Cut set 3 provides the least pure sample meaning there is significant contamination from background in the Ω mass peak, however, it also provides higher statistics. There are no significant differences between the signals using different cuts. Since the Ω triggered correlations were within error of both the background and the signal expected from other trigger particles, it is not possible to get a statistically significant measurement of Ω triggered di-hadron correlations in $Cu+Cu$ collisions at $\sqrt{s_{NN}} =$ 200 GeV.

6.4 Summary

No differences are observed in the jet-like correlation between $d+Au$, $Cu+Cu$ and $Au+Au$ collisions as a function of $p_T^{trigger}$ and $p_T^{associated}$. A system size dependence is observed, with the jet-like correlation increasing by about 50% from $d+Au$ collisions to central $Au+Au$ collisions at $\sqrt{s_{NN}} = 200$ GeV. The jet-like correlation is somewhat broader in $Au+Au$ collisions at $\sqrt{s_{NN}} = 200$ GeV than in $Cu+Cu$ collisions at $\sqrt{s_{NN}} = 200$ GeV. No trigger particle type dependence is observed.

The *Ridge* is observed for the first time in collisions at $\sqrt{s_{NN}} = 62$ GeV and is observed in $Cu+Cu$ collisions. The *Ridge* is independent of the collision system at a given N_{part}, and the Y_{Ridge}/Y_{Jet} ratio is independent of collision energy for the kinematic cuts studied. No trigger particle dependence is observed.

Chapter 7

Discussion

7.1 The jet-like correlation

Various different measurements indicate that the jet-like correlation is dominantly produced by vacuum fragmentation. The spectra of particles in the jet-like correlation shown in Figure 2.9 demonstrated behavior suggesting that the jet-like correlation is dominated by fragmentation. For instance, the spectra of particles in the jet-like correlation have shallower slopes than the inclusive spectra and become shallower the higher the momentum of the trigger particle. Likewise, the minimal dependence of the jet-like yield on the angle relative to the reaction plane shown in Figure 2.12 and the agreement between the di-hadron fragmentation functions in $d + Au$ and $Au + Au$ shown in Figure 2.10 also suggest that the jet-like correlation is dominantly produced by fragmentation. The lack of trigger particle dependence demonstrated in Figure 6.5, Figure 6.6, and Figure 6.7 is expected if the jet-like correlation were dominated by fragmentation, however, strange particle production in jets is still not understood well enough to draw strong conclusions on this basis.

The particle composition of the jet-like correlation further indicates that this feature is dominantly produced by fragmentation. Particle ratios in $p + p$ collisions at high p_T are likely to be dominated by fragmentation. Figure 2.11 demonstrated that the baryon to meson ratio in the jet-like correlation in central $Au + Au$ collisions is comparable to that in $p + p$ collisions for both strange and non-strange particles;

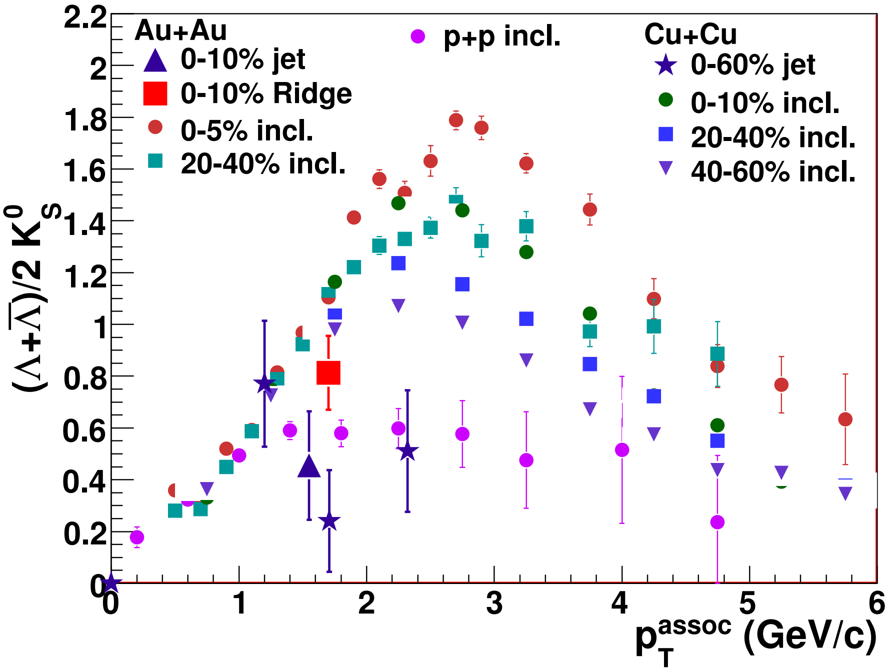

Figure 7.1: Comparison of the inclusive $\frac{\Lambda+\bar{\Lambda}}{2K^0_S}$ in $Cu + Cu$ [139] and $Au + Au$ [140] collisions at $\sqrt{s_{NN}}$ = 200 GeV to that in the jet-like correlation in 0-60% central $Cu+Cu$ and 0-12% central $Au+Au$ collisions at $\sqrt{s_{NN}}$ = 200 GeV and to the *Ridge* in 0-12% central collisions in $Au + Au$ collisions at $\sqrt{s_{NN}}$ = 200 GeV. [79].

Figure 7.1 demonstrates that the baryon to meson ratio in the jet-like correlation in $Cu + Cu$ is also comparable to the inclusive particle ratios in $p + p$ collisions.

There is some indication that the jet-like correlation may be slightly modified, particularly in central $Au+Au$. Figure 6.3 shows roughly a 50% increase in Y_{Jet} from $d + Au$ collisions to central $Au + Au$ collisions at $\sqrt{s_{NN}}$ = 200 GeV, and Figure 6.4 indicates that the jet-like correlation is slightly wider in $Au + Au$ collisions at $\sqrt{s_{NN}}$ = 200 GeV. The data are consistent with the same percentage increase in $Au + Au$ collisions at $\sqrt{s_{NN}}$ = 62 GeV, however, the error bars are too large to determine whether this increase is also present in collisions at $\sqrt{s_{NN}}$ = 62 GeV. There are three mechanisms which may lead to this increase. First, both the $\Delta\phi$ and the $\Delta\eta$ methods assume that the *Ridge* is independent of $\Delta\eta$, and if this is not true, some of the *Ridge* may be misidentified as part of the jet-like correlation. Collisions with higher N_{part} also have a larger *Ridge* and the *Ridge* increases with N_{part}. Second, the slight difference in yields may also be due to a modification of the jet spectrum leading to the jet-like correlation in $Au + Au$ collisions. For instance, if energy loss in the medium leads to a greater percentage energy loss for lower energy partons, the spectrum that contributes to the jet-like correlation would be less steep in central $Au + Au$ collisions. This would mean a greater percentage of high energy partons would contribute to the jet-like correlation. Since higher energy partons fragment into more particles, the jet-like yield would be greater. Third, it is also possible that the jet-like correlation is modified because of interactions of the parton with the medium and that this modification increases with the system size. For instance, if some partons fragment in the medium, the fragmentation functions may be slightly modified in $A + A$ collisions relative to $p + p$ collisions.

The lack of dependence on the collision system of the jet-like correlation demonstrated in the $p_T^{trigger}$ dependence shown in Figure 6.1, the $p_T^{associated}$ dependence shown in Figure 6.2, the N_{part} dependence shown in Figure 6.3, and the widths in $\Delta\phi$ and $\Delta\eta$ shown in Figure 6.4 further support the hypothesis that the jet-like correlation is dominantly produced by fragmentation. While each of these independent measurements has large errors, they all systematically indicate that the jet-like correlation is comparable to what would be expected from fragmentation.

7.1.1 Comparisons to PYTHIA

In order to test whether these data are understood quantitatively, they are compared to PYTHIA [141]. PYTHIA is a Monte Carlo event generator for collisions such as $e^+ + e^-$ and $p + p$ which incorporates analytical results and QCD-based models. PYTHIA 6.4.10 was used with tune A which has been tuned to match data from the Tevatron at $\sqrt{s_{NN}} = 1.8$ TeV [142] and describes spectra of π and p well at RHIC energies [105, 143, 144]. To determine the jet-like yield in PYTHIA, $p + p$ collisions at $\sqrt{s_{NN}} = 200$ GeV are simulated. The analysis described in Chapter 5 is repeated except that no separation of the jet-like correlation and the *Ridge* is necessary because there is no *Ridge* in $p + p$. The combinatorial background is assumed to be constant

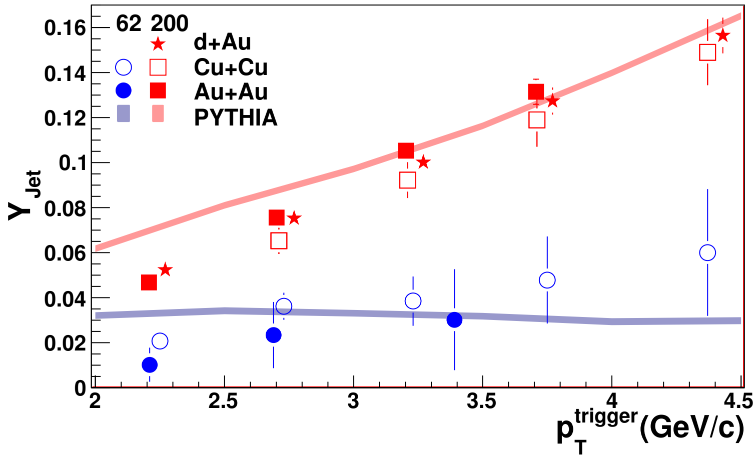

Figure 7.2: $p_T^{trigger}$ dependence of Y_{Jet} for 1.5 GeV/c $< p_T^{associated} < p_T^{trigger}$ for 0-60% central $Cu+Cu$ and 0-80% central $Au+Au$ collisions at $\sqrt{s_{NN}} = 62$ GeV and minimum bias $d+Au$, 0-60% central $Cu+Cu$ and 0-12% central $Au+Au$ collisions at $\sqrt{s_{NN}} = 200$ GeV. Data from $d+Au$ and $Au+Au$ collisions at $\sqrt{s_{NN}} = 200$ GeV are from [77, 79, 117–119, 137]. Lines indicate predictions from PYTHIA.

because there is no hydrodynamical flow in PYTHIA collisions. Enough events were generated for the statistical error bars to be negligible. Systematic error bars were not determined.

Figure 7.2 shows the dependence of the jet-like correlation on $p_T^{trigger}$ for all systems and energies studied, as shown in Figure 6.1, compared to predictions from PYTHIA. Since the $d+Au$ data from di-hadron correlations match $p+p$ where comparisons are possible, PYTHIA should be able to describe the $d+Au$ data. However, since there are no differences observed between $d+Au$, $Cu+Cu$, and $Au+Au$, PYTHIA should be able to describe all of the data. PYTHIA overestimates the data at low p_T but matches the data at higher p_T. The data used to tune PYTHIA were from considerably higher jet energies and therefore may not constrain this kinematic region well. Deviations of PYTHIA from the data could be explained if either PYTHIA does not use the correct fragmentation functions or if the jet spectrum which produces the jet-like correlation is not correct in PYTHIA. Preliminary studies of the fragmentation functions in heavy ion collisions indicate that PYTHIA describes the fragmentation functions in heavy ion collisions [90], although the jet sample used for these studies

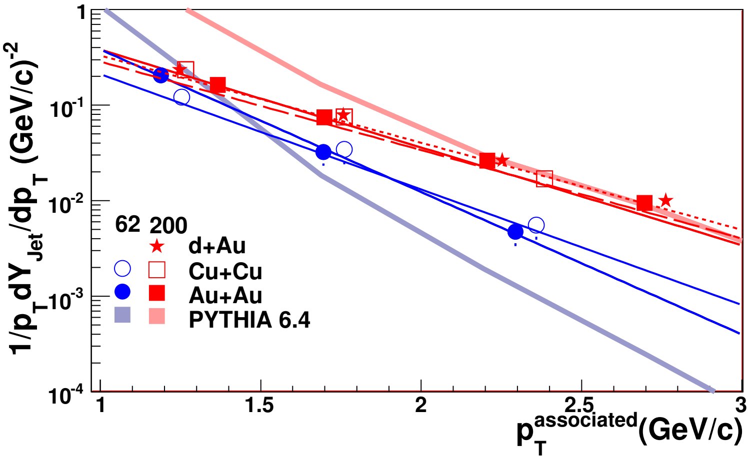

Figure 7.3: $p_T^{associated}$ dependence of Y_{Jet} for 1.5 GeV/c $< p_T^{associated} < p_T^{trigger}$ for $3.0 < p_T^{trigger} <$ 6.0 GeV/c for 0-60% central $Cu+Cu$ and 0-80% central $Au+Au$ collisions at $\sqrt{s_{NN}}$ = 62 GeV and minimum bias $d+Au$, 0-60% central $Cu+Cu$ and 0-12% central $Au+Au$ collisions at $\sqrt{s_{NN}}$ = 200 GeV. Data from $d+Au$ and $Au+Au$ collisions at $\sqrt{s_{NN}}$ = 200 GeV are from [77, 79, 117–119, 137]. The lines that match the data indicate fits, as shown in Figure 7.3, and the thicker, shaded lines indicate predictions from PYTHIA.

may be biased towards unmodified jets and the average jet energy which leads to the jet-like correlation presented in Figure 7.2 is considerably lower.

Figure 7.3 shows the dependence of the jet-like yield on $p_T^{associated}$, as shown in Figure 6.2, compared to PYTHIA. PYTHIA does not correctly describe the spectrum of particles in the jet-like correlation in collisions.

The jet-like yield expected in PYTHIA is compared to the data in Figure 6.3 in Figure 7.4. PYTHIA describes the data in this kinematic range well. The widths in $\Delta\phi$ and $\Delta\eta$ shown in Figure 6.4 are compared to PYTHIA in Figure 7.5. PYTHIA underestimates the widths in $\Delta\phi$, particularly for the lowest $p_T^{trigger}$. While the $d+Au$ data are higher than PYTHIA, the widths in $A+A$ are larger than $d+Au$ and the width grows with N_{part}. The widths in $\Delta\eta$ generally agree with the data except for the lowest $p_T^{associated}$ in $Cu+Cu$ collisions and for the lowest $p_T^{trigger}$ in $Au+Au$ collisions at $\sqrt{s_{NN}}$ = 200 GeV. The width in $\Delta\eta$ in $Au+Au$ collisions at $\sqrt{s_{NN}}$ = 200 GeV matches PYTHIA in the most peripheral collisions but by the most central

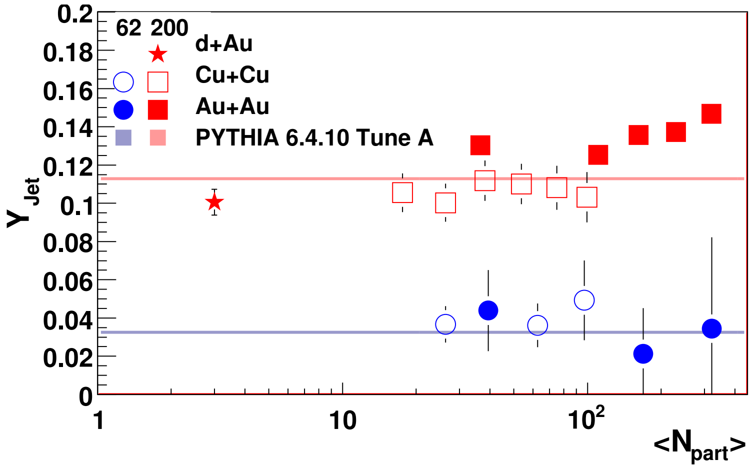

Figure 7.4: N_{part} dependence of Y_{Jet} for $3.0 < p_T^{trigger} < 6.0$ GeV/c and 1.5 GeV/c $< p_T^{associated} < p_T^{trigger}$ for $Cu + Cu$ and $Au + Au$ collisions at $\sqrt{s_{NN}} = 62$ GeV and $d + Au$, $Cu + Cu$ and $Au + Au$ collisions at $\sqrt{s_{NN}} = 200$ GeV. Data from $d + Au$ and $Au + Au$ collisions at $\sqrt{s_{NN}} = 200$ GeV are from [77, 79, 117–119, 137]. Lines indicate predictions from PYTHIA.

collisions the width in $\Delta\eta$ has almost doubled.

Before these studies were done, PYTHIA was not necessarily expected to compare well with any aspect of di-hadron correlations because it is clear from the observation of jet quenching shown in Figure 2.3 and the *Ridge* that di-jets are strongly modified in $A + A$ collisions. Additionally, PYTHIA has not been tuned to data from di-hadron correlations. PYTHIA not only qualitatively describes the jet-like correlation but also describes the jet-like correlation fairly well quantitatively. The fact that few differences are observed between the jet-like correlation in $d + Au$, $Cu + Cu$, and $Au + Au$ collisions implies that there are no strong nuclear effects modifying the jet-like correlation in $A + A$ collisions. This means that the deviations of PYTHIA from the data at the lowest $p_T^{trigger}$ and $p_T^{associated}$ can be interpreted as a need for better tuning of PYTHIA to lower p_T data. Deviations from $p + p$, peripheral $A + A$, and PYTHIA observed in the central $Au + Au$ can be understood to result from either modifications of the jet-like correlation or evidence of a slight dependence of the *Ridge* on $\Delta\eta$.

The agreement of the jet-like correlation with PYTHIA means that a leading

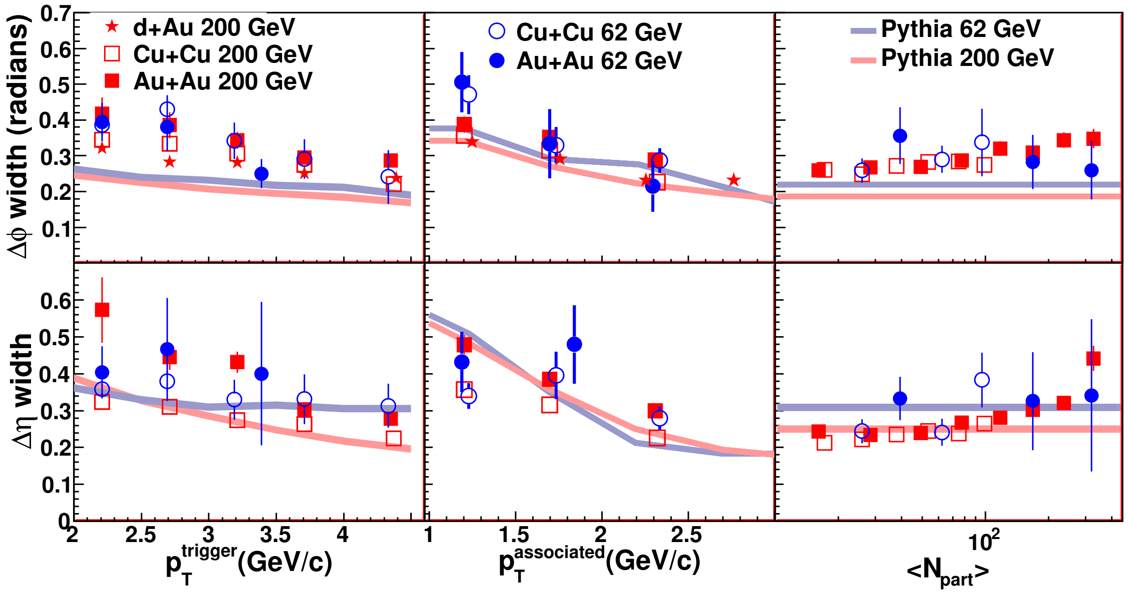

Figure 7.5: Collision energy and system size dependence of Gaussian widths in $\Delta\phi$ and $\Delta\eta$ as a function of $p_T^{trigger}$, $p_T^{associated}$, and N_{part} for $Cu+Cu$ and $Au+Au$ collisions at $\sqrt{s_{NN}}$ = 62 GeV and $d + Au$, $Cu + Cu$ and $Au + Au$ collisions at $\sqrt{s_{NN}}$ = 200 GeV. Kinematic cuts and centralities are the same as used in Figure 6.1, Figure 6.2, and Figure 6.3 except that the $Au+Au$ data at $\sqrt{s_{NN}}$ = 200 GeV for the $p_T^{trigger}$ and $p_T^{associated}$ are from 0-80% central collisions. Lines indicate predictions from PYTHIA.

order pQCD model such as PYTHIA can be used to understand how the kinematic cuts applied in di-hadron correlations affect the jet sample. This demonstrates that di-hadron correlations are an effective means for studying jets in heavy ion collisions and that the jet-like correlation can be calculated from first principles. Therefore, the jet-like correlation provides a means to determine the distribution of jet energies of jets leading to di-hadron correlations, a useful tool for studies of both the away-side and the *Ridge*. It also means that models for the *Ridge* which would affect the per trigger yield of the jet-like correlation are not correct.

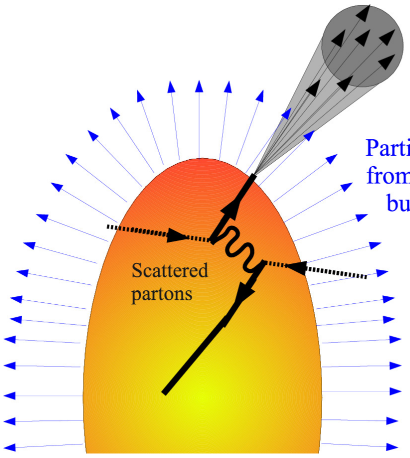

Figure 7.6: Schematic diagram depicting the radial flow plus trigger bias model

7.2 The *Ridge*

7.2.1 Theoretical descriptions of the *Ridge*

The *Ridge* is a novel feature only observed in heavy ion collisions. Multiple different models have been proposed to explain the *Ridge*. These models build on the theoretical frameworks used to describe heavy ion collisions discussed in Chapter 1.

Radial flow plus trigger bias

The radial flow plus trigger bias model explains the *Ridge* as an incidental rather than a causal correlation between particles [145]. As discussed in Chapter 1, there is evidence that the medium produced in central heavy ion collisions at RHIC can be described as a fluid and that there are pressure gradients in this fluid. Hydrodynamical models predict the expansion of the medium through radial flow, meaning that particles in the bulk get a radial velocity boost so that they are mostly emitted perpendicular to the surface of the medium. In the radial flow plus trigger bias model, hard partons are also emitted mostly perpendicular to the surface of the medium. The hard partons may either get a radial velocity boost from radial flow, or they may be surface-biased jets. Either mechanism means that both the particles from the jet and particles from the medium come mostly from the surface, resulting in

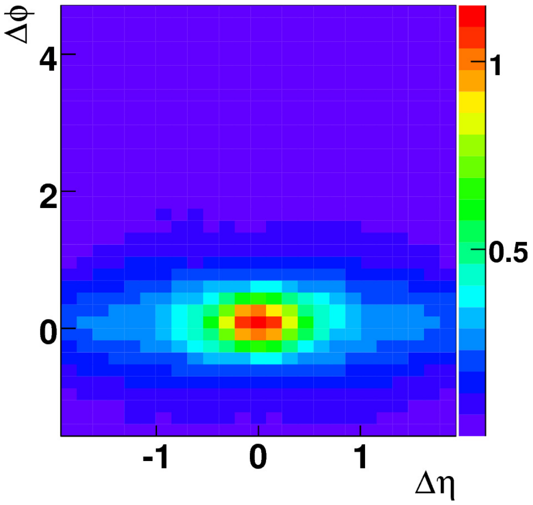

Figure 7.7: Di-hadron correlation predicted in the radial flow plus trigger bias model for a radial velocity boost $\beta_r = 0.4$, and $3.0 < p_T^{trigger} < 20.0$ GeV/c, $1.0 < p_T^{associated} < 2.0$ GeV/c [146]. $\Delta\phi$ is in radians.

a correlation between these particles. This is depicted schematically in Figure 7.6. The *Ridge* is then made up of particles in the bulk that are correlated with the hard parton through this mechanism. Because the distribution of particles in the bulk is broad in pseudorapidity, the *Ridge* is then broad in pseudorapidity.

The calculation in [146] by Pruneau, Gavin, and Voloshin (PGV) uses PYTHIA for generating p+p events and gives the particles in these events a radial velocity boost to mimic the effect of radial flow. This calculation does not conserve momentum but is able to recreate many features observed in the data. It produces an enhancement on the near-side similar to the *Ridge* and a dip on the away-side similar to the dip observed in the data. Figure 7.7 shows the di-hadron correlation produced in this model for similar kinematic cuts to those used in the data in this thesis and with a radial velocity boost comparable to that inferred from comparisons of the inclusive particle spectra in central $Au+Au$ collisions at $\sqrt{s_{NN}} = 200$ GeV to a Blast Wave model. In this kinematic region, the away-side is negligible. No quantitative comparisons between this model and the data presented in this thesis have been done.

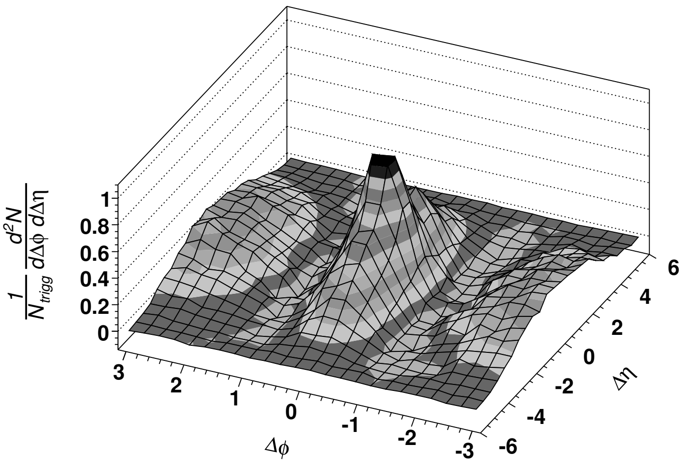

Figure 7.8: Di-hadron correlation predicted for 2.5 GeV/c < $p_T^{trigger}$ and 1.0 GeV/c < $p_T^{associated}$ in [147]. $\Delta\phi$ is in radians.

Theoretical calculations involving both jets and hydrodynamics are difficult because hydrodynamics inherently describes processes that occur in a fluid at equilibrium and jets are inherently not at equilibrium. Attempts to calculate the production of the *Ridge* through the radial flow plus trigger bias mechanism using a hydrodynamical framework have been done, although they do not yet agree with the data. This may be due to the inherent difficulty in such calculations. The calculation by Shuryak in [148] gets the width of the *Ridge* in azimuth a factor of two larger than observed in the data. The calculation in [147] by Takahashi et al is a full 3D hydrodynamical calculation which reproduces many of the general features in the data, as shown in Figure 7.8. In this calculation a hard parton is mimicked by introducing hot cells into the hydrodynamical calculation. In addition to producing a *Ridge*, this leaves a correlation which looks like the jet-like correlation, even though there are no jets generated.

Glasma flux tubes

In the Color Glass Condensate (CGC) picture, the incoming nuclei are described as two sheets of Glasma. When these sheets collide, strong color magnetic and electric

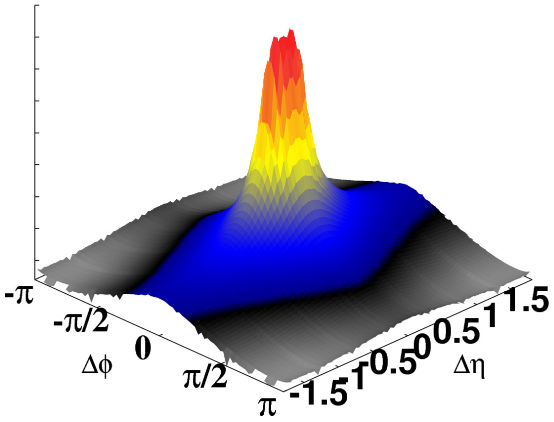

Figure 7.9: The *Ridge* produced in the CGC [151]. $\Delta\phi$ is in radians.

fields form and in a short period of time these fields change from transverse to longitudinal [25]. In the CGC picture the *Ridge* is formed by flux tubes of longitudinal color electric and magnetic fields that form in this initial state [149,150]. These correlations are enhanced by the radial flow plus trigger bias mechanism; without enhancement by radial flow the *Ridge* produced in this model is not large enough to be consistent with the data.

Most quantitative comparisons with the data have been with the untriggered, or "Soft", *Ridge* [152], however, the triggered, or "Hard", *Ridge* should be described in this model. Calculations of the "Hard" *Ridge* in this model are difficult. The calculation of the "Hard" *Ridge* done in [151], shown in Figure 7.9, qualitatively reproduces the shape of the *Ridge*, however, the size of the *Ridge* relative to the jet-like correlation is considerably smaller than what is observed in the data. In this model the jet-like correlation would not be affected because the parton would fragment after having left the medium.

Recombination and the Correlated Emission Model

Recombination was introduced in response to a baryon enhancement in the inclusive data. In Recombination, hadrons form by the combination of partons in the medium. The partons may either be thermal partons, those coming from the medium, or shower partons, those coming from hard scattering. In this model the jet-like correlation comes from shower partons or combinations of thermal and shower partons. The inclusive spectra were fit to determine the thermal and shower contributions to the spectra and based on these fits it was predicted by Hwa that there would be no correlation observed for Ω triggered correlations [153]. The data in [81, 138] contradicted this prediction. In [154] Hwa explained the discrepancy by hypothesizing that the *Ridge* comes from "phantom jets", that the Ω trigger is actually from the *Ridge*, and that the Ω triggered correlation in central $Au + Au$ collisions at $\sqrt{s_{NN}} = 200$ GeV presented in [81, 138] comprises only a *Ridge* but no jet-like correlation. There are not enough statistics to separate the jet-like correlation from the *Ridge* in the Ω triggered correlation. This model presumes, however, that there is a jet which created the *Ridge*; the Ω trigger is in the *Ridge* for this jet.

This model was used to calculate the *Ridge* in central $Au+Au$ collisions at $\sqrt{s_{NN}}$ = 200 GeV and is able to describe the data [155]. No predictions for Cu+Cu collisions or to collisions at $\sqrt{s_{NN}} = 62$ GeV have been made yet. Hwa's Correlated Emission Model uses recombination to generate particles from the bulk and relies on the radial flow plus trigger bias model mechanism to get the correlated emission of particles from the bulk and from hard partons responsible for the *Ridge* [156]. Since some of the particles in the jet-like correlation would come from a combination of thermal and shower partons, this model may lead to a modification of the jet-like correlation.

Momentum Kick Model

Wong's Momentum Kick Model [157] posits that the *Ridge* arises from collisions of hard partons with partons from the medium before fragmentation. The medium partons are assumed to have a roughly uniform distribution in azimuth and pseudorapidity before the collision with the hard parton. Collisions of the hard parton give medium partons momentum kicks in the direction of the hard parton, creating an azimuthal correlation between medium partons and the hard parton. The momentum kick does not create a strong correlation in pseudorapidity because jets are dominantly produced at midrapidity [157, 158]. This scenario is depicted in Figure 7.10.

The Momentum Kick Model does not explain how the initial uniformity of the

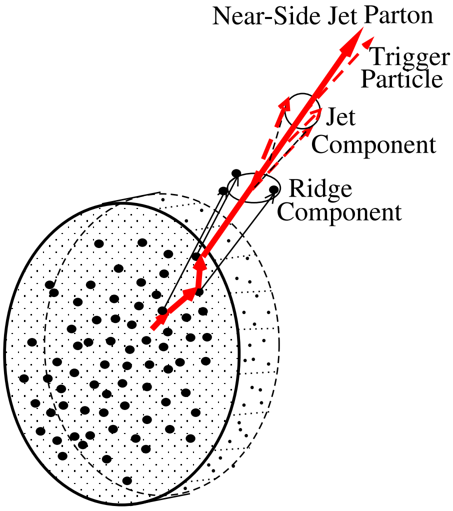

Figure 7.10: Schematic diagram exhibiting the mechanism for *Ridge* production in the momentum kick model [159]. The solid red lines show the trajectory of the parton as it traverses the medium and the dashed red lines show the directions of the momenta of the hadrons from the fragmentation of the hard parton.

parton distribution at mid-rapidity arises. It may come from string fragmentation, or from another mechanism such as a Color Glass Condensate initial state. The Momentum Kick Model fits the experimental data on the *Ridge* and determines the initial parton momentum from these data. It successfully fits the $p_T^{associated}$ and N_{part} dependence of the *Ridge* [159]. It also successfully predicted the shape of the *Ridge* at large $\Delta\eta$ in PHOBOS using the data available at mid-rapidity from STAR [76].

The Momentum Kick Model has been used to describe the data on the collision energy dependence of the *Ridge* presented in this thesis. This was not done by fitting the data from $\sqrt{s_{NN}} = 62$ GeV but by assuming that the size of the *Ridge* scales with the density of partons and that the density of partons scales with the density of participants [159]. This energy dependence is shown in Figure 7.11 and agrees with the data.

The Momentum Kick Model predicts a sharp drop in the *Ridge* as a function of the rapidity of the associated particle and $p_T^{associated}$ spectra which are strongly dependent on rapidity. These features are dependent on the kinematic cuts used in the analysis. This is depicted in Figure 7.12. Data which extend beyond this region would be useful

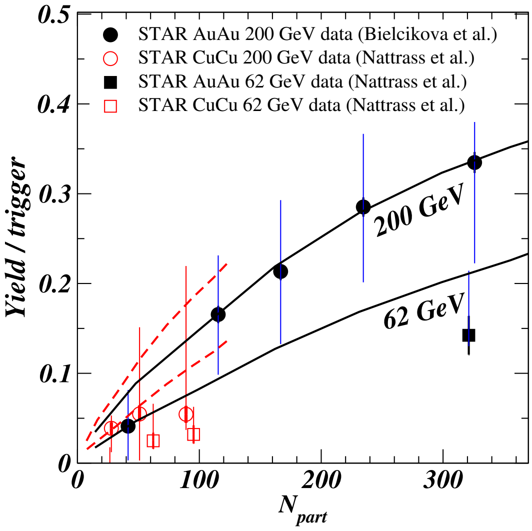

Figure 7.11: Collision energy dependence of the *Ridge* in the Momentum Kick model [159] for the unidentified hadron correlations shown in Figure 6.10.

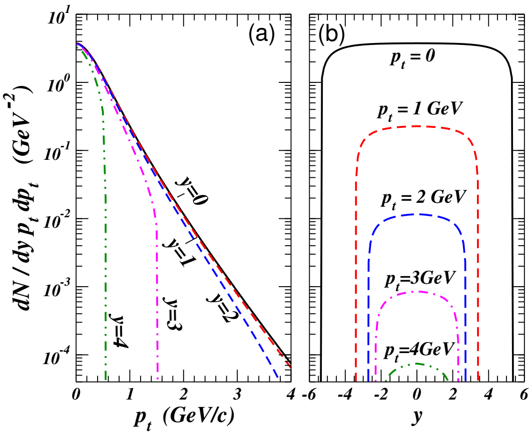

Figure 7.12: Rapidity dependence of the *Ridge* yield in the Momentum Kick Model [159].

for testing the Momentum Kick Model. The PHOBOS measurement [76] extends to $\Delta\eta = 4$, however, there is no measurement of $p_T^{associated}$ and the lower limit on $p_T^{associated}$ is determined by the acceptance of the detector. This lower limit is around 35 MeV/c so this measurement cannot exclude the Momentum Kick Model. STAR's acceptance is limited in rapidity, although higher statistics data sets may allow a high enough $p_T^{associated}$ to test the prediction in Figure 7.12.

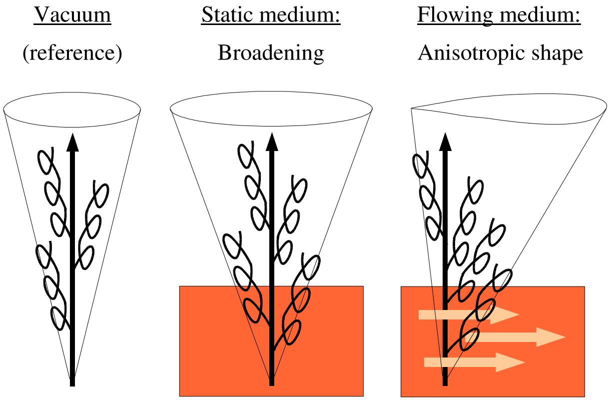

Figure 7.13: *Ridge* production through radiated gluons broadened by transverse flow [65]

Bremsstrahlung gluons broadened by medium interactions

The hard partons which fragment into jets may emit bremsstrahlung gluons. It is hypothesized in [65] that the *Ridge* is the result of gluon bremsstrahlung in the medium broadened by transverse flow, as depicted schematically in Figure 7.13. This model describes moderate broadening of the jet-like correlation in $\Delta\eta$, however, it has difficulty with producing a structure as broad in $\Delta\eta$ as the *Ridge*. The calculations in [65] predict a *Ridge* which is only about 10% broader in $\Delta\eta$ than the jet-like correlation.

The formation of the *Ridge* from bremsstrahlung gluons is also hypothesized in [160], however, in this model the gluons are broadened by strong, turbulent color fields. These strong color fields are predicted to be produced in response to plasma instabilities. If such fields exist, they would deflect brehmstralung gluons. Figure 7.14 shows the broadening predicted in [160] for two different jet energies; the structure in these figures is not broad enough to be consistent with the data.

7.2.2 Discussion

Data on the *Ridge* is extensive and there are several observations which may be key to distinguishing production mechanisms for the *Ridge*:

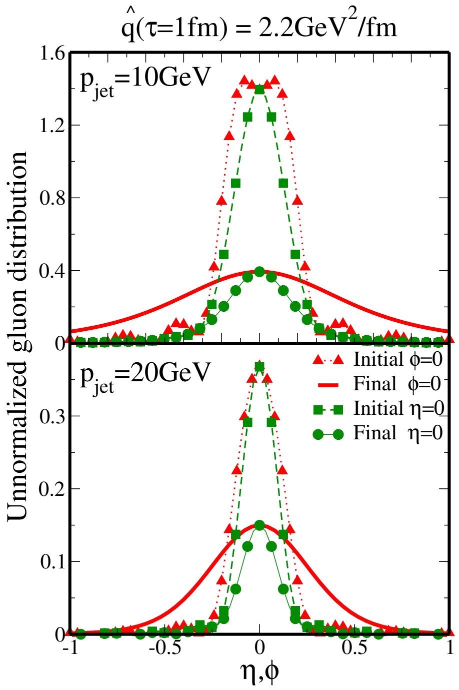

Figure 7.14: Broadening of the jet-like correlation from plasma instabilities for two different jet energies [160]. $\Delta\phi$ is in radians.

1. **The jet-like correlation is not substantially modified.** Section 7.1 discusses the overwhelming evidence that the jet-like correlation is produced dominantly by vacuum fragmentation. This means that the production of the *Ridge* must not substantially modify the jet-like correlation.

2. **The particle ratios in the *Ridge* are comparable to those in the bulk.** Figure 2.11 and Figure 7.1 demonstrate that the *Ridge* has a particle composition similar to the bulk. By contrast, the jet-like correlation has a particle composition similar to what would be expected from vacuum fragmentation.

3. **The *Ridge* is larger in collisions at $\sqrt{s_{NN}}$ = 200 GeV than at $\sqrt{s_{NN}}$ = 62 GeV.** This is shown in Figure 6.10.

4. **The *Ridge* is larger in plane than out of plane.** This is shown in Figure 2.12. This corresponds to a larger *Ridge* when the path length traveled by a parton through the medium would be lower on average.

5. **There is either no dependence on the trigger particle or a larger *Ridge* for a heavier trigger particle.** Figure 6.12 shows the dependence of the *Ridge* on N_{part} for different trigger particle species. It is unclear how correlated the systematic errors due to v_2 are so it is difficult to conclusively say that there is mass dependence. However, if the systematic errors are correlated, then the *Ridge* is larger for Λ trigger particles than for unidentified trigger particles and it is smaller for K^0_S trigger particles than for an unidentified trigger particles. Figure 2.11 shows that in the kinematic range of the trigger particle there are roughly as many protons as pions. Since protons and pions are the most abundant particles, this means that the unidentified hadron trigger particles are roughly 50% protons and roughly 50% pions, making the average mass for unidentified triggers between the Λ mass and the K^0_S mass. This means that if the systematic errors in Figure 6.12 are correlated, the *Ridge* is larger for heavier trigger particles. A smaller *Ridge* for heavier trigger particles is strongly disfavored by the data.

6. **The *Ridge* is broad in $\Delta\eta$.** The *Ridge* is roughly independent of $\Delta\eta$ within the STAR acceptance. There is some room for a slight $\Delta\eta$ dependence, but there cannot be a strong dependence on $\Delta\eta$. The PHOBOS measurement [76] demonstrated that the *Ridge* extends to $\Delta\eta = 4$, however, the associated particles were determined from single hits, so the kinematic reach was limited by the acceptance of the detector. This limit is about $p_T > 35$ MeV/c. The extent of the *Ridge* may cause some problems for causal models because a parton at midrapidity has to affect particles separated by a large gap in $\Delta\eta$.

Radial flow plus trigger bias mechanism and related models

The Glasma Flux Tube model and the Correlated Emission Model both primarily produce the *Ridge* using the radial flow plus trigger bias mechanism. The radial flow plus trigger bias mechanism naturally leads to agreement with many of the experimental observations. Because hard partons fragment as in a vacuum in the PGV and Shuryak calculations, these models do not modify the jet-like correlation, in agreement with observation 1. The Recombination model by Hwa may lead to some modification of the jet-like correlation because some of the jet-like correlation could come from recombination of shower and thermal partons rather than vacuum fragmentation. A calculation needs to be done in this framework to ensure that the Recombination model is consistent with observation 1. In all models, particles in the *Ridge* come from the bulk, in agreement with observation 2. Assuming that the reaction plane dependence calculated in the Correlated Emission Model [156] is a common feature of the radial flow plus trigger bias mechanism, these models are also in agreement with observation 4. The *Ridge* would also be expected to have roughly the same extent in $\Delta\eta$ as inclusive particles, in agreement with observation 6.

It is not clear whether the energy dependence (observation 3) is consistent with this model but the energy dependence would be readily calculated in the same way as done by PGV [146]. The amount of radial flow can be determined by comparisons with the inclusive spectra. As shown in Figure 1.16 for v_2, lighter particles are affected more by hydrodynamical flow. If these models are dependent on a velocity boost for the surface bias of the hard parton, then a dependence on the mass of the trigger particle should be observed and lighter trigger particles should correspond to a larger *Ridge*. This contradicts observation 5. This means that if the radial flow plus trigger bias mechanism is the proper mechanism for producing the *Ridge*, the surface bias of the hard partons likely does not come from radial flow but from jet quenching.

The Momentum Kick Model

In the Momentum Kick Model the jet-like correlation is produced by vacuum fragmentation of the parton after it interacts with the medium. The jet-like correlation is not affected, in agreement with observation 1. The *Ridge* is created by medium partons so naturally has the same composition as the bulk, in agreement with observation 2. As shown in Figure 7.11, the Momentum Kick Model describes the energy dependence of the *Ridge*, in agreement with observation 3. No calculations have been made for the dependence of the *Ridge* on trigger particle type, so it is unclear if this model is consistent with observation 5.

Naively the larger path length out of plane would lead to a larger *Ridge*, in contradiction to observation 4. It may be possible to reconcile this with the data if the parton loses so much energy when it travels out of plane that it is not observed. In that case only jets from the surface would be observed out of plane. The reaction plane dependence of the *Ridge* in the Momentum Kick Model has not been calculated yet.

The Momentum Kick Model is the only causal model that produces a *Ridge* broad enough to be consistent with the data, in agreement with observation 6. However, this model also has a sharp drop just outside of reach of current measurements. This unusual feature, if observed, would be one signature that the Momentum Kick Model is the correct mechanism for the production of the *Ridge*.

Gluon Bremsstrahlung Models

In gluon bremsstrahlung models, the hard parton fragments in the vacuum after having emitted bremsstrahlung gluons, in agreement with observation 1. In these models, the *Ridge* would come from the fragmentation of gluons, which would naively seem to contradict observation 2, that the *Ridge* composition is similar to the bulk. If the bremsstrahlung gluons are sufficiently soft that they reinteract with the medium, this may be able to be reconciled with the data. No calculation of the collision energy dependence has been done, however, the expectations from these models seem to be consistent with observation 3. These models seem to have the same contradiction with observation 4 that the Momentum Kick Model does, that naively the larger path length out of plane would lead to a larger *Ridge*. If heavier trigger particles correspond on average to heavier partons, then lighter trigger particles should produce a larger *Ridge* because the amount of bremsstrahlung is proportional to m^{-4}. This is in contradiction to observation 5. These models also have difficulty producing a *Ridge* broad enough in pseudorapidity to match the data, in contradiction to observation 6.

7.2.3 Summary

The origin of the *Ridge* is not yet conclusive. More quantitative theoretical calculations are needed in order to compare the data with the models. Gluon bremsstrahlung models are likely excluded by the data because they are apparently in contradiction with the observations on the reaction plane dependence of the *Ridge*, the trigger particle type dependence of the *Ridge*, and the extent of the *Ridge* in $\Delta\eta$. This does not mean that these mechanisms do not modify hadron fragmentation in heavy ion collisions, only that they are not likely to be the cause of the *Ridge*. Indeed, gluon bremsstrahlung could cause the observed broadening of the jet-like correlation in central $Au + Au$ collisions at $\sqrt{s_{NN}} = 200$ GeV.

The Momentum Kick Model is consistent with the data so far. A calculation of the reaction plane dependence is crucial to determine if this model is in agreement with the data. Measurements which would test the prediction of a sharp drop of the *Ridge* with $\Delta\eta$ are also crucial.

Models which rely on the radial flow plus trigger bias mechanism qualitatively agree with the data. More precise calculations are needed. Radial flow plus trigger bias would be the simplest mechanism to describe the *Ridge* since hydrodynamics describes the azimuthal asymmetry of particles produced in heavy ion collisions and radial flow has been observed in the inclusive spectra of particles. If the radial flow plus trigger bias model is sufficient to explain the data, there is no need for more complicated, speculative mechanisms to produce the *Ridge*. The significance of the *Ridge* in such a scenario would be that it would show up as a background in methods such as jet reconstruction and it is vital to understand how this background would affect reconstructed jets. It also may be possible to learn something quantitative about radial flow from the *Ridge*; more theoretical developments along these lines would be necessary to determine if this is possible.

Chapter 8

Conclusions and outlook

The data in this thesis, combined with the data available from previous studies, demonstrate that the jet-like correlation is produced dominantly by fragmentation. These data are described well both qualitatively and quantitatively by PYTHIA, making the jet-like correlation one of the best understood features in heavy ion collisions. The small deviations of the jet-like correlation in different collision systems indicate modifications of the jet-like correlation. The jet-like correlation can be used to determine how kinematic cuts affect the sample of jets leading to di-hadron correlations and can therefore be used as a tool to study both the away-side of di-hadron correlations and the *Ridge*.

These studies are in the momentum regime where the baryon to meson ratio is greatest, as shown in Figure 1.19, which led to the hypothesis that partons do not hadronize by the same mechanism in $A + A$ collisions as in $p + p$ collisions but rather hadronized via Recombination. Recombination proposes that the dominant production for hadrons at intermediate p_T (2-6 GeV/c) is by the combination of quarks from the medium. The data presented here indicate that hadrons at $p_T \approx 3$ GeV/c in $A + A$ collisions are as likely to be produced from vacuum fragmentation as hadrons at $p_T \approx 3$ GeV/c in $p + p$ collisions. If partons hadronize through a different mechanism in $A+A$ collisions than in $p+p$ collisions, the jet-like correlation should be affected. A 3 GeV/c hadron formed through Recombination naively would not have a jet-like correlation associated with it. If there were some combination of

Recombination and vacuum, there would be more trigger particles at 3 GeV/c but the same number of associated particles. This would make the jet-like yield smaller, the opposite of what is observed in the data. It is not clear how to reconcile these two pictures.

The interpretation of the *Ridge* is less conclusive, in large part because theoretical models are still not well developed. There are many proposed mechanisms for the production of the *Ridge*, however, so far there are few quantitative comparisons. Models for the production of the *Ridge* through partonic energy loss via gluon brehmstrahlung have difficulty producing a *Ridge* wide enough in $\Delta\eta$ to be in agreement with the data. The Momentum Kick Model, a model for the production of the *Ridge* through partonic energy loss via collisions, may have difficulty with the reaction plane dependence. All causal models may have difficulty with the extent of the *Ridge* in $\Delta\eta$. Most non-causal models rely heavily on the same mechanism, radial flow plus trigger bias, for the production of the *Ridge*. The radial flow plus trigger bias mechanism would not require any new speculative mechanisms and these models qualitatively reproduce many of the features of the data from central $Au+Au$ collisions at $\sqrt{s_{NN}}$ = 200 GeV. However, none of the calculations to date have been complete enough to conclusively determine that this is the mechanism that produces the *Ridge*. If the *Ridge* is produced by radial flow plus trigger bias, this would support the description of the medium as a fluid since it would be another indication of the collective flow of partons. Further theoretical studies are needed to test these mechanisms and, if the *Ridge* is produced by radial flow, to determine if the *Ridge* can be used to better understand radial flow.

8.1 Future measurements

8.1.1 Studies at $\sqrt{s_{NN}} = 200$ GeV

The STAR detector has been upgraded to include a Time of Flight (TOF) detector, with most of this detector already installed for the 2009 $p+p$ run. This will provide better particle identification over a wider p_T range and therefore improve the measurements of the particle ratios in the *Ridge* and the jet-like correlations. As shown in Figure 3.9, particle identification using dE/dx in the TPC is difficult for momenta greater than 1 GeV/c. Particle identification in the relativistic rise region is only possible for momenta above 2.5 GeV/c. The TOF is capable of particle identification in the region that the TPC is not, as shown in the time of flight verses the momentum as measured by the TOF in the 2009 $p+p$ run in Figure 8.1. This will also aid in the efficient identification of Ω triggers for future studies since pions misidentified as kaons make significant contributions to the background of the Ω mass peak. Studies of the *Ridge* with higher mass trigger particles could provide crucial tests of the radial flow plus trigger bias model. In addition, there have been substantial improvements in the use of the calorimeters in STAR for triggering both on high-p_T particles and on jets. The current luminosity is substantially higher than in the year 4 $Au+Au$ run. Measurements are currently limited at high-p_T by the cross section and the improved triggering capacity of STAR will allow measurements at higher $p_T^{trigger}$. The electromagnetic calorimeter can trigger on events with large deposits of energy in the calorimeter, mostly from electrons, π^0 and γ. This will enable studies of whether there is a *Ridge* with a direct photon trigger, a measurement which may give insight into the production mechanism of the *Ridge*.

The largest development in studies of jets in heavy ion collisions has been jet reconstruction, as discussed in Chapter 2. Full jet reconstruction allows the determination of partonic energy and therefore allows more detailed measurements of partonic energy loss. Di-hadron correlations suffer from the ambiguity of whether or not a jet was formed and the large combinatorial background in di-hadron correlations comes from hadrons which were not formed in jets. This ambiguity is not an issue for fully reconstructed jets. The most obvious question is whether the *Ridge* is still evident when a jet is fully reconstructed, a measurement crucial for distinguishing between causal and non-causal production mechanisms for the *Ridge*. This measurement can be done using a reconstructed jet as a trigger and looking at the distribution of hadrons relative to the jet axis in $\Delta\phi$ and $\Delta\eta$.

Whether or not the *Ridge* should be considered part of the jet depends on whether

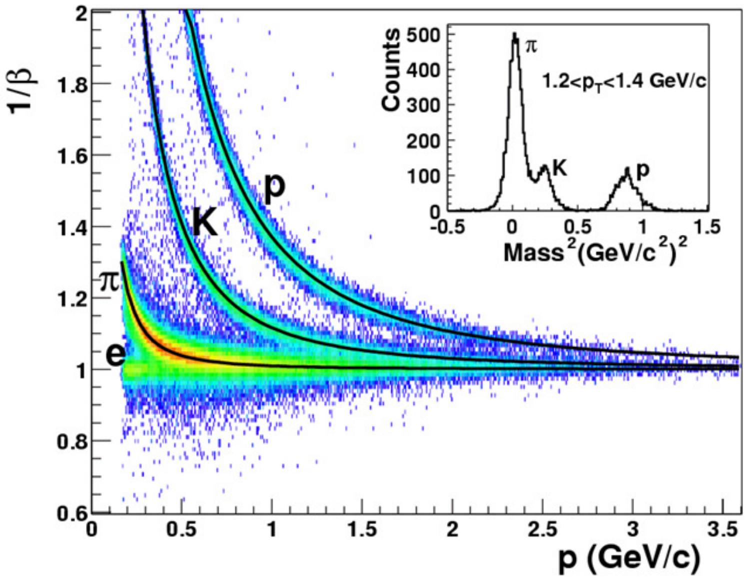

Figure 8.1: Separation of particles in STAR TOF using $\beta = \frac{v}{c}$ as a function of momentum. Data from run 9 [161].

it comes from energy loss or arises from a non-causal correlation with the trigger hadron. If the *Ridge* is produced by a mechanism such as radial flow plus trigger bias, then the particles in the *Ridge* should not be used in determining the jet energy since they do not result from the scattered parton. However, if the *Ridge* comes from a mechanism such as gluon brehmstrahlung or collisional energy loss of a hard parton, the energy in the *Ridge* comes from the parton.

If the *Ridge* is a background for jet reconstruction, it is important to understand how this contributes to the reconstructed jet energy. In many jet reconstruction methods, such as a cone algorithm, most of the *Ridge* would not be included in the reconstructed jet because hadrons in the jet are required to be within $(\Delta\phi^2 + \Delta\eta^2) < R_{max}$ with a typical $R_{max} \approx 0.4$ in heavy ion collisions [162]. If it is a background, a method needs to be developed to subtract it. If it is not a background but is from partonic energy loss, the energy in the *Ridge* needs to be quantified so it can be included in the jet energy.

8.1.2 Studies of the energy dependence

Future studies of the collision energy dependence of the *Ridge* will be possible at both RHIC and the Large Hadron Collider (LHC). The RHIC program will have a beam energy scan which will provide $Au + Au$ collisions from $\sqrt{s_{NN}}$ = 5 - 39 GeV in 2010. The LHC will provide $Pb + Pb$ collisions at 5.5 TeV, with the first heavy ion run scheduled in 2011.

RHIC beam energy scan

It is unclear theoretically whether or not a *Ridge* is expected at lower $\sqrt{s_{NN}}$. If the *Ridge* arises from partonic energy loss in the colored medium, it may only be present above the critical temperature. If the *Ridge* comes from radial flow plus trigger bias, there will be a *Ridge* if the medium is opaque enough to create a surface bias for the trigger particle and the medium is described well by hydrodynamics.

An estimate of the *Ridge* yield at lower energies can be made from a straightforward extrapolation of the data. Figure 6.11 showed that, at least for the kinematic cuts used in these studies, the Y_{Ridge}/Y_{Jet} ratio is the same for collisions at $\sqrt{s_{NN}}$ = 62 GeV and $\sqrt{s_{NN}}$ = 200 GeV. If this trend holds for lower collision energies, the *Ridge* should be 3-4 times as large as the jet-like correlation so if it is possible to measure the jet-like correlation, it will be possible to measure the *Ridge*.

PYTHIA studies were done to determine whether or not measurements of the *Ridge* will be feasible with the RHIC beam energy scan. PYTHIA provides a reasonable estimate of the jet-like correlation at lower energies since it describes the energy dependence well for comparisons of $\sqrt{s_{NN}}$ = 62 GeV to $\sqrt{s_{NN}}$ = 200 GeV. Whether or not the *Ridge* is present at lower energies, it is necessary to be able to measure the jet-like correlation in order to at least put an upper limit on the *Ridge* yield. PYTHIA 8.1 was used with the default parameters except that $\hat{p_{T}}_{min}$, the minimum momentum transfer in a two-to-two scattering process, was set to 0.1. PYTHIA 8.1 with these settings was found overestimate the jet-like yield, although it accurately describes the collision energy dependence of the jet-like yield. PYTHIA was used to determine the energy scaling of the jet-like yield.

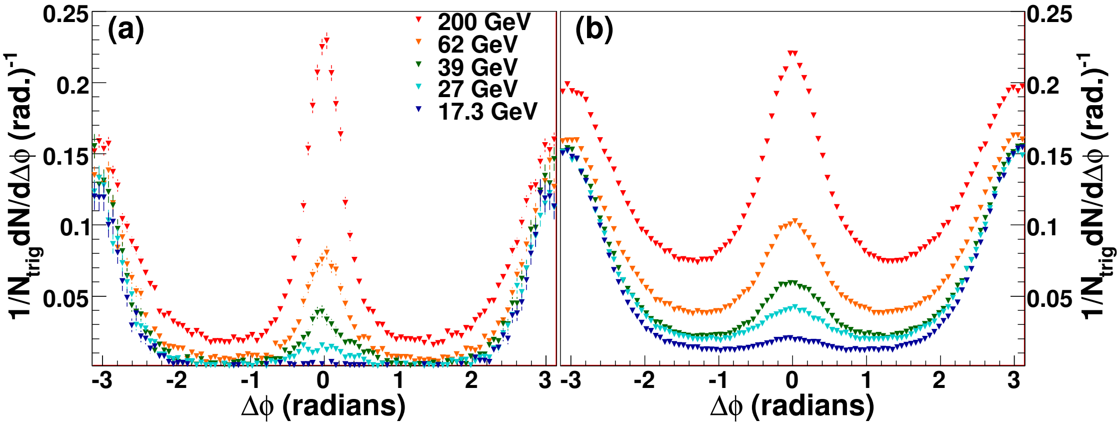

Figure 8.2: Di-hadron correlations in PYTHIA for RHIC beam energy scan energies using (a) 3.0 < $p_T^{trigger}$ < 6.0 GeV/c and 1.5 GeV/c < $p_T^{associated}$ < $p_T^{trigger}$ and (b) 2.0 < $p_T^{trigger}$ < 4.0 GeV/c and 1.0 < $p_T^{associated}$ < $p_T^{trigger}$ GeV/c.

These estimates were done for both the kinematic cuts used in this thesis, 3.0 < $p_T^{trigger}$ < 6.0 GeV/c and 1.5 GeV/c < $p_T^{associated}$ < $p_T^{trigger}$, and the kinematic cuts used by NA49 for di-hadron correlations at $\sqrt{s_{NN}} = 17.3$ GeV, 2.0 < $p_T^{trigger}$ < 4.0 GeV/c and 1.0 < $p_T^{associated}$ < $p_T^{trigger}$ GeV/c [163,164]. Lowering $p_T^{associated}$ and $p_T^{trigger}$ leads to higher statistics, however, this leads to a larger combinatorial background and therefore increases systematic errors. At higher energies this may make the systematic error too large to determine meaningful results.

Raw correlations in PYTHIA are shown in Figure 8.2. These results were used to extrapolate to the number of events needed at each of the proposed energies, given in Table 8.1 and compared to the proposed number of events. It was assumed that the statistical error bars could be at most twice what they are in $Au + Au$ collisions at $\sqrt{s_{NN}} = 62$ GeV. From these estimates, studies of the *Ridge* at $\sqrt{s_{NN}} = 39$ GeV and 27 GeV should be feasible. Studies at lower energies are unlikely.

These studies will also benefit from the TOF. EMCal triggering will not help studies of the *Ridge* because the proposed luminosities are low enough that STAR will record all collisions.

Table 8.1: Number of events proposed for the RHIC beam energy scan and the number of events needed for studies of the *Ridge* using STAR kinematic cuts (3.0 < $p_T^{trigger}$ < 6.0 GeV/c and 1.5 GeV/c < $p_T^{associated}$ < $p_T^{trigger}$) and NA49 kinematic cuts (2.0 < $p_T^{trigger}$ < 4.0 GeV/c and 1.0 < $p_T^{associated}$ < $p_T^{trigger}$ GeV/c). The current proposal for the beam energy scan includes $\sqrt{s_{NN}}$ = 5.0, 7.7, 11.5, 17.3, 27, and 39 GeV.

$\sqrt{s_{NN}}$	Proposed	STAR cuts	NA49 cuts
39 GeV	24M	6M	4.5M
27 GeV	33M	14M	8.8M
17.3 GeV	15M	103M	33M

At the LHC

Most models for the *Ridge* would qualitatively predict a *Ridge* at the LHC, however, no quantitative predictions of the *Ridge* at 5.5 TeV have been made. In causal models the *Ridge* would be expected to be the same size or larger because jet energies would be larger so the amount of energy lost by a hard parton would be at least as much as at RHIC energies. The size of the *Ridge* in models dependent on the radial flow plus trigger bias model depends on the amount of collective flow. If collective flow is larger at the LHC, the *Ridge* would also be expected to be bigger.

A straightforward extrapolation from the data at RHIC can provide estimates for the expectations for measurements of the *Ridge* at the LHC. If the trend observed in Figure 6.11 is also true at LHC energies, the Y_{Ridge}/Y_{Jet} ratio will be the same for the same kinematic cuts. The combinatorial background will be much larger at 5.5 TeV for 1.5 GeV/c < $p_T^{associated}$ < $p_T^{trigger}$ and 3.0 < $p_T^{trigger}$ < 6.0 GeV/c. The dominant systematic error at RHIC is due to v_2 subtraction, so measurements of the *Ridge* for the same kinematic cuts may be difficult if v_2 at the LHC is comparable to that at RHIC. The combinatorial background can be reduced by increasing $p_T^{trigger}$ and $p_T^{associated}$. Figure 6.1 shows that Y_{Jet} increases rapidly with $p_T^{trigger}$. Figure 2.8 shows that Y_{Ridge} is roughly independent of $p_T^{trigger}$. This means that increasing $p_T^{trigger}$ decreases Y_{Ridge}/Y_{Jet}. Figure 2.8 shows that the spectrum of particles in the *Ridge* is softer than those in Y_{Jet}. This means that increasing $p_T^{trigger}$ will also decrease Y_{Ridge}/Y_{Jet}. Measurements of the *Ridge* at the LHC may be difficult because of the large combinatorial background if these naive extrapolations of RHIC data are correct.

Appendix A

Terminology

Transverse momentum

Transverse momentum, p_T, is defined as the total momentum of a particle transverse to the beam:

$$p_T = \sqrt{p_x^2 + p_y^2} \tag{A.1}$$

where x and y are the coordinates in the plane transverse to the beam direction.

Transverse mass

Transverse mass, m_T, is defined as:

$$m_T = \sqrt{p_T^2 + m^2}. \tag{A.2}$$

Rapdity and pseudorapidity

Rapidity is defined as

$$y = \frac{1}{2} ln(\frac{E + p_z}{E - p_z}) \tag{A.3}$$

where z is the direction along the beam axis.
Pseudorapidity is defined as

$$\eta = -ln(tan(\frac{\theta}{2})) \tag{A.4}$$

where θ is the angle between the momentum of the particle and the beam axis. Note that both pseudorapidity and rapidity are unitless. Pseudorapdity is numerically

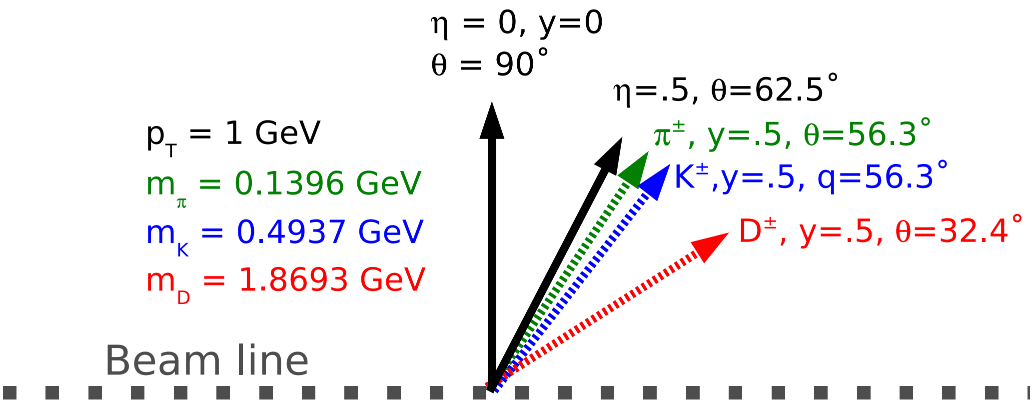

Figure A.1: Rapidity and pseudorapidity for different particle species

close to rapidity for light particles at midrapidity traveling near the speed of light. Figure A.1 shows the rapidity and pseudorapidity for particles with $p_T = 1$ GeV/c for particles with different masses. At y = 0, η = y. For a pion, y and η are almost the same, however, the difference is large for a heavy particle such as a D meson.

Appendix B

Geometric cuts

B.1 V^0 Geometric Cuts

Table B.1: Geometric cuts for Λ in $Cu + Cu$ collisions at $\sqrt{s_{NN}} = 200$ GeV. Cuts for $\bar{\Lambda}$ the same with cuts for the p daughter of the Λ applied to the $\bar{p}$ daughter of the $\bar{\Lambda}$ and cuts for the π^- daughter of the Λ applied to the π^+ daughter of the $\bar{\Lambda}$. These are in addition to cuts listed in Table 4.2. Primary vertex is abbreviated to PV.

	0-10%	10-20%	20-30%	30-40 %	40-50%	50-60%
0.4 GeV/c < p_T < 0.6 GeV/c						
Decay length (cm) >	7.5	7.5	7.5	7.5	7.5	7.5
DCA to PV (cm) <	0.8	0.8	0.8	0.8	0.8	0.8
DCA of daughters (cm) <	0.8	0.8	0.8	0.8	0.8	0.8
DCA of p to PV (cm) >	0.0	0.0	0.0	0.0	0.0	0.0
DCA of π^- to PV (cm) >	2.3	2.3	2.3	1.5	1.5	0.0
$n_{\sigma,dE/dx}$ of daughters <	2.0	2.0	2.0	2.0	2.0	2.0
| n_Γ from mass peak center | ¡	1.0	1.0	1.0	1.0	1.0	1.0
0.6 GeV/c < p_T < 0.8 GeV/c						
Decay length (cm) >	5.0	5.0	5.0	5.0	0.0	0.0
DCA to PV (cm) <	0.8	0.8	0.8	0.8	0.8	0.8
DCA of daughters (cm) <	0.8	0.8	0.8	0.8	0.8	0.8

Continued on next page

Table B.1 – continued from previous page

	0-10%	10-20%	20-30%	30-40 %	40-50%	50-60%
DCA of p to PV (cm) >	0.0	0.0	0.0	0.0	0.0	0.0
DCA of π^- to PV (cm) >	2.2	2.2	2.2	1.5	1.5	1.5
$n_{\sigma,dE/dx}$ of daughters <	2.0	2.0	2.0	2.0	2.0	2.0
| n_Γ from mass peak center | ¡	2.0	2.0	2.0	2.0	2.0	2.0
0.8 GeV/c < p_T < 1.0 GeV/c						
Decay length (cm) >	6.5	0.0	0.0	0.0	0.0	0.0
DCA to PV (cm) <	0.8	0.8	0.8	0.8	0.8	0.8
DCA of daughters (cm) <	0.8	0.8	0.8	0.8	0.8	0.8
DCA of p to PV (cm) >	0.0	0.0	0.0	0.0	0.0	0.0
DCA of π^- to PV (cm) >	1.4	1.5	1.5	1.1	1.1	0.0
$n_{\sigma,dE/dx}$ of daughters <	2.0	2.0	2.0	2.0	2.0	2.0
| n_Γ from mass peak center | ¡	2.0	2.0	2.0	2.0	2.0	2.0
1.0 GeV/c < p_T < 1.5 GeV/c						
Decay length (cm) >	6.5	5.5	5.5	3.5	3.5	7.5
DCA to PV (cm) <	0.7	0.8	0.8	0.8	0.8	0.8
DCA of daughters (cm) <	0.8	0.8	0.8	0.8	0.8	0.8
DCA of p to PV (cm) >	0.0	0.0	0.0	0.0	0.0	0.0
DCA of π^- to PV (cm) >	1.5	1.4	1.4	1.4	1.4	0.0
$n_{\sigma,dE/dx}$ of daughters <	2.5	2.5	2.5	2.5	2.5	2.5
| n_Γ from mass peak center | ¡	2.0	2.0	2.0	2.0	2.0	2.0
1.5 GeV/c < p_T < 2.0 GeV/c						
Decay length (cm) >	9.0	7.0	7.0	0.0	0.0	6.0
DCA to PV (cm) <	0.7	0.7	0.8	0.8	0.8	0.8
DCA of daughters (cm) <	0.8	0.8	0.8	0.8	0.8	0.8
DCA of p to PV (cm) >	0.0	0.0	0.0	0.0	0.0	0.0
DCA of π^- to PV (cm) >	1.4	1.5	1.5	1.4	1.4	0.0
$n_{\sigma,dE/dx}$ of daughters <	2.5	2.5	2.5	2.5	2.5	2.5
| n_Γ from mass peak center | ¡	2.0	2.0	2.0	2.0	2.0	2.0
2.0 GeV/c < p_T < 2.5 GeV/c						
Decay length (cm) >	7.0	5.5	5.5	7.5	0.0	0.0

Continued on next page

Table B.1 – continued from previous page

	0-10%	10-20%	20-30%	30-40 %	40-50%	50-60%
DCA to PV (cm) <	0.7	0.4	0.4	0.8	0.8	0.8
DCA of daughters (cm) <	0.8	0.8	0.8	0.8	0.8	0.8
DCA of p to PV (cm) >	0.0	0.0	0.0	0.0	0.0	0.0
DCA of π^- to PV (cm) >	1.7	1.4	1.4	1.4	1.4	1.6
$n_{\sigma,dE/dx}$ of daughters <	2.5	2.5	2.5	2.5	2.5	2.5
| n_Γ from mass peak center | ¡	2.0	2.0	2.0	2.0	2.0	2.0
2.5 GeV/c < p_T < 3.0 GeV/c						
Decay length (cm) >	15.0	11.0	12.0	11.0	12.0	0.0
DCA to PV (cm) <	0.5	0.8	0.8	0.8	0.8	0.8
DCA of daughters (cm) <	0.8	0.8	0.8	0.8	0.8	0.8
DCA of p to PV (cm) >	0.0	0.0	0.0	0.0	0.0	0.0
DCA of π^- to PV (cm) >	1.4	1.2	1.8	1.0	1.8	1.5
$n_{\sigma,dE/dx}$ of daughters <	2.5	2.5	2.5	2.5	2.5	2.5
| n_Γ from mass peak center | ¡	2.0	2.0	2.0	2.0	2.0	2.0
3.0 GeV/c < p_T < 3.5 GeV/c						
Decay length (cm) >	17.0	8.0	8.0	8.0	8.0	8.0
DCA to PV (cm) <	0.5	0.5	0.5	0.5	0.5	0.5
DCA of daughters (cm) <	0.8	0.8	0.8	0.8	0.8	0.8
DCA of p to PV (cm) >	0.0	0.0	0.0	0.0	0.0	0.0
DCA of π^- to PV (cm) >	1.7	1.6	1.6	1.2	1.2	0.6
$n_{\sigma,dE/dx}$ of daughters <	2.5	2.5	2.5	2.5	2.5	2.5
| n_Γ from mass peak center | ¡	2.0	2.0	2.0	2.0	2.0	2.0
3.5 GeV/c < p_T < 4.0 GeV/c						
Decay length (cm) >	13.0	13.0	13.0	13.0	13.0	13.0
DCA to PV (cm) <	0.4	0.4	0.4	0.4	0.4	0.4
DCA of daughters (cm) <	0.8	0.8	0.8	0.8	0.8	0.8
DCA of p to PV (cm) >	0.3	0.3	0.3	0.3	0.3	0.3
DCA of π^- to PV (cm) >	1.2	1.2	1.2	1.2	1.2	1.2
$n_{\sigma,dE/dx}$ of daughters <	2.5	2.5	2.5	2.5	2.5	2.5
| n_Γ from mass peak center | ¡	1.5	1.5	1.5	1.5	1.5	1.5

Continued on next page

Table B.1 – continued from previous page

	0-10%	10-20%	20-30%	30-40 %	40-50%	50-60%
4.0 GeV/c $< p_T <$ 5.0 GeV/c						
Decay length (cm) >	15.0	15.0	15.0	15.0	15.0	15.0
DCA to PV (cm) <	0.4	0.4	0.4	0.4	0.4	0.4
DCA of daughters (cm) <	0.8	0.8	0.8	0.8	0.8	0.8
DCA of p to PV (cm) >	0.3	0.3	0.3	0.3	0.3	0.3
DCA of π^- to PV (cm) >	1.2	1.2	1.2	1.2	1.2	1.2
$n_{\sigma,dE/dx}$ of daughters <	2.5	2.5	2.5	2.5	2.5	2.5
$\vert n_{\Gamma}$ from mass peak center $\vert$ ¡	1.5	1.5	1.5	1.5	1.5	1.5
5.0 GeV/c $< p_T <$ 10.0 GeV/c						
Decay length (cm) >	7.5	7.5	7.5	7.5	0.0	7.5
DCA to PV (cm) <	0.8	0.8	0.8	0.8	0.8	0.8
DCA of daughters (cm) <	0.8	0.8	0.8	0.8	0.8	0.8
DCA of p to PV (cm) >	1.5	1.5	1.5	1.5	1.5	3.0
DCA of π^- to PV (cm) >	1.5	1.5	1.5	1.5	0.0	1.5
$n_{\sigma,dE/dx}$ of daughters <	2.0	2.0	2.0	2.0	2.0	2.0
$\vert n_{\Gamma}$ from mass peak center $\vert$ ¡	1.5	1.5	1.5	1.5	1.5	1.5

Table B.2: Geometric cuts for K_S^0 in $Cu+Cu$ collisions at $\sqrt{s_{NN}} = 200$ GeV. These are in addition to cuts listed in Table 4.2. Primary vertex is abbreviated to PV.

	0-10%	10-20%	20-30%	30-40 %	40-50%	50-60%
0.4 GeV/c $< p_T <$ 0.6 GeV/c						
Decay length (cm) >	0.0	0.0	0.0	0.0	0.0	0.0
DCA to PV (cm) <	0.6	0.8	0.8	0.8	0.8	0.8
DCA of daughters (cm) <	0.8	0.8	0.8	0.8	0.8	0.8
DCA of π^-, π^+ to PV (cm) >	2.1	1.1	1.1	1.1	1.1	1.1
$n_{\sigma,dE/dx}$ of daughters <	2.0	2.0	2.0	2.0	2.0	2.0
$\vert n_{\Gamma}$ from mass peak center $\vert$ ¡	1.5	1.5	1.5	1.5	1.5	1.5

Continued on next page

Table B.2 – continued from previous page

	0-10%	10-20%	20-30%	30-40 %	40-50%	50-60%
0.6 GeV/c $< p_T <$ 0.8 GeV/c						
Decay length (cm) >	0.0	0.0	0.0	0.0	0.0	0.0
DCA to PV (cm) <	0.8	0.8	0.8	0.8	0.8	0.8
DCA of daughters (cm) <	0.8	0.8	0.8	0.8	0.8	0.8
DCA of π^-, π^+ to PV (cm) >	1.0	1.0	1.0	1.0	1.0	1.0
$n_{\sigma,dE/dx}$ of daughters <	2.0	2.0	2.0	2.0	2.0	2.0
| n_Γ from mass peak center | ¡	1.5	1.5	1.5	1.5	2.0	2.0
0.8 GeV/c $< p_T <$ 1.0 GeV/c						
Decay length (cm) >	0.0	0.0	0.0	0.0	0.0	0.0
DCA to PV (cm) <	0.8	0.8	0.8	0.8	0.8	0.8
DCA of daughters (cm) <	0.8	0.8	0.8	0.8	0.8	0.8
DCA of π^-, π^+ to PV (cm) >	0.9	0.9	0.9	0.9	0.9	0.9
$n_{\sigma,dE/dx}$ of daughters <	2.0	2.0	2.0	2.0	2.0	2.0
| n_Γ from mass peak center | ¡	1.5	1.5	1.5	2.0	2.0	2.0
1.0 GeV/c $< p_T <$ 1.5 GeV/c						
Decay length (cm) >	4.5	4.5	4.5	4.5	4.5	4.5
DCA to PV (cm) <	0.6	0.6	0.6	0.8	0.8	0.8
DCA of daughters (cm) <	0.8	0.8	0.8	0.8	0.8	0.8
DCA of π^-, π^+ to PV (cm) >	0.9	0.9	0.9	0.9	0.9	0.9
$n_{\sigma,dE/dx}$ of daughters <	2.5	2.5	2.5	2.5	2.5	2.5
| n_Γ from mass peak center | ¡	1.5	1.5	1.5	1.5	1.5	2.0
1.5 GeV/c $< p_T <$ 2.0 GeV/c						
Decay length (cm) >	4.5	4.5	4.5	4.5	4.5	4.5
DCA to PV (cm) <	0.4	0.4	0.4	0.8	0.8	0.8
DCA of daughters (cm) <	0.8	0.8	0.8	0.8	0.8	0.8
DCA of π^-, π^+ to PV (cm) >	1.5	1.5	1.5	1.2	1.1	0.0
$n_{\sigma,dE/dx}$ of daughters <	2.5	2.5	2.5	2.5	2.5	2.5
| n_Γ from mass peak center | ¡	1.5	2.0	2.0	1.5	1.5	1.5
2.0 GeV/c $< p_T <$ 2.5 GeV/c						
Decay length (cm) >	0.0	0.0	0.0	0.0	0.0	0.0

Continued on next page

Table B.2 – continued from previous page

	0-10%	10-20%	20-30%	30-40 %	40-50%	50-60%
DCA to PV (cm) $<$	0.4	0.4	0.4	0.8	0.8	0.8
DCA of daughters (cm) $<$	0.8	0.8	0.8	0.8	0.8	0.8
DCA of π^-, π^+ to PV (cm) $>$	1.6	1.4	1.4	1.4	1.1	1.1
$n_{\sigma,dE/dx}$ of daughters $<$	2.5	2.5	2.5	2.5	2.5	2.5
$\vert$ n_Γ from mass peak center $\vert$ ¡	1.5	2.0	2.0	1.5	1.5	1.5
2.5 GeV/c $< p_T <$ 3.0 GeV/c						
Decay length (cm) $>$	0.0	0.0	0.0	0.0	0.0	0.0
DCA to PV (cm) $<$	0.4	0.4	0.4	0.4	0.4	0.4
DCA of daughters (cm) $<$	0.8	0.8	0.8	0.8	0.8	0.8
DCA of π^-, π^+ to PV (cm) $>$	1.2	1.2	1.0	0.0	0.0	0.0
$n_{\sigma,dE/dx}$ of daughters $<$	2.5	2.5	2.5	2.5	2.5	2.5
$\vert$ n_Γ from mass peak center $\vert$ ¡	1.5	2.0	2.0	1.5	2.0	2.0
3.0 GeV/c $< p_T <$ 3.5 GeV/c						
Decay length (cm) $>$	0.0	0.0	0.0	0.0	0.0	0.0
DCA to PV (cm) $<$	0.4	0.4	0.4	0.5	0.5	0.5
DCA of daughters (cm) $<$	0.8	0.8	0.8	0.8	0.8	0.8
DCA of π^-, π^+ to PV (cm) $>$	0.8	0.8	0.8	0.8	0.8	0.8
$n_{\sigma,dE/dx}$ of daughters $<$	2.5	2.5	2.5	2.5	2.5	2.5
$\vert$ n_Γ from mass peak center $\vert$ ¡	1.5	1.5	1.5	1.5	1.5	2.0
3.5 GeV/c $< p_T <$ 4.0 GeV/c						
Decay length (cm) $>$	0.0	0.0	0.0	0.0	0.0	0.0
DCA to PV (cm) $<$	0.4	0.4	0.4	0.4	0.4	0.4
DCA of daughters (cm) $<$	0.8	0.8	0.8	0.8	0.8	0.8
DCA of π^-, π^+ to PV (cm) $>$	0.8	0.8	0.6	0.6	0.6	0.6
$n_{\sigma,dE/dx}$ of daughters $<$	2.5	2.5	2.5	2.5	2.5	2.5
$\vert$ n_Γ from mass peak center $\vert$ ¡	1.5	1.5	1.5	1.5	1.5	1.5
4.0 GeV/c $< p_T <$ 5.0 GeV/c						
Decay length (cm) $>$	0.0	0.0	0.0	0.0	0.0	0.0
DCA to PV (cm) $<$	0.4	0.4	0.4	0.4	0.4	0.4
DCA of daughters (cm) $<$	0.8	0.8	0.8	0.8	0.8	0.8

Continued on next page

Table B.2 – continued from previous page

	0-10%	10-20%	20-30%	30-40 %	40-50%	50-60%
DCA of π^-, π^+ to PV (cm) $>$	0.8	0.8	0.6	0.6	0.6	0.6
$n_{\sigma,dE/dx}$ of daughters $<$	2.5	2.5	2.5	2.5	2.5	2.5
$\mid n_\Gamma$ from mass peak center $\mid$ ¡	2.0	2.0	2.0	2.0	2.0	2.0
5.0 GeV/c $< p_T <$ 10.0 GeV/c						
Decay length (cm) $>$	0.0	0.0	0.0	0.0	0.0	0.2
DCA to PV (cm) $<$	0.4	0.4	0.6	0.6	0.8	1.5
DCA of daughters (cm) $<$	0.8	0.8	0.8	0.8	0.8	2.0
DCA of π^-, π^+ to PV (cm) $>$	1.4	1.4	1.4	1.4	1.4	1.5
$n_{\sigma,dE/dx}$ of daughters $<$	1.5	1.5	2.0	2.0	2.0	7.5
$\mid n_\Gamma$ from mass peak center $\mid$ ¡	2.0	2.0	2.0	2.0	2.0	0.0

B.2 Ξ^- Geometric Cuts

Table B.3: Geometric cuts for Ξ^- in $Cu+Cu$ collisions at $\sqrt{s_{NN}} = 200$ GeV. These are in addition to cuts listed in Table 4.4. Cuts for Ξ^+ the same with cuts for the p daughter of the Λ applied to the $\bar{p}$ daughter of the $\bar{\Lambda}$, cuts for the π^- daughter of the Λ applied to the π^+ daughter of the $\bar{\Lambda}$, and cuts for the Λ applied to the $\bar{\Lambda}$. A and B refer to the parameters in Equation 4.4. Primary vertex is abbreviated to PV.

	0-10%	10-20%	20-30%	30-40 %	40-50%	50-60%
0.6 GeV/c $< p_T <$0.8 GeV/c						
Ξ^- Decay length (cm)	> 3.5	> 3.5	> 3.5	> 3.5	> 3.5	> 3.5
Λ Decay length (cm)	> 0	> 0	> 0	> 0	> 0	> 0
DCA of Ξ^- to primary vertex (cm)	< 0.55	< 0.55	< 0.55	< 0.55	< 0.55	< 0.55
DCA of Λ to primary vertex (cm)	> 0.18	> 0.18	> 0.18	> 0.18	> 0.18	> 0.18
DCA of Ξ^- to daughters (cm)	< 0.6	< 0.6	< 0.6	< 0.6	< 0.6	< 0.6
DCA of Λ to daughters (cm)	< 0.8	< 0.8	< 0.8	< 0.8	< 0.8	< 0.8
DCA of p to PV (cm)	> 0	> 0	> 0	> 0	> 0	> 0

Continued on next page

Table B.3 – continued from previous page

	0-10%	10-20%	20-30%	30-40 %	40-50%	50-60%
DCA of π^- to PV (cm)	> 0	> 0	> 0	> 0	> 0	> 0
DCA of bachelor π^- to PV (cm)	> 0	> 0	> 0	> 0	> 0	> 0
$n_{\sigma,dE/dx}$ of daughters	> 3	> 3	> 3	> 3	> 3	> 3
$\mid n_\Gamma$ from mass peak center $\mid$	> 1.5	> 1.5	> 2	> 2	> 2	> 2
A	1.8333	1.8333	1.8333	1.8333	1.3333	1.8333
B	-0.03	-0.03	-0.03	-0.05	-0.37	-0.06
0.8 GeV/c $< p_T <$1 GeV/c						
Ξ^- Decay length (cm)	> 3.5	> 3.5	> 3.5	> 3.5	> 3.5	> 3.5
Λ Decay length (cm)	> 0	> 0	> 0	> 0	> 0	> 0
DCA of Ξ^- to primary vertex (cm)	< 0.55	< 0.55	< 0.55	< 0.55	< 0.55	< 0.55
DCA of Λ to primary vertex (cm)	> 0.18	> 0.18	> 0.18	> 0.18	> 0.18	> 0.18
DCA of Ξ^- to daughters (cm)	< 0.6	< 0.6	< 0.6	< 0.6	< 0.6	< 0.6
DCA of Λ to daughters (cm)	< 0.8	< 0.8	< 0.8	< 0.8	< 0.8	< 0.8
DCA of p to PV (cm)	> 0	> 0	> 0	> 0	> 0	> 0
DCA of π^- to PV (cm)	> 0	> 0	> 0	> 0	> 0	> 0
DCA of bachelor π^- to PV (cm)	> 0	> 0	> 0	> 0	> 0	> 0
$n_{\sigma,dE/dx}$ of daughters	> 3	> 3	> 3	> 3	> 3	> 3
$\mid n_\Gamma$ from mass peak center $\mid$	> 1.5	> 1.5	> 2	> 2	> 2	> 2
A	1.8333	1.8333	1.8333	1.3333	N/A	1.8333
B	-0.2	-0.2	-0.2	-1000	N/A	-0.06
1 GeV/c $< p_T <$1.5 GeV/c						
Ξ^- Decay length (cm)	> 3.5	> 3.5	> 3.5	> 3.5	> 3.5	> 3.5
Λ Decay length (cm)	> 0	> 0	> 0	> 0	> 0	> 0
DCA of Ξ^- to primary vertex (cm)	< 0.55	< 0.55	< 0.55	< 0.55	< 0.55	< 0.55
DCA of Λ to primary vertex (cm)	> 0.18	> 0.18	> 0.18	> 0.18	> 0.18	> 0.18
DCA of Ξ^- to daughters (cm)	< 0.6	< 0.6	< 0.6	< 0.6	< 0.6	< 0.6
DCA of Λ to daughters (cm)	< 0.8	< 0.8	< 0.8	< 0.8	< 0.8	< 0.8
DCA of p to PV (cm)	> 0	> 0	> 0	> 0	> 0	> 0
DCA of π^- to PV (cm)	> 0	> 0	> 0	> 0	> 0	> 0
DCA of bachelor π^- to PV (cm)	> 0	> 0	> 0	> 0	> 0	> 0

Continued on next page

Table B.3 – continued from previous page

	0-10%	10-20%	20-30%	30-40 %	40-50%	50-60%
$n_{\sigma,dE/dx}$ of daughters	> 3	> 3	> 3	> 3	> 3	> 3
$\mid n_\Gamma$ from mass peak center $\mid$	> 1.5	> 1.5	> 2	> 2	> 2	> 2
A	1.3333	1.3333	1.3333	N/A	N/A	1.8333
B	-0.35	-0.35	-0.35	N/A	N/A	-0.06
1.5 GeV/c $< p_T <$2 GeV/c						
Ξ^- Decay length (cm)	> 3.5	> 3.5	> 3.5	> 3.5	> 3.5	> 3.5
Λ Decay length (cm)	> 0	> 0	> 0	> 0	> 0	> 0
DCA of Ξ^- to primary vertex (cm)	< 0.55	< 0.55	< 0.55	< 0.55	< 0.55	< 0.55
DCA of Λ to primary vertex (cm)	> 0.18	> 0.18	> 0.18	> 0.18	> 0.18	> 0.18
DCA of Ξ^- to daughters (cm)	< 0.6	< 0.6	< 0.6	< 0.6	< 0.6	< 0.6
DCA of Λ to daughters (cm)	< 0.8	< 0.8	< 0.8	< 0.8	< 0.8	< 0.8
DCA of p to PV (cm)	> 0	> 0	> 0	> 0	> 0	> 0
DCA of π^- to PV (cm)	> 0	> 0	> 0	> 0	> 0	> 0
DCA of bachelor π^- to PV (cm)	> 0	> 0	> 0	> 0	> 0	> 0
$n_{\sigma,dE/dx}$ of daughters	> 3	> 3	> 3	> 3	> 3	> 3
$\mid n_\Gamma$ from mass peak center $\mid$	> 1.5	> 1.5	> 2	> 2	> 2	> 2
A	1.3333	1.3333	1.3333	N/A	N/A	1.8333
B	-0.4	-0.4	-0.4	N/A	N/A	-0.06
2 GeV/c $< p_T <$2.5 GeV/c						
Ξ^- Decay length (cm)	> 3.5	> 3.5	> 3.5	> 3.5	> 3.5	> 3.5
Λ Decay length (cm)	> 0	> 0	> 0	> 0	> 0	> 0
DCA of Ξ^- to primary vertex (cm)	< 0.55	< 0.55	< 0.55	< 0.55	< 0.55	< 0.55
DCA of Λ to primary vertex (cm)	> 0.18	> 0.18	> 0.18	> 0.18	> 0.18	> 0.18
DCA of Ξ^- to daughters (cm)	< 0.6	< 0.6	< 0.6	< 0.6	< 0.6	< 0.6
DCA of Λ to daughters (cm)	< 0.8	< 0.8	< 0.8	< 0.8	< 0.8	< 0.8
DCA of p to PV (cm)	> 0	> 0	> 0	> 0	> 0	> 0
DCA of π^- to PV (cm)	> 0	> 0	> 0	> 0	> 0	> 0
DCA of bachelor π^- to PV (cm)	> 0	> 0	> 0	> 0	> 0	> 0
$n_{\sigma,dE/dx}$ of daughters	> 3	> 3	> 3	> 3	> 3	> 3
$\mid n_\Gamma$ from mass peak center $\mid$	> 1.5	> 1.5	> 2	> 2	> 2	> 2

Continued on next page

Table B.3 – continued from previous page

	0-10%	10-20%	20-30%	30-40 %	40-50%	50-60%
A	1.8333	1.8333	1.8333	1.3333	1.8333	1.8333
B	0.05	0.05	0.05	0	-0.06	0
2.5 GeV/c $< p_T <$3 GeV/c						
Ξ^- Decay length (cm)	> 3	> 3	> 3	> 3	> 3	> 3
Λ Decay length (cm)	> 0	> 0	> 0	> 0	> 0	> 0
DCA of Ξ^- to primary vertex (cm)	< 0.45	< 0.45	< 0.45	< 0.45	< 0.45	< 0.45
DCA of Λ to primary vertex (cm)	> 0.1	> 0.1	> 0.1	> 0.1	> 0.1	> 0.1
DCA of Ξ^- to daughters (cm)	< 0.45	< 0.45	< 0.45	< 0.45	< 0.45	< 0.45
DCA of Λ to daughters (cm)	< 0.8	< 0.8	< 0.8	< 0.8	< 0.8	< 0.8
DCA of p to PV (cm)	> 0	> 0	> 0	> 0	> 0	> 0
DCA of π^- to PV (cm)	> 0	> 0	> 0	> 0	> 0	> 0
DCA of bachelor π^- to PV (cm)	> 0	> 0	> 0	> 0	> 0	> 0
$n_{\sigma,dE/dx}$ of daughters	> 3	> 3	> 3	> 3	> 3	> 3
$\mid n_\Gamma$ from mass peak center $\mid$	> 1.5	> 1.5	> 2	> 2	> 2	> 2
A	1.8333	1.8333	1.8333	1.3333	1.8333	1.8333
B	0	0	0.05	0	-0.06	0
3 GeV/c $< p_T <$3.5 GeV/c						
Ξ^- Decay length (cm)	> 0	> 0	> 0	> 0	> 0	> 0
Λ Decay length (cm)	> 0	> 0	> 0	> 0	> 0	> 0
DCA of Ξ^- to primary vertex (cm)	< 0.8	< 0.8	< 0.8	< 0.8	< 0.8	< 0.8
DCA of Λ to primary vertex (cm)	> 0	> 0	> 0	> 0	> 0	> 0
DCA of Ξ^- to daughters (cm)	< 0.8	< 0.8	< 0.8	< 0.8	< 0.8	< 0.8
DCA of Λ to daughters (cm)	< 0.8	< 0.8	< 0.8	< 0.8	< 0.8	< 0.8
DCA of p to PV (cm)	> 0	> 0	> 0	> 0	> 0	> 0
DCA of π^- to PV (cm)	> 0	> 0	> 0	> 0	> 0	> 0
DCA of bachelor π^- to PV (cm)	> 0	> 0	> 0	> 0	> 0	> 0
$n_{\sigma,dE/dx}$ of daughters	> 3	> 3	> 3	> 3	> 3	> 3
$\mid n_\Gamma$ from mass peak center $\mid$	> 2	> 2	> 2	> 2	> 2	> 2
A	1.8333	1.8333	1.8333	1.3333	1.8333	1.8333
B	-0.03	-0.03	-0.05	-0.37	-0.06	0

Continued on next page

Table B.3 – continued from previous page

	0-10%	10-20%	20-30%	30-40 %	40-50%	50-60%
3.5 GeV/c < p_T <4.5 GeV/c						
Ξ^- Decay length (cm)	> 0	> 0	> 0	> 0	> 0	> 0
Λ Decay length (cm)	> 0	> 0	> 0	> 0	> 0	> 0
DCA of Ξ^- to primary vertex (cm)	< 0.8	< 0.8	< 0.8	< 0.8	< 0.8	< 0.8
DCA of Λ to primary vertex (cm)	> 0	> 0	> 0	> 0	> 0	> 0
DCA of Ξ^- to daughters (cm)	< 0.8	< 0.8	< 0.8	< 0.8	< 0.8	< 0.8
DCA of Λ to daughters (cm)	< 0.8	< 0.8	< 0.8	< 0.8	< 0.8	< 0.8
DCA of p to PV (cm)	> 0	> 0	> 0	> 0	> 0	> 0
DCA of π^- to PV (cm)	> 0	> 0	> 0	> 0	> 0	> 0
DCA of bachelor π^- to PV (cm)	> 0	> 0	> 0	> 0	> 0	> 0
$n_{\sigma,dE/dx}$ of daughters	> 3	> 3	> 3	> 3	> 3	> 3
$\mid n_\Gamma$ from mass peak center $\mid$	> 2	> 2	> 2	> 2	> 2	> 2
A	1.8333	1.8333	1.3333	N/A	1.8333	N/A
B	-0.2	-0.2	-1000	N/A	-0.06	N/A
p_T >4.5 GeV/c						
Ξ^- Decay length (cm)	> 0	> 0	> 0	> 0	> 0	> 0
Λ Decay length (cm)	> 0	> 0	> 0	> 0	> 0	> 0
DCA of Ξ^- to primary vertex (cm)	< 0.8	< 0.8	< 0.8	< 0.8	< 0.8	< 0.8
DCA of Λ to primary vertex (cm)	> 0	> 0	> 0	> 0	> 0	> 0
DCA of Ξ^- to daughters (cm)	< 0.8	< 0.8	< 0.8	< 0.8	< 0.8	< 0.8
DCA of Λ to daughters (cm)	< 0.8	< 0.8	< 0.8	< 0.8	< 0.8	< 0.8
DCA of p to PV (cm)	> 0	> 0	> 0	> 0	> 0	> 0
DCA of π^- to PV (cm)	> 0	> 0	> 0	> 0	> 0	> 0
DCA of bachelor π^- to PV (cm)	> 0	> 0	> 0	> 0	> 0	> 0
$n_{\sigma,dE/dx}$ of daughters	> 3	> 3	> 3	> 3	> 3	> 3
$\mid n_\Gamma$ from mass peak center $\mid$	> 2	> 2	> 2	> 2	> 2	> 2
A	1.3333	1.3333	N/A	N/A	1.8333	N/A
B	-0.35	-0.35	N/A	N/A	-0.06	N/A

Appendix C

Efficiencies

C.1 Unidentified hadron efficiencies

Table C.1: Fit parameters from fits of the efficiencies for unidentified hadrons in $Au + Au$ at $\sqrt{s_{NN}} = 62$ GeV to $a\ exp(\frac{b}{p_T}^{c})$

centrality	a	b	c
0-5%	.767	.1498	1.316
5-10%	.7856	.1419	1.33
10-20%	.7975	.1408	1.464
20-30%	.8113	.1374	1.606
30-40%	.822	.1376	1.743
40-50%	.8321	.1327	1.781
50-60%	.8386	.1357	1.912
60-70%	.8387	.1511	2.381
70-80%	.8415	.1455	2.153

Table C.2: Fit parameters from fits of the efficiencies for unidentified hadrons in $Au + Au$ at $\sqrt{s_{NN}}$ = 62 GeV to $a\ exp(\frac{b}{p_T}^c)$

centrality	a	b	c
0-10%	0.838435	0.0704	0.9409
10-20%	0.843666	0.0681	1.0000
20-30%	0.843211	0.0610	1.0000
30-40%	0.848090	0.0638	1.0000
40-50%	0.856875	0.0606	0.9496
50-60%	0.851112	0.0584	1.0000

Table C.3: Fit parameters from fits of the efficiencies for unidentified hadrons in $Au + Au$ at $\sqrt{s_{NN}}$ = 62 GeV to $a\ exp(\frac{b}{p_T}^c)$

centrality	a	b	c
0-10%	0.8655	0.1333	0.9890
10-20%	0.8736	0.1207	0.9330
20-30%	0.8643	0.1503	1.1071
30-40%	0.8693	0.1269	0.9922
40-50%	0.8608	0.1511	1.1616
50-60%	0.8606	0.1971	1.3211

C.2 V^0 Efficiencies

Table C.4: Fit parameters from fits of the efficiencies for Λ baryons in $Au + Au$ at $\sqrt{s_{NN}}$ = 62 GeV to $a\ exp(\frac{b}{p_T}^c)$

		0-10%	10-20%	20-30%	30-40 %	40-50%	50-60%
	a	0.172	0.164	0.168	0.158	0.161	0.166
1< p_T <1.5	b	0.946	0.838	0.819	0.774	0.758	0.861
	c	1.587	1.800	1.825	1.902	2.020	1.895
	a	0.174	0.162	0.169	0.159	0.161	0.164
1.5< p_T <2	b	1.043	0.887	0.855	0.772	0.755	0.821

Continued on next page

Table C.4 – continued from previous page

		0-10%	10-20%	20-30%	30-40 %	40-50%	50-60%
	c	1.701	1.884	1.835	1.842	2.033	1.947
$2< p_T <2.5$	a	0.172	0.145	0.152	0.159	0.161	0.163
	b	0.969	0.915	0.913	0.845	0.755	0.789
	c	1.586	2.106	2.066	1.999	2.033	1.790
$2.5< p_T <3$	a	0.177	0.152	0.157	0.149	0.154	0.159
	b	1.468	0.953	0.924	0.889	0.911	0.926
	c	1.890	2.120	2.149	2.280	2.406	2.023
$3< p_T <3.5$	a	0.177	0.152	0.157	0.149	0.154	0.159
	b	1.468	0.953	0.924	0.889	0.911	0.926
	c	1.890	2.120	2.149	2.280	2.406	2.023
$3.5< p_T <4$	a	0.137	0.110	0.198	0.246	0.252	0.140
	b	0.038	0.051	0.023	0.011	0.009	0.048
	c	-0.005	-0.006	-0.004	-0.003	-0.003	-0.006
$4< p_T <5$	a	0.137	0.110	0.198	0.246	0.252	0.140
	b	0.038	0.051	0.023	0.011	0.009	0.048
	c	-0.005	-0.006	-0.004	-0.003	-0.003	-0.006
$p_T >5$	a	0.177	0.152	0.157	0.149	0.154	0.159
	b	1.468	0.953	0.924	0.889	0.911	0.926
	c	1.890	2.120	2.149	2.280	2.406	2.023

Table C.5: Fit parameters from fits of the efficiencies for $\bar{\Lambda}$ baryons in $Au + Au$ at $\sqrt{s_{NN}}$ = 62 GeV to $a\ exp(\frac{b}{p_T}^{c})$

		0-10%	10-20%	20-30%	30-40 %	40-50%	50-60%
$1< p_T <1.5$	a	0.158	0.163	0.169	0.169	0.186	0.196
	b	0.924	0.888	0.884	0.784	0.897	1.015
	c	1.767	1.683	1.752	1.659	1.479	1.444
$1.5< p_T <2$	a	0.163	0.158	0.174	0.178	0.187	0.205
	b	1.092	1.054	1.076	1.026	1.104	1.200

Continued on next page

Table C.5 – continued from previous page

		0-10%	10-20%	20-30%	30-40 %	40-50%	50-60%
	c	1.948	2.156	1.950	1.763	1.758	1.527
	a	0.161	0.139	0.152	0.167	0.189	0.198
2< p_T <2.5	b	1.042	0.946	0.968	0.860	0.904	0.981
	c	1.893	2.284	2.084	1.916	1.402	1.294
	a	0.163	0.146	0.155	0.155	0.165	0.183
2.5< p_T <3	b	1.414	0.967	0.953	0.914	1.006	1.058
	c	1.983	2.281	2.155	2.206	2.166	1.632
	a	0.163	0.146	0.155	0.155	0.165	0.183
3< p_T <3.5	b	1.414	0.967	0.953	0.914	1.006	1.058
	c	1.983	2.281	2.155	2.206	2.166	1.632
	a	0.113	0.149	0.227	0.148	0.072	0.224
3.5< p_T <4	b	0.047	0.036	0.010	0.042	0.070	0.013
	c	-0.006	-0.005	-0.002	-0.005	-0.008	-0.003
	a	0.113	0.149	0.227	0.148	0.072	0.224
4< p_T <5	b	0.047	0.036	0.010	0.042	0.070	0.013
	c	-0.006	-0.005	-0.002	-0.005	-0.008	-0.003
	a	0.163	0.146	0.155	0.155	0.165	0.183
p_T >5	b	1.414	0.967	0.953	0.914	1.006	1.058
	c	1.983	2.281	2.155	2.206	2.166	1.632

Table C.6: Fit parameters from fits of the efficiencies for K_S^0 baryons in $Au + Au$ at $\sqrt{s_{NN}}$ = 62 GeV to $a\ exp(\frac{b}{p_T}^c)$

		0-10%	10-20%	20-30%	30-40 %	40-50%	50-60%
	a	0.176	0.174	0.280	0.270	0.257	0.294
1< p_T <1.5	b	0.972	0.917	1.065	1.014	0.964	1.129
	c	1.606	1.796	1.589	1.778	1.924	1.563
	a	0.176	0.174	0.280	0.270	0.257	0.299
1.5< p_T <2	b	0.972	0.917	1.065	1.014	0.964	1.000

Continued on next page

Table C.6 – continued from previous page

		0-10%	10-20%	20-30%	30-40 %	40-50%	50-60%
	c	1.606	1.796	1.589	1.778	1.924	1.298
$2< p_T <2.5$	a	0.194	0.182	0.284	0.275	0.262	0.299
	b	0.989	0.895	0.936	0.907	0.866	1.000
	c	1.222	1.502	1.329	1.511	1.652	1.298
$2.5< p_T <3$	a	0.194	0.182	0.284	0.275	0.262	0.299
	b	0.989	0.895	0.936	0.907	0.866	1.000
	c	1.222	1.502	1.329	1.511	1.652	1.298
$3< p_T <3.5$	a	0.194	0.182	0.284	0.275	0.262	0.299
	b	0.989	0.895	0.936	0.907	0.866	1.000
	c	1.222	1.502	1.329	1.511	1.652	1.298
$3.5< p_T <4$	a	0.127	0.114	0.164	0.141	0.177	0.234
	b	0.014	0.022	0.041	0.051	0.038	0.014
	c	-0.002	-0.003	-0.004	-0.005	-0.004	-0.002
$4< p_T <5$	a	0.127	0.114	0.164	0.141	0.177	0.234
	b	0.014	0.022	0.041	0.051	0.038	0.014
	c	-0.002	-0.003	-0.004	-0.005	-0.004	-0.002
$p_T >5$	a	0.194	0.182	0.284	0.275	0.262	0.299
	b	0.989	0.895	0.936	0.907	0.866	1.000
	c	1.222	1.502	1.329	1.511	1.652	1.298

Appendix D

Centrality

	R	N_{part}	N_{bin}
0-10%	$101 \leq$ R	96	162
10-20%	$71 \leq$ R < 101	72	108
20-30%	$49 \leq$ R < 71	52	68
30-40%	$33 \leq$ R < 49	36	42
40-50%	$22 \leq$ R < 33	25	26
50-60%	$14 \leq$ R < 22	16	15

Table D.1: Centrality definitions for $Cu + Cu$ collisions at $\sqrt{s_{NN}} = 62$ GeV

	R	N_{part}	N_{bin}
0-10%	$139 \leq$ R	99	189
10-20%	$98 \leq$ R < 139	75	124
20-30%	$67 \leq$ R < 98	54	78
30-40%	$46 \leq$ R < 67	38	48
40-50%	$30 \leq$ R < 46	26	29
50-60%	$19 \leq$ R < 30	17	17

Table D.2: Centrality definitions for $Cu + Cu$ collisions at $\sqrt{s_{NN}} = 200$ GeV

	R	N_{part}	N_{bin}
0-5%	$373 \leq$ R	347	904
5-10%	$313 \leq$ R < 373	293	714
10-20%	$222 \leq$ R < 313	229	512
20-30%	$154 \leq$ R < 222	162	321
30-40%	$102 \leq$ R < 154	112	193
40-50%	$65 \leq$ R < 102	74	109
50-60%	$38 \leq$ R < 65	46	57
60-70%	$20 \leq$ R < 38	26	27
70-80%	$9 \leq$ R < 20	13	11

Table D.3: Centrality definitions for $Au + Au$ collisions at $\sqrt{s_{NN}} = 62$ GeV

Bibliography

[1] S. Bethke, *Experimental Tests of Asymptotic Freedom*, Prog. Part. Nucl. Phys. **58**, 351 (2007), hep-ex/0606035.

[2] G. Baym, *RHIC: From dreams to beams in two decades*, Nucl. Phys. **A698**, XXIII (2002), hep-ph/0104138.

[3] N. P. Samios, *RHIC: the early years*, Journal of Physics G: Nuclear and Particle Physics **34**, S181 (2007).

[4] L. McLerran, *T. D. Lee: Relativistic Heavy Ion Collisions and the Riken Brookhaven Center*, (2006).

[5] N. P. Samios and T. W. Ludlam, *Future high energy heavy ion physics at Brookhaven*, Nucl. Phys. A **498**, 323c (1989).

[6] M. A. Stephanov, *QCD phase diagram: An overview*, PoS **LAT2006**, 024 (2006), hep-lat/0701002.

[7] S. D. Bass, *How Does the Proton Spin?*, Science **315**, 1672 (2007).

[8] M. G. Alford, A. Schmitt, K. Rajagopal, and T. Schafer, *Color superconductivity in dense quark matter*, Rev. Mod. Phys. **80**, 1455 (2008), 0709.4635.

[9] U. M. Heller, *Recent progress in finite temperature lattice QCD*, PoS **LAT2006**, 011 (2006), hep-lat/0610114.

[10] M. A. Alford, *Color superconductivity in ultra-dense quark matter*, PoS **LAT2006**, 001 (2006).

[11] E. Shuryak, *Some thoughts on critical and tricritical points and deconfinement*, PoS **CPOD2006**, 026 (2006), nucl-th/0609011.

[12] S. Bass, Collision dynamics and cascades, Talk at Quark Matter 2001, 2001.

[13] T. Ullrich, Rhic experimental overview - what we have learned, Talk at Colliders to Cosmic Rays 2007, 2007.

[14] T. Ullrich, The charm and beauty of an (almost) perfect liquid - open heavy flavor production at rhic, Seminar given at the NSCL at MSU on February 7, 2007, 2007.

[15] T. Renk, *Mach cones and dijets: Jet quenching and fireball expansion dynamics*, (2006), hep-ph/0608333.

[16] S. A. Bass *et al.*, *Last call for RHIC predictions*, Nucl. Phys. **A661**, 205 (1999), nucl-th/9907090.

[17] C. Adler *et al.* (STAR Collaboration), *Centrality dependence of high p_T hadron suppression in Au+Au collisions at $\sqrt{s}_{NN}$ = 130-GeV*, Phys. Rev. Lett. **89**, 202301 (2002), nucl-ex/0206011.

[18] J. W. Cronin *et al.*, *Production of Hadrons with Large Transverse Momentum at 200-GeV, 300-GeV, and 400-GeV*, Phys. Rev. **D11**, 3105 (1975).

[19] J. Adams *et al.* (STAR Collaboration), *Evidence from d + Au measurements for final-state suppression of high p(T) hadrons in Au + Au collisions at RHIC*, Phys. Rev. Lett. **91**, 072304 (2003), nucl-ex/0306024.

[20] A. Adare *et al.* (PHENIX Collaboration), *Suppression pattern of neutral pions at high transverse momentum in Au+Au collisions at sqrt(sNN) = 200 GeV and constraints on medium transport coefficients*, Phys. Rev. Lett. **101**, 232301 (2008), 0801.4020.

[21] R. Baier and D. Schiff, *Deciphering the properties of the medium produced in heavy ion collisions at RHIC by a pQCD analysis of quenched large p(T) pi0 spectra*, JHEP **09**, 059 (2006), hep-ph/0605183.

[22] K. J. Eskola, H. Honkanen, C. A. Salgado, and U. A. Wiedemann, *The fragility of high-p(T) hadron spectra as a hard probe*, Nucl. Phys. **A747**, 511 (2005), hep-ph/0406319.

[23] F. Arleo, *Tomography of cold and hot QCD matter: Tools and diagnosis. ((V))*, JHEP **11**, 044 (2002), hep-ph/0210104.

[24] A. Adare *et al.* (PHENIX Collaboration), *Energy Loss and Flow of Heavy Quarks in Au+Au Collisions at sqrt(sNN) = 200 GeV*, Phys. Rev. Lett. **98**, 172301 (2007), nucl-ex/0611018.

[25] L. McLerran, *The Color Glass Condensate and Glasma*, (2008), 0804.1736.

[26] B. C. Reisert (ZEUS Collaboration), *HERA Combined Cross Sections and Parton Densities*, (2008), 0809.4946.

[27] F. Becattini, *An introduction to the Statistical Hadronization Model*, (2009), 0901.3643.

[28] S. Wheaton and J. Cleymans, *THERMUS: A thermal model package for ROOT*, Comput. Phys. Commun. **180**, 84 (2009), hep-ph/0407174.

[29] J. Adams *et al.* (STAR Collaboration), *Experimental and theoretical challenges in the search for the quark gluon plasma: The STAR collaboration's critical assessment of the evidence from RHIC collisions*, Nucl. Phys. **A757**, 102 (2005), nucl-ex/0501009.

[30] P. Braun-Munzinger, K. Redlich, and J. Stachel, *Particle production in heavy ion collisions*, (2003), nucl-th/0304013.

[31] P. F. Kolb, J. Sollfrank, and U. W. Heinz, *Anisotropic transverse flow and the quark-hadron phase transition*, Phys. Rev. **C62**, 054909 (2000), hep-ph/0006129.

[32] P. Huovinen, P. F. Kolb, U. W. Heinz, P. V. Ruuskanen, and S. A. Voloshin, *Radial and elliptic flow at RHIC: further predictions*, Phys. Lett. **B503**, 58 (2001), hep-ph/0101136.

[33] D. Teaney, J. Lauret, and E. V. Shuryak, *A hydrodynamic description of heavy ion collisions at the SPS and RHIC*, (2001), nucl-th/0110037.

[34] T. Hirano, K. Morita, S. Muroya, and C. Nonaka, *Hydrodynamical analysis of hadronic spectra in the 130- GeV/nucleon Au + Au collisions*, Phys. Rev. **C65**, 061902 (2002), nucl-th/0110009.

[35] P. F. Kolb and U. W. Heinz, *Hydrodynamic description of ultrarelativistic heavy-ion collisions*, (2003), nucl-th/0305084.

[36] A. Krasnitz, Y. Nara, and R. Venugopalan, *Elliptic flow of colored glass in high energy heavy ion collisions*, Phys. Lett. **B554**, 21 (2003), hep-ph/0204361.

[37] D. Teaney and R. Venugopalan, *Classical computation of elliptic flow at large transverse momentum*, Phys. Lett. **B539**, 53 (2002), hep-ph/0203208.

[38] B. Z. Kopeliovich, A. H. Rezaeian, and I. Schmidt, *Azimuthal Asymmetry of pions in pp and pA collisions*, (2008), 0809.4327.

[39] K. G. Boreskov, A. B. Kaidalov, and O. V. Kancheli, *Anisotropic flows from initial state of a fast nucleus*, Eur. Phys. J. **C58**, 445 (2008), 0809.0625.

[40] S. A. Voloshin, A. M. Poskanzer, and R. Snellings, *Collective phenomena in non-central nuclear collisions*, (2008), 0809.2949.

[41] M. L. Miller, K. Reygers, S. J. Sanders, and P. Steinberg, *Glauber modeling in high energy nuclear collisions*, Ann. Rev. Nucl. Part. Sci. **57**, 205 (2007), nucl-ex/0701025.

[42] A. Adare *et al.* (PHENIX Collaboration), *Scaling properties of azimuthal anisotropy in Au + Au and Cu + Cu collisions at s(NN)**(1/2) = 200-GeV*, Phys. Rev. Lett. **98**, 162301 (2007), nucl-ex/0608033.

[43] B. I. Abelev *et al.* (STAR Collaboration), *Centrality dependence of charged hadron and strange hadron elliptic flow from* $\sqrt{s_N N}$ *= 200 GeV Au+Au collisions*, Phys. Rev. **C77**, 054901 (2008), 0801.3466.

[44] B. I. Abelev *et al.* (the STAR Collaboration), *Mass, quark-number, and s(NN)**(1/2) dependence of the second and fourth flow harmonics in ultra-relativistic nucleus nucleus collisions*, Phys. Rev. **C75**, 054906 (2007), nucl-ex/0701010.

[45] S. Salur, *Statistical models and STAR's strange data*, (2006), nucl-ex/0606006.

[46] R. J. Fries, V. Greco, and P. Sorensen, *Coalescence Models For Hadron Formation From Quark Gluon Plasma*, (2008), 0807.4939.

[47] M. E. Peskin and D. V. Schroeder, *An Introduction to Quantum Field Theory; 1995 ed.* (Westview, Boulder, CO, 1995), Includes exercises.

[48] J.-y. Jia, *How to Make Sense of the Jet Correlations Results at RHIC?*, (2008), 0810.0051.

[49] J. Adams *et al.* (STAR Collaboration), *The energy dependence of p(t) angular correlations inferred from mean-p(t) fluctuation scale dependence in heavy ion collisions at the SPS and RHIC*, J. Phys. **G33**, 451 (2007), nucl-ex/0605021.

[50] J. Adams *et al.* (STAR Collaboration), *Direct observation of dijets in central Au + Au collisions at s(NN)**(1/2) = 200-GeV*, Phys. Rev. Lett. **97**, 162301 (2006), nucl-ex/0604018.

[51] J. Adams *et al.* (STAR Collaboration), *Distributions of charged hadrons associated with high transverse momentum particles in p p and Au + Au collisions at s(NN)**(1/2) = 200-GeV*, Phys. Rev. Lett. **95**, 152301 (2005), nucl-ex/0501016.

[52] J. Adams *et al.* (STAR Collaboration), *Azimuthal anisotropy and correlations at large transverse momenta in p + p and Au + Au collisions at s(NN)**(1/2) = 200-GeV*, Phys. Rev. Lett. **93**, 252301 (2004), nucl-ex/0407007.

[53] J. Adams *et al.* (STAR Collaboration), *Evidence from d + Au measurements for final-state suppression of high p(T) hadrons in Au + Au collisions at RHIC*, Phys. Rev. Lett. **91**, 072304 (2003), nucl-ex/0306024.

[54] C. Adler *et al.* (STAR Collaboration), *Disappearance of back-to-back high p(T) hadron correlations in central Au + Au collisions at s(NN)**(1/2) = 200-GeV*, Phys. Rev. Lett. **90**, 082302 (2003), nucl-ex/0210033.

[55] C. Adler *et al.* (STAR Collaboration), *Azimuthal anisotropy and correlations in the hard scattering regime at RHIC*, Phys. Rev. Lett. **90**, 032301 (2003), nucl-ex/0206006.

[56] S. Afanasiev *et al.* (PHENIX Collaboration), *Particle-species dependent modification of jet-induced correlations in Au+Au collisions at s(NN)**(1/2) = 200 GeV*, Phys. Rev. Lett. **101**, 082301 (2008), 0712.3033.

[57] A. Adare *et al.* (PHENIX Collaboration), *Dihadron azimuthal correlations in Au+Au collisions at sqrts(NN)**(1/2) = 200 GeV*, Phys. Rev. **C78**, 014901 (2008), 0801.4545.

[58] A. Adare *et al.* (PHENIX Collaboration), *Transverse momentum and centrality dependence of dihadron correlations in Au+Au collisions at s(NN)**(1/2)=200 GeV: Jet-quenching and the response of partonic matter*, Phys. Rev. **C77**, 011901 (2008), 0705.3238.

[59] A. Adare *et al.* (PHENIX Collaboration), *System size and energy dependence of jet-induced hadron pair correlation shapes in Cu + Cu and Au + Au collisions at s(NN)**(1/2) = 200-GeV and 62.4-GeV*, Phys. Rev. Lett. **98**, 232302 (2007), nucl-ex/0611019.

[60] S. S. Adler *et al.* (PHENIX Collaboration), *Jet properties from dihadron correlations in p + p collisions at s**(1/2) = 200-GeV*, Phys. Rev. **D74**, 072002 (2006), hep-ex/0605039.

[61] S. S. Adler *et al.* (PHENIX Collaboration), *Modifications to di-jet hadron pair correlations in Au + Au collisions at s(NN)**(1/2) = 200-GeV*, Phys. Rev. Lett. **97**, 052301 (2006), nucl-ex/0507004.

[62] S. S. Adler *et al.* (PHENIX Collaboration), *Jet structure from dihadron correlations in d + Au collisions at s(NN)**(1/2) = 200-GeV*, Phys. Rev. **C73**, 054903 (2006), nucl-ex/0510021.

[63] M. J. Horner (STAR Collaboration), *Azimuthal di-hadron correlations in Au + Au collisions at s(NN)**(1/2) = 200-GeV from STAR*, AIP Conf. Proc. **842**, 125 (2006), nucl-ex/0606025.

[64] N. Borghini, *Momentum conservation and correlation analyses in heavy- ion collisions at ultrarelativistic energies*, Phys. Rev. **C75**, 021904 (2007), nucl-th/0612093.

[65] N. Armesto, C. A. Salgado, and U. A. Wiedemann, *Measuring the collective flow with jets*, Phys. Rev. Lett. **93**, 242301 (2004), hep-ph/0405301.

[66] V. Koch, A. Majumder, and X.-N. Wang, *Cherenkov Radiation from Jets in Heavy-ion Collisions*, Phys. Rev. Lett. **96**, 172302 (2006), nucl-th/0507063.

[67] J. Hofmann, H. Stocker, U. Heinz, W. Scheid, and W. Greiner, *Possibility of Detecting Density Isomers in High-Density Nuclear Mach Shock Waves*, Phys. Rev. Lett. **36**, 88 (1975).

[68] J. Casalderrey-Solana and E. V. Shuryak, *Conical flow in a medium with variable speed of sound*, (2005), hep-ph/0511263.

[69] J. G. Ulery, *Conical Emission in Heavy Ion Collisions*, J. Phys. **G35**, 104032 (2008), 0807.1613.

[70] J. G. Ulery, *Two- and Three-Particle Jet-Like Correlations*, (2008), 0801.4904.

[71] J. G. Ulery (STAR Collaboration), *Three-Particle Azimuthal Correlations*, Nucl. Phys. **A783**, 511 (2007), nucl-ex/0609047.

[72] C. A. Pruneau, *Three-particle cumulant Study of Conical Emission*, (2008), 0810.1461.

[73] C. Pruneau (STAR Collaboration), *Search for Conical Emission with Three-Particle Correlations*, (2007), nucl-ex/0703010.

[74] J. Putschke (STAR Collaboration), *Intra-jet correlations of high-p(t) hadrons from STAR*, J. Phys. G **34**, 679 (2007).

[75] M. P. McCumber and f. t. P. Collaboration, *The 'Shoulder' and the 'Ridge' in PHENIX*, J. Phys. **G35**, 104081 (2008), 0804.4319.

[76] B. Alver *et al.* (PHOBOS Collaboration), *High p_T Triggered Delta-eta,Delta-phi Correlations over a Broad Range in Delta-eta*, J. Phys. **G35**, 104080 (2008), 0804.3038.

[77] J. Bielcikova (STAR Collaboration), *Azimuthal and pseudo-rapidity correlations with strange particles at intermediate-p(T) at RHIC*, J. Phys. **G34**, S929 (2007), nucl-ex/0701047.

[78] X.-N. Wang, *High-p_T Hadron Spectra, Azimuthal Anisotropy and Back- to-Back Correlations in High-energy Heavy-ion Collisions*, Phys. Lett. **B595**, 165 (2004), nucl-th/0305010.

[79] J. Bielcikova (STAR Collaboration), *Two-particle correlations with strange baryons and mesons at RHIC*, (2007), 0707.3100.

[80] C. Suarez, Particle dependence of the ridge and the jet, Poster given at Quark Matter 2008, 2008.

[81] B. I. Abelev (STAR Collaboration), *Multi-strange baryon correlations at RHIC*, (2007), 0705.3371.

[82] A. Feng (STAR Collaboration), *Reaction Plane Dependent Away-side Modification and Near-side Ridge in Au+Au Collisions*, J. Phys. G **35**, 104082 (2008).

[83] P. K. Netrakanti (STAR Collaboration), *Identifying the underlying physics of the ridge via 3- particle $\Delta\eta - \Delta\eta$ correlations*, J. Phys. **G35**, 104010 (2008), 0804.4417.

[84] M. Daugherity (STAR Collaboration), *Anomalous centrality variation of minijet angular correlations in Au-Au collisions at 62 and 200 GeV from STAR*, J. Phys. **G35**, 104090 (2008), 0806.2121.

[85] S. Salur (STAR Collaboration), *A Short Review on Jet Identification*, nucl-ex/0810.0500.

[86] B. I. Abelev *et al.* (STAR Collaboration), *Longitudinal double-spin asymmetry for inclusive jet production in p+p collisions at sqrt(s)=200 GeV*, Phys. Rev. Lett. **100**, 232003 (2008), 0710.2048.

[87] M. Cacciari, G. P. Salam, and G. Soyez, *The Catchment Area of Jets*, JHEP **04**, 005 (2008), 0802.1188.

[88] M. Cacciari, *FastJet: A Code for fast k_t clustering, and more*, (2006), hep-ph/0607071.

[89] S. Salur (STAR Collaboration), *Searching for Jets in Heavy Ion Collisions*, nucl-ex/0809.1606.

[90] J. Putschke (STAR Collaboration), *Searching for Jets in Heavy Ion Collisions*, nucl-ex/0809.1419.

[91] S. Salur (STAR Collaboration), *First Direct Measurement of Jets in $\sqrt{s_{NN}} = 200$ GeV Heavy Ion Collisions by STAR*, nucl-ex/0809.1609.

[92] T. Ullrich, Rhic: From colliding ions to physics results, Series of lectures presented at the QCD school in Les Houches, France, 2008.

[93] M. Anderson, T. Ludlam, and S. Ozaki, *RHIC project overview*, Nucl. Instrum. Meth. A **499**, 235 (2003).

[94] K. H. Ackermann *et al.*, *STAR detector overview*, Nucl. Instrum. Meth. A **499**, 624 (2003).

[95] M. Anderson *et al.*, *The STAR time projection chamber: a unique tool for studying high multiplicity events at RHIC*, Nucl. Instrum. Meth. A **499**, 659 (2003).

[96] G. Van Buren, private communication, 2009.

[97] M. Anderson *et al.*, *A readout system for the STAR time projection chamber*, Nucl. Instrum. Meth. A **499**, 679 (2003).

[98] W.-M. Yao *et al.*, *Review of Particle Physics*, Journal of Physics G **33**, 1+ (2006).

[99] S. Sevil, *Investigation of Hadronic Resonances with STAR*, PhD thesis, Yale, 2006.

[100] P. Maybeck, *Stochastic models, estimation, and control Volume 1* (Academic Press, 1979).

[101] B. I. Abelev *et al.* (STAR Collaboration), *Forward* Λ *Production and Nuclear Stopping Power in* $d + Au$ *Collisions at* $\sqrt{s_{NN}} = 200$ *GeV*, Phys. Rev. **C76**, 064904 (2007), 0706.0472.

[102] B. I. Abelev *et al.* (STAR Collaboration), *Enhanced strange baryon production in Au+Au collisions compared to p+p at sqrts = 200 GeV*, Phys. Rev. **C77**, 044908 (2008), 0705.2511.

[103] B. I. Abelev *et al.* (the STAR Collaboration), *Mass, quark-number, and s(NN)**(1/2) dependence of the second and fourth flow harmonics in ultra-relativistic nucleus nucleus collisions*, Phys. Rev. **C75**, 054906 (2007), nucl-ex/0701010.

[104] B. I. Abelev *et al.* (STAR Collaboration), *Neutral kaon interferometry in Au + Au collisions at s(NN)**(1/2) = 200-GeV*, Phys. Rev. **C74**, 054902 (2006), nucl-ex/0608012.

[105] B. I. Abelev *et al.* (STAR Collaboration), *Strange particle production in p + p collisions at s**(1/2) = 200-GeV*, Phys. Rev. **C75**, 064901 (2007), nucl-ex/0607033.

[106] J. Adams *et al.* (STAR Collaboration), *Scaling Properties of Hyperon Production in Au+Au Collisions at sqrt(s_NN) = 200 GeV*, Phys. Rev. Lett. **98**, 062301 (2007), nucl-ex/0606014.

[107] J. Adams *et al.* (STAR Collaboration), *Proton Lambda correlations in central Au + Au collisions at s(NN)**(1/2) = 200-GeV*, Phys. Rev. **C74**, 064906 (2006), nucl-ex/0511003.

[108] J. Adams *et al.* (STAR Collaboration), *Multi-strange baryon elliptic flow in Au + Au collisions at s(NN)**(1/2) = 200-GeV*, Phys. Rev. Lett. **95**, 122301 (2005), nucl-ex/0504022.

[109] J. Adams *et al.* (STAR Collaboration), *Multi-strange baryon production in Au Au collisions at s(NN)**(1/2) = 130-GeV*, Phys. Rev. Lett. **92**, 182301 (2004), nucl-ex/0307024.

[110] J. Adams *et al.* (STAR Collaboration), *Particle dependence of azimuthal anisotropy and nuclear modification of particle production at moderate p(T) in Au + Au collisions at s(NN)**(1/2) = 200-GeV*, Phys. Rev. Lett. **92**, 052302 (2004), nucl-ex/0306007.

[111] C. Adler *et al.* (STAR Collaboration), *Kaon production and kaon to pion ratio in Au + Au collisions at s(NN)**(1/2) = 130-GeV*, Phys. Lett. **B595**, 143 (2004), nucl-ex/0206008.

[112] C. Adler *et al.* (STAR Collaboration), *Azimuthal anisotropy of K0(S) and Lambda + anti-Lambda production at mid-rapidity from Au + Au collisions at s(NN)**(1/2) = 130-GeV*, Phys. Rev. Lett. **89**, 132301 (2002), hep-ex/0205072.

[113] C. Adler *et al.* (STAR Collaboration), *Mid-rapidity Lambda and Antilambda production in Au + Au collisions at s(NN)**(1/2) = 130-GeV*, Phys. Rev. Lett. **89**, 092301 (2002), nucl-ex/0203016.

[114] W. M. Yao *et al.* (Particle Data Group Collaboration), *Review of particle physics*, J. Phys. **G33**, 1 (2006).

[115] Y. Guo, *Identified Particle Correlations At Intermediate Transverse Momentum In Relativistic Heavy Ion Collisions*, PhD thesis, Wayne State University, 2005.

[116] S. Galliard, *A study of jets at the STAR experiment at the Relativistic Heavy Ion Collider vi two-particle correlations*, PhD thesis, University of Birmingham, 2008.

[117] J. Bielcikova (STAR Collaboration), *Medium properties and jet-medium interaction from STAR*, (2008), 0806.2261.

[118] J. Bielcikova (STAR Collaboration), *High-p(T) strange particle spectra and correlations in STAR*, Nucl. Phys. **A783**, 565 (2007), nucl-ex/0612028.

[119] J. Bielcikova (STAR Collaboration), *High-p(T) azimuthal correlations of neutral strange baryons and mesons in STAR at RHIC*, AIP Conf. Proc. **842**, 53 (2006), nucl-ex/0603008.

[120] M. Bombara (STAR Collaboration), *Is there a strange baryon / meson dependence in correlations in STAR?*, J. Phys. **G35**, 044065 (2008).

[121] Y. Guo (STAR Collaboration), *Identified particle correlation studies in central Au + Au collisions at s(NN)**(1/2) = 200-GeV*, J. Phys. **G31**, S549 (2005), nucl-ex/0502015.

[122] Y. Guo (STAR Collaboration), *Identified high p(T) particle correlation studies in central Au + Au collisions at s(NN)**(1/2) = 200-GeV*, (2004), hep-ex/0403018.

[123] B. Abelev, *Multi-Strange Baryon Correlations at RHIC*, PhD thesis, Yale, 2007.

[124] A. Iordanova (STAR Collaboration), *Particle Production at RHIC*, (2008), 0806.0286.

[125] M. Estienne, *Proprits chimiques et dynamiques des collisions d'ions lourds aux nergies du RHIC par la mesure de la production des baryons doublement tranges dans l'exprience STAR*, PhD thesis, SUBATECH, 2005.

[126] A. Timmins, *Neutral Strange Particle Production in Relativistic Cu+Cu Collisions at* $\sqrt{s_{NN}} = 200$ *GeV*, PhD thesis, University of Birmingham, 2008.

[127] J. Adams *et al.* (STAR Collaboration), *Pion interferometry in Au + Au collisions at s(NN)**(1/2) = 200-GeV*, Phys. Rev. **C71**, 044906 (2005), nucl-ex/0411036.

[128] B. B. Back *et al.* (PHOBOS Collaboration), *Centrality and pseudorapidity dependence of elliptic flow for charged hadrons in Au + Au collisions at s(NN)**(1/2) = 200-GeV*, Phys. Rev. **C72**, 051901 (2005), nucl-ex/0407012.

[129] B. B. Back *et al.* (PHOBOS Collaboration), *Energy dependence of elliptic flow over a large pseudorapidity range in Au + Au collisions at RHIC*, Phys. Rev. Lett. **94**, 122303 (2005), nucl-ex/0406021.

[130] J. Adams *et al.* (STAR Collaboration), *FILL IN THE NAME OF OANA'S PAPER*, CHECKME **WRONG**, 451 (2007), nucl-ex/0605021.

[131] J. Adams *et al.* (STAR Collaboration), *FILL IN THE NAME OF JOERN'S RIDGE PAPER*, CHECKME **WRONG**, 451 (2007), nucl-ex/0605021.

[132] J. Bielcikova, S. Esumi, K. Filimonov, S. Voloshin, and J. P. Wurm, *Elliptic flow contribution to two-particle correlations at different orientations to the reaction plane*, Phys. Rev. **C69**, 021901 (2004), nucl-ex/0311007.

[133] S. A. Voloshin (STAR Collaboration), *Energy and system size dependence of charged particle elliptic flow and v(2)/epsilon scaling*, J. Phys. **G34**, S883 (2007), nucl-ex/0701038.

[134] J. Adams *et al.* (STAR Collaboration), *Azimuthal anisotropy and correlations at large transverse momenta in p + p and Au + Au collisions at s(NN)**(1/2) = 200-GeV*, Phys. Rev. Lett. **93**, 252301 (2004), nucl-ex/0407007.

[135] A. Tang, private communication, 2007.

[136] S. Shi (STAR Collaboration), *Strange hadron elliptic flow from 200 GeV Cu+Cu collisions*, (2008), 0806.0763.

[137] J. Bielcikova, Private communication, 2007-2009.

[138] B. Abelev, *Multi-Strange Baryon Correlations at RHIC*, PhD thesis, Yale University, 2007.

[139] A. R. Timmins (STAR Collaboration), *The Centrality Dependence of Strange Baryon and Meson Production in Cu+Cu and Au+Au sqrt(sNN) = 200 GeV collisions*, Int. J. Mod. Phys. **E16**, 2055 (2007), 0708.3290.

[140] M. A. C. Lamont (STAR Collaboration), *Identified particles at large transverse momenta in STAR in Au + Au collisions at s(NN)**(1/2) = 200-GeV*, J. Phys. **G30**, S963 (2004), nucl-ex/0403059.

[141] T. Sjostrand, L. Lonnblad, S. Mrenna, and P. Skands, *Pythia 6.3 physics and manual*, (2003), hep-ph/0308153.

[142] R. D. Field (CDF Collaboration), *The underlying event in hard scattering processes*, (2002), hep-ph/0201192.

[143] J. Adams *et al.* (STAR Collaboration), *The Multiplicity dependence of inclusive p_t spectra from pp collisions at $\sqrt{s}$ = 200-GeV*, Phys. Rev. **D74**, 032006 (2006), nucl-ex/0606028.

[144] J. Adams *et al.* (STAR Collaboration), *Identified hadron spectra at large transverse momentum in p + p and d + Au collisions at s(NN)**(1/2) = 200-GeV*, Phys. Lett. **B637**, 161 (2006), nucl-ex/0601033.

[145] S. A. Voloshin, *Anisotropic collective phenomena in ultra-relativistic nuclear collisions*, (2009), 0902.0581.

[146] C. A. Pruneau, S. Gavin, and S. A. Voloshin, *Transverse Radial Flow Effects on Two- and Three-Particle Angular Correlations*, Nucl. Phys. **A802**, 107 (2008), 0711.1991.

[147] J. Takahashi *et al.*, *Topology studies of hydrodynamics using two particle correlation analysis*, (2009), 0902.4870.

[148] E. V. Shuryak, *On the Origin of the 'Ridge' phenomenon induced by Jets in Heavy Ion Collisions*, Phys. Rev. **C76**, 047901 (2007), 0706.3531.

[149] A. Dumitru, F. Gelis, L. McLerran, and R. Venugopalan, *Glasma flux tubes and the near side ridge phenomenon at RHIC*, Nucl. Phys. **A810**, 91 (2008), 0804.3858.

[150] F. Gelis, T. Lappi, and R. Venugopalan, *High energy factorization and long range rapidity correlations in the Glasma*, (2008), 0810.4829.

[151] R. Mizukawa *et al.*, *Search for a Ridge Structure Origin with Shower Broadening and Jet Quenching*, J. Phys. G **35**, 104083 (2008).

[152] S. Gavin, L. McLerran, and G. Moschelli, *Long Range Correlations and the Soft Ridge in Relativistic Nuclear Collisions*, (2008), 0806.4718.

[153] R. C. Hwa and C. B. Yang, *Production of strange particles at intermediate p(T) at RHIC*, (2006), nucl-th/0602024.

[154] C. B. Chiu and R. C. Hwa, *Particles Associated with Omega Produced at Intermediate pT*, Phys. Rev. **C76**, 024904 (2007), 0704.2616.

[155] R. C. Hwa, *Hadron Correlations in Jets and Ridges through Parton Recombination*, (2009), 0904.2159.

[156] C. B. Chiu and R. C. Hwa, *Dependence of Ridge Formation on Trigger Azimuth: Correlated Emission Model*, (2008), 0809.3018.

[157] C. yin Wong, *Ridge Structure associated with the Near-Side Jet in the (Delta phi)-(Delta eta) Correlation*, Phys. Rev. C **76**, 054908 (2007).

[158] C. yin Wong, private communication, 2008.

[159] C. yin Wong, *The Momentum Kick Model Description of the Near-Side Ridge and Jet Quenching*, hep-ph/0806.2154.

[160] A. Majumder, B. Muller, and S. A. Bass, *Longitudinal Broadening of Quenched Jets in Turbulent Color Fields*, Phys. Rev. Lett. **99**, 042301 (2007), hep-ph/0611135.

[161] H. Crawford, Star future plans and upgrades, Presented at 2009 RHIC/AGS User's Meeting, 2009.

[162] J. Putschke (STAR Collaboration), *First fragmentation function measurements from full jet reconstruction in heavy-ion collisions at* $\sqrt{s_{\rm NN}} = 200$ *GeV by STAR*, (2008), 0809.1419.

[163] M. Szuba (NA49 Collaboration), *Energy and System-size Dependence of Two-particle Azimuthal Correlations of High-pT Charged Hadrons at the CERN SPS*, (2008), 0809.5210.

[164] M. Szuba and f. t. N. Collaboration, *Two-particle Azimuthal Correlations of High-pT Charged Hadrons at the CERN SPS*, (2008), 0805.4637.